

**Development and Translation of Light Scatter Imaging and micro-Computed
Tomography to Improve the Surgical Resection of Breast Cancer**

A Thesis

Submitted to the Faculty

in partial fulfillment of the requirements for the

degree of

Doctor of Philosophy

by

DAVID M McCLATCHY III

Thayer School of Engineering

Dartmouth College

Hanover, New Hampshire

Date

May, 2018

Examining Committee:

Chairman _____
Brian W. Pogue, Ph. D.

Member _____
Keith D. Paulsen, Ph. D.

Member _____
Wendy A. Wells, M.D.

Member _____
Stephen C. Kanick, Ph. D.

Member _____
Bruce J. Tromberg, Ph. D.

F. Jon Kull, Ph.D.
Dean of Graduate and Advanced Studies

Abstract

Breast conserving surgery (BCS), when combined with radiation therapy, is a common treatment for localized breast cancer and offers similar outcomes to a mastectomy but with a far less invasive surgical procedure. Unfortunately, 20%-40% of patients who undergo BCS require a second surgery because of an incomplete initial excision, as determined by pathologically positive surgical specimen margins. The fundamental goal of this thesis work is to develop and translate two emerging technologies: light scatter imaging and micro-Computed Tomography (CT), to aid in the surgical resection of breast cancer. A new technique for wide-field sensing and quantification of superficial light scattering was developed, utilizing high spatial frequency structured illumination. This method was validated on solutions of particle suspensions with tunable scattering properties, and subsequently tested on a cohort of n=31 freshly resected breast tissue specimens of various malignant and benign pathologies. This work demonstrated that the quantified light scattering parameters were sensitive to the tissue diagnosis and also predictive of histological features, which in turn could distinguish malignant from benign specimens with 90% sensitivity, 81% specificity, and 84% accuracy. A second generation, multi-spectral structured illumination imaging system was developed and combined with a micro-CT system, allowing for superficial optical scattering to be spatially co-registered to volumetric tumor architecture rendered from the micro-CT, with which a total of n=69 BCS slices have been imaged across 8 malignant tumor subtypes. A reader study was performed to give an initial measurement of the diagnostic potential micro-CT. A cohort of n=32 whole, inked specimens were imaged, and the reader's binary margin diagnosis matched the final pathology for 66% of the specimens with a negative predictive value of

90%. This thesis work experimentally motivates the value for a multi-modal imaging approach for BCS guidance, as the more sensitive light scatter imaging can be guided by the rapid, volumetric micro-CT reading, and will be prospectively evaluated in a future clinical trial.

Preface

When I was 20 years old as a 3rd year undergraduate at Dartmouth, I sent out a flurry of uninvited emails to essentially all of the biomedical engineering professors at Thayer, in the hopes that one of them would respond and let me come work for them. Professor Pogue was the sole respondent, setting off a chain of events which have led me to completing my doctoral thesis. If he had just written off or deleted the email, literally none of this would have happened. Along with Brian, Dr. Keith Paulsen has been with me from the beginning and has been instrumental in getting me involved the Optics in Medicine group. I would also like to especially thank Dr. Wendy Wells, who has gone above and beyond her duties as a clinical collaborator and personally sees to the progress of work and my academic development. Additionally, I would thank to thank Dr. Richard Barth and Dr. Rebecca Zuurbier for enthusiastically pushing this research into the clinic. I would also like thank Prof. “Chad” Kanick, who, to the chagrin of many, always outwardly displayed his affection for scattering phase functions, and taught me almost everything I now know about the subject. Finally, I would like to like my friends and family, without whom I would not have started or completed this journey. In particular, my supportive parents and loving girlfriend Nadia.

Table of Contents

Abstract	ii
Preface	iv
Table of Contents	v
List of Figures	viii
List of Acronyms	xi
1. Introduction	1
1.1. Breast Conserving Surgery and Positive Surgical Margins	1
1.2. State of the Art: Review of Solutions and Shortcomings	3
1.3. Project Rationale	5
1.3.1. Light Scattering as a Contrast Mechanism	5
1.3.2. Multimodal Imaging	7
1.4. Thesis Overview	9
2. Light Scatter Imaging: Theory and Measurement	18
2.1. Light Transport in Turbid Media	18
2.1.1. Radiative Transport Equation and Optical Properties	18
2.1.2. Monte Carlo as a Numerical Solution to RTE	19
2.1.3. The Diffusion Approximation of the RTE	21
2.1.4. Transport in the Spatial Frequency Domain	23
2.2. Wide-Field Light Scatter Imaging with High Spatial Frequency Structured Illumination	26
2.3. Quantification of Light Scattering with Structured Illumination	30
2.3.1. Phase Function Quantification, and Inversion Problem	31

2.3.2. Proof of Concept in Silico, in Vitro, and in Vivo	32
3. Intraoperative Near Infrared Imaging of Inked Lumpectomy Specimens Utilizing Molecular Dyes	39
3.1. Background and Goals	39
3.2. Published Work	39
4. Quantitative Imaging of Tissue Microstructure in Freshly Resected Human Breast Specimens	44
4.1. Background and Goals	44
4.2. Published Work	44
5. Monochromatic Quantitative Imaging of Intratumoral Morphological Heterogeneity in a Murine Model	59
5.1. Background and Goals	59
5.2. Published Work	59
6. Prediction of Stromal Versus Epithelial Proportions in Freshly Resected Human Breast Specimens	68
6.1. Background and Goals	68
6.2. Submitted Manuscript for Publication	68
7. Calibration and Analysis of a Multimodal Micro-Computed Tomography and Structured Light Imaging System	94
7.1. Background and Goals	94
7.2. Published Work	94
8. Assessment of Whole Lumpectomy Specimens with Micro-CT	114
8.1. Background and Goals	114

8.2. Submitted Manuscript for Publication	114
9. Conclusions	132
9.1. Key Findings and Impact	132
9.1.1. Molecular Dyes for Intraoperative NIR Imaging during BCS	132
9.1.2. Light Scatter Imaging and Quantification	132
9.1.3. Optical-CT Multimodal System Development & Translation	134
9.1.4. Micro-CT Analysis of Whole Lumpectomy Specimens	136
9.2. Limitations	137
9.2.1. Biological Limitations	137
9.2.2. Technical Limitations	138
9.3. Proposed Recommendations for Future Work	140
10. Appendix: Selected MATLAB Code	142

List of Figures

Figure 1.1 (a) Representative hematoxylin and eosin (H&E) stained histology sections revealing the organization of epithelial cells (purple), extra-cellular stroma (pink), and adipocytes (white) in adipose, invasive cancer, and fibroglandular human breast tissue. Representative scanning electron microscopy (SEM) sections at 4k-5k magnification (b) and 29k-28k magnification (c), reveal ultrastructural variations in organelles and collagen, which are unresolvable with a microscope. In (d) the fluctuations in arising from the cellular ultrastructure are plotted (dotted line in (c)), revealing a size scale of 10s to 100s of nm.....7

Figure 1.2 A tabulation of the many proposed technologies to aid in margin detection for BCS, with corresponding clinical and logistical pros and cons for each technology, which are assigned weights determined with physician input. Adapted with permission from B. W. Maloney et al., “*Review of Method for Intraoperative Margin Detection for Breast Conserving Surgery*”, which is currently under review.....9

Figure 2.1 Reflectance as a function of radius from an isotropic point source is shown for different combinations of μ_s' and μ_a showing how sensitivity to optical properties varies with source-detector geometry. For the green lines, $\mu_s' = 2 \text{ mm}^{-1}$, and for the red lines, $\mu_s' = 1 \text{ mm}^{-1}$. Data using from the virtual photonics toolbox (<http://www.virtualphotonics.org/vts/>).....21

Figure 2.2 Reflectance as a function of radius from a point source is shown for the standard diffusion approximation (dotted lines) and Monte Carlo simulations (solid lines), at $\mu_s' = [0.5, 1, 1.5] \text{ mm}^{-1}$ and $\mu_a = 0.01 \text{ mm}^{-1}$. The two models diverge as ρ decrease to $< l^* = 1/\mu_{tr} \approx 1/\mu_s'$. Data generated from the virtual photonics toolbox (<http://www.virtualphotonics.org/vts/>).....23

Figure 2.3 Cross sectional images of 1% Intralipid (IL) in a transparent plastic tank. Normally incident spatially modulated red light is projection onto the medium surface, and propagates more superficially with increasing spatial illumination frequency. Scale bars indicate the length of each illumination period, $T = 1/f_x [\text{mm}]$24

Figure 2.4 (a) A flow diagram exhibiting the major physical components of a spatial frequency domain / structured light imaging system. Modulated fringe images, a demodulated AC image, and a diffuse DC image of a lumpectomy specimen are shown. (b) Cartoon conceptualizing the envelope extracting demodulation process, which is calculated at each pixel.....25

Figure 2.5 (a) Reflectance as a function spatial illumination frequency is shown for the standard diffusion approximation (dotted lines) and MC simulations (solid lines), at $\mu_{tr} \approx \mu_s' = [0.3, 0.6, 1.2] \text{ mm}^{-1}$ and $\mu_s'/\mu_a = 30$. The two models diverge as f_x increases to $> 3l^* = (1/3)/\mu_{tr} \approx (1/3)/\mu_s'$, meaning diffusion theory is invalid when $f_x > (1/3)/\mu_s'$. (b) MC

simulated reflectance as a function spatial illumination frequency is shown for $\mu_s' = [5,1,0.5] \text{ mm}^{-1}$ (red, green, blue lines respectively), and $\mu_a = [0.01,0.05,0.1] \text{ mm}^{-1}$. At low f_x , sensitivity to μ_s'/μ_a is maximized, but as f_x increases, sensitivity is limited to just μ_s' . Data generated from the virtual photonics toolbox (<http://www.virtualphotonics.org/vts/>).....27

Figure 2.6 White light images, NIR (730 nm LED source) diffuse images, and demodulated images (730 nm LED source, $f_x = 0.5 \text{ mm}^{-1}$) are shown for (a) avian tissue with a layer of whole bovine blood coating the left half of the tissue and (b) a slice of a pomegranate.....29

Figure 2.7 White light image of a cross section of a mastectomy, along with demodulated images (658 nm LED source) at $f_x = [0, 0.05, 0.15, 0.5] \text{ mm}^{-1}$. Green and cyan arrows demarcate a lack of contrast on the visible white light image, but enhance contrast on the high spatial frequency images. Depth sensitivity estimates are given calculated as $\delta_{\text{eff}} = 1/(\mu_{\text{eff}}^2 + 2\pi f_x^2)^{1/2}$30

Figure 2.8 (a) Index showing the IL% within each well for the corresponding μ_s' map in (b) and γ map in (c). Plots of known versus estimated μ_s' and γ values are shown in (d) and (e), respectively. The strong linear relationship demonstrates the proof-of-principle of the inversion methods. Calibrated reflectance maps at 730 nm are shown in for diffuse illumination and for $f_x = 0.5 \text{ mm}^{-1}$ are shown in (f) and (g) respectively, while the corresponding μ_s' and γ maps are shown in (h) and (i) respectively. The green arrows highlight a superficial scar which is undetectable in the diffuse image and μ_s' map, but is noticeable in $f_x = 0.5 \text{ mm}^{-1}$ reflectance and γ maps. Data adapted with permission from S.C. Kanick, D.M. McClatchy III, et al., “Sub-diffusive scattering parameter maps recovered using wide-field high-frequency structured light imaging”, 2014.....33

Figure 2.9 (a) White light images of avian tissues exposed to formalin (4% formaldehyde) for 1,2,3,4, and 5 minutes. Corresponding μ_s' and γ maps are shown in (b) and (c) respectively, spatially quantifying the morphological changes to the tissue in response to the formalin exposure.....34

Figure 9. 1 Representative color images of five common malignant lesion diagnoses, which were reconstructed from diffuse ($f_x = 0 \text{ mm}^{-1}$, top row) and high spatial frequency ($f_x = 1.37 \text{ mm}^{-1}$, bottom row) visible wavelengths as described in McClatchy et al. 2017. Lesions boundaries are outlined in red. Below the images is a table summarizing the pathologic distribution of primary lesions from all specimens imaged to date for which corresponding pathology is available. Abbreviations: Ca = Invasive Cancer; IDc = Invasive Ductal Carcinoma; LG = Low Grade; IG = Intermediate Grade; HG = High Grade; ILc = Invasive Lobular Carcinoma; FCD = Fibrocystic Disease; Norm-Rx = Treated with Neoadjuvant Chemotherapy.....136

Figure 9.2 (a) Annotated gross analysis image of a “bread loafed” invasive ductal carcinoma surgical specimen. (b) Corresponding tessellated histology reveals a negative margin with connective stroma between the invasive lesion and specimen margin (green

arrows). (c) A superficial micro-CT slice of the “bread loafed” specimen. The lack of contrast between the invasive region and the connective stroma is a well-known limitation of X-ray CT.....138

List of Acronyms

Anterior-Posterior	AP
Breast Conserving Surgery	BCS
Charged Coupled Device	CCD
Computed Tomography	CT
Confidence Interval	CI
Dartmouth Hitchcock Medical Center	DHMC
Digital Light Projector	DLP
Digital Micro-Mirror Device	DMD
Ductal Carcinoma in Situ	DCIS
Extra-Cellular Matrix	ECM
Fibrocystic Disease	FCD
Field of View	FOV
Frozen Section Pathology	FSP
Hematoxylin & Eosin	H&E
Hue Saturation Value	HSV
Inter-Quartile Range	IQR
Internal Review Board	IRB
Intralipid	IL
Invasive Cancer	ICa
Invasive Ductal Carcinoma	IDc
Invasive Lobular Carcinoma	ILc
Leave One Out Cross Fold Validation	LOO-CV
Light Emitting Diode	LED
Lobular Carcinoma in Situ	LCIS
Modulation Transfer Function	MTF
Monte Carlo	MC
Near Infrared	NIR
One Dimensional	1D
Operating Room	OR
Peak Kilovoltage	kVp
Radiation Transport Equation	RTE
Rebecca A Zuurbier	RAZ
Red Green Blue	RGB
Region of Interest	ROI
Root Square Mean Error	RMSE
Scanning Electron Microscopy	SEM
Signal to Noise Ratio	SNR
Spatial Frequency Domain	SFD
Spatial Frequency Domain Imaging	SFDI
Structured Light Scatteroscopy	SLS
Sub-Diffusive Spatial Frequency Domain Imaging	sd-SFDI
Three Dimensional	3D
Two Dimensional	2D
Wendy A Wells	WAW

Chapter 1: Introduction

1.1. Breast Conserving Surgery and Positive Surgical Margins

Breast cancer is the most prevalent cancer in women with a 1/8 lifetime risk of diagnosis in the United States[1]. Approximately 250k new invasive cases and 60k non-invasive in-situ cases were diagnosed in 2017[1]. Relative survival rates for breast cancer in the United States are 91% at 5-years and 86% at 10-years[1]. Fortunately, due in part to widespread screening practices, over half of all female breast cancers are first diagnosed at a localized stage, for which the 5-year survival rate jumps to 99%[1]. Based on 2013 data, 97% of stage I & II and 93% of stage III breast cancers were treated with surgery, and almost always were combined with radiotherapy, systemic chemotherapy, and/or targeted therapy[1]. There are two major surgical treatments: (1) mastectomy, where the entire breast is surgically removed and (2) breast conserving surgery (BCS), where only a small volume of tissue encapsulating a localized tumor is removed.

The mastectomy was standard of care for all breast cancer since the turn of the 19th century[2]. But, the regularity of this practice came into question as it became clear that surgery alone was not curative, and therefore, a less invasive surgery combined with radiation therapy to control microscopic disease may offer equivalent survival with a less morbid surgical procedure[3]. This hypothesis was tested in the 1973 B-06 randomized, prospective clinical trial, which demonstrated after 20 years follow up that BCS combined with radiotherapy offers equivalent survival compared to mastectomy for stage I & II breast cancer less than 4 cm in diameter, given that the surgical specimen margins are free of residual cancer[4]. BCS is now standard of care for localized breast cancer, with over half of stage I & II cancers being treated with BCS in combination with radiotherapy[1].

Additionally, the widespread adoption of neoadjuvant chemotherapy to preoperatively shrink tumor size, has resulted in increased rates of BCS compared to mastectomy[5].

The landmark B-06 study standard did have a clear caveat, being that the surgical margins must be free of residual cancer. Obtaining clear surgical margins is a notorious clinical challenge as the current rates of additional surgery after BCS are in the range of 20-40%, with great variability among surgeons and clinics in re-excision protocols and preferences[6-8]. To help standardize this clinical practice, the Society of Surgical Oncology and the American Society of Radiation Oncology performed an extensive meta-analysis and recently issued re-excisions guides for invasive breast cancer [9] and also ductal carcinoma in situ (DCIS) [10]. For invasive cancer, the guidelines suggested “no ink on tumor” to be a clear margin, showing no additional benefit to wider margins and a two-fold increase in ipsilateral breast tumor recurrence for positive margins[9]. For DCIS, the guidelines suggested that 2mm margins be considered clear, disease on ink again considered positive, but for disease within 2mm, clinical judgement should be used in determining need for additional surgery[10]. Additionally, there is evidence to suggest that for DCIS patients who received radiotherapy, re-excision may not be necessary for margins within 2 mm but not “on-ink”[11]. Shortly after the dissemination of these guidelines, a multicenter study observed a 16% decrease in additional surgeries after initial lumpectomy, suggesting that the no tumor on ink re-excision guideline for invasive breast cancer had gained significant clinical adoption[7]. Despite these guidelines, obtaining clear surgical margins remains a challenge. Developing technology to aid in intraoperative breast tumor margin assessment is the primary goal of this thesis work. In the next section, the current standard of care for breast tumor margin diagnosis and state of the art for intraoperative

specimen margin assessment are described, along with their respective shortcomings.

1.2. State of the Art: Review of Solutions & Shortcomings

At Dartmouth Hitchcock Medical Center (DHMC), standard of care for BCS includes, but is not limited to, preoperative wire localization for non-palpable lesions and single projection specimen mammography to ensure that the lesion is excised before the surgical cavity is closed. Immediately after a specimen is excised, it is inked on all sides to record its orientation [12], and sent to the Surgical Gross lab. A trained pathologists' assistant dissects the specimen with parallel slices ("bread loafing") and grossly inspects these slices for regions of representative lesional tissue and areas of potential margin involvement. These cut tissue regions are then dehydrated, fixed with formalin, paraffin embedded, microtomed to a thickness of a few (4-8) microns and mounted onto a glass slide to be stained with hematoxylin and eosin (H&E), which stain nucleic acids purple and protein pink respectively. The gold standard for determining the margin status for BCS specimens is the analysis of these H&E stained slides by a trained histopathologist. However, this entire process from start to finish can take multiple days, motivating the need for rapid, intraoperative breast tumor margin assessment techniques.

Common radiographic techniques for BCS surgical guidance include preoperative wire [13, 14] or radioactive seed tumor localization [15], and intraoperative specimen mammography[16]. Single projection specimen mammography currently offers poor sensitivity, with reported sensitivity and specificity of 36% and 71%[16]. However, improvements are seen with two projection specimen mammography, as studies have reported sensitivities and specificities of 54.6% and 87.8%[17] and more recently 58.5% and 91.8%[18]. Additionally, a hand held electrical impedance spectroscopy probe

(MarginProbe, Dune Medical) has received FDA approval for intraoperative BCS guidance, and demonstrated a 56% reduction in the re-excision rate in a randomized, prospective, multicenter clinical trial [19]. However, raster-scanning a point probe over an entire specimen surface is time consuming and not clinically ergonomic.

Intraoperative histopathologic evaluation using frozen section pathology (FSP) [20] or touch prep cytology [21] have been common BCS guidance techniques. In both techniques, a pathologist makes a diagnosis on rapidly prepared histology slides before the surgical cavity is closed. With FSP, cut tissue specimens are flash frozen, mounted, and stained during the surgery, and with touch prep cytology, cells are exfoliated from the surface of the specimen and similarly slide mounted and stained. While these techniques have shown diagnostic value, it remains extremely time consuming, draining on department resources, suffers from under sampling of the specimen surface, and FSP additionally suffers from well-known freezing artifacts [22, 23]. There have been promising scientific advances in creating virtual histology slides from thick unprocessed breast tissue with topically applied fluorescent dyes, using light sheet microscopy [24] and multiphoton microscopy [25]. Additionally, microscopy techniques utilizing ultraviolet (UV) autofluoresce can similarly create virtual histology slides from thick breast tissue without the need for topical dyes [26, 27]. Furthermore, optical coherence tomography can provide, microscopic resolution in unprocessed human breast tissue[28, 29]. But with all of these point measurement, microscopic sampling techniques, the time it takes to scan and evaluate microscopic fields of view over an entire lumpectomy specimen creates a significant clinical translation challenge. Therefore, wide field diffuse optical imaging has

also been investigated, as endogenous optical contrast [30, 31] and fluorescence from exogenous labels [32] can be rapidly quantified and spatially resolved.

Finally, the surgical practice of undirected whole margin cavity shaving on all BCS procedures has been investigated in a prospective, randomized clinical trial, which demonstrated a ~50% reduction in the re-excision rate [33]. However, directed re-excision with some significant amount of specificity as to which patients certainly do not need to have excess tissue removed would clearly be advantageous. In the following section, the rationale for the prosed methods investigated in this thesis work is discussed.

1.3. Project Rationale

1.3.1. Light Scattering as a Contrast Mechanism

Light scattering is an endogenous, label-free contrast mechanism, which is fundamentally related to changes to tissue ultrastructure and morphology. Over the last 20 years, the diagnostic potential of localized light scattering measurements to distinguish malignant from benign lesions has been investigated across a variety of human disease sites in several measurement schemes and geometries[31, 34-47]. The spectral and angular dependence of light scattering, which are the fundamental signals used for tissue diagnosis, originate from the size-scale of fluctuations in the refractive index being smaller and larger than the wavelength of light [48-52]. Specifically, features smaller than the wavelength of light present a strong spectral dependence but isotropic angular dependence, while features larger than the wavelength of light have a less pronounce spectral dependence but an anisotropic, forward-peaked angular dependence [49, 50, 52] . The origins of light scattering from tissue ultrastructure is conceptualized in Fig. 1.1 for adipose, invasive cancer and fibroglandular human breast tissue. In Fig. 1.1 (a) H&E sections reveal the

cellular and stromal organization between the different pathologies. Increasing magnification by ~10X and ~100X (note scale bar) with scanning electron microscopy (SEM), shown in Fig. 1.1 (b) and (c) respectively, reveals ultrastructural features within the organelles, extra-cellular matrix (ECM), collagen orientation, and collagen striations. In Fig. 1.1 (d), line profiles through the SEM section illustrate fluctuations in ultrastructure on the size-scale of 10s to 100s of nm, which uniquely contribute to observed light scattering. Furthermore, the microscopic heterogeneity within tissue also becomes apparent, illustrating how a light scattering measurement can more sensitive with increased signal localization.

Over the last 10 years here at the Thayer School of Engineering and DHMC, multiple devices have been previously developed and translated with an aim of localizing, quantifying, and mapping light scattering in resected human breast tissue specimens to with the goal of detecting superficial malignant lesions. The first device was a dark-field scanning spectroscopy platform which could distinguish malignant from benign lesions with 93% sensitivity and 95% specificity, based on spectroscopic reflectance textures[36]. However, this scanning device took ~15 min to scan a $1 \times 1 \text{ cm}^2$ field of view (FOV), which is completely impractical for imaging whole lumpectomy specimens. To overcome this limitation, a second device was investigated, spatial frequency domain imaging (SFDI), which will be further discussed in Chapter 2. SFDI rapidly provided wide-field maps of chromophore concentrations and diffuse light scattering, which could distinguish malignant from benign lesions with 79% sensitivity and 93% specificity, with the scattering features contributing the most to the tissue classification[31]. This thesis work aims to build upon these previous efforts and develop new technology utilizing both the rapid, wide-field

sensing achieved with SFDI and also the increased scatter sensitivity achieved with the finer light propagation constraints of the dark-field scanning spectroscopy system. Additionally, this thesis aims to make light scatter technology more clinically amenable by providing a biologic interpretation of the scatter signal and also combining this technology with a standard radiographic tomography, described in the next sub-section.

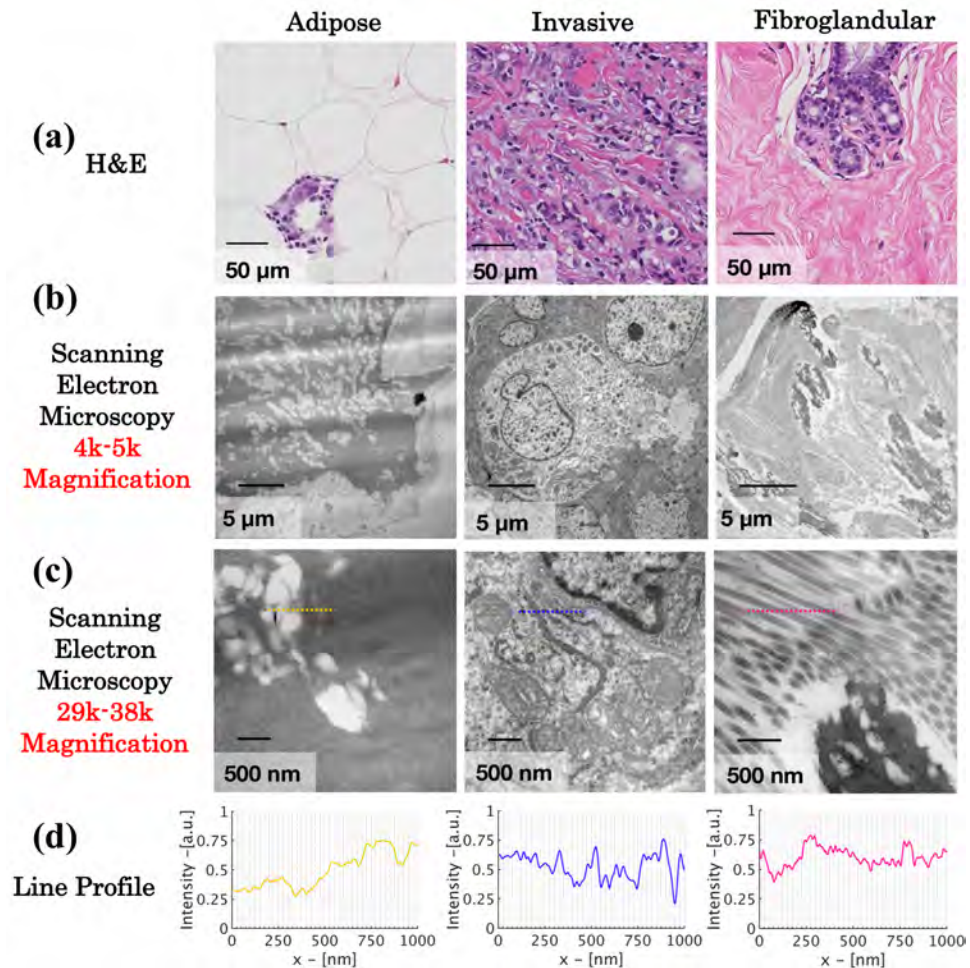


Figure 1.1 (a) Representative hematoxylin and eosin (H&E) stained histology sections revealing the organization of epithelial cells (purple), extra-cellular stroma (pink), and adipocytes (white) in adipose, invasive cancer, and fibroglandular human breast tissue. Representative scanning electron microscopy (SEM) sections at 4k-5k magnification (b) and 29k-28k magnification (c), reveal ultrastructural variations in organelles and collagen, which are unresolvable with a microscope. In (d) the fluctuations in arising from the cellular ultrastructure are plotted (dotted line in (c)), revealing a size scale of 10s to 100s of nm.

1.3.2. Multimodal Imaging

A major focus of this thesis work was on clinical translation, and optimizing a potential surgical guidance technology for the standard of care BCS workflow. As mentioned in Section 1.2, there are numerous technologies under investigation for BCS guidance, which vary widely in the tradeoffs between resolution, FOV, scanning time, sensitivity, and contrast mechanisms. A recently submitted review paper from Maloney et al. attempted to quantify and compare these clinical and logistical tradeoffs over the full gamut of established and emerging BCS guidance technologies, which is tabulated in Fig. 1.2[53]. From this analysis, it is clear that a multimodal approach to scan tissue over multiple size scales would be ideal, as no single technology is able to rapidly survey the entire tissue specimen in a timely manner with adequate sensitivity. While optics, specifically light scatter imaging, can provide wide-field, superficial morphologic information, it is unable to provide a high-resolution (sub-millimeter) tomographic reconstruction of an entire specimen. But, by combining light scatter imaging with a standard tomographic medical imaging modality, providing full volumetric reading of the tissue sample, the light scatter measurements can be better contextualized, giving the technology a better chance of complete clinical acceptance through maximal information flow.

Micro-computed tomography (CT) has been chosen as the volumetric imaging modality to be utilized. Micro-CT is an emerging technology, which has only been recently been proposed as a potential BCS guidance tool[54, 55]. X-ray CT does not require a specialized non-ferromagnetic surgical suite, such as intraoperative MRI and also does not require raster-scanning a transducer as needed in volumetric ultrasound. Furthermore, miniaturized micro-CT can be fully self-shielded and also come in a cart form-factor, which is very ergonomic for an intraoperative setting. Also, because the specimens are

imaged *ex-vivo*, the X-ray peak kilovoltage (kVp) can be lowered from a clinical CT range (~100-150 kVp) to the range of diagnostic mammography (~20-50 kVp), drastically enhancing soft-tissue contrast with increasing absorption due to the photoelectric effect[56].

Issues/ Desires	Weight	Radiographic	Micro-CT	MRI	PET/CT	CLI	Radiofrequency	HF Ultrasound	Bioimpedance Spectroscopy	PAT	Spectral Imaging	SFDI	ESR/DRS	Fluorescence	MUSE	Lightsheet Micros	Non-linear	OCT	Raman	Frozen Sectioning	Imprint Cytology	Permanent Hist.
Clinical																						
Large Area Scan	4	5	5	4	4	3	1	2	2	4	5	5	2	5	4	4	1	2	1	1	4	4
Tumor Extent Inside/ Tumor Confirmation	5	4	5	4	5	2	1	2	1	2	2	2	1	1	1	1	2	3	1	1	5	
Surface for Invasive	5	1	2	1	1	4	4	3	4	3	4	4	3	3	5	5	5	4	4	5	4	5
2mm Depth for DCIS	5	1	2	1	1	4	4	3	4	3	4	4	2	3	3	3	4	3	3	3	3	5
Lack of User/Reader Necessity	3	2	2	1	1	3	5	3	5	3	4	4	3	5	4	4	2	2	2	1	1	1
Logistical/ Technical																						
Inside(I) vs Outside(O)	I	I	I	I/O	O	O	O	O	O	O	O	O	O	O	O	O	O	O	O	O	O	I/O
Micro(u) vs Macro(M)	M	M	M	M	M	u	M	M	M	M	M	M	M	M	u	u	u	u	u	u	u	u
Small Data Volume	2	2	2	3	4	2	4	2	2	3	2	2	2	4	1	1	1	4	3	3	4	1
Short Time	3	4	3	3	2	3	4	4	3	5	1	1	3	4	4	5	5	4	4	2	3	1
Lack of Processing/ Stain	3	2	2	2	1	1	5	5	5	4	5	5	5	1	2	2	2	1	5	1	3	1
Robust Performance	4	5	5	5	4	2	4	3	3	2	3	4	3	4	5	4	1	4	3	4	4	5
Small Footprint	3	1	3	1	1	3	5	5	5	3	5	4	4	3	4	3	2	4	3	2	2	1
TOTAL		101	119	93	90	104	130	115	123	115	131	132	99	118	125	121	93	110	114	89	107	125

Figure 1. 2 A tabulation of the many proposed technologies to aid in margin detection for BCS, with corresponding clinical and logistical pros and cons for each technology, which are assigned weights determined with physician input. Adapted with permission from B. W. Maloney et al., “Review of Method for Intraoperative Margin Detection for Breast Conserving Surgery”, which is currently under review.

1.4. Thesis Overview

In this thesis work, two imaging technologies were both independently and congruently analyzed for the purpose of the characterizing surgically excised human breast cancer specimens. Chapter 2 covers the background on light transport and structured light imaging, and Chapter 9 concludes the thesis with overall key findings and limitations. Chapters 3-8 are reproductions of first authored peer-reviewed manuscripts, which have either been

published or are currently under review. The organization of this thesis is described below along with the publications, upon which each chapter is based:

Chapter 2 is a background on light transport in biological media, defining technical terminology used throughout the thesis, and also serves as an introduction into structured light imaging and light scattering quantification. The first section of this chapter focuses on the description of steady state light transport terms in the spatial and spatial frequency domains. The second section of the chapter focuses on wide-field sensing of light scattering with high spatial frequency structured light imaging, and the third section focuses on light scattering quantification. The second and third sections largely focus on the collaborative publications of V. Krishnaswamy et al.[57] and S. C. Kanick et al.[58], and also selected conference proceedings by D. M. McClatchy et al.[59, 60].

Chapter 3 documents the manuscript “*Molecular dyes used for surgical specimen margin orientation allow for intraoperative optical assessment during breast conserving surgery*” by D. M. McClatchy III et al., which describes a novel tissue marking method allowing for intraoperative NIR imaging during BCS.

Chapter 4 documents the manuscript “*Wide-field quantitative imaging of tissue microstructure using sub-diffuse spatial frequency domain imaging*” by D. M. McClatchy III et al., which describes systematic study introducing a method to quantify sub-diffusive light scattering parameters when optical absorbers are present. This method was validated on custom made phantoms with tunable scattering properties, and then tested on a cohort of n=22 freshly resected human breast tissue specimens, which showed sensitivity of the scattering parameters to different tissue diagnoses.

Chapter 5 documents the manuscript “*Monochromatic subdiffusive spatial frequency domain imaging provides in-situ sensitivity to intratumoral morphological heterogeneity in a murine model*” by D. M. McClatchy III et al., which describes a method to analysis morphological heterogeneity within n=2 murine mammary tumors by comparing co-registered scattering parameters to quantitative digitized histology.

Chapter 6 documents the manuscript “*Label-free light scatter imaging can predict stromal versus epithelial proportions in freshly resected human breast cancer specimens*” by D. M. McClatchy III et al., which will be submitted for publication. In this study, the morphology analysis methodology developed in Chapter 5, was further developed and applied to an expanded data set of scatter parameter maps of n=31 freshly resected breast tissue specimens discussed in Chapter 4. This work demonstrated that the physical light scatter parameters are explicitly related to and predictive of clinically relevant, quantitative histologic metrics.

Chapter 7 documents the manuscript “*Calibration and analysis of a multimodal micro-CT and structured light imaging system for the evaluation of excised breast tissue*” by D. M. McClatchy III et al., which describes the development of a second-generation multispectral SLI system, spanning the visible and NIR spectrums, spatially co-registered to a micro-CT. Experimentally measured technical performance metrics of the system are reported along with illustrative data from a proof-of-principle freshly resected breast tissue specimen slice.

Chapter 8 documents the manuscript “*Surgical breast tumor margins evaluated with micro-CT: results in 32 resected Breast Conserving Surgery (BCS) specimens*” by D. M. McClatchy III et al., which will be submitted for publication. This study was the first

systematic analysis comparing radiologic readings of whole BCS specimen micro-CT scans to the final margin diagnoses determined by pathology, and yielded the initial diagnostic performance of this imaging technology for BCS guidance.

Chapter 9 concludes the thesis and provides an executive summary of the key findings of impact of the body of work documented in this thesis. Additionally, both biological and technical limitations are discussed, with recommendations for ongoing and future work to overcome these limitations.

References:

1. *Breast Cancer Facts & Figures 2017-2018*. 2017: Atlanta: American Cancer Society, Inc.
2. Halsted, W.S., *I. A Clinical and Histological Study of certain Adenocarcinomata of the Breast: and a Brief Consideration of the Supraclavicular Operation and of the Results of Operations for Cancer of the Breast from 1889 to 1898 at the Johns Hopkins Hospital*. Annals of Surgery, 1898. **28**(5): p. 557-576.
3. Fisher, B., *Laboratory and clinical research in breast cancer--a personal adventure: the David A. Karnofsky memorial lecture*. Cancer Res, 1980. **40**(11): p. 3863-74.
4. Fisher, B., et al., *Twenty-year follow-up of a randomized trial comparing total mastectomy, lumpectomy, and lumpectomy plus irradiation for the treatment of invasive breast cancer*. N Engl J Med, 2002. **347**(16): p. 1233-41.
5. Lee, M.C., et al., *Determinants of breast conservation rates: reasons for mastectomy at a comprehensive cancer center*. The breast journal, 2009. **15**(1): p. 34-40.
6. McCahill, L.E., et al., *Variability in reexcision following breast conservation surgery*. JAMA, 2012. **307**(5): p. 467-75.
7. Morrow, M., et al., *Trends in Reoperation After Initial Lumpectomy for Breast Cancer: Addressing Overtreatment in Surgical Management*. JAMA Oncol, 2017. **3**(10): p. 1352-1357.
8. Pleijhuis, R.G., et al., *Obtaining adequate surgical margins in breast-conserving therapy for patients with early-stage breast cancer: current modalities and future directions*. Ann Surg Oncol, 2009. **16**(10): p. 2717-30.
9. Moran, M.S., et al., *Society of Surgical Oncology-American Society for Radiation Oncology consensus guideline on margins for breast-conserving surgery with whole-breast irradiation in stages I and II invasive breast cancer*. Ann Surg Oncol, 2014. **21**(3): p. 704-16.
10. Morrow, M., et al., *Society of Surgical Oncology-American Society for Radiation Oncology-American Society of Clinical Oncology Consensus Guideline on Margins for Breast-Conserving Surgery with Whole-Breast Irradiation in Ductal Carcinoma In Situ*. Ann Surg Oncol, 2016. **23**(12): p. 3801-3810.
11. Tadros, A.B., et al., *Ductal Carcinoma In Situ and Margins <2 mm: Contemporary Outcomes With Breast Conservation*. Ann Surg, 2017.

12. Gibson, G.R., et al., *A comparison of ink-directed and traditional whole-cavity re-excision for breast lumpectomy specimens with positive margins*. Ann Surg Oncol, 2001. **8**(9): p. 693-704.
13. Frank, H.A., F.M. Hall, and M.L. Steer, *Preoperative localization of nonpalpable breast lesions demonstrated by mammography*. N Engl J Med, 1976. **295**(5): p. 259-60.
14. Kopans, D.B. and S. DeLuca, *A modified needle-hookwire technique to simplify preoperative localization of occult breast lesions*. Radiology, 1980. **134**(3): p. 781.
15. Lovrics, P.J., et al., *A multicentered, randomized, controlled trial comparing radioguided seed localization to standard wire localization for nonpalpable, invasive and in situ breast carcinomas*. Ann Surg Oncol, 2011. **18**(12): p. 3407-14.
16. Kaufman, C.S., et al., *Intraoperative digital specimen mammography: rapid, accurate results expedite surgery*. Ann Surg Oncol, 2007. **14**(4): p. 1478-85.
17. McCormick, J.T., et al., *Analysis of the use of specimen mammography in breast conservation therapy*. Am J Surg, 2004. **188**(4): p. 433-6.
18. Bathla, L., et al., *High resolution intra-operative two-dimensional specimen mammography and its impact on second operation for re-excision of positive margins at final pathology after breast conservation surgery*. Am J Surg, 2011. **202**(4): p. 387-94.
19. Allweis, T.M., et al., *A prospective, randomized, controlled, multicenter study of a real-time, intraoperative probe for positive margin detection in breast-conserving surgery*. Am J Surg, 2008. **196**(4): p. 483-9.
20. Bianchi, S., et al., *Accuracy and reliability of frozen section diagnosis in a series of 672 nonpalpable breast lesions*. American journal of clinical pathology, 1995. **103**(2): p. 199-205.
21. Cox, C.E., et al., *Touch preparation cytology of breast lumpectomy margins with histologic correlation*. Archives of surgery (Chicago, Ill : 1960), 1991. **126**(4): p. 490-3.
22. Barakat, F.H., I. Sulaiman, and M.A. Sughayer, *Reliability of frozen section in breast sentinel lymph node examination*. Breast Cancer, 2014. **21**(5): p. 576-82.
23. St John, E.R., et al., *Diagnostic accuracy of intraoperative techniques for margin assessment in breast cancer surgery: a meta-analysis*. Annals of Surgery, 2017. **265**(2): p. 300-310.
24. Glaser, A.K., et al., *Light-sheet microscopy for slide-free non-destructive pathology of large clinical specimens*. Nature Biomedical Engineering, 2017. **1**: p. 0084.

25. Tao, Y.K., et al., *Assessment of breast pathologies using nonlinear microscopy*. Proceedings of the National Academy of Sciences, 2014. **111**(43): p. 15304-15309.
26. Wong, T.T.W., et al., *Fast label-free multilayered histology-like imaging of human breast cancer by photoacoustic microscopy*. Science Advances, 2017. **3**(5): p. e1602168-e1602168.
27. Fereidouni, F., et al., *Microscopy with ultraviolet surface excitation for rapid slide-free histology*. Nature Biomedical Engineering, 2017. **1**(12): p. 957-966.
28. Allen, W.M., et al., *Wide-field optical coherence micro-elastography for intraoperative assessment of human breast cancer margins*. Biomed Opt Express, 2016. **7**(10): p. 4139-4153.
29. Erickson-Bhatt, S.J., et al., *Real-time imaging of the resection bed using a handheld probe to reduce incidence of microscopic positive margins in cancer surgery*. Cancer research, 2015. **75**(18): p. 3706-3712.
30. Wilke, L.G., et al., *Rapid noninvasive optical imaging of tissue composition in breast tumor margins*. Am J Surg, 2009. **198**(4): p. 566-74.
31. Laughney, A.M., et al., *Spectral discrimination of breast pathologies in situ using spatial frequency domain imaging*. Breast Cancer Res, 2013. **15**(4): p. R61.
32. Davis, S.C., et al., *Topical dual-stain difference imaging for rapid intra-operative tumor identification in fresh specimens*. Opt Lett, 2013. **38**(23): p. 5184-7.
33. Chagpar, A.B., et al., *A Randomized, Controlled Trial of Cavity Shave Margins in Breast Cancer*. N Engl J Med, 2015. **373**(6): p. 503-10.
34. Mulvey, C.S., C.A. Sherwood, and I.J. Bigio, *Wavelength-dependent backscattering measurements for quantitative real-time monitoring of apoptosis in living cells*. Journal of biomedical optics, 2009. **14**(6): p. 064013-064013.
35. Zonios, G., et al., *Diffuse reflectance spectroscopy of human adenomatous colon polyps in vivo*. Applied Optics, 1999. **38**(31): p. 6628-6637.
36. Laughney, A.M., et al., *Scatter spectroscopic imaging distinguishes between breast pathologies in tissues relevant to surgical margin assessment*. Clinical Cancer Research, 2012. **18**(22): p. 6315-6325.
37. Krishnaswamy, V., et al., *Structured light scatteroscopy*. Journal of biomedical optics, 2014. **19**(7): p. 070504-070504.
38. McClatchy, D.M., 3rd, et al., *Wide-field quantitative imaging of tissue microstructure using sub-diffuse spatial frequency domain imaging*. Optica, 2016. **3**(6): p. 613-621.

39. McClatchy, D.M., 3rd, et al., *Monochromatic subdiffusive spatial frequency domain imaging provides in-situ sensitivity to intratumoral morphological heterogeneity in a murine model*. J Biophotonics, 2017. **10**(2): p. 211-216.
40. Gurjar, R.S., et al., *Imaging human epithelial properties with polarized light-scattering spectroscopy*. Nat Med, 2001. **7**(11): p. 1245-8.
41. Zhang, L., et al., *Light scattering spectroscopy identifies the malignant potential of pancreatic cysts during endoscopy*. Nat Biomed Eng, 2017. **1**.
42. Yang, Y., et al., *Optical scattering coefficient estimated by optical coherence tomography correlates with collagen content in ovarian tissue*. J Biomed Opt, 2011. **16**(9): p. 090504.
43. Wells, W.A., et al., *Phase contrast microscopy analysis of breast tissue: differences in benign vs. malignant epithelium and stroma*. Anal Quant Cytol Histol, 2009. **31**(4): p. 197-207.
44. Kennedy, S., et al., *Correlation of breast tissue histology and optical signatures to improve margin assessment techniques*. J Biomed Opt, 2016. **21**(6): p. 66014.
45. Lu, G., et al., *Detection of Head and Neck Cancer in Surgical Specimens Using Quantitative Hyperspectral Imaging*. Clinical Cancer Research, 2017. **23**(18): p. 5426.
46. Mourant, J.R., et al., *Spectroscopic diagnosis of bladder cancer with elastic light scattering*. Lasers Surg Med, 1995. **17**(4): p. 350-7.
47. Wallace, M.B., et al., *Endoscopic detection of dysplasia in patients with Barrett's esophagus using light-scattering spectroscopy*. Gastroenterology, 2000. **119**(3): p. 677-82.
48. Radosevich, A.J., et al., *Structural length-scale sensitivities of reflectance measurements in continuous random media under the Born approximation*. Optics letters, 2012. **37**(24): p. 5220-5222.
49. Xu, M. and R.R. Alfano, *Fractal mechanisms of light scattering in biological tissue and cells*. Optics letters, 2005. **30**(22): p. 3051-3053.
50. Schmitt, J.M. and G. Kumar, *Optical scattering properties of soft tissue: a discrete particle model*. Applied Optics, 1998. **37**(13): p. 2788-2797.
51. Mourant, J.R., et al., *Mechanisms of light scattering from biological cells relevant to noninvasive optical-tissue diagnostics*. Appl Opt, 1998. **37**(16): p. 3586-93.
52. Wang, X., et al., *Approximation of Mie scattering parameters in near-infrared tomography of normal breast tissue in vivo*. Journal of biomedical optics, 2005. **10**(5): p. 051704-051704.

53. Maloney, B.W., et al., *Review of Method for Intraoperative Margin Detection for Breast Conserving Surgery*. Under Review, 2018.
54. Tang, R., et al., *Micro-computed tomography (Micro-CT): a novel approach for intraoperative breast cancer specimen imaging*. *Breast Cancer Res Treat*, 2013. **139**(2): p. 311-6.
55. Tang, R., et al., *A pilot study evaluating shaved cavity margins with micro-computed tomography: a novel method for predicting lumpectomy margin status intraoperatively*. *Breast J*, 2013. **19**(5): p. 485-9.
56. Johns, P.C. and M.J. Yaffe, *X-ray characterisation of normal and neoplastic breast tissues*. *Phys Med Biol*, 1987. **32**(6): p. 675-95.
57. Krishnaswamy, V., et al., *Structured light scatteroscopy*. *J Biomed Opt*, 2014. **19**(7): p. 070504.
58. Kanick, S.C., et al., *Sub-diffusive scattering parameter maps recovered using wide-field high-frequency structured light imaging*. *Biomed Opt Express*, 2014. **5**(10): p. 3376-90.
59. McClatchy, D.M., et al. *High spatial frequency structured light imaging for intraoperative breast tumor margin assessment*. in *SPIE BiOS*. 2015. SPIE.
60. McClatchy Iii, D.M., et al. *Wide Field Imaging of Ultrastructures Using High Spatial Frequency Structured Light*. in *Biomedical Optics 2014*. 2014. Miami, Florida: Optical Society of America.

Chapter 2: Light Scatter Imaging: Theory and Measurement

2.1. Light Transport in Turbid Media

A photon is quantized packet of electromagnetic radiation, which does not have mass or electric charge, and exhibits properties of both a particle and a wave. The energy of a photon is inversely proportional to its wavelength, λ [nm], and the analysis of how photons interact with matter as a function of wavelength, is generally referred to as spectroscopy. Photons in the visible spectrum ($\lambda = 400\text{-}700$ [nm]), along with ultraviolet (UV, $\lambda = 100\text{-}400$ [nm]) and near infrared (NIR, $\lambda = 700\text{-}2000$ [nm]) spectrums, are commonly referred to as light. Over the last 30-40 years, light-tissue interactions, specifically absorption, scattering, and fluorescence, have been extensively studied to both diagnose and treat human disease[1]. As mentioned in Chapter 1, the focus of this thesis work is on the quantification of light scattering, as it is inherently related to the ultrastructure of tissue. In the following sub-sections, the mathematical underpinnings of modeling and measuring light-tissue interactions are conceptually described.

2.1.1. Radiative Transport Equation and Optical Properties

Maxwell's equations provide a complete and exact description of electromagnetic wave propagation, but to computationally solve these equations, the permeability and permittivity of the medium are needed on the size scale much smaller than λ [2, 3]. So while these equations are utilized for microscopic applications [4], they are not amenable to macroscopic biomedical applications the size-scale of which could be on the order of centimeters. The Boltzmann radiation transport equation (RTE) treats photon propagation as discrete ballistic particles experiencing probabilistic absorption and scattering events, neglecting near field effects, such as interference and diffraction, and is often more

appropriate for biomedical applications. The RTE is a 5 dimensional scalar equation describing the propagation of radiative energy as a function of space, time, and solid angle[5]. All work discussed in this thesis is done in the steady state, meaning both the optical source and the interrogated media are assumed to not change with time, and so all time dependent variables will not be considered. The steady state RTE is an energy balance equation with terms to take into account the divergence of photons out of a given angle, photons absorbed or scattered out of a given angle, photon scattered into a given angle, and internal photon sources. The probability density function defining the angular distribution of photon scattering is known as the phase function, $P(\theta)$, where θ is the scattering angle. Light absorption and scattering are quantified by the absorption coefficient, μ_a [mm⁻¹], and scattering coefficient μ_s [mm⁻¹], both of which are simply described as one over the average distance between absorption or scattering events, respectively. It is often convenient to quantify light scattering over multiple scattering events when transport becomes isotropic without need to consider the phase function, which will be discussed further in subsection 2.1.3. Isotropic light scattering is quantified by the reduced scattering coefficient μ_s' [mm⁻¹], which can be conceptually described as one over the average distance between apparent isotropic scattering events.

Mathematically, $\mu_s' = \mu_s(1-g)$, where g is the first statistical moment of the scattering phase function, $P(\theta)$, or put another way is the mean cosine of the scattering angles. A more conceptual definition for g , which is commonly referred to as the anisotropy factor, is the relative amount of forward scattering (i.e. $g=1$ means total forward scattering, $g=0$ mean total isotropic scattering and $\mu_s' = \mu_s$).

2.1.2. Monte Carlo as a Numerical Solution to RTE

Because the RTE is a probabilistic integro-differential equation, determining analytic solutions are only possible for very specific geometries, boundary conditions, and homogenous media, although exact solutions have been discovered[6]. Therefore, a more common approach is to computationally solve the RTE through probabilistic Monte Carlo (MC) simulations[7, 8]. A single MC simulation is essentially a random walk of a photon through a user defined media. A photon is initially “launched”, then travels a given distance until it is scattered, then changes direction, and continues along discrete probabilistic paths until it reaches a predefined boundary. Absorption is commonly accounted for by applying Beer-Lambert’s Law (exponential attenuation over path length [9]) at either each discrete step or after the entire photon path length has been determined[10]. Probability density functions (PDFs) describing the spatial and angular distribution of the photon source are custom defined by the user. PDFs describing the photon path length between scattering events is defined according to the scattering coefficient. Finally, the PDF describing the scattering angle is simply the phase function. These probability density functions are then sequentially sampled using a random number generator. For MC simulations to be of any statistical value, a large number of photons need to be launched, generally on the order of 10^6 - 10^9 depending on the source detector geometry. To speed up MC simulations, photon trajectories are commonly run in parallel using graphical processing units (GPUs)[11].

MC simulations are a powerful tool to investigate how light interacts with tissue given specific source-detector and tissue geometries, for both therapeutic and diagnostic purposes. Results from a simple series of MC simulations for a normally incident narrow beam on a semi-infinite medium for $\mu_s' = [1, 2] \text{ mm}^{-1}$ and $\mu_a = [0.005, 0.05] \text{ mm}^{-1}$ are

shown in Fig. 2.1. The reflectance, or fraction of incident photons remitted per unit area, is plotted as function of radius from the source. Close to the source, the reflectance is uniquely sensitive to μ_s' , while far from the source reflectance sensitivity to μ_a increases and sensitivity to μ_s' diminishes. At close source detector separations, photons experience shorter and more superficial total path lengths, resulting in minimal sensitivity to μ_a , as sensitivity to μ_a is exponential as a function of path length according to Beer-Lambert's Law. This observation that sensitivity to μ_s' and μ_a uniquely vary with source detector separation is crucial. This implies that that μ_s' and μ_a within tissue can be quantified by matching experimental reflectance measurements at multiple source detector separations to predicted MC simulated, which has many diagnostic applications [12].

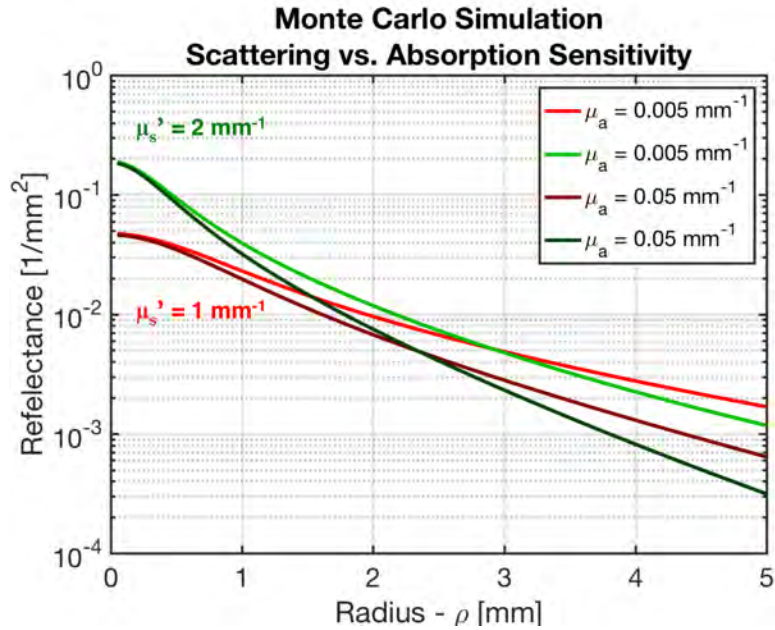


Figure 2. 1 Reflectance as a function of radius from an isotropic point source is shown for different combinations of μ_s' and μ_a showing how sensitivity to optical properties varies with source-detector geometry. For the green lines, $\mu_s' = 2 \text{ mm}^{-1}$, and for the red lines, $\mu_s' = 1 \text{ mm}^{-1}$. Data generated from the virtual photonics toolbox (<http://www.virtualphotonics.org/vts/>).

2.1.3. The Diffusion Approximation of the RTE

The RTE can give a complete description of radiative energy transport and can be solved numerically with MC based solutions. However, MC simulations are computationally expensive, as a simulation has to be run for each individual photon trajectory. Furthermore, a full MC simulation may not be necessary to model many common measurement geometries for probing tissues. Instead, the so called diffusion approximation to the RTE can be used if a few specific conditions are met. The diffusion approximation to the RTE involves a decomposition of the radiance into spherical harmonics and a truncation of this series so that the radiance is anisotropic to the first order[13]. The resulting diffusion approximation is a partial differential equation that describes light transport terms of the fluence, which is the radiance integrated over all solid angles, and is just a function of μ_s' and μ_a . Steady state diffusion theory is valid when the following two conditions are met: (1) $\mu_s' \gg \mu_a$ so that diffusion occurs and (2) the source detector separation is wide enough ($\gg l^* = 1/\mu_{tr} \approx 1/\mu_s'$) so that multiple light scattering can take place resulting in transport that is isotropic to a first order[13, 14]. The main advantage of the diffusion approximation is that it can be efficiently solved with finite difference or element analysis[15], or analytically with boundary conditions consistent with common measurement geometries, such as a point source incident on a semi-infinite plane[16, 17]. Despite these advantages, diffusion theory is limited by the fact that it is inaccurate at close source detector separations and in the presence of strong absorbers[14, 18]. In Fig. 2.2, the divergence of MC simulations and diffusion theory at close source detector separations is shown. Furthermore, it can be seen that the reduced scattering coefficient is related to both the magnitude of the model divergence

close to the source and also the source detector separation at which the two models diverge.

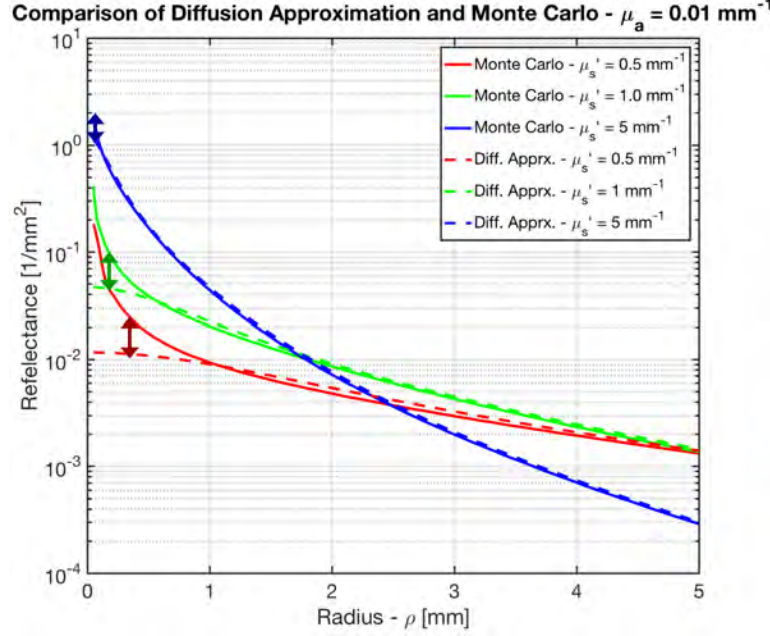


Figure 2.2 Reflectance as a function of radius from a point source is shown for the standard diffusion approximation (dotted lines) and Monte Carlo simulations (solid lines), at $\mu_s' = [0.5, 1, 5] \text{ mm}^{-1}$ and $\mu_a = 0.01 \text{ mm}^{-1}$. The two models diverge as Q decrease to $< l^* = 1/\mu_{tr} \approx 1/\mu_s'$. Data generated from the virtual photonics toolbox (<http://www.virtualphotonics.org/vts/>).

2.1.4. Transport in the Spatial Frequency Domain

The spatial frequency domain (SFD) is the Fourier analogue to the spatial domain.

Instead of modeling light remission as a function of radius from a source, reflectance is modeled as a function of spatial illumination frequency, $f_x [\text{mm}^{-1}]$. In subsection 2.1.2, it was previously illustrated using spatial domain MC measurements, that at close source detector separations photons experience short, superficial path lengths and are uniquely sensitive to scattering, while at wider source detector separations photons experience long, diffuse path-lengths and have increased sensitivity to absorption and diminished sensitivity to scattering. In the spatial frequency domain, “finer” (high f_x) spatial illumination frequencies propagate more superficially than “wider” (low f_x) spatial

illumination frequencies, which are able to propagate more deeply. This phenomenon is illustrated in Fig. 2. 3, where cross sectional images of normally incident 1D sinusoidal patterns of $f_x = [0.05, 0.15, 0.5] \text{ mm}^{-1}$ are projected onto a turbid media of 1% fat emulsion, more commonly known as Intralipid (IL).

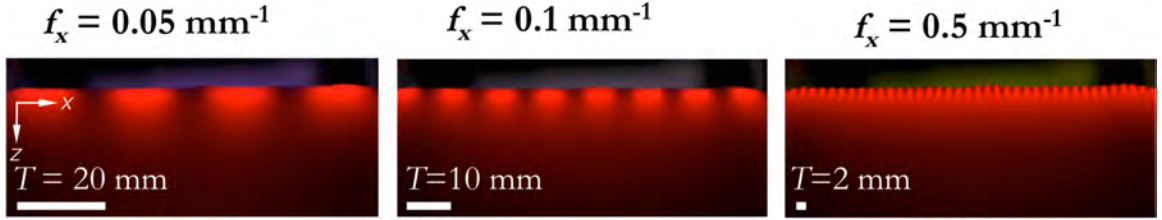


Figure 2. 3 Cross sectional images of 1% Intralipid (IL) in a transparent plastic tank. Normally incident spatially modulated red light is projection onto the medium surface, and propagates more superficially with increasing spatial illumination frequency. Scale bars indicate the length of each illumination period, $T = 1/f_x$ [mm].

The experimental measurement of optical properties by exploiting the relationship between depth sensitivity and the spatial frequency of illumination patterns was first described by Dögnitz et al.[19]. Cuccia et al. subsequently demonstrated that optical properties could be spatially mapped with planar 1D sinusoidal illumination patterns, with a technique termed spatial frequency domain imaging (SFDI) [20, 21]. The basic physical components and computational steps of an SFDI system are shown in Fig. 2.4(a). Light is focused onto a digital micro-mirror device (DMD) to create 1D sinusoidal illumination patterns of a given spatial frequency at three evenly offset phases, $\phi = [-2\pi/3, 0, 2\pi/3]$ radians. These light structures are projected onto a tissue surface and perturbed by the light-tissue interactions, resulting in “modulated” images captured by an oblique camera. A diffuse planar illumination image, I_{DC} , is simply the average of the three modulated phases, but the demodulated image, I_{AC} , is calculated with a common three phase envelope extraction formula[22]. In Fig. 2.4(b), the demodulation, which is calculated at each pixel, is conceptually shown to simply be the amplitude of the

sinusoidal carrier wave. These demodulated maps can then be normalized to a homogenous medium with known optical properties to create maps of calibrated reflectance. Then at each pixel, optical properties can be determined by minimizing the difference between experimentally measured calibrated reflectance and either diffusion theory or MC predicted reflectance, with the criteria that a “low” and “high” spatial frequency are needed to deconvolve the contributions of absorption and scattering to the reflectance signal[20]. By multiplexing at multiple wavelengths, maps of optical properties can be further transformed into chromophore concentration maps[23]. This method has proven to be valuable for a variety of diffuse spectroscopic applications[24-27], and research into the use of this methodology continues to expand today.

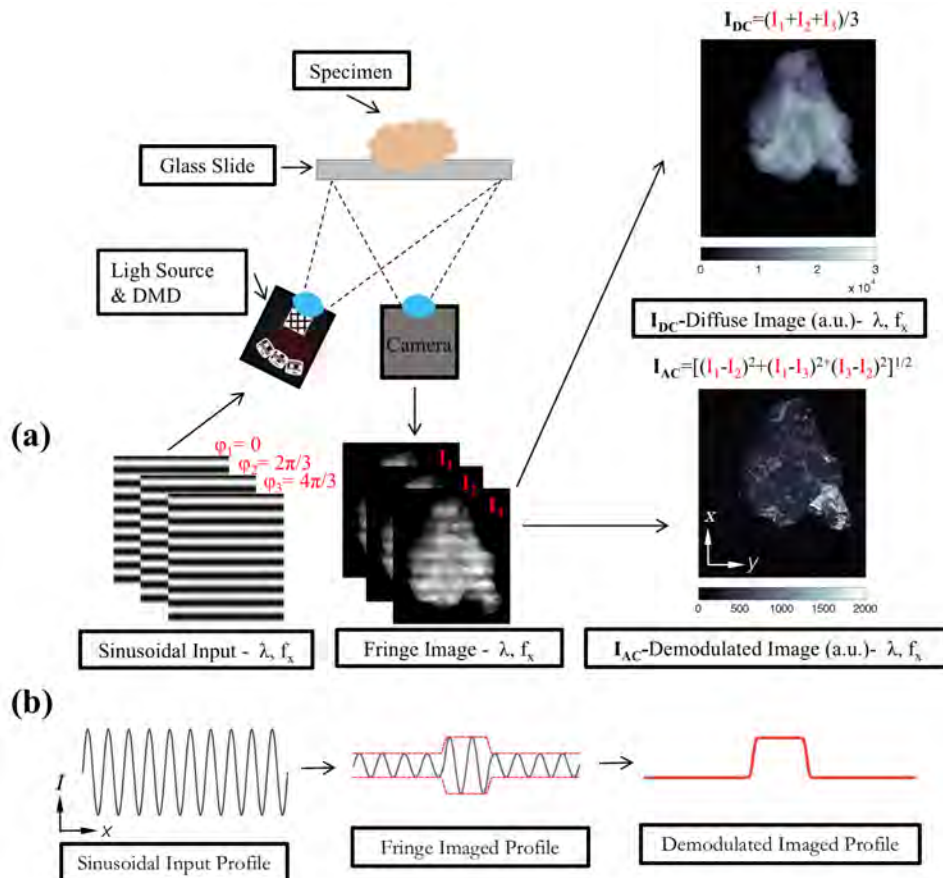


Figure 2.4 (a) A flow diagram exhibiting the major physical components of a spatial frequency domain / structured light imaging system. Modulated fringe images, a demodulated AC image,

and a diffuse DC image of a lumpectomy specimen are shown. (b) Cartoon conceptualizing the envelope extracting demodulation process, which is calculated at each pixel.

2.2. Wide-Field Light Scatter Imaging with High Spatial Frequency Structured Illumination

The main goal of SFDI as described by Cuccia et al. was to spatially map and quantify diffuse optical properties, specifically μ_a and μ_s' , which in turn could spatially map chromophore concentrations with spectroscopic analysis. This technology was thoroughly analyzed by Laughney et al. for the purpose of distinguishing malignant from benign lesions in surgically excised human breast tissue[24, 25]. From this work, it was shown that the diffuse scattering parameters, specifically the scatter amplitude, A, and scatter slope, B, following a power law $\mu_s'(\lambda) = A(\lambda / [800 \text{ nm}])^{-B}$, contributed the most discriminatory information to the lesion classifier[25]. From this observation, and previous dark-field microscopy work from Laughney et al. [28], it is apparent that localized scatter sensitivity is advantageous for distinguishing tissue morphology. With the known inverse relationship between spatial illumination frequency and penetration depth, a new imaging method, originally referred to as structured light scatteroscopy (SLS), was incepted to magnify scatter sensitivity by increasing the spatial illumination frequency out of diffusion limited transport[29]. In this “sub-diffusive” regime, sensitivity to μ_s' is sustained and sensitivity to the shape the phase function is greatly increased [30, 31], as shown in the simulations in Fig. 2.5. In Fig 2.5(a), reflectance as function of spatial frequency is shown for both diffusion theory and MC simulations for various transport coefficients $\mu_{tr} = \mu_s' + \mu_a$, illustrating the divergence between radiative and diffusive transport at spatial frequencies greater than $(1/3)\mu_{tr}$, because of sensitivity to anisotropic scattering from the phase function[20]. It should be noted that imaging

with these high spatial frequencies, generally in the range of $f_x > 0.5 \text{ mm}^{-1}$ for breast tissue, is easily achievable with available structured light imaging systems. In Fig 2.5(b), MC simulated reflectance as a function of spatial frequency is shown for independent variations in μ_s' and μ_a , revealing low spatial frequencies are most sensitive to μ_s'/μ_a , but with increasing spatial frequency, sensitivity to μ_a disappears and sensitivity to μ_s' increases.

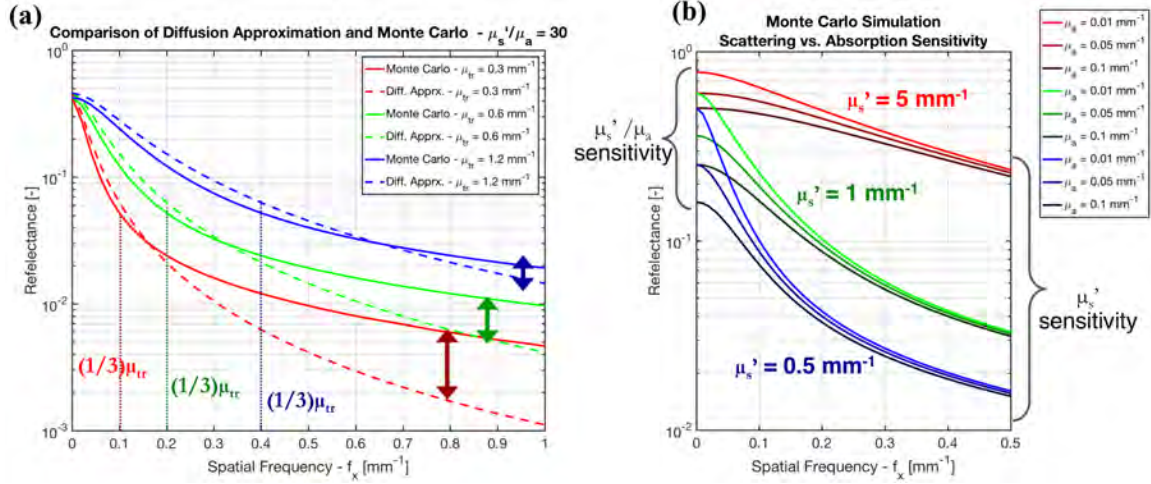


Figure 2.5 (a) Reflectance as a function spatial illumination frequency is shown for the standard diffusion approximation (dotted lines) and MC simulations (solid lines), at $\mu_{tr} \approx \mu_s' = [0.3, 0.6, 1.2] \text{ mm}^{-1}$ and $\mu_s'/\mu_a = 30$. The two models diverge as f_x increases to $> 3l^* = (1/3)/\mu_{tr} \approx (1/3)/\mu_s'$, meaning diffusion theory is invalid when $f_x > (1/3)/\mu_s'$. (b) MC simulated reflectance as a function spatial illumination frequency is shown for $\mu_s' = [5, 1, 0.5] \text{ mm}^{-1}$ (red, green, blue lines respectively), and $\mu_a = [0.01, 0.05, 0.1] \text{ mm}^{-1}$. At low f_x , sensitivity to μ_s'/μ_a is maximized, but as f_x increases, sensitivity is limited to just μ_s' . Data generated from the virtual photonics toolbox (<http://www.virtualphotonics.org/vts/>).

Experimental examples of wide-field scatter sensitivity with high-spatial frequency illumination are shown in Fig. 2.6 and Fig. 2.7. A white light image, NIR diffuse image (730 nm LED source, $f_x = 0 \text{ mm}^{-1}$), and a high spatial frequency image (730 nm LED source, $f_x = 0.5 \text{ mm}^{-1}$) are shown for avian tissue with the left half superficially coated in whole bovine blood in Fig. 2.6(a) and for a pomegranate slice in Fig. 2.6(b).

For the avian tissue, the white light contrast is clearly dominated by the blood. In the NIR

image where the hemoglobin absorption coefficient drops roughly an order of magnitude[32], absorption based blood contrast is still noticeable and the resolution is blurry due to increased optical diffusion. The high spatial frequency demodulated image has a marked increase in contrast and resolution between the muscle and fat, and a marked decrease to absorption based contrast from blood. This is conceptually explained by the fact that the demodulation of the light structured suppresses sensitivity to multiply scattered photons having long tortuous path lengths, which contribute to blurring effects from volumetric signal averaging and are most sensitive to absorption. Similarly, in Fig. 2.6(b), the white light image is dominated by red color contrast, which is somewhat diminished in the NIR image. But, in the high spatial frequency demodulated image has a completely different appearance due to scatter based contrast from the fibrous structures in the fruit.

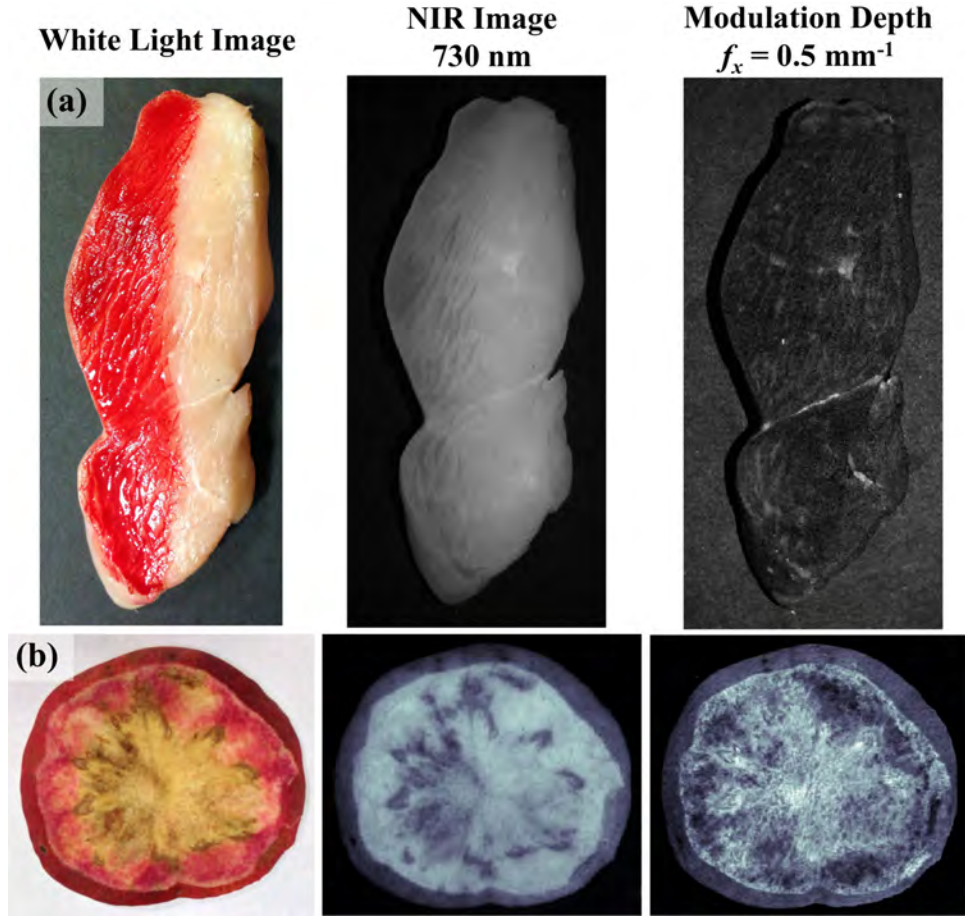


Figure 2.6 White light images, NIR (730 nm LED source) diffuse images, and demodulated images (730 nm LED source, $f_x = 0.5 \text{ mm}^{-1}$) are shown for (a) avian tissue with a layer of whole bovine blood coating the left half of the tissue and (b) a slice of a pomegranate.

A white light image and demodulated images at spatial frequencies increasing from 0 to 0.5 mm^{-1} for 658 nm illumination are shown for a cross section of a surgical resected mastectomy specimen in Fig. 2.7. Again the contrast of the white light image is dominated by visible chromophores, specifically red hemoglobin in blood and orange β -carotene in fat [32], with little contrast between the glandular features of interest, which all appear to be white. But, with increasing spatial frequency, both contrast and resolution increases, revealing textural and intensity changes within regions of the glandular tissue, highlighted by the green and cyan arrows. The approximate depth penetration at each spatial frequency is also shown, calculated by $\delta_{\text{eff}} = 1/(\mu_{\text{eff}}^2 + 2\pi f_x^2)^{1/2}$, where $\mu_{\text{eff}} =$

$(3\mu_a\mu_{tr})^{1/2}$ as derived by Cuccia et al. using diffusion theory and a spatially modulated source [20].

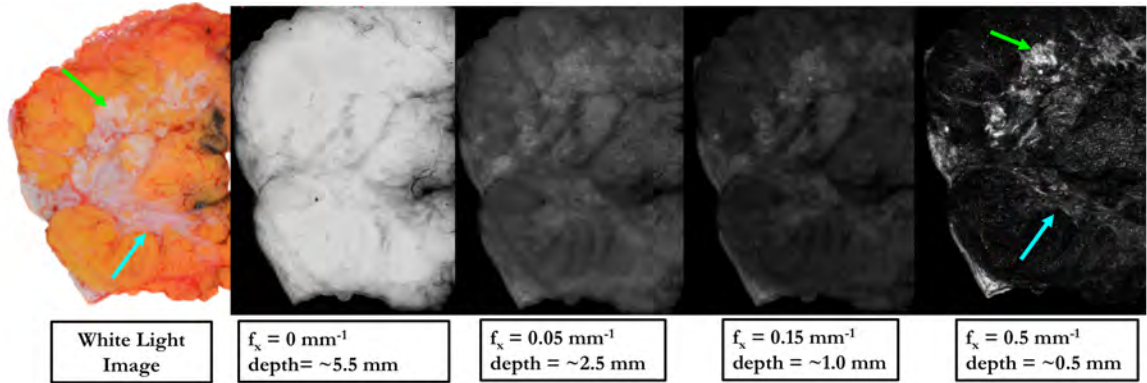


Figure 2.7 White light image of a cross section of a mastectomy, along with demodulated images (658 nm LED source) at $f_x = [0, 0.05, 0.15, 0.5] \text{ mm}^{-1}$. Green and cyan arrows demarcate a lack of contrast on the visible white light image, but enhance contrast on the high spatial frequency images. Depth sensitivity estimates are given calculated as $\delta_{eff} = 1/(\mu_{eff}^2 + 2\pi f_x^2)^{1/2}$ [20].

2.3. Quantification of Light Scattering with Structured Illumination

In the previous section, wide-field scatter-sensitive images were created by constraining the period spatially illumination frequency to be finer than three mean free paths. Furthermore, it was described that in this regime the assumptions of diffusion theory are broken. Specifically, transport can no longer assumed to be isotropic to a first order, with reflectance being highly sensitive to the angular distribution of scattering events, or phase function. Therefore, to quantify reflectance in this so called sub-diffusive regime, a new optical property quantifying the relative strength of forward to backward scattering has to be introduced, as described in the following sub-sections. Furthermore, this phase function parameter is inherently related to the size-scale distribution of scattering features on the order of the wavelength of light, making it an excellent biomarker to detect morphological change in tissue. This section is largely based on the work of Kanick et

al.[33], in which D.M. McClatchy played a significant role in acquiring and interpreting the data.

2.3.1. *Phase Function Quantification, and Inversion Problem*

In the spatial domain, it was well known that remission within one mean-free path was sensitive to the phase function[18]. To quantify this effect, a new optical property taking into account higher order moments of the scattering phase function was introduced, $\gamma = (1-g_2)/(1-g_1)$, where g_1 and g_2 are the 1st and 2nd Legendre moments of the scattering phase function (g_1 is simply the anisotropy factor g) [34, 35]. A more conceptual definition of γ is the relative magnitude of forward to backward scattering, or similarly, the relative distribution of scattering features larger and smaller than the wavelength of light [36]. For instance, if a coplanar source and detector pair were within one mean free path of each other and the density of scatterers was held constant, a lower γ value would indicate a higher probability of back scattering resulting in an increased remitted signal, while a larger γ value would indicate a higher probability of forward directed scattering resulting in a decrease remitted signal. The group at Erasmus Medical Center developed a MC-based, spatially resolved model to predict and quantify sub-diffusive reflectance as a function of radius for a given value of μ_s' , γ , and fiber diameter [37, 38]. Building upon this work, Kanick et al. transformed this model from the spatial domain into the spatial frequency domain through a Henkel transform as was done in Cuccia et al.[20]. With this sub-diffusive spatial frequency reflectance model, both μ_s' and γ could be spatially mapped through a non-linear least squares fitting routine. In essence, the optical property values at which the difference between experimentally measured demodulated reflectance and model predicted reflectance were calculated at each pixel. This was demonstrated

using wavelengths in the range of [658, 730, 850, 970] nm and spatial frequencies in the range of [0.05-0.5] mm⁻¹[39]. It should be noted that a critical piece of development for accurate optical property recovery in the sub-diffusive regime was the removal of cross polarizers, which rejects weakly backscattered light[40]. In the following sub-section, proof of principle demonstrations of spatially mapping the reduced scattering coefficient, μ_s' , and the phase function parameter, γ , are shown, along with examples of how these scattering parameters could be used as biomarkers for morphological change.

2.3.2. *Proof of Concept in Silico, in Vitro, and in Vivo*

The very first proof of concept demonstrations of spatially mapping both the reduced scattering coefficient, μ_s' , and the phase function parameter, γ , are shown below in Fig. 2.8 [33]. To demonstrate the accuracy of this method, Intralipid (IL) phantoms of various concentrations were imaged, and recovered μ_s' and γ values were compared to well accepted scattering values for IL produced by Michels et al. [41]. In Fig. 2.8(a), a schematic of the IL concentrations in each well are shown, with corresponding μ_s' and γ maps shown in Fig. 2.8 (b) and (c) respectively. As expected, recovered μ_s' values increase with IL concentration and recovered γ values are independent of IL concentration, as the density of scatters varies with IL concentration but the size scale distribution of scatters remains constant. Plots of known versus recovered μ_s' and γ values, in Fig. 2.8 (d) and (e) respectively, show a strong correlation over all IL concentrations and wavelengths. To demonstrate the value of this technique in quantifying changes in tissue morphology, a human hand with a superficial scar (D.M.M) was imaged. In Fig. 2.8(f) a NIR diffuse image of the hand is shown, where the scar is not at all visible and contrast is primarily due to optical absorption of hemoglobin the

veins. But in Fig. 2.8(g), the high spatial frequency image is completely insensitive to the veins and superficial scatter based contrast of the scar can be seen (green arrows). This is quantified in the μ_s' and γ maps shown in Fig. 2.8 (h) and (i) respectively, where diffuse multiple light scattering is insensitive to the superficial scar having a similar bulk density as skin, but the superficial phase function quantification parameter is in fact sensitive to the collagen reorganization within the scar compared to neighboring skin. However, a limitation of this results is that the effect of optical absorption at low spatial frequencies is not taken into effect, although absorption values are likely similar between the scar and skin.

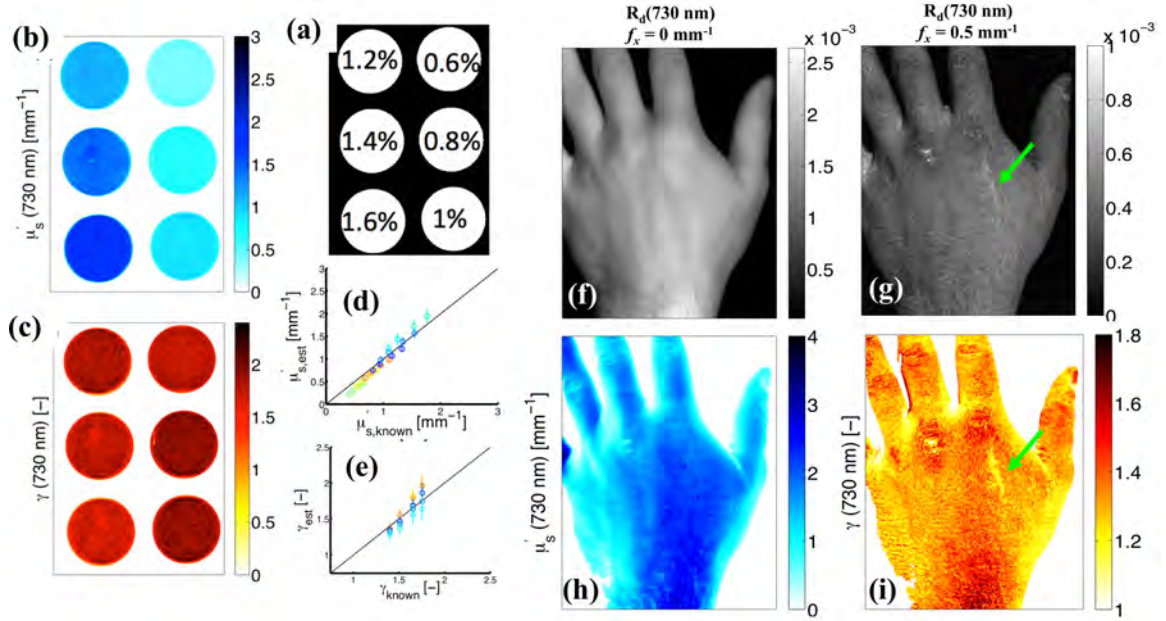


Figure 2.8 (a) Index showing the IL% within each well for the corresponding μ_s' map in (b) and γ map in (c). Plots of known versus estimated μ_s' and γ values are shown in (d) and (e), respectively. The strong linear relationship demonstrates the proof-of-principle of the inversion methods. Calibrated reflectance maps at 730 nm are shown in (f) and (g) respectively, while the corresponding μ_s' and γ maps are shown in (h) and (i) respectively. The green arrows highlight a superficial scar which is undetectable in the diffuse image and μ_s' map, but is noticeable in $f_x = 0.5 \text{ mm}^{-1}$ reflectance and γ maps. Data adapted with permission from S.C. Kanick, D.M. McClatchy III, et al., “Sub-diffusive scattering parameter maps recovered using wide-field high-frequency structured light imaging”, 2014.

In Fig. 2.9, mapping of sub-diffusive optical scattering properties is shown to

spatially quantify changes to tissue morphology in vitro. Specifically, avian tissue was submerged in a formalin (4% formaldehyde) solution for 1,2,3,4, and 5 minutes to induce structural changes to the tissue, such as protein cross-linking and swelling[42]. These induced morphological alternations are not visible under white light illumination as shown in Fig. 2.9(a). However, a clear increase in μ_s' as a function of formalin exposure can be seen in Fig. 2.9(b), which is in accordance with previously published studies[43]. Conversely, a clear decrease in γ as a function of formalin exposure can be seen in Fig. 2.9(c), suggesting that the morphological changes induced by formalin exposure lead to an increase backwards directed light scattering. In addition to bulk changes in μ_s' and γ between time points, significant spatial heterogeneity within each tissue specimen can be seen, which would otherwise go undetected with a point probing device.

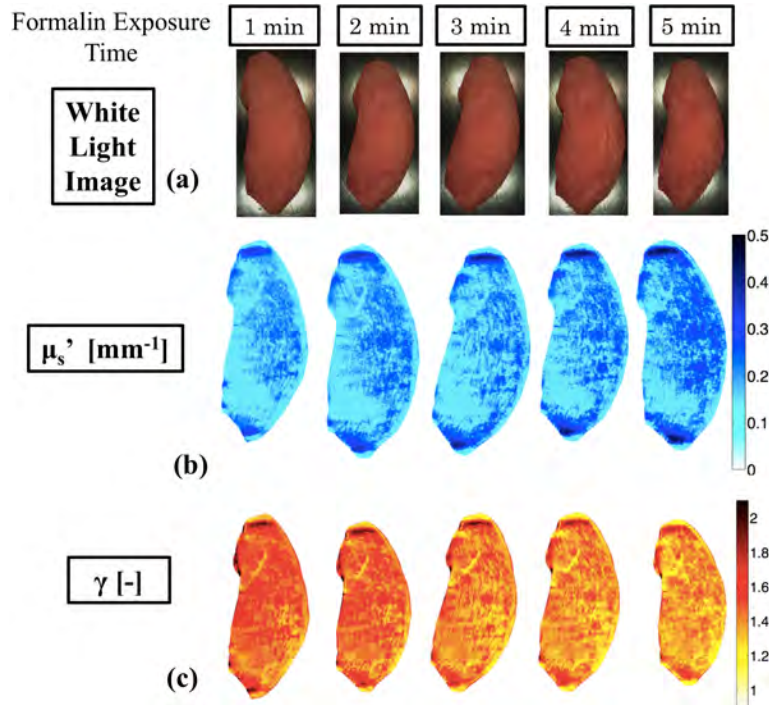


Figure 2.9 (a) White light images of avian tissues exposed to formalin (4% formaldehyde) for 1,2,3,4, and 5 minutes. Corresponding μ_s' and γ maps are shown in (b) and (c) respectively, spatially quantifying the morphological changes to the tissue in response to the formalin exposure.

References:

1. Chance, B., *Photon migration in tissues*. 1989, New York: Plenum Press. x, 195 p.
2. Maxwell, J.C., *A treatise on electricity and magnetism*. 1873, Oxford,: Clarendon press.
3. Yee, K.S., *Numerical Solution of Initial Boundary Value Problems Involving Maxwell's Equations in Isotropic Media*. Ieee Transactions on Antennas and Propagation, 1966. **Ap14**(3): p. 302-&.
4. Denk, W. and D.W. Pohl, *Near-Field Optics - Microscopy with Nanometer-Size Fields*. Journal of Vacuum Science & Technology B, 1991. **9**(2): p. 510-513.
5. Ishimaru, A., *Wave propagation and scattering in random media*. IEEE/OUP series on electromagnetic wave theory. 1997, New York Oxford; New York: IEEE Press; Oxford University Press. xxv, 574 p.
6. Liemert, A. and A. Kienle, *Exact and efficient solution of the radiative transport equation for the semi-infinite medium*. Sci Rep, 2013. **3**: p. 2018.
7. Wang, L., S.L. Jacques, and L. Zheng, *MCML--Monte Carlo modeling of light transport in multi-layered tissues*. Computer methods and programs in biomedicine, 1995. **47**(2): p. 131-46.
8. Rogers, D.W.O., *Fifty years of Monte Carlo simulations for medical physics*. Physics in medicine and biology, 2006. **51**(13): p. R287-301.
9. Lambert, J.H. and D.L. DiLaura, *Photometry, or, On the measure and gradations of light, colors, and shade : translation from the Latin of Photometria, sive, De mensura et gradibus luminis, colorum et umbrae*. 2001, New York: Illuminating Engineering Society of North America. ccxix, xii, 423, 17 p., 8 folded leaves of plates.
10. Hayakawa, C.K., J. Spanier, and V. Venugopalan, *Comparative analysis of discrete and continuous absorption weighting estimators used in Monte Carlo simulations of radiative transport in turbid media*. Journal of the Optical Society of America A, Optics, image science, and vision, 2014. **31**(2): p. 301-11.
11. Alerstam, E., T. Svensson, and S. Andersson-Engels, *Parallel computing with graphics processing units for high-speed Monte Carlo simulation of photon migration*. J Biomed Opt, 2008. **13**(6): p. 060504.
12. Palmer, G.M. and N. Ramanujam, *Monte Carlo-based inverse model for calculating tissue optical properties. Part I: Theory and validation on synthetic phantoms*. Applied optics, 2006. **45**(5): p. 1062-71.

13. Ishimaru, A., *Diffusion of light in turbid material*. Appl Opt, 1989. **28**(12): p. 2210-5.
14. Flock, S.T., et al., *Monte Carlo modeling of light propagation in highly scattering tissue--I: Model predictions and comparison with diffusion theory*. IEEE transactions on bio-medical engineering, 1989. **36**(12): p. 1162-8.
15. Schweiger, M., et al., *The finite element method for the propagation of light in scattering media: boundary and source conditions*. Med Phys, 1995. **22**(11 Pt 1): p. 1779-92.
16. Farrell, T.J., M.S. Patterson, and B. Wilson, *A diffusion theory model of spatially resolved, steady-state diffuse reflectance for the noninvasive determination of tissue optical properties in vivo*. Med Phys, 1992. **19**(4): p. 879-88.
17. Haskell, R.C., et al., *Boundary conditions for the diffusion equation in radiative transfer*. JOSA A, 1994. **11**(10): p. 2727-2741.
18. Bolt, R.A. and J.J. Ten Bosch, *Method for measuring position-dependent volume reflection*. Appl Opt, 1993. **32**(24): p. 4641-5.
19. Dögnitz, N. and G. Wagnières, *Determination of tissue optical properties by steady-state spatial frequency-domain reflectometry*. Lasers in Medical Science, 1998. **13**(1): p. 55-65.
20. Cuccia, D.J., et al., *Quantitation and mapping of tissue optical properties using modulated imaging*. Journal of biomedical optics, 2009. **14**(2): p. 024012-024012.
21. Cuccia, D.J., et al., *Modulated imaging: quantitative analysis and tomography of turbid media in the spatial-frequency domain*. Opt. Lett, 2005. **30**(11): p. 1354-1356.
22. Neil, M., R. Juskaitis, and T. Wilson, *Method of obtaining optical sectioning by using structured light in a conventional microscope*. Optics letters, 1997. **22**(24): p. 1905-1907.
23. Mazhar, A., et al., *Wavelength optimization for rapid chromophore mapping using spatial frequency domain imaging*. Journal of biomedical optics, 2010. **15**(6): p. 061716.
24. Laughney, A.M., et al., *System analysis of spatial frequency domain imaging for quantitative mapping of surgically resected breast tissues*. Journal of biomedical optics, 2013. **18**(3): p. 036012-036012.
25. Laughney, A.M., et al., *Spectral discrimination of breast pathologies in situ using spatial frequency domain imaging*. Breast Cancer Res, 2013. **15**(4): p. R61.

26. Gioux, S., et al., *First-in-human pilot study of a spatial frequency domain oxygenation imaging system*. Journal of biomedical optics, 2011. **16**(8): p. 086015-086015.
27. Syeda Tabassum, et al., *Feasibility of spatial frequency domain imaging (SFDI) for optically characterizing a preclinical oncology model*. Biomed Opt Express, 2016. **7**(10): p. 4154-4170.
28. Laughney, A.M., et al., *Scatter spectroscopic imaging distinguishes between breast pathologies in tissues relevant to surgical margin assessment*. Clinical Cancer Research, 2012. **18**(22): p. 6315-6325.
29. Krishnaswamy, V., et al., *Structured light scatteroscopy*. J Biomed Opt, 2014. **19**(7): p. 070504.
30. Bodenschatz, N., et al., *Sources of errors in spatial frequency domain imaging of scattering media*. Journal of biomedical optics, 2014. **19**(7): p. 071405-071405.
31. Bodenschatz, N., et al., *Model-based analysis on the influence of spatial frequency selection in spatial frequency domain imaging*. Applied optics, 2015. **54**(22): p. 6725-6731.
32. Jacques, S.L., *Optical properties of biological tissues: a review*. Physics in medicine and biology, 2013. **58**(11): p. R37.
33. Kanick, S.C., et al., *Sub-diffusive scattering parameter maps recovered using wide-field high-frequency structured light imaging*. Biomed Opt Express, 2014. **5**(10): p. 3376-90.
34. Bevilacqua, F. and C. Depeursinge, *Monte Carlo study of diffuse reflectance at source--detector separations close to one transport mean free path*. JOSA A, 1999. **16**(12): p. 2935-2945.
35. Bevilacqua, F., et al., *In vivo local determination of tissue optical properties: applications to human brain*. Applied optics, 1999. **38**(22): p. 4939-4950.
36. Chamot, S., et al., *Physical interpretation of the phase function related parameter \$\$ studied with a fractal distribution of spherical scatterers*. Optics express, 2010. **18**(23): p. 23664-23675.
37. Gamm, U.A., et al., *Quantification of the reduced scattering coefficient and phase-function-dependent parameter gamma of turbid media using multidiameter single fiber reflectance spectroscopy: experimental validation*. Opt Lett, 2012. **37**(11): p. 1838-40.
38. Kanick, S.C., et al., *Measurement of the reduced scattering coefficient of turbid media using single fiber reflectance spectroscopy: fiber diameter and phase function dependence*. Biomedical optics express, 2011. **2**(6): p. 1687-702.

39. Kanick, S.C., et al., *Sub-diffusive scattering parameter maps recovered using wide-field high-frequency structured light imaging*. Biomedical optics express, 2014. **5**(10): p. 3376-3390.
40. Wiest, J., et al., *Polarization influence on reflectance measurements in the spatial frequency domain*. Physics in medicine and biology, 2015. **60**(15): p. 5717-32.
41. Michels, R., F. Foschum, and A. Kienle, *Optical properties of fat emulsions*. Optics Express, 2008. **16**(8): p. 5907-5925.
42. Crawford, G.N.C. and R. Barer, *The Action of Formaldehyde on Living Cells as Studied by Phase-Contrast Microscopy*. Quarterly Journal of Microscopical Science, 1951. **92**(4): p. 403-&.
43. Wood, M.F., et al., *Effects of formalin fixation on tissue optical polarization properties*. Phys Med Biol, 2011. **56**(8): p. N115-22.

Chapter 3: Intraoperative Near Infrared Imaging of Inked Lumpectomy Specimens Utilizing Molecular Dyes

3.1. Background and Goals

A major focus of this thesis work was on clinical translation, with a specific goal of intraoperative assessment of resected BCS specimen margins through optical imaging of the tissue surface. A well-known, but rarely discussed, hindrance to intraoperative BCS imaging is the application of multicolored inks to the BCS specimen surface, which is performed as the specimen is excised to record its orientation. The following manuscript describes a novel specimen marking method allowing for intraoperative NIR sensing and imaging during BCS, which has implications for any optical technique aiming to probe BCS specimens with NIR light.

3.2. Published Work

The following published manuscripts is reprinted from:

McClatchy DM, 3rd, Krishnaswamy V, Kanick SC, Elliott JT, Wells WA, Barth RJ, Jr., Paulsen KD, Pogue BW. Molecular dyes used for surgical specimen margin orientation allow for intraoperative optical assessment during breast conserving surgery. *J Biomed Opt.* 2015;20(4):040504. <http://dx.doi.org/10.1117/1.JBO.20.4.040504>

This article was published in a journal managed by SPIE under a Creative Commons License, which permits reuse for any purpose as long as the manuscript is cited: © The Authors. Published by SPIE under a Creative Commons Attribution 3.0 Unported License. Distribution or reproduction of this work in whole or in part requires full attribution of the original publication, including its DOI.

D. M. McClatchy and V. Krishnaswamy were responsible for the experimental imaging of the whole lumpectomy specimens, which were delivered and managed by R. J. Barth. D. M. McClatchy was also responsible for data analysis and quantification, design of avian tissue experiments, and preparing the manuscript. W. A. Wells was in charge of the protocol to image surgical human breast tissue. V. Krishnaswamy, S. C. Kanick, J. T. Elliott, K. D. Paulsen and B. W. Pogue all played a role in the original conception of the dye marking system, provided advising, and participated in editing and writing the manuscript.

Molecular dyes used for surgical specimen margin orientation allow for intraoperative optical assessment during breast conserving surgery

David M. McClatchy III,^{a,*} Venkataramanan Krishnaswamy,^a Stephen C. Kanick,^a Jonathan T. Elliott,^a Wendy A. Wells,^b Richard J. Barth Jr.,^c Keith D. Paulsen,^{a,d} and Brian W. Pogue^{a,c}

^aDartmouth College, Thayer School of Engineering, 14 Engineering Drive, Hanover, New Hampshire 03755, United States

^bDartmouth College, Department of Pathology, Geisel School of Medicine, 1 Rope Ferry Road, Hanover, New Hampshire 03755, United States

^cDartmouth College, Department of Surgery, Geisel School of Medicine, 1 Rope Ferry Road, Hanover, New Hampshire 03755, United States

^dDartmouth College, Department of Diagnostic Radiology, Geisel School of Medicine, 1 Rope Ferry Road, Hanover, New Hampshire 03755, United States

Abstract. A variety of optical techniques utilizing near-infrared (NIR) light are being proposed for intraoperative breast tumor margin assessment. However, immediately following a lumpectomy excision, the margins are inked, which preserves the orientation of the specimen but prevents optical interrogation of the tissue margins. Here, a workflow is proposed that allows for both NIR optical assessment following full specimen marking using molecular dyes which have negligible absorption and scattering in the NIR. The effect of standard surgical inks in contrast to molecular dyes for an NIR signal is shown. Further, the proposed workflow is demonstrated with full specimen intraoperative imaging on all margins directly after the lumpectomy has been excised and completely marked. This work is an important step in the path to clinical feasibility of intraoperative breast tumor margin assessment using NIR optical methods without having to compromise on the current clinical practice of inking resected specimens for margin orientation. © The Authors. Published by SPIE under a Creative Commons Attribution 3.0 Unported License. Distribution or reproduction of this work in whole or in part requires full attribution of the original publication, including its DOI. [DOI: [10.1117/1.JBO.20.4.040504](https://doi.org/10.1117/1.JBO.20.4.040504)]

Keywords: breast tumor margins; breast conserving surgery; tissue diagnostics; near-infrared; molecular dyes.

Paper 140489LR received Jul. 29, 2014; accepted for publication Mar. 31, 2015; published online Apr. 22, 2015.

With advances in breast cancer screening technologies and the recent widespread adoption of neoadjuvant chemotherapy, an increasing number of patients are undergoing breast conserving surgery (BCS) in lieu of a full mastectomy. It has been shown that the long-term survival of patients who undergo BCS is equivalent to those who undergo a full mastectomy if all of the tumor margins are negative.¹ This process is encouraging in that less invasive surgeries are completed as compared to full mastectomy, yet this smaller excision volume also presents added pressure on the clinical need to accurately ensure that there was a complete excision with no remaining residual cancer in the body. If a positive margin is diagnosed from the resection specimen after the procedure, then a second re-excision surgery is performed to remove further tissue at added cost and patient morbidity. Due to the lack of effective intraoperative surgical guidance and the difficulty in tumor localization with decreasing tumor size, re-excision rates have been reported to be as high as 20 to 40%.² However, re-excision rates vary greatly between institutions because of differing protocols for what constitutes a positive margin. The current standard of care for BCS involves a preoperative wire localization of the tumor core, guided by mammography or ultrasound, as shown in Fig. 1. This wire is a landmark to aid in discerning the central location of the tumor during the procedure and a rough guide to the boundary. After the tumor is excised, its margins are immediately inked by the surgeon in order to preserve its orientation in the event that a second re-excision is required.³ Histopathological analysis performed over the following one to two days determines if there is cancerous involvement at the margins. Currently, a myriad of optical techniques are being investigated to intraoperatively determine if there is cancerous involvement at the margins.^{4–8} However, severe signal degradation by the surgical inks prevents all of these proposed techniques from potential clinical translation, so the subject of this letter is to outline the use of organic dyes which serve the same function as surgical inks but then allow spectroscopic imaging of the underlying tissue through most of the near-infrared (NIR) spectrum.

Given the prevalence of BCS, there is a clinical need for intraoperative surgical specimen margin assessment to augment pathological analysis, and hopefully to curb the high rate of re-excision procedures on subsequent days following the initial surgery. Because cancerous processes locally alter tissue ultrastructure in both epithelial and stromal structure, its presence can be detected through changes in the optical spectrum.^{9,10} Many microscopic optical techniques have been examined for intraoperative margin assessment of localized spots, including frozen section phase microscopy, optical coherence tomography, confocal microscopy, fluorescence imaging, Raman spectroscopic microscopy, and polarization.^{4–6} Macroscopic imaging of the entire tissue field has had limited study, but both raster scanning and spatial frequency domain imaging systems have recently shown promise.^{7,8} These studies have focused on the NIR spectrum of light due to the diminished absorption attenuation from surface blood on the specimen, and thus far, there have been many promising results demonstrating a realistic potential for future clinical use.

However, many of these studies involve a workflow of either obtaining optical tissue measurements before inking or after specimens are loafed into slices during postsurgical processing. While these workflows are acceptable for research investigations, the standard practice of inking the specimen during excision to preserve its orientation must be incorporated into these emerging

*Address all correspondence to: David M. McClatchy III, E-mail: david.m.mcclatchy.iii.th@dartmouth.edu

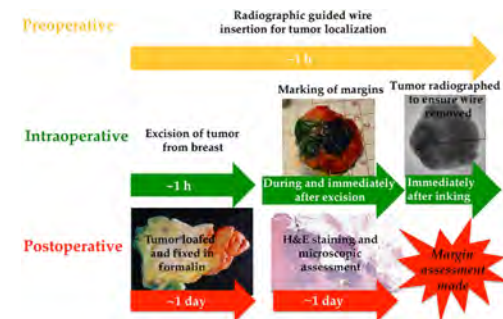


Fig. 1 A workflow diagram showing the typical phases of a breast conserving surgery. The arrows indicate the approximate time of each phase.

optical techniques in order for translation into the current standard of care for BCS. Marking the specimen margins during excision is critical as adipose tissue largely compromises the lumpectomy margin so they are extremely amorphous. In addition to their shapelessness, the presence of surface blood makes it very difficult to keep track of the margin orientation. If the orientation of the specimen was not preserved, then it would be unclear where to re-excite tissue in the event of a positive margin being found. Unfortunately, these surgical inks indefinitely limit optical probing of the tissue due to their extreme scattering and absorption properties (as seen in Fig. 2). Techniques to manually fix the specimen in place so that its orientation can be set without the use of ink have been reported, but these techniques are difficult as lumpectomies can drastically differ in both size and shape requiring many different fixing mechanisms.¹¹ Furthermore, the margins of a given lumpectomy can be asymmetrical after removal from the anatomical support of the breast.

To more easily translate direct optical intraoperative margin assessment techniques into a standard BCS procedure with as little interference as possible, a marking system is needed that has negligible optical effects in the NIR wavelengths but still provides contrast under white light. Common surgical

inks are densely composed of particulate carbon and pigments leading to both strong absorption and scattering in the NIR. In this letter, molecular dyes are introduced which have a composition of a minimally scattering gel with molecular absorbers, which are Food, Drug & Cosmetics food dyes that happen to only absorb in the visible spectrum. The difference in optical attenuation in the NIR between the molecular dyes and standard surgical inks can be seen in Fig. 2. Avian muscle tissue was marked with every color of a standard surgical ink (The Davidson System, Bradley Products, Inc., Bloomington, Minnesota) and a molecular dye (Ataco, Glen Cove, New York), which is simply a consumer food dye gel. The tissue was illuminated with three light-emitting diodes spanning the NIR (730, 850, and 970 nm) and imaged with a CCD which were part of a commercial planar imaging system (Modulated Imaging, Inc., Irvine, California).¹² In Figs. 2(a) and 2(b), one can see under white illumination that both the surgical ink and molecular dyes have very similar visible contrast. But in Figs. 2(c) and 2(d), it is apparent that the surgical inks completely degrade the optical signal at all three wavelengths while the molecular dye appears virtually invisible except for faint absorption of the black dye at 730 nm. Figures 2(e) and 2(f) show bar graphs for the relative change in signal intensity between each of the six markings and neighboring unmarked tissue for the NIR wavelength wide-field imaging. Figure 2(e) shows that the maximum change in signal intensity for the molecular dyes is roughly 15% for the black dye at 730 nm. However, Fig. 2(f) shows that all of the surgical inks with the exception of red at all wavelengths and green at 970 nm have an absolute signal intensity change of at least 70% at all of the NIR wavelengths. The faint absorption of the black molecular dye is insignificant though as many of the potential optical techniques have a subdiffusive sensitivity where absorption effects are minimized. On the contrary, surgical inks are specifically manufactured so that they are visible under microscopic assessment. It should also be noted, however, that the water-soluble molecular dyes cannot survive standard tissue processing standards that precede histopathological assessment. As such, the molecular dyes simply act as a temporary proxy for the surgical inks to allow intraoperative optical assessment, after which the standard surgical inks are applied.

A pilot study was also conducted to introduce a potential clinical workflow that would allow for both intraoperative optical margin assessment and the surgeon to perform routine specimen orientation inking during resection, but with the molecular dyes. The major goals of this pilot study were to demonstrate that the proposed molecular dyes could be used as an effective temporary substitute to the traditional surgical inks in a clinical setting and, consequently, show that NIR optical probing could be performed in the presence of the molecular dyes after the margins were marked. The workflow for the study involved the surgeon marking the lumpectomy margins with the molecular dye during resection, and then all six of the margins were imaged in a room adjacent to the operating room (OR). After imaging, the specimen went back to the OR, where the surgeon applied standard surgical inks for standard histopathological assessment. All patients ($n = 6$ patients) gave informed consent to participate in this clinical trial, which was approved by the Dartmouth institutional review board. To demonstrate NIR optical probing through the molecular dyes, a previously described wide-field imaging technique called structured light scatterometry (SLS) was performed.¹³ This technique has been shown to have insensitivity to surface blood and enhanced

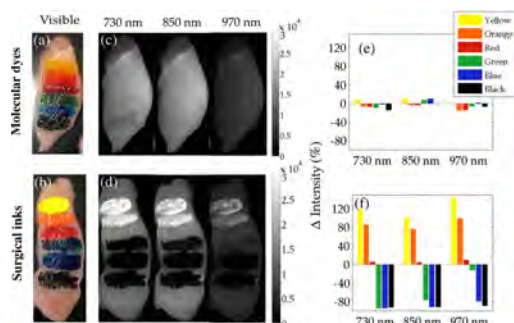


Fig. 2 White light color image of avian muscle phantom with six standard margin orientation colors of (a) molecular dyes and (b) surgical inks. Near-infrared wavelength (730, 850, and 970 nm) full-field imaging of the phantom with (c) molecular dyes and (d) surgical inks. Bar graph of the relative change in signal intensity for the (e) molecular dyes and (f) surgical inks between each color and surrounding unmarked tissue for each wavelength.

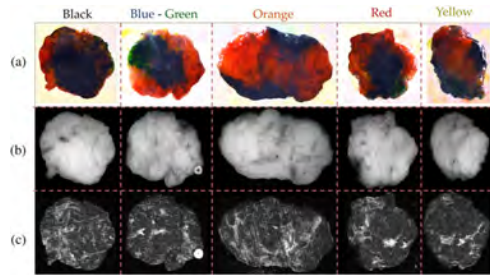


Fig. 3 Sample data set of full specimen intraoperative imaging through a glass slide after margins were completely marked with molecular dye. (a) Color photographs, (b) wide-field imaging with 850-nm light-emitting diodes, and (c) structured light scatteroscopy imaging (850 nm) with a sinusoidal pattern of 0.5 mm^{-1} .

sensitivity to scattering, which was a significant diagnostic factor in previous breast tumor margin NIR imaging studies.^{7,8,13} However, retrospective analyses of SLS data and histopathology were not included as a part of this study, as the main goal was demonstrating the utility of molecular dyes for NIR methods aimed toward intraoperative breast tumor margin assessment. SLS involves illuminating high spatial frequency structured light and demodulating the perturbed pattern.¹³ For this study, a sinusoidal pattern with a spatial frequency of 0.5 mm^{-1} was illuminated, having an effective penetration depth of $\sim 0.3 \text{ mm}$. The pattern was projected at three evenly spaced phase offsets of $0, 2\pi/3, 4\pi/3$, yielding images I_1, I_2, I_3 , which were used to calculate the demodulated image I_d .¹⁴

$$I_d = (2^{1/2}/3)[(I_1 - I_2)^2 + (I_1 - I_3)^2 + (I_2 - I_3)^2]^{1/2}. \quad (1)$$

In addition, standard full-field illumination imaging was performed by averaging I_1, I_2 , and I_3 . The acquisition time to image one face of the margin is only $\sim 1 \text{ min}$, and the entire imaging procedure was $\sim 20 \text{ min}$ with transporting and handling the tissue. Data were acquired with the same commercial NIR imaging system from Modulating Imaging, Inc., and the molecular dyes and surgical inks were also the same as used in the chicken breast phantom. Figure 3 shows the 850 nm channel collected for a single lumpectomy specimen. In Fig. 3(a), white light images show how the entire specimen is visible when marked with colored dye. The specimens were placed on a glass slide and imaged from below. Because of their shapelessness, often two previously orthogonal margins could be imaged at once, as is the case in Fig. 3 with the blue and green margins. Figures 3(b) and 3(c) show the diffuse full-field images and the demodulated images, I_d , respectively, for the 850 nm channel. While both sets of images in Figs. 3(b) and 3(c) show insensitivity to the molecular dyes, the SLS image in Fig. 3(c) shows

high contrast features arising from local changes in light scattering from changes in tissue morphology. This presented workflow demonstrates feasibility for using molecular dyes as a temporary proxy for standard surgical inks with minimal interference to both NIR optical signals and the current standard of care BCS procedure.

Due to the increasing prevalence of BCS and accompanying high rates of re-excision, there is a strong clinical need for an intraoperative tumor margin assessment system. While many optical methods have been proposed and have demonstrated sensitivity in pilot studies, they fail to negotiate margin orientation inking. Using molecular dyes for full specimen marking after resection would allow for NIR optical assessment of the margins without significantly altering the current standard of care practice of BCS.

References

- U. Veronesi et al., "Twenty-year follow-up of a randomized study comparing breast-conserving surgery with radical mastectomy for early breast cancer," *N. Engl. J. Med.* **347**(16), 1227–1232 (2002).
- R. G. Pleijhuis et al., "Obtaining adequate surgical margins in breast-conserving therapy for patients with early-stage breast cancer: current modalities and future directions," *Ann. Surg. Oncol.* **16**(10), 2717–2730 (2009).
- G. R. Gibson et al., "A comparison of ink-directed and traditional whole-cavity re-excision for breast lumpectomy specimens with positive margins," *Ann. Surg. Oncol.* **8**(9), 693–704 (2001).
- J. Q. Brown et al., "Optical assessment of tumor resection margins in the breast," *IEEE J. Sel. Topics Quantum Electron.* **16**(3), 530–544 (2010).
- R. Patel et al., "Multimodal optical imaging for detecting breast cancer," *J. Biomed. Opt.* **17**(6), 066008 (2012).
- R. Patel et al., "Polarization sensitive multimodal imaging for detecting breast cancer," *Cancer Res.* **74**, 4685–4693 (2014).
- A. M. Laughney et al., "Scatter spectroscopic imaging distinguishes between breast pathologies in tissues relevant to surgical margin assessment," *Clin. Cancer Res.* **18**(22), 6315–6325 (2012).
- A. M. Laughney et al., "Spectral discrimination of breast pathologies *in situ* using spatial frequency domain imaging," *Breast Cancer Res.* **15**(4), R61 (2013).
- Y. L. Kim et al., "Low-coherent backscattering spectroscopy for tissue characterization," *Appl. Opt.* **44**(3), 366–377 (2005).
- V. Krishnaswamy et al., "Quantitative imaging of scattering changes associated with epithelial proliferation, necrosis, and fibrosis in tumors using microsampling reflectance spectroscopy," *J. Biomed. Opt.* **14**(1), 014004 (2009).
- T. Karni et al., "A device for real-time, intraoperative margin assessment in breast-conservation surgery," *Am. J. Surg.* **194**, 467–473 (2007).
- D. J. Cuccia et al., "Quantitation and mapping of tissue optical properties using modulated imaging," *J. Biomed. Opt.* **14**(2), 024012 (2009).
- V. Krishnaswamy et al., "Structured light scatteroscopy," *J. Biomed. Opt.* **19**(7), 070504 (2014).
- M. A. Neil, R. Juskaitis, and T. Wilson, "Method of obtaining optical sectioning by using structured light in a conventional microscope," *Opt. Lett.* **22**(24), 1905–1907 (1997).

Chapter 4: Quantitative Imaging of Tissue Microstructure in Freshly Resected Human Breast Specimens

4.1. Background and Goals

In Chapter 2, Section 2.3, a method to quantify and map sub-diffusive light scattering parameters was introduced based on the work of Kanick et al. However, this method completely neglected the effect of optical absorption on the low spatial frequency measurements presenting an obstacle to image surgically resected breast tissue, which contain strong optical absorbers. Additionally, the initial report did not independently separate known variations in both the phase-function and scatter density. Therefore, the goal of this study were multi-pronged: (1) incorporate absorption effects into the model, (2) validate the model on phantoms with user defined differences in both scatter density and the phase function, and most importantly (3) determined if these sub-diffusive scattering parameters could distinguish various breast pathologies from each another. This following manuscript details this new model, its validation on custom made aqueous phantoms with tunable scattering properties, and its evaluation on a cohort of n=22 freshly resected human breast tissue specimens, which did in fact show sensitivity of multispectral scattering parameters to different breast tissue diagnoses.

4.2. Published Work

The following published manuscripts is reprinted from:

McClatchy DM, 3rd, Rizzo EJ, Wells WA, Cheney PP, Hwang JC, Paulsen KD, Pogue BW, Kanick SC. Wide-field quantitative imaging of tissue microstructure using sub-diffuse spatial frequency domain imaging. Optica. 2016;3(6):613-21.

<http://dx.doi.org/10.1364/OPTICA.3.000613>

This article was published in a journal managed by OSA under an Open Access Publishing Agreement, which allows the final publisher Version of Record manuscript to be reproduced by authors or third party users for non-commercial personal or academic purposes (includes the uses listed above and e.g. creation of derivative works, translation, text and data mining).

https://www.osapublishing.org/submit/review/copyright_permissions.cfm

D. M. McClatchy was responsible for all phantom and tissue data acquisition, analysis, and quantification as well as preparing the manuscript. E. J. Rizzo was responsible for receiving and dissecting the surgical human breast tissue. P.P. Cheney and J.C. Hwang provided the dark field microscopy system and participated in signal interpretation. W. A. Wells was responsible of the protocol to image surgical human breast tissue, along with diagnosing and annotating digitized histology slides. S. C. Kanick, K. D. Paulsen and B. W. Pogue provided advising and participated in editing the manuscript. S. C. Kanick and W. A. Wells were responsible for the human tissue imaging study design. S.C. was responsible for original conception of imaging fractal dimensions of scatters and adapting Mie theory code for this experiment.

Wide-field quantitative imaging of tissue microstructure using sub-diffuse spatial frequency domain imaging

DAVID M. McCCLATCHY III,¹ ELIZABETH J. RIZZO,² WENDY A. WELLS,^{2,3} PHILIP P. CHENEY,⁴ JEESEONG C. HWANG,⁴ KEITH D. PAULSEN,^{1,3} BRIAN W. POOGUE,^{1,3} AND STEPHEN C. KANICK^{1,3,*}

¹Thayer School of Engineering, Dartmouth College, 14 Engineering Drive, Hanover, New Hampshire 03755, USA

²Department of Pathology, Dartmouth Hitchcock Medical Center, 1 Medical Center Drive, Lebanon, New Hampshire 03756, USA

³Norris Cotton Cancer Center, Dartmouth Hitchcock Medical Center, 1 Medical Center Drive, Lebanon, New Hampshire 03756, USA

⁴Quantum Electromagnetics Division, National Institute of Standards and Technology, 325 Broadway Street, Boulder, Colorado 80305, USA

*Corresponding author: stephen.c.kanick@dartmouth.edu

Received 12 January 2016; revised 27 April 2016; accepted 13 May 2016 (Doc. ID 256858); published 9 June 2016

Localized measurements of scattering in biological tissue provide sensitivity to microstructural morphology but have limited utility to wide-field applications, such as surgical guidance. This study introduces sub-diffusive spatial frequency domain imaging (sd-SFDI), which uses high spatial frequency illumination to achieve wide-field sampling of localized reflectances. Model-based inversion recovers macroscopic variations in the reduced scattering coefficient (μ'_s) and the phase function backscatter parameter (γ). Measurements in optical phantoms show quantitative imaging of user-tuned phase-function-based contrast with accurate decoupling of parameters that define both the density and the size-scale distribution of scatterers. Measurements of fresh *ex vivo* breast tissue samples revealed, for the first time, unique clustering of sub-diffusive scattering properties for different tissue types. The results support that sd-SFDI provides maps of microscopic structural biomarkers that cannot be obtained with diffuse wide-field imaging and characterizes spatial variations not resolved by point-based optical sampling. © 2016 Optical Society of America

OCIS codes: (170.3660) Light propagation in tissues; (170.3880) Medical and biological imaging; (170.6510) Spectroscopy, tissue diagnostics; (170.6935) Tissue characterization.

<http://dx.doi.org/10.1364/OPTICA.3.000613>

1. INTRODUCTION

Measurements of light scattering are known to be sensitive to the composition and orientation of cells, intracellular constituents, and the extracellular matrix [1]. A variety of optical imaging techniques have been developed to sample tissue over a variety of length scales, each providing sensitivities to different structural features within biological tissue. Diffuse wide-field imaging of tissue exploits a signal dominated by multiply scattered light where the remission at each pixel is representative of an average of long and tortuous photon path lengths covering relatively large volumes (cubic millimeters to cubic centimeters). Optical measurement geometries based on small fiber optics or confocal setups have been designed to sample reflectance remissions within highly localized volumes of tissue (cubic micrometers to cubic millimeters). Reflectance remissions that are collected near the source location are dominated by low-ordered scattered photons, which are sensitive to both the frequency of scattering events and the anisotropic character of the scatterers [2–6]. Under these conditions, the light-transport regime has been termed sub-diffuse. Previous work has characterized the interconnectedness of the tissue ultrastructure evaluated using microscopic approaches and the

distribution of scattering structures that defines light scattering in the local tissue microenvironment [7–10]. Histology, shown in Fig. 1 for adipose, fibroglandular, and invasive breast tissue, is the “gold standard” for assessing tissue morphology in a clinical setting. With hematoxylin and eosin (H&E) stained histology sections, a pathologist interprets the types and organization of nuclei, cells, and extracellular components that comprise the tissue in order to make a diagnosis. Techniques such as scanning transmission electron microscopy allow the resolution of smaller structures, including organelles within and fibrous components outside of the cell. The density, composition, and size-scale dimension of these biological structures combine to determine the spatial distribution of refractive index fluctuations on length scales ranging from tens of nanometers to tens of micrometers [11], which is the source of light scattering in tissue. These parameters define the angular probability of scattering events, given as the scattering phase function, with trade-offs between larger scatterers, which are on the size scale of the wavelength of light and preferentially scatter in a forward direction, and Rayleigh-type scatterers, which are smaller than the wavelength of light and scatter isotropically. Because histology and electron microscopy

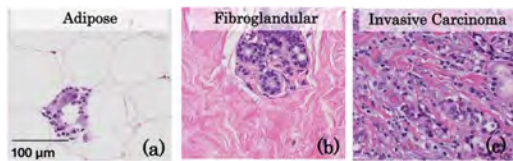


Fig. 1. Representative histology slides of human breast (a) adipose, (b) fibroglandular, and (c) invasive carcinoma tissues illustrating their unique density, size-scale distribution, and organization of biological features.

are both destructive to tissue and time consuming to evaluate, light scattering as a means to assess the microscopic character of tissue morphology *in vivo*, rapidly and over large tissue volumes, is of considerable interest.

Fiber-optic methods that sample localized elastically scattered remissions near the source location are sensitive to the composition and morphology of biological tissue [12–14]. Advanced optical approaches have been developed that use low-coherence interferometry to either resolve the angular remission of light [15,16] from tissue or sample interference-based amplification of reflectance signals [17,18]. Such methods are capable of resolving fine details of the tissue microarchitecture, including the fractal dimension or correlation distance of cellular features [19] or the correlation length of the microscopic mass-density distribution [20], and hold promise for the diagnosis of pathologies such as cancer [21] by returning information usually reserved for destructive tissue analysis methods. However, point-based assessments of reflectance (including both non coherent and low-coherent) do not characterize tissue heterogeneity over macroscopic length scales. While approaches to raster-scan localized-sampling methods are able to identify pathology and possibly guide clinical decisions during surgeries [22], they are time consuming when applied over large areas of tissue and may not be practical. Polarization imaging is one method that is reported to be sensitive to clinically relevant spatial variations in tissue microstructure [23], but it has yet to gain wide clinical acceptance.

This study focuses on a novel alternative that applies sub-diffusive spatial frequency domain imaging (sd-SFDI) to achieve localized reflectance sampling over a wide field of view quickly. It extends previous microscopy work reported by Neil *et al.* [24], which acquired sub-diffractive signals without raster scanning by using structured illumination. Recently, our group showed that macroscopic imaging based on structured light with a high-frequency photon density wave, whose periodicity was finer than the length scale of diffuse photon propagation, resulted in sub-diffusive signal localization in a wide-field geometry. A spectroscopic [25] and multi-frequency [26] interpretation of high spatial frequency reflectance provided sensitivity to, and quantified images of, sub-diffuse scattering parameters, including the reduced scattering coefficient, μ'_s , and a phase function parameter, $\gamma = \frac{(1-g_2)}{(1-g_1)}$, that characterizes the backscatter likelihood of the medium and is expressed as a weighted ratio of the first two Legendre moments of the scattering phase function, g_1 and g_2 [3,27]. The current study applies sd-SFDI to validate wide-field quantitative images of the sub-diffusive scattering parameters in phantoms containing user-tuned phase functions and then applies

the approach to image fresh *ex vivo* tissue samples. The resulting sub-diffusive parameter maps show clear discrimination of tissue types based on scattering parameters that reflect their microstructural differences.

2. METHODS

A. Sub-Diffusive Spatial Frequency Domain Imaging: Basic Concept

By spatially modulating the intensity of light incident on a turbid medium, the effective penetration depth of the resulting photon density wave can be altered by the fineness of the intensity pattern. Even though this technique is well known and has been used for diffuse spectroscopic imaging in a variety of applications [28,29], sub-diffusive imaging at high-spatial frequencies has only recently been explored [26,30]. While low spatial frequency photon density waves are described by isotropic scattering and are preserved [1–2] mm into the tissue on average, as the spatial frequency is increased, the photon density waves penetrate less deeply into the tissue. Here, the forward and backward propagation is influenced by the scattering anisotropy and yields a sub-surface fluence pattern that is preserved only to sub-millimeter depths of penetration. Diffuse reflectance can be completely described by the absorption and isotropic scattering of photons through μ_a and μ'_s , respectively. However, sub-diffusive reflectance collected within one-mean free path of propagation is sensitive to not only the frequency of scattering events, but also the relative likelihood that the scattering is large angled [2,3], which is quantified with phase-function parameter, γ . A first-order approximation to conceptualizing γ is the ratio of relative contributions of large to small scatters [27]. Previous work has reported γ values in tissue in the range of [1.3–2.2] [-] [12,14,26,31], with smaller values representative of scatterers that are smaller than the wavelength of scattered light and larger values representative of scatterers approaching the same length scale as the wavelength of light. While γ has been shown to be linearly proportional to the fractal dimension of scatterers in a turbid medium, a deterministic link between the two parameters is complicated by other physical parameters that influence the exact form of the scattering phase function [27]; therefore, a concise description of γ may best be as a metric proportional to the length scale of biological scattering features. Quantification of these parameters through a model inversion yields a complete description of the sub-diffusive reflectance and may offer biomarkers for discriminating between tissue types.

Details of sd-SFDI acquisition and analysis appear in **Supplement 1**. In brief, sd-SFDI was performed using spatial frequencies over the range of $f_x = [0 - 0.2, 0.5 - 0.9] \text{ mm}^{-1}$ in steps of 0.05 mm^{-1} with source LEDs centered about [658,730,850] nm. Demodulated reflectance images were calibrated and fit to a combined model of diffuse and sub-diffuse reflectance on a pixel-by-pixel basis, returning spatial maps of μ'_s , γ , and μ_a at each measured wavelength. Here μ'_s was assumed to follow a power law, $\mu'_s(\lambda) = A(\frac{\lambda}{800 \text{ nm}})^{-B}$, in which A is the scatter amplitude and corresponds directly to $\mu'_s(800 \text{ nm})$, B is the spectral scattering power, and $\gamma(\lambda)$ was fitted as a free parameter at each wavelength. Figure 2 illustrates the workflow of acquiring, analyzing, and spatially co-registering optical parameter maps with *ex vivo* tissue samples.

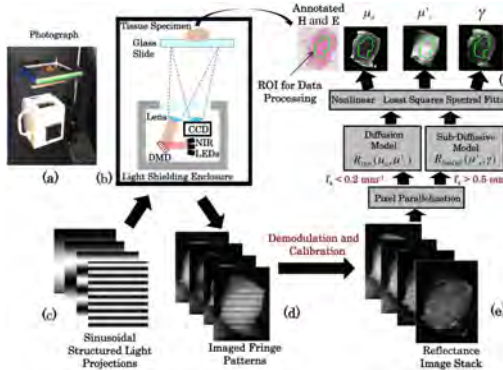


Fig. 2. (a) Photograph of sub-diffusive spatial frequency domain imaging system and (b) diagram of major system components. Sinusoidal intensity patterns (c) are sent to the digital micromirror device and projected on the tissue, with the remitted fringe pattern imaged (d). The stack of fringe patterns over multiple spatial frequencies and wavelengths were demodulated and calibrated to a reference standard yielding a reflectance map stack (e), which was then used to calculate optical property maps (f).

B. Phantom Imaging of Fractal Distribution of Mie Scatterers

Polystyrene spheres are a well-characterized scattering standard. Previous work demonstrated that proper selection of the fractal dimension, D_f , of the distribution of diameters yielded biologically relevant scattering phase functions [32], where the frequency of scatter sizes, C , follows a fractal distribution as a function of the particle diameter, d , defined as $C(d) \propto d^{-D_f}$. As the fractal dimension increases, the phase function becomes more isotropic with a relative increase in Rayleigh scatterers that are much smaller than the wavelength of light. Conversely, as the fractal dimension decreases, the phase function becomes more forward peaked with an increase in larger Mie scatterers. Phantoms were constructed with physiologically relevant fractal dimension in the range of $D_f = [3.6 - 4.85]$ [-]. In brief, D_f has a pronounced effect on the spectral power of μ_s' , as defined for models considering both discrete scatterers [8] and continuous random media [33], and introduces spectrally invariant differences in γ . Chamot *et al.* investigated γ in the context of a distribution of spherical particles [27] and showed, both theoretically and experimentally, that γ is proportional to the D_f of spheres.

Three sets of aqueous phantoms were prepared using mixtures of ten discrete diameter spheres, $d = [0.099, 0.14, 0.21, 0.39, 0.5, 0.8, 0.96, 4.5, 10, 20]$ μm and $n = 1.56$ (Polysciences Inc., Warrington, Pennsylvania and Bangs Laboratories, Fishers, Indiana). The first set contained six phantoms, each with a different fractal dimension, $D_f = [3.6:0.25:4.85]$, where the volume fraction of polystyrene spheres in each solution was adjusted to result in a matching reduced scattering coefficient at a selected wavelength, such that $\mu_s'(658 \text{ nm}) = [1.2] \text{ mm}^{-1}$. The second set contained nine phantoms with three selected fractal dimensions, $D_f = [3.6, 4.1, 4.6]$, each prepared with the volume fraction of spheres adjusted to yield three values of $\mu_s'(658 \text{ nm}) = [1.2, 1.8, 2.4] \text{ mm}^{-1}$. The third phantom set contained nine phantoms with coupled variation of $D_f = [3.6, 4.1, 4.6]$ and

the absorption coefficient, which was varied by adding incremental amounts of Evans Blue dye to achieve $\mu_a(658 \text{ nm}) = [0.02 - 0.18] \text{ mm}^{-1}$ such that the ratio $\frac{\mu_s'}{\mu_a}$ ranged from 5.6 to 50 at 658 nm. The first phantom set was evaluated to establish the sensitivity of high-spatial frequency reflectance imaging to the uniquely tuned phase functions in each phantom and to test whether the model inversion accurately quantified the sub-diffuse scattering parameters (i.e., μ_s' and γ). The second phantom set was imaged to demonstrate the separability of μ_s' and γ in phantoms with differences in both the number density of scatterers and the scattering phase functions within the same image. The third phantom set was used to confirm the accuracy of scattering parameters in the presence of absorption-based attenuation. For all phantom images reported, a 1 cm circular region of interest is presented, as the optical properties are spatially homogeneous, and also to eliminate pixels close to the well wall that are influenced by boundary effects.

Additionally, solid agarose phantoms with a step-change in scatter contrast (i.e., both scatter density and scatter size) were constructed to estimate the spatial resolution and sensitivity to heterogeneously distributed optical scatter parameters. Details regarding the fabrication of these phantoms can be found in Supplement 1.

C. Ex Vivo Human Breast Tissue Imaging and Histological Analysis

To demonstrate the ability of sd-SFDI to differentiate tissue morphologies, optical scatter parameter maps of surgically excised human breast tissue were compared to spatially co-registered histopathologic diagnoses. The study, approved by the Dartmouth-Hitchcock Medical Center (DHMC) Institutional Review Board for the protection of human subjects, included 22 breast tissue specimens from 17 patients undergoing elective and consented breast surgeries at DHMC. After excision and margin inkling, specimens were sent to the Department of Pathology and “bread loafed” according to standard-of-care protocol. Upon gross inspection of the loafed specimen, excess tissue that was not needed to make a pathologic diagnosis was evaluated. Specifically, excess tissue conforming to a standardized gross diagnosis of fibroglandular, adipose, benign fibroadenoma, or invasive carcinoma (both lobular and ductal) was cut to a size of approximately 25 mm \times 25 mm \times 5 mm and immediately imaged. The totals for each tissue type sampled are as follows: adipose (3 patients, 3 specimens, 5785 pixels), fibrolandular (8 patients, 10 specimens, 19391 pixels), benign fibroadenoma (3 patients, 4 specimens, 10459 pixels), and invasive carcinoma (5 patients, 5 specimens, 6984 pixels).

All tissue samples were imaged with sd-SFDI as in Fig. 2, with samples placed on a glass slide and imaged in an inverted geometry to minimize surface curvature and height variations. Additionally, the distance between the glass slide and optical system was fixed to ensure that the projected sinusoid was the correct spatial frequency and in focus. Spatial frequency imaging of the tissue samples required ≈ 2 min to complete. Additionally, a select set of specimens were also imaged with a dark-field reflectance microscope, the details of which are described in Supplement 1. Following optical imaging, the tissue samples underwent standard histological processing, including formalin fixation and H&E staining. The prepared tissue sections were evaluated by an expert pathologist (W.A.W.), who outlined final

diagnoses over digital scans of the entire section. These annotated digital histology sections were readily co-registered to the optical scattering maps with simple rigid transformations and were used to create binary masks for pixel-based clustering analysis. Pixels near the boundary of the tissue were excluded from the clustering analysis, as shown in Fig. 2(f), to avoid boundary artifacts. All of the breast specimens included in the clustering analysis were uniformly comprised of a single breast tissue type in order to capture differences between well-defined tissue morphologies. However, one localized invasive cancer surrounded by adipose and fibrous tissue was analyzed to demonstrate the application of the method to a heterogeneous tissue specimen.

3. RESULTS AND DISCUSSION

A. Optical Parameter Recovery in Phantoms

The data in Fig. 3 demonstrate contrast obtained with wide-field sd-SFDI from the scattering phase function. Here, each phantom contains a matched absorption and reduced scattering coefficient at $\lambda = 658$ nm, but a unique fractal distribution of scatterers, and therefore, a unique γ and scatter slope B . In Fig. 3(a), a photograph of the phantom set shows the individual phantoms to be indistinguishable under white light. Similarly, diffuse reflectance at $f_x = 0 \text{ mm}^{-1}$, shown in Fig. 3(c), provides little contrast between the unique fractal distributions, which are annotated in panel Fig. 3(b). However, as the spatial frequency increases

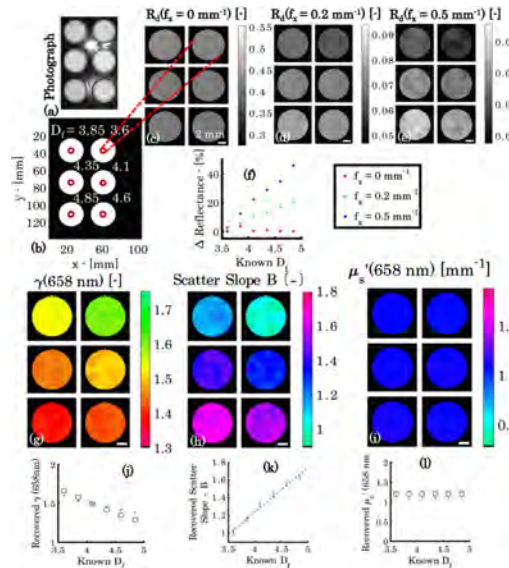


Fig. 3. Phantoms with μ'_s held constant with γ variation. (a) Photograph, (b) annotated D_f , and (c)–(e) demodulated reflectance images at $\lambda = 658$ nm and $f_x = [0, 0.2, 0.5] \text{ mm}^{-1}$. (f) Normalized plot of percentage change in reflectance versus D_f for each spatial frequency. Recovered maps of $\gamma(658 \text{ nm})$, scatter slope B , and $\mu'_s(658 \text{ nm})$ are shown in (g), (h), and (i), respectively. Below are plots of recovered optical property values versus D_f in (j), (k), and (l), where the blue error bars represent recovered mean values \pm one standard deviation, the black circles represent the Mie theory-predicted $\gamma(658 \text{ nm})$ and $\mu'_s(658 \text{ nm})$ values, and the black dotted line represents a regression of scatter slope B versus D_f ($r = 0.993$). Scale bar is 2 mm.

to $f_x = 0.2 \text{ mm}^{-1}$ and 0.5 mm^{-1} in Figs. 3(d) and 3(e), respectively, contrast appears in the calibrated reflectance, arising purely from sub-diffusive remissions, which are sensitive to the underlying particle size-scale distribution. This relationship between reflectance and fractal dimension of the distribution is shown to be linear in Fig. 3(f), with the magnitude of the proportionality increasing as the spatial frequency increases. At $f_x = 0.5 \text{ mm}^{-1}$, a 40% change in reflectance occurs that is due to the relative differences in large-angle backscattering in each unique phase function. These changes in reflectance are quantified with the model inversion to yield optical property maps of γ , scatter slope B , and μ'_s shown in Figs. 3(g)–3(i). The reduced scatter coefficient, describing isotropic diffusion, is constant throughout the phantoms, while both γ and the scatter slope show a strong dependence on the varied particle size distributions. Figures 3(j) and 3(l) show that the absolute values of the scattering parameters obtained with the model inversion, which are represented by the blue error bars, agree with those determined from the Mie theory, represented by the black circles. Interestingly, Figs. 3(j) and 3(k) also show a strong negative linear relationship between the fractal dimension versus γ , and a strong positive linear relationship between the fractal dimension versus scatter slope, respectively, as γ and scatter slope both describe the relative ratio of large to small scatterers.

The data in Fig. 4 show that sd-SFDI is capable of distinguishing the relative density of scatterers from their size-scale distribution. The phantoms appear similar under white light illumination in Fig. 4(a) for the combinations of μ'_s and D_f specified in Fig. 4(b). The diffuse reflectance images sampled at $f_x = [0, 0.2, 0.5] \text{ mm}^{-1}$ shown in Figs. 4(c)–4(e) provide contrast along each column that arises from a 2-fold increase in particle concentration, and spatial frequency-dependent contrast in D_f is evident along each row. Reflectance maps of the phantoms are shown in panels (c)–(e), while the reflectance intensities quantified per fractal dimension are plotted in the accompanying panels, (f)–(h). Inspection of the reflectance data at $f_x = 0.2 \text{ mm}^{-1}$ shows a contrast between the μ'_s values in each column in the image in panel (d) and a μ'_s -dependent proportionality between the reflectance intensity and D_f in (g), with measurements of the lowest scattering coefficient resulting in the highest sensitivity to changes in the scattering phase function. The reflectance images at $f_x = 0.5 \text{ mm}^{-1}$, shown in Figs. 4(e) and 4(h), again provide contrast between the columns, but now in the fully sub-diffusive regime, contrast occurs along every column that arises from the change in particle size-scale distribution, as shown in Fig. 4(h). Here, the reflectance intensity becomes nonunique for coupled variations of the concentration and distribution of particles sizes when sampled in the sub-diffusive regime. This phenomenon is highlighted by the orange and pink reflectance indicators R_A and R_B in Figs. 4(e) and 4(h), which show similar reflectance values for pairs of different combinations of μ'_s and D_f . However, by applying the multi-spatial frequency inversion, differences in γ , the scatter slope, and μ'_s are readily distinguished, as shown in Figs. 4(i)–4(k), respectively. The maps of both γ and the scatter slope show clear stratification along the rows related to the varied particle concentration, while column-wise stratification with changing particle concentration appears in the map of μ'_s . As shown in Figs. 4(l) and 4(n), the absolute value of the parameters is in agreement with the Mie theory values, represented by blue error bars and black circles, respectively. A third tissue-simulating

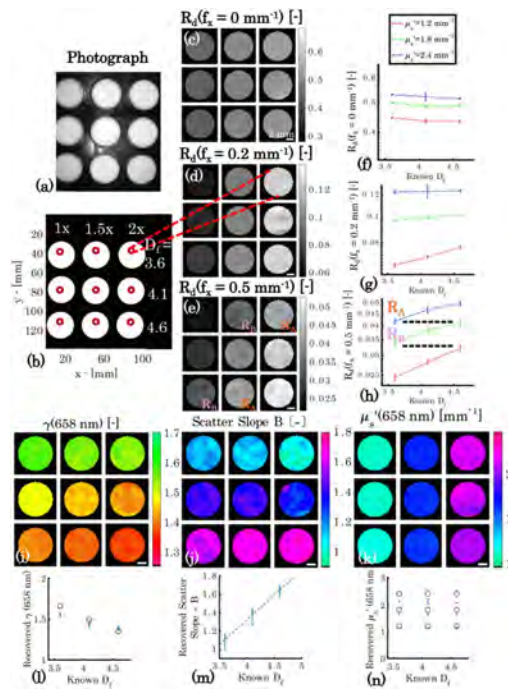


Fig. 4. Phantoms with coupled μ'_s and γ variation. (a) Photograph, (b) annotation of μ'_s and D_f values. Panels (c)–(e) show reflectance images at $\lambda = 658$ nm and $f_x = [0, 0.2, 0.5]$ mm $^{-1}$, while panels (f)–(h) show absolute values of reflectance versus D_f at each level of μ'_s for each spatial frequency. The dashed lines in (h) correspond to areas within (e) and highlight the nonuniqueness of the reflectance intensity with respect to combinations of μ'_s and γ . Panels (i), (j), and (k) show recovered $\gamma(658$ nm), scatter slope B, and $\mu'_s(658$ nm) maps. Below are corresponding plots of recovered optical property values versus D_f in (l), (m), and (n), where the blue error bars represent recovered mean values \pm one standard deviation, the black circles represent the Mie theory-predicted $\gamma(658$ nm) and $\mu'_s(658$ nm) values, and the black dotted line represents a regression of scatter slope B versus D_f ($r = 0.983$). Scale bar is 2 mm.

phantom experiment was performed with coupled variation in D_f and μ'_s for constant μ'_s ; imaging data are presented in *Supplement 1* and show that both μ'_s and γ are accurately recovered in the presence of a strong optical absorber.

While Figs. 3 and 4 present recovered values for μ'_s and γ at $\lambda = 658$ nm, optical scatter parameters were also recovered at $\lambda = 730$ and 850 nm. Mean absolute residuals, defined as $(100\% \frac{|\text{recovered}-\text{true}|}{\text{true}})$, where recovered is the experimental optical property value and true is the value obtained with the Mie theory, were calculated and averaged over all wavelengths. Similarly, Pearson product coefficients were calculated for the varied optical properties and averaged over all wavelengths. A summary of these parameters is included in Table 1, which shows all residuals $<12\%$, with the exception of μ'_s for the μ_a , γ variation experiment, and all correlation coefficients, $r > 0.95$. However, the authors would like to note that with the value of μ'_s for the μ_a , γ variation experiment, the mean residual is heavily weighted by the 850 nm wavelength, where $\mu'_s \approx 0.5$ mm $^{-1}$, but at 658 and

Table 1. Summary of Aggregate Residuals and Correlation Coefficients for Phantom Experiments

Phantom Set	$\langle \text{residual} \rangle [\%]$	$\langle r \rangle [-]$
μ'_s constant	$\mu'_s \langle 11.8 \pm 9.2 \rangle$	n/a
γ variation	$\gamma \langle 3.9 \pm 2.8 \rangle$	$\langle 0.996 \pm 0.003 \rangle$
μ'_s variation	$\mu'_s \langle 10.2 \pm 7.8 \rangle$	$\langle 0.997 \pm 0.0003 \rangle$
γ variation	$\gamma \langle 4.5 \pm 2.6 \rangle$	$\langle 0.964 \pm 0.01 \rangle$
μ_a variation	$\mu'_s \langle 23.8 \pm 20.4 \rangle$	n/a
γ variation	$\gamma \langle 5.1 \pm 3.4 \rangle$	$\langle 0.954 \pm 0.052 \rangle$

730 nm, the absolute residual $\approx 10\%$. It is important to note that the uncertainties in the recovered optical parameters reported in Figs. 3(j)–3(l) and Figs. 4(l)–4(n) represent a lower limit of scatter contrast that can accurately be resolved at an interface between scatterer (or tissue) types. Furthermore, analysis of the edge response function and line spread function for recovered maps of μ'_s and γ in heterogeneous optical phantoms yielded estimates of spatial resolution and sensitivity. Details are provided in *Supplement 1*; in brief, μ'_s and γ were accurately recovered with a resolution of ≈ 2 mm (i.e., 10 pixels) and ≈ 0.8 mm (i.e., 4 pixels), respectively.

B. Spatial Analysis of Breast Tissue Optical Properties

While phantom results demonstrate the technical accuracy of sd-SFDI and offer insights into the foundations of the optical signal, the composition of biological tissue has important differences from phantoms, especially at the microscopic level. Therefore, scatter parameter maps of freshly resected human breast tissue were co-registered to histopathologic diagnoses to demonstrate the potential of sub-diffusive scattering parameters to discriminate between microscopic morphologies of different tissue types. These data and comparisons are summarized in Fig. 5. Four ubiquitous breast tissue morphologies were considered: adipose, fibroglandular, benign fibroadenoma, and invasive carcinoma, corresponding to the columns in Fig. 5. Rows I and II contain “microscopic imaging” data and present representative high-magnification H&E and representative dark-field microscopy images from each tissue type. Rows III–VII include “macroscopic imaging” data and show co-registered H&E and white light images and optical parameter maps from a representative case for each tissue type.

An inspection of the microscopic imaging data reveals differences in microscopic morphology between tissue types. Figure 5, row I presents high-magnification histology sections for each tissue, revealing the relative proportions of fibrous stroma (appearing pink), nuclei density (appearing purple), and fat (appearing white due to clearing during processing). The adipose tissue in Fig. 5(a) is almost completely comprised of adipocytes with large lipid vacuoles on the size scale >25 μm , creating a tissue that is markedly forward scattering. The fibroglandular tissue in Fig. 5(b) appears to be largely comprised of stromal collagen, as shown by the overwhelming pink color in the H&E composite, with some fat and also functional, organized, yet sparse cellularity appearing in the high-magnification H&E. Although collagen fibers are relatively weak scatterers with a diameter of only a few micrometers, collagen fibrils are (≈ 20 nm–70 nm) in diameter with striations (<100 nm) and act as Rayleigh scatterers [34]. A fibroadenoma, shown in Fig. 5(c), is characterized by the benign proliferation of stromal collagen around the functional

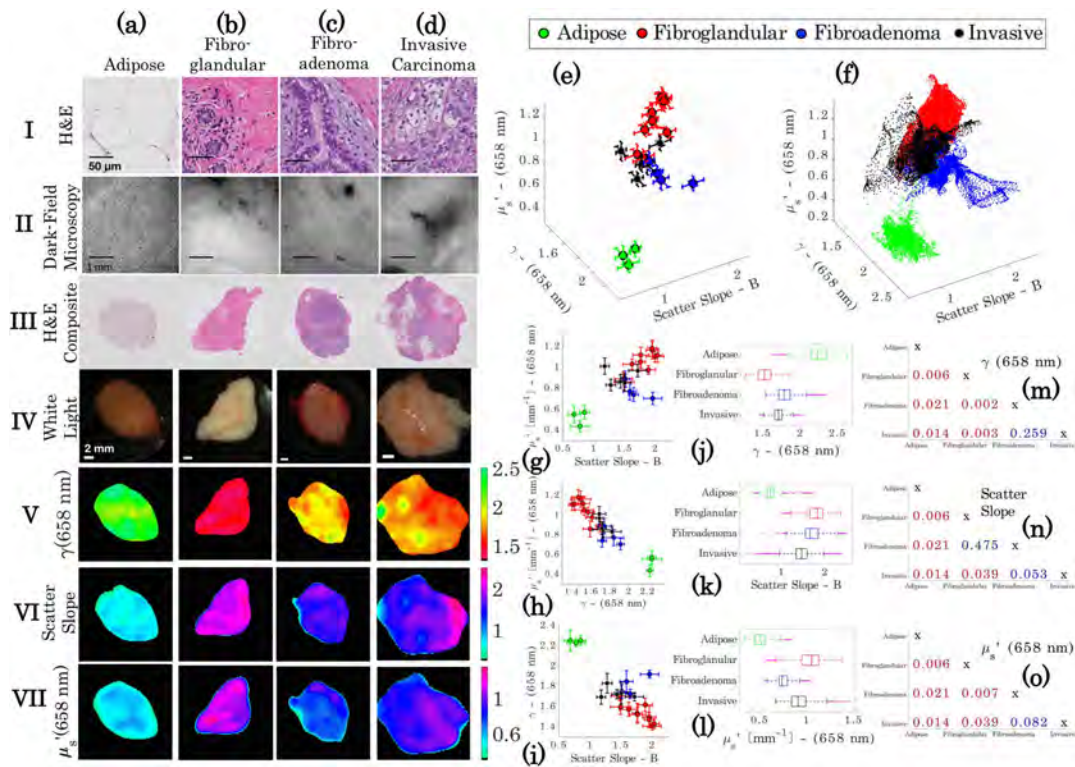


Fig. 5. Clustering of optical scatter parameters of homogeneous breast tissue of known diagnoses of (a) adipose, (b) fibroglandular, (c) benign fi-broadenoma, and (d) invasive carcinoma. The first row of images shows high-magnification H&E stained histology slides of a representative area of each tissue type, and below is a corresponding representative dark-field microscopy image in the second row. In the third row, a scanned co-registered composite histology slide appears with a white-light photograph (below in the following row). The final three rows contain the three optical scatter parameter maps, γ [-], scatter slope B [-], and μ'_s [mm^{-1}]. Three-dimensional clustering plots are shown for the means \pm one standard deviation and for all pixels for each specimen in (e) and (f). (g)–(i) Show two-dimensional clustering of the specimen means \pm one standard deviation for each pair of optical scatter parameters. (j)–(l) Show box and whisker plots for all points used in the cluster analysis for each scatter parameter. (m)–(o) Show two-sample Kolmogorov–Smirnov p-values for each pairwise combination of tissue diagnoses with each scatter parameter as the tested distribution.

epithelium, which in turn compresses and expands the cellular epithelium. The invasive carcinoma, shown in Fig. 5(d), is characterized by uncontrolled growth of the epithelium, with very high nuclear density and an increase in the nuclear-to-cytoplasmic ratio and mitochondrial density. The size scale of both nuclei ($\approx 5 \mu\text{m}$) and mitochondria ($\approx 1 \mu\text{m}$) characterizes them as weak, large scatterers.

Figure 5, row II contains dark-field microscopy reflectance images from fresh tissue samples, which show back-scattered light intensity from structural features. The dark-field images in row II were acquired on a slightly larger length scale from the high-magnification H&E images in row I. Dark-field images provide a unique scatter-based contrast from thick tissue samples and show clear differences in the microarchitecture of adipose with the more densely packed tissues. The effects of multiple scattering confound the resolution of many of the ultrastructural features in the fresh, thick tissue sample that is provided by the H&E analysis.

The panels in Fig. 5, row III show scanned composite sections of the histology that provide a description of the relative distribution of structural features on the millimeter-centimeter

length scale. Figure 5, row IV contains white-light photographs of each tissue type, with adipose tissue exhibiting a markedly yellow color, while the other more fibrous tissues appear as various shades of white and red. Figure 5, rows V–VII present $\gamma(658 \text{ nm})$, scatter slope B , and $\mu'_s(658 \text{ nm})$ for each tissue type, respectively. A quick inspection of these images shows differences between the tissue samples. The adipose tissue has a pronounced high γ and low μ'_s , which is consistent with large cells and lipid vacuoles that dominate light transport as large (forward) scatterers. Conversely, fibroglandular tissue presents a low γ and a high μ'_s , which is associated with a denser tissue composed of fibrils and striations with rapid and dense fluctuations in the refractive index that contribute meaningfully to Rayleigh-like scattering. A comparative inspection of the parameter maps of the fibroadenoma and invasive carcinoma with fibroglandular tissue show a reduced γ and an increased scatter slope, suggestive of a relative increase in larger scatterers. Additionally, both the glandular tissue and invasive carcinoma show an increased μ'_s compared with fibroadenoma, which is descriptive of the density of scattering structures within each tissue type.

Figure 5(e) presents a cluster plot with the three axes specified as $\gamma(658 \text{ nm})$, scatter slope B , and $\mu'_s(658 \text{ nm})$, for the means of each specimen with three-dimensional error bars representing one standard deviation, while Fig. 5(f) displays all pixels over all the specimens. Four distinct clusters appear, despite noticeable overlap in the cluster visualization. In Figs. 5(g)–5(i), scatter plots of specimen-based means with two-dimensional error bars are shown for each pair of scattering parameters. To quantitatively assess separation between tissue diagnoses, box and whisker plots are reported in Figs. 5(j)–5(l) for each optical scatter parameter. For the adipose tissue, the inter-quartile range (IQR) is fully separated from all tissue types for all three parameters. For $\gamma(658 \text{ nm})$ in Fig. 5(j), the IQRs of the fibroglandular and invasive carcinoma are completely separated by their unique structure size-scale distributions; however, for the invasive carcinoma and fibroadenoma, significant overlap occurs. In Fig. 5(k), the IQRs for the scatter slope of the invasive carcinoma, fibroadenoma, and fibroglandular overlap, but for μ'_s in Fig. 5(l), the fibroadenoma has noticeable separation from the invasive carcinoma and fibroglandular, which overlap due to their similar high densities. For further quantification, two-sample Kolmogorov-Smirnov nonparametric distribution tests were performed on the means of the specimens between each tissue type. P-values are tabulated in Figs. 5(m)–5(o) for all three scatter parameters, with a red color indicating a significant p-value at the $\alpha < 0.05$ level. Differences in the distributions of $\gamma(658 \text{ nm})$ were statistically significant for all tissue type pairings, except for invasive carcinoma compared with fibroadenoma, which did not yield a significant difference in distributions for all scattering parameters; however, the results may be due in part to the small sample size in this initial study.

The data presented in Fig. 5 represent individual samples of selected tissue types. A more clinically relevant situation is the measurement of tissue samples that contain multiple tissue types. Figure 6(a) shows a photograph of freshly excised cancerous breast tissue, with surrounding fat and normal fibrous tissue. In Figs. 6(b) and 6(c), scanning dark-field microscopy and a

calibrated reflectance image at $f_x = 0.6 \text{ mm}^{-1}$ with no median filtering are shown, respectively. The improved spatial resolution of scatter-based features offered by the dark-field microscopy compared with the sub-diffuse reflectance has a trade-off with increased the acquisition time; it is important to note that improved sd-SFDI resolution could be achieved with optimized projection and imaging magnification and CCD sensitivity. Figures 6(d)–6(f) shows maps of the optical scatter parameters $\gamma(658 \text{ nm})$, scatter slope B , and $\mu'_s(658 \text{ nm})$, respectively. Histology-guided regions of interest appear in Fig. 6(g), where spatial variations in tissue type exist, which stratify into the three distinct clusters shown in Fig. 6(h). These data demonstrate the ability to rapidly assess whole-tissue specimens through sub-diffuse imaging, where point-source or microscopic-based tissue interrogation methods would have to randomly sample a large number of locations to achieve similar robustness. Moreover, these data motivate a sampling strategy that uses multiple length-scale imaging for evaluation of malignancy within clinical tissue samples; such an approach would use sub-diffuse imaging to return a wide-field map of micro-structural parameters that may identify regions of interest, either for more detailed interrogation via microscopic imaging, or for guided selection of biopsy locations to obtain a definitive histological confirmation.

One promising clinical application for sd-SFDI is intraoperative tumor margin assessment for breast-conserving surgery, with sensitivity to the tissue composition at sub-millimeter levels that can be rapidly mapped over large fields of view. This wide-field imaging may be complementary to highly sensitive point-evaluation approaches (e.g., using Raman [35] or optical-coherence tomography [36]) by guiding the sampling locations within the surgical field. The envisioned embodiment of this approach may be as a back-bench setup to image excised tissue samples during surgery. Alternatively, an embodiment to image a surgical resection bed *in vivo* would be enabled by approaches to correct for height variations and boundary artifacts in the imaged field; profile-based corrections for height variations have been proposed for diffuse-SFDI [37] but have not yet been

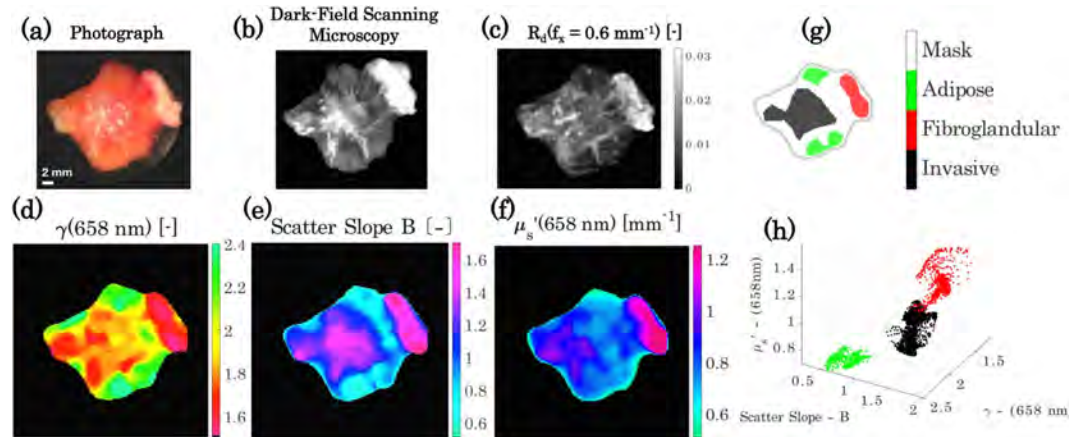


Fig. 6. Spatial contextualization of scattering parameters for heterogeneous breast tissue. (a) Photograph of tissue, (b) dark field scanning microscopy, and (c) sub-diffuse calibrated reflectance image with $f_x = 0.6 \text{ mm}^{-1}$ with no median filtering. (d)–(f) Show scatter optical property maps of γ [-], scatter slope B [-], and $\mu'_s[\text{mm}^{-1}]$, respectively. (g) Regions of interest corresponding to areas of localized tissue diagnoses and (h) clustering of the scatter properties for each tissue diagnosis.

developed for the sub-diffusive regime and are an area of ongoing investigation.

4. CONCLUSIONS

This study presents the use of sub-diffuse spatial frequency domain imaging to differentiate between tissue types based on microscopic-level morphological differences. The approach samples tissue rapidly, on the scale of minutes, and acquires large fields of view, on the scale of square centimeters. The measurements in optical phantoms show, for the first time, validation of the ability to detect and quantitate phase-function-based contrast from a wide-field imaging technique, with accurate decoupling of parameters that define both the density and the size-scale distribution of scatterers. Data from a small clinical pilot study indicate that the complete set of sub-diffuse optical scattering parameter maps appears to distinguish between various breast tissue morphologies in both homogeneous and heterogeneous freshly resected human breast tissue samples. This study imaged extracted clinical tissue samples through a glass plate to mitigate height variations in the imaged field; future work will need to consider the appropriateness of profile-correction algorithms in the sub-diffusive regime to image tissues *in vivo* in a noncontact manner. The data presented in this paper show that sd-SFDI provides wide-field maps of scattering parameters that are usually reserved for microscopic evaluations.

Funding. National Institute of Standards and Technology (NIST) (60NANB13D210); National Cancer Institute (NCI) (K25CA164248).

Acknowledgment. The authors thank Venkataraman Krishnaswamy and Jonathan T. Elliott for the technical support and helpful discussions. Certain commercial equipment, instruments, and materials are identified in this paper. Such identification does not imply recommendation or endorsement by the National Institute of Standards and Technology, nor does it imply that the materials or equipment identified are necessarily the best available for the purpose.

See Supplement 1 for supporting content.

REFERENCES

- N. N. Boustany, S. A. Boppart, and V. Backman, "Microscopic imaging and spectroscopy with scattered light," *Annu. Rev. Biomed. Eng.* **12**, 285–314 (2010).
- J. R. Mourant, J. Boyer, A. H. Hielscher, and I. J. Bigio, "Influence of the scattering phase function on light transport measurements in turbid media performed with small source-detector separations," *Opt. Lett.* **21**, 546–548 (1996).
- F. Bevilacqua and C. Depeursinge, "Monte carlo study of diffuse reflectance at source-detector separations close to one transport mean free path," *J. Opt. Soc. Am. A* **16**, 2935–2945 (1999).
- S. Kanick, U. Gamm, M. Schouten, H. Sterenborg, D. Robinson, and A. Amelink, "Measurement of the reduced scattering coefficient of turbid media using single fiber reflectance spectroscopy: fiber diameter and phase function dependence," *Biomed. Opt. Express* **2**, 1687–1702 (2011).
- E. Vitkin, V. Turzhitsky, L. Qiu, L. Guo, I. Itzkan, E. B. Hanlon, and L. T. Perelman, "Photon diffusion near the point-of-entry in anisotropically scattering turbid media," *Nat. Commun.* **2**, 587 (2011).
- K. W. Calabro and I. J. Bigio, "Influence of the phase function in generalized diffuse reflectance models: review of current formalisms and novel observations," *J. Biomed. Opt.* **19**, 075005 (2014).
- J. Schmitt and G. Kumar, "Turbulent nature of refractive-index variations in biological tissue," *Opt. Lett.* **21**, 1310–1312 (1996).
- J. M. Schmitt and G. Kumar, "Optical scattering properties of soft tissue: a discrete particle model," *Appl. Opt.* **37**, 2788–2797 (1998).
- M. Xu and R. R. Alfano, "Fractal mechanisms of light scattering in biological tissue and cells," *Opt. Lett.* **30**, 3051–3053 (2005).
- X. Wang, B. W. Pogue, S. Jiang, X. Song, K. D. Paulsen, C. Kogel, S. P. Poplack, and W. A. Wells, "Approximation of mie scattering parameters in near-infrared tomography of normal breast tissue *in vivo*," *J. Biomed. Opt.* **10**, 051704 (2005).
- A. J. Radosevich, J. Yi, J. D. Rogers, and V. Backman, "Structural length-scale sensitivities of reflectance measurements in continuous random media under the born approximation," *Opt. Lett.* **37**, 5220–5222 (2012).
- F. Bevilacqua, D. Piguet, P. Marquet, J. D. Gross, B. J. Tromberg, and C. Depeursinge, "In vivo local determination of tissue optical properties: applications to human brain," *Appl. Opt.* **38**, 4939–4950 (1999).
- C. S. Mulvey, C. A. Sherwood, and I. J. Bigio, "Wavelength-dependent backscattering measurements for quantitative real-time monitoring of apoptosis in living cells," *J. Biomed. Opt.* **14**, 064013 (2009).
- F. van Leeuwen-van Zaane, U. Gamm, P. van Driel, T. Snoeks, H. de Brujin, A. van der Ploeg-van den Heuvel, I. Mol, C. Löwik, H. Sterenborg, A. Amelink, and D. Robinson, "In vivo quantification of the scattering properties of tissue using multi-diameter single fiber reflectance spectroscopy," *Biomed. Opt. Express* **4**, 696–708 (2013).
- V. Backman, V. Gopal, M. Kalashnikov, K. Badizadegan, R. Gurjar, A. Wax, I. Georgakoudi, M. Mueller, C. W. Boone, R. R. Dasari, and M. S. Feld, "Measuring cellular structure at submicrometer scale with light scattering spectroscopy," *IEEE J. Sel. Top. Quantum Electron.* **7**, 887–893 (2001).
- A. Wax, C. Yang, V. Backman, K. Badizadegan, C. W. Boone, R. R. Dasari, and M. S. Feld, "Cellular organization and substructure measured using angle-resolved low-coherence interferometry," *Biophys. J.* **82**, 2256–2264 (2002).
- H. Subramanian, P. Pradhan, Y. Liu, I. R. Capoglu, J. D. Rogers, H. K. Roy, R. E. Brand, and V. Backman, "Partial-wave microscopic spectroscopy detects subwavelength refractive index fluctuations: an application to cancer diagnosis," *Opt. Lett.* **34**, 518–520 (2009).
- V. Turzhitsky, A. J. Radosevich, J. D. Rogers, N. N. Mutyal, and V. Backman, "Measurement of optical scattering properties with low-coherence enhanced backscattering spectroscopy," *J. Biomed. Opt.* **16**, 067007 (2011).
- A. Wax, C. Yang, V. Backman, M. Kalashnikov, R. R. Dasari, and M. S. Feld, "Determination of particle size by using the angular distribution of backscattered light as measured with low-coherence interferometry," *J. Opt. Soc. Am. A* **19**, 737–744 (2002).
- A. J. Gomes, S. Ruderman, M. DelaCruz, R. K. Wali, H. K. Roy, and V. Backman, "In vivo measurement of the shape of the tissue-refractive-index correlation function and its application to detection of colorectal field carcinogenesis," *J. Biomed. Opt.* **17**, 047005 (2012).
- V. Backman and H. K. Roy, "Light-scattering technologies for field carcinogenesis detection: a modality for endoscopic prescreening," *Gastroenterology* **140**, 35–41.e5 (2011).
- A. M. Laughney, V. Krishnaswamy, E. J. Rizzo, M. C. Schwab, R. J. Barth, B. W. Pogue, K. D. Paulsen, and W. A. Wells, "Scatter spectroscopic imaging distinguishes between breast pathologies in tissues relevant to surgical margin assessment," *Clin. Cancer Res.* **18**, 6315–6325 (2012).
- L. Qiu, D. K. Pleskow, R. Chuttani, E. Vitkin, J. Leyden, N. Ozden, S. Itani, L. Guo, A. Sacks, J. D. Goldsmith, M. D. Modell, E. B. Hanlon, I. Itzkan, and L. T. Perelman, "Multispectral scanning during endoscopy guides biopsy of dysplasia in Barrett's esophagus," *Nat. Med.* **16**, 603–606 (2010).
- M. Neil, R. Juskaitis, and T. Wilson, "Method of obtaining optical sectioning by using structured light in a conventional microscope," *Opt. Lett.* **22**, 1905–1907 (1997).
- V. Krishnaswamy, J. T. Elliott, D. M. McClatchy, R. J. Barth, W. A. Wells, B. W. Pogue, and K. D. Paulsen, "Structured light scatterometry," *J. Biomed. Opt.* **19**, 070504 (2014).
- S. C. Kanick, D. M. McClatchy, V. Krishnaswamy, J. T. Elliott, K. D. Paulsen, and B. W. Pogue, "Sub-diffusive scattering parameter maps recovered using wide-field high-frequency structured light imaging," *Biomed. Opt. Express* **5**, 3376–3390 (2014).

27. S. Chamot, E. Migacheva, O. Seydoux, P. Marquet, and C. Depeursinge, "Physical interpretation of the phase function related parameter γ studied with a fractal distribution of spherical scatterers," *Opt. Express* **18**, 23664–23675 (2010).
28. D. J. Cuccia, F. Bevilacqua, A. J. Durkin, F. R. Ayers, and B. J. Tromberg, "Quantitation and mapping of tissue optical properties using modulated imaging," *J. Biomed. Opt.* **14**, 024012 (2009).
29. S. Gioux, A. Mazhar, B. T. Lee, S. J. Lin, A. M. Tobias, D. J. Cuccia, A. Stockdale, R. Oketokoun, Y. Ashitate, E. Kelly, M. Weinmann, N. J. Durr, L. A. Moffitt, A. J. Durkin, B. J. Tromberg, and J. V. Frangioni, "First-in-human pilot study of a spatial frequency domain oxygenation imaging system," *J. Biomed. Opt.* **16**, 086015 (2011).
30. N. Bodenschatz, P. Krauter, A. Liemert, J. Wiest, and A. Kienle, "Model-based analysis on the influence of spatial frequency selection in spatial frequency domain imaging," *Appl. Opt.* **54**, 6725–6731 (2015).
31. A. J. Radosevich, A. Eshein, and V. Backman, "Subdiffusion reflectance spectroscopy to measure tissue ultrastructure and microvasculature: model and inverse algorithm," *J. Biomed. Opt.* **20**, 097002 (2015).
32. B. Gélibart, E. Tiné, J. M. Tualle, and S. Avrillier, "Phase function simulation in tissue phantoms: a fractal approach," *Pure Appl. Opt.* **5**, 377–388 (1996).
33. J. D. Rogers, I. R. Çapoğlu, and V. Backman, "Nonscalar elastic light scattering from continuous random media in the born approximation," *Opt. Lett.* **34**, 1891–1893 (2009).
34. K. E. Kadler, D. F. Holmes, J. A. Trotter, and J. A. Chapman, "Collagen fibril formation," *Biochem. J.* **316**, 1–11 (1996).
35. M. D. Keller, E. Vargas, N. de Matos Granja, R. H. Wilson, M.-A. Mycek, M. C. Kelley, and A. Mahadevan-Jansen, "Development of a spatially offset raman spectroscopy probe for breast tumor surgical margin evaluation," *J. Biomed. Opt.* **16**, 077006 (2011).
36. F. T. Nguyen, A. M. Zysk, E. J. Chaney, J. G. Kotynek, U. J. Oliphant, F. J. Bellafiore, K. M. Rowland, P. A. Johnson, and S. A. Boppart, "Intraoperative evaluation of breast tumor margins with optical coherence tomography," *Cancer Res.* **69**, 8790–8796 (2009).
37. S. Gioux, A. Mazhar, D. J. Cuccia, A. J. Durkin, B. J. Tromberg, and J. V. Frangioni, "Three-dimensional surface profile intensity correction for spatially modulated imaging," *J. Biomed. Opt.* **14**, 034045 (2009).



Wide-field quantitative imaging of tissue microstructure using sub-diffuse spatial frequency domain imaging: supplementary material

DAVID M. McCLOTHY III¹, ELIZABETH J. RIZZO², WENDY A. WELLS^{2,3}, PHILIP P. CHENEY⁴, JEESEONG C. HWANG⁴, KEITH D. PAULSEN^{1,3}, BRIAN W. POGUE^{1,3}, AND STEPHEN C. KANICK^{1,3*}

¹Thayer School of Engineering, Dartmouth College, 14 Engineering Drive, Hanover, NH 03755

²Department of Pathology, Dartmouth Hitchcock Medical Center, 1 Medical Center Drive, Lebanon, NH 03756

³Norris Cotton Cancer Center, Dartmouth Hitchcock Medical Center, 1 Medical Center Drive, Lebanon, NH 03756

⁴Quantum Electromagnetics Division, National Institute of Standards and Technology, 325 Broadway Street, Boulder, CO 80305

* Corresponding author: stephen.c.kanick@dartmouth.edu

Published 9 June 2016

This document provides supporting content for the article "Wide-field quantitative imaging of tissue microstructure using sub-diffuse spatial frequency domain imaging," <http://dx.doi.org/10.1364/optica.3.000613>. © 2016 Optical Society of America

<http://dx.doi.org/10.1364/optica.3.000613.s001>

1. EXPANDED METHODS AND MATERIALS

A. Sub-diffuse Spatial Frequency Domain Imaging Setup and Parameter Fitting

Imaging was performed using a commercial spatial frequency domain imaging system (Modulating Imaging, Inc., Irvine, CA). This unit acquired spatial frequencies over the range of $f_x = [0 - 0.2, 0.5 - 0.9] \text{ mm}^{-1}$ in steps of 0.05 mm^{-1} with source LEDs centered about [658, 730, 850] nm. In order to maximize signal from low-ordered scattered photons, cross-polarizing filters were removed. However, to mitigate the effect of specularly reflected photons, projections were obliquely illuminated and a signal acquired from a measurement of water in a deep (≈ 50 cm) well with dark non-reflecting walls was subtracted from both the sample and reference intensity maps to approximate the specular reflection [1]. Maps of calibrated reflectance were calculated by ratioing demodulated intensity maps of the sample with a reference measurement of Intralipid 1 % and multiplying by a model reflectance value calculated from Eqs. S1 & S2 using well-documented optical properties for Intralipid [2]. The reflectance model is broken into piecewise contributions from a semi-empirical sub-diffusive expression, Eq. S1, described in Kanick *et al.* [3] and a diffusion theory model, Eq. S2, described in Cuccia *et al.* [4]. The combination is complementary because the sub-diffusive model, $R_{\text{SubDiff}}(f_x, \mu'_s, \gamma)$, is sensitive to scatter directionality but does not account for optical

absorption whereas the diffusion theory model, $R_{\text{Diff}}(f_x, \mu_a, \mu'_s)$, assumes diffusive photon propagation but characterizes both diffuse scatter and absorption. Thus, only spatial frequencies above 0.5 mm^{-1} [5], which have negligible signal contribution from absorption for typical optical properties of tissue in the near-infrared (NIR) window [6], were analyzed with the sub-diffusive model, and spatial frequencies below 0.2 mm^{-1} , which meet assumptions of diffusion for typical tissue optical properties in the NIR window, were analyzed with the diffusion theory model. The calibrated images of demodulated reflectance over the acquired spatial frequencies and wavelengths $R_d(f_x, \lambda)$ were inverted into maps of μ'_s , γ , and μ_a with a non-linear least squares minimization using the expressions:

$$R_{\text{SubDiff}}(f_x, \mu'_s, \gamma) = \eta \left(1 + (\zeta_4 \gamma^{-2}) (\mu'_s f_x^{-1})^{(-\zeta_3 \gamma)} \right) \left[\frac{(\mu'_s f_x^{-1})^{(-\zeta_2 \gamma)}}{\zeta_1 \gamma^2 + (\mu'_s f_x^{-1})^{(-\zeta_2 \gamma)}} \right] \quad (\text{S1})$$

$$R_{\text{Diff}}(f_x, \mu_a, \mu'_s) = \frac{3\alpha' \frac{\mu'_s}{\mu_{\text{tr}}}}{\left(\frac{\sqrt{3\mu_a \mu_{\text{tr}} + (2\pi f_x)^2}}{\mu_{\text{tr}}} + 1 \right) \left(\frac{\sqrt{3\mu_a \mu_{\text{tr}} + (2\pi f_x)^2}}{\mu_{\text{tr}}} + 3\alpha' \right)} \quad (\text{S2})$$

$$R_d(f_x, \mu_a, \mu'_s, \gamma) = \begin{cases} R_{\text{Diff}} & \text{if } f_x \leq 0.2 \text{ mm}^{-1} \\ R_{\text{SubDiff}} & \text{if } f_x \geq 0.5 \text{ mm}^{-1} \end{cases}$$

In the diffusive model, the parameter α' is a proportionality constant, accounting for surface boundary effects [7]. In the sub-diffusive model, the fitted model parameter set $[\eta, \zeta]$ reported in [3] provided accurate descriptions of reflectance intensities over a wide range of scattering properties, including: $\mu'_s = [0.3 - 10] \text{ mm}^{-1}$ and $\gamma = [1.3 - 1.9]$. The present study utilized Monte Carlo (MC) simulations to characterize an expanded range of γ values spanning a range that have been previously reported in tissue [3, 8–10]; this full range of γ is not able to be considered using the Modified Henyey Greenstein phase function [11] that was used to develop Eqn. S1 in [3]. Here, a customized MC model was used to consider scattering phase functions calculated using Mie Theory, with input parameters used to specify a discrete set of scatterers in suspension. These simulations constructed phase functions with 7 discrete particle sizes in the range of $[0.1 - 2.0 \mu\text{m}]$ with a fractal dimension of the scatterers in the range of $[2.6 - 4.9]$ in steps of 0.1, with an index of refraction mismatch of $(1.37/1.33)$ between the scatterers and surrounding fluid; these input combinations yielded a set of 24 phase functions with a wide range of values for both $\gamma_1 = [0.55 - 0.98]$ and $\gamma = [1.2 - 2.4]$. The MC simulations returned reflectance intensity vs. distance from a point source at an air-medium interface and a 1-dimensional Hankel transformation was used for conversion to a spatial frequency basis [4]. Values for μ'_s and f_x were selected to yield 40 values of dimensionless scattering (i.e. f_x/μ'_s) over the range $[0 - 1] [-]$ for each sampled phase function. Figure S1 shows reflectance vs. dimensionless scattering for both MC simulations and predictions of Eqn. S1, in plots S1a and S1b respectively. The predictions of the semi-empirical model accurately match the simulated data, with the squared Pearson product moment correlation coefficient of $r^2 = 0.987$ and a mean absolute error between model and simulation data of $< 9\%$ over $f_x/\mu'_s = [0 - 1] [-]$ for all simulated phase functions. Inspection of the data in Figure S1 highlight the non-uniqueness of reflectance intensity in terms of μ'_s and γ ; with reflectance monotonically decreasing with increasing f_x/μ'_s and exhibiting a γ -specific proportionality for high spatial frequencies.

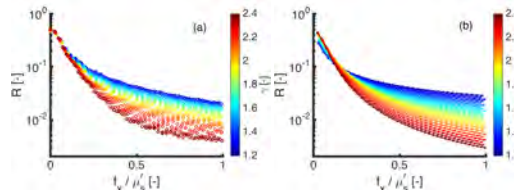


Fig. S1. Reflectance vs. dimensionless scattering from (a) Monte Carlo simulations and (b) semi-empirical model predictions.

Imaged $R_d(f_x, \lambda)$ data were fit to Eqs. S1 & S2 on a pixel-by-pixel basis, returning images of μ'_s , γ , and μ_a at each measured wavelength where μ'_s was assumed to follow a power law, $\mu'_s(\lambda) = A(\frac{\lambda}{800\text{nm}})^{-B}$, in which A is the scatter amplitude and corresponds directly to $\mu'_s(800 \text{ nm})$, B is the scatter power, and

$\gamma(\lambda)$ was fitted as a free parameter at each wavelength. An analysis algorithm was coded in MATLAB (R2015a, MathWorks Inc. Natick, MA) that automatically identified and excluded pixels that were non-scattering or contained specular reflection, and the code was deployed on an 8-core parallel processing CPU. The average time to recover a parameter map for a $2.5 \text{ cm} \times 2.5 \text{ cm}$ tissue sample that contained roughly 3000 pixels was ≈ 1 hour. Fitting time could be rapidly decreased by employing a look-up-table (LUT) and/or further parallelization of the fit procedure. All demodulated images were processed with a median filter having a kernel size of $2 \text{ mm} \times 2 \text{ mm}$ ($[10 \times 10]$ pixels) to reduce noise originating from a poor signal-to-noise ratio at higher spatial frequencies. Moreover, it is important to note that 97.5 % of pixel-based estimates of γ from tissue samples were within the validated parameter space for the semi-empirical model (i.e. $1.3 < \gamma < 2.4$), with the remaining 2.5% of pixels designated as outliers.

It is important to note that the model-based interpretation of high spatial frequency data in this study assumes statistical homogeneity in scatterer orientation. Previous work by Konecky *et al.* [12] showed that rotation of the illumination pattern could provide sensitivity to the micro-alignment and organization of scatterers within an imaged sample. Future work could consider rotation of the incident illumination to provide a coupled assessment of density, size, and orientation.

B. Imaging of Sub-Diffuse Scattering Properties in the Presence of a Strong Absorber

An aqueous phantom set was constructed to confirm the accuracy of scattering parameters in the presence of absorption based attenuation. This phantom set contained nine phantoms with coupled variation of $D_f = [3.6, 4.1, 4.6]$ and the absorption coefficient, which was varied by adding incremental amounts of Evans Blue dye to achieve $\mu_a = [0.02 - 0.18] \text{ mm}^{-1}$ such that the ratio $\frac{\mu'_s}{\mu_a}$ ranged from 5.6 to 50 at 658 nm. Data in Fig. S2 show that both μ'_s and γ are accurately recovered in the presence of a strong optical absorber.

C. Heterogeneous Optical Property Phantoms: Step Change in Scatter Contrast

While the aqueous polystyrene bead phantoms allow for the direct quantification of μ'_s and γ with comparison to theoretical values from Mie theory, these phantoms fail to demonstrate the ability to spatially resolve scattering optical properties in a heterogeneous phantom. As such, agarose phantoms with a step change in either scatter size or density were constructed and imaged (I) to demonstrate proof of principle, and (II) to estimate resolution and sensitivity of the optical scattering parameters. Phantoms were gelled with 10 g/L of agarose in phosphate buffered solution, which was brought to a boil, cooled to approximately 40°C , mixed with the scattering agent, and finally poured into a rectangular mold submerged in ice for gelling to occur. For the step change in scatter size, 2 g/L of titanium dioxide powder and 1.5 % Intralipid were used as the scattering agents, while the step change in scatter density was 1 % and 5 % Intralipid concentrations. A summary of the heterogeneous phantom data is shown in Figure S3. As shown in Figure S3(a,b), there is little visible contrast between the titanium dioxide and Intralipid phantoms and only slight contrast between the 1 % and 5 % Intralipid concentrations. However, the γ and μ'_s optical property maps in Figure S3(c,d) very clearly recover scatter size and density based contrast. In Figure S3(e,f), the edge response

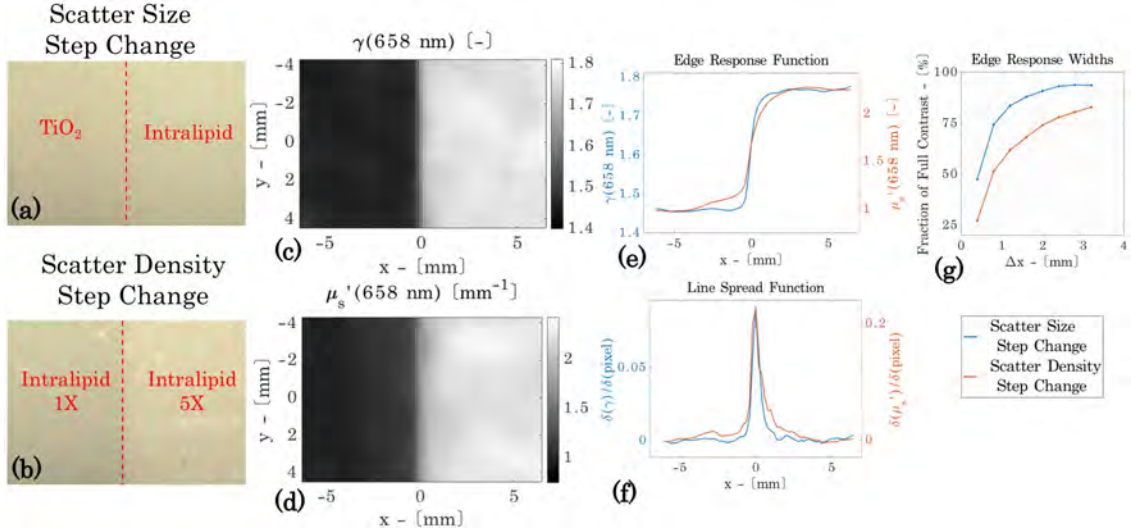


Fig. S3. Annotated photographs of scatter size (a) and density (b) step change agarose phantoms with titanium dioxide and Intralipid in (a) and 1% and 5% Intralipid in (b). Corresponding gray-scale optical property maps are shown, with γ for scatter size change in (c) and μ'_s for scatter density change in (d). Edge response functions are shown in (e) for both γ and μ'_s averaged in the y direction. Corresponding line spread functions are shown in (f), which is the derivative of (e) approximated by a forward finite difference. In (g), the percentage of full contrast reached as a function of edge width across the step is plotted for both scatter size and density contrast. Note that a pixel width is 200 μm , and so in (g) each point is plotted in steps of 400 μm , iteratively adding a pixel to each side of the boundary.

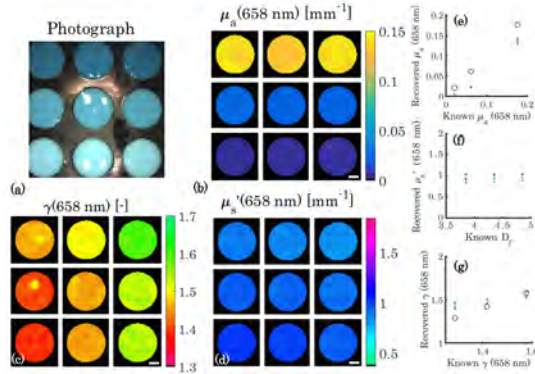


Fig. S2. (a) Photograph of the γ and μ_a variation phantom set, showing visible blue contrast between the various phantoms in each row with a change in D_f in each column. (b) Recovered μ_a , (c) γ , and (d) μ'_s maps at 658 nm. (e-g) Reports recovered experimental mean values versus D_f for each well with error bars representing one standard deviation above and below the mean and black circles representing theoretical values for each optical property.

function and line spread function for γ and μ'_s shows the spatial resolution and sensitivity of a step change of known contrast. The percentage of full contrast as a function of distance across the boundary is shown in Figure S3(g). The distance over which

75% contrast is reached is approximately 800 μm (4 pixels) for γ and 2000 μm (10 pixels) for μ'_s . This difference in resolution originates from the sub-diffusive spatial frequency dependence of γ , with spatial resolution < 1 mean free path, while μ'_s has both diffusive and sub-diffusive spatial frequency dependence resulting in a resolution $\approx 1 - 2$ mean free paths. Sensitivity to changes in optical properties is given by the line spread function in Figure S3(f), which is the derivative of the edge response function. The maximum change in recovered optical property between adjacent pixels is 0.09 for γ and 0.22 mm^{-1} for μ'_s .

D. Dark Field Imaging of Ex-Vivo Tissue Samples

Each of the tissue specimens was imaged with the spatial frequency imaging technique as shown in Figure 2, while a select set of specimens were also imaged with a dark-field reflectance microscope. The details of the dark-field microscope setup is described elsewhere [13]. The illumination and bandwidth for the dark-field imaging were selected by a home-built LabView program to take a series of single shot images, one wavelength at a time, with wavelength scanned from 450 nm to 650 nm with a 10 nm bandwidth. Only a limited set of images were acquired for a selected sample area, as it would take roughly 20 min to scan the entire specimen by patch-wise imaging to cover the entire sample and put the patches together. The origin of the dark-field signal is inherently related to localized backscattering; hence, it provided a unique standard with which to compare the structured light scatter signal. As with structured light imaging, dark field microscopy imaging was performed through a glass slide to minimize surface curvature effects.

E. Selection of Colormaps for Optical Parameter Visualization

The selection of color maps used to display maps of optical properties were chosen as follows. For γ , μ_s' , and scatter slope, fully saturated HSV color maps were used, with a saturation and brightness value of one. Each of these color maps goes through half of the hue spectrum, with the γ color map spanning red, yellow, and green and the μ_s' color map spanning cyan, blue, and magenta. The range of the color bar axes in each figure was different, as the range of scattering values in the phantom sets versus the tissue is different. However, the range of the color bar axes within each figure, most notably in Figure 5, is the same in order to provide direct visual comparison between the tissue types. For the μ_a map in Figure S1(b), the default MATLAB, 2015a "parula" map was used.

REFERENCES

- N. Bodenschatz, A. Brandes, A. Liemert, and A. Kienle, "Sources of errors in spatial frequency domain imaging of scattering media," *Journal of biomedical optics* **19**, 071405–071405 (2014).
- R. Michels, F. Foschum, and A. Kienle, "Optical properties of fat emulsions," *Optics Express* **16**, 5907–5925 (2008).
- S. C. Kanick, D. M. McClatchy, V. Krishnaswamy, J. T. Elliott, K. D. Paulsen, and B. W. Pogue, "Sub-diffusive scattering parameter maps recovered using wide-field high-frequency structured light imaging," *Biomedical optics express* **5**, 3376–3390 (2014).
- D. J. Cuccia, F. Bevilacqua, A. J. Durkin, F. R. Ayers, and B. J. Tromberg, "Quantitation and mapping of tissue optical properties using modulated imaging," *Journal of biomedical optics* **14**, 024012–024012 (2009).
- V. Krishnaswamy, J. T. Elliott, D. M. McClatchy, R. J. Barth, W. A. Wells, B. W. Pogue, and K. D. Paulsen, "Structured light scatterometry," *Journal of biomedical optics* **19**, 070504–070504 (2014).
- S. L. Jacques, "Optical properties of biological tissues: a review," *Physics in medicine and biology* **58**, R37 (2013).
- R. C. Haskell, L. O. Svaasand, T.-T. Tsay, T.-C. Feng, B. J. Tromberg, and M. S. McAdams, "Boundary conditions for the diffusion equation in radiative transfer," *JOSA A* **11**, 2727–2741 (1994).
- F. Bevilacqua, D. Piguet, P. Marquet, J. D. Gross, B. J. Tromberg, and C. Depeursinge, "In vivo local determination of tissue optical properties: applications to human brain," *Applied optics* **38**, 4939–4950 (1999).
- F. van Leeuwen-van Zaane, U. Gamm, P. van Driel, T. Snoeks, H. de Bruijn, A. van der Ploeg-van den Heuvel, I. Mol, C. Löwik, H. Sterenborg, A. Amelink, and D. Robinson, "In vivo quantification of the scattering properties of tissue using multi-diameter single fiber reflectance spectroscopy," *Biomedical optics express* **4**, 696–708 (2013).
- A. J. Radosevich, A. Eshein, and V. Backman, "Subdiffusion reflectance spectroscopy to measure tissue ultrastructure and microvasculature: model and inverse algorithm," *Journal of biomedical optics* **20**, 097002–097002 (2015).
- F. Bevilacqua and C. Depeursinge, "Monte carlo study of diffuse reflectance at source-detector separations close to one transport mean free path," *JOSA A* **16**, 2935–2945 (1999).
- S. D. Konecky, T. Rice, A. J. Durkin, and B. J. Tromberg, "Imaging scattering orientation with spatial frequency domain imaging," *Journal of biomedical optics* **16**, 126001–1260018 (2011).
- A. Ray, R. Kopelman, B. Chon, K. Briggman, and J. Hwang, "Scattering based hyperspectral imaging of plasmonic nanoplate clusters towards biomedical applications," *Journal of biophotonics* (2015).

Chapter 5: Monochromatic Quantitative Imaging of Intratumoral Morphological Heterogeneity in a Murine Model

5.1. Background and Goals

In Chapter 4, it was shown that sub-diffusive scatter parameters could distinguish bulk differences in adipose, fibroglandular, fibroadenoma, and invasive morphologies across n=22 freshly resected human breast tissue specimens, through clustering of the reduced scattering coefficient, phase function parameter, and scatter slope. After this result, two hypotheses were formed: (1) could similar clustering between tissue morphologies be achieved with a monochromatic system, thereby neglecting the scatter slope and requiring a less complicated imaging device, and (2) could the spatially resolved scattering parameters distinguish morphological differences within a tumor rather than just between bulk specimens. The goal of following manuscript were two test these two hypotheses. A method was developed to analysis intratumoral morphological heterogeneity by comparing co-registered and monochromatic scattering parameters to quantitative digitized histology and proof-of-principle was demonstrated on n=2 murine mammary tumors. This methodology is somewhat akin to flow cytometry, where different degrees of forward and side scatter can cluster morphology differences within a population of cell subtypes.

5.2. Published Work

The following published manuscripts is reprinted from:

McClatchy DM, 3rd, Hoopes PJ, Pogue BW, Kanick SC. Monochromatic subdiffusive spatial frequency domain imaging provides in-situ sensitivity to intratumoral

morphological heterogeneity in a murine model. Journal of biophotonics.

2017;10(2):211-6. <http://dx.doi.org/10.1002/jbio.201600181>

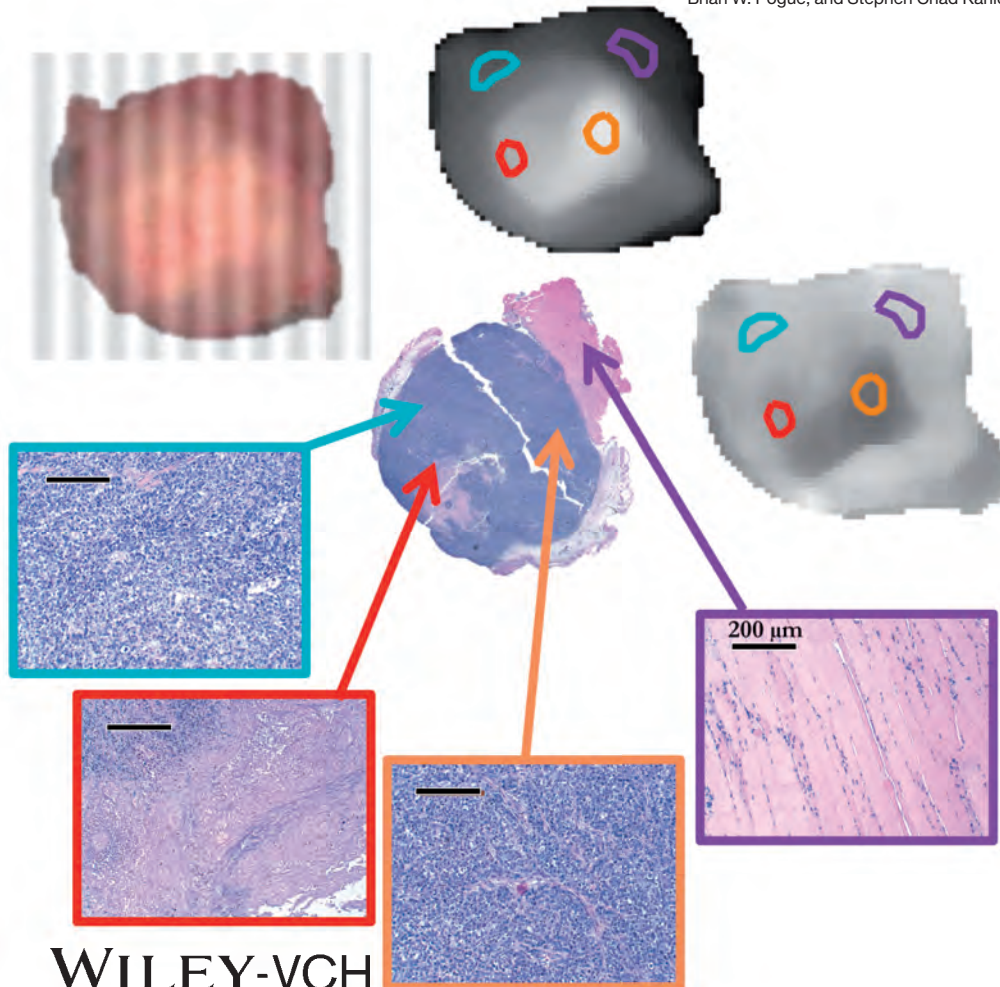
This article has the following copyright: Copyright Wiley-VCH Verlag GmbH & Co. KGaA, and is reproduced with their permission. Additionally, per the Copyright Transfer Agreement “*Wiley-VCH hereby licenses back to the Contributor the following rights with respect to the final published version of the Contribution: (a)... (b) Re-use in other publications. The right to re-use the final Contribution or parts thereof for any publication authored or edited by the Contributor (excluding journal articles) where such re-used material constitutes less than half of the total material in such publication. In such case, any modifications should be accurately noted.*” This article constitutes less than half from thesis has not been modified.

D. M. McClatchy was responsible for all tissue data acquisition, analysis, and quantification as well as preparing the manuscript. P. J. Hoopes was responsible for diagnosing and characterizing regions within each digitized histology slide. S. C. Kanick and B. W. Pogue were responsible for the conception of the study, provided advising, and participated in editing the manuscript.

BIPHOTONICS

www.biophotonics-journal.org

Subdiffusive spatial frequency domain
imaging of tumor heterogeneity
David M. McClatchy III, P. Jack Hoopes,
Brian W. Pogue, and Stephen Chad Kanick



WILEY-VCH

LETTER

Monochromatic subdiffusive spatial frequency domain imaging provides *in-situ* sensitivity to intratumoral morphological heterogeneity in a murine model

David M. McClatchy III*,¹, P. Jack Hoopes^{1,2}, Brian W. Pogue^{1,2}, and Stephen Chad Kanick^{1,2}

¹ Dartmouth College, Thayer School of Engineering, Hanover, NH, USA

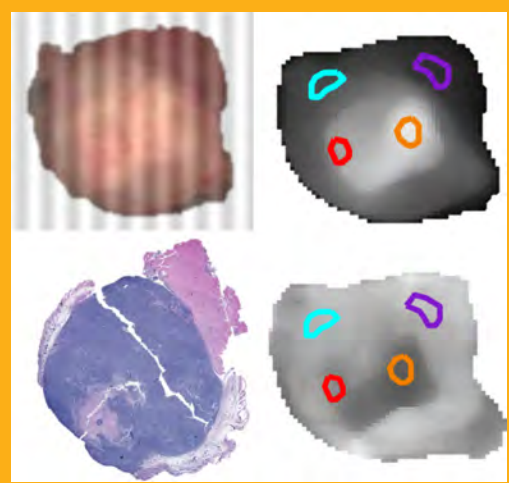
² Norris Corron Cancer Center, Dartmouth Hitchcock Medical Center, Lebanon, NH, USA

Received 17 June 2016, revised 4 October 2016, accepted 5 October 2016

Published online 3 November 2016

Key words: scatter imaging, tissue characterization, SFDI

For the first time, spatially resolved quantitative metrics of light scattering recovered with sub-diffusive spatial frequency domain imaging (sd-SFDI) are shown to be sensitive to changes in intratumoral morphology and viability by direct comparison to histopathological analysis. Two freshly excised subcutaneous murine tumor cross-sections were measured with sd-SFDI, and recovered optical scatter parameter maps were co-registered to whole mount histology. Unique clustering of the optical scatter parameters μ_s vs. γ (i.e. diffuse scattering vs. relative backscattering) evaluated at a single wavelength showed complete separation between regions of viable tumor, aggressive tumor with stromal growth, varying levels of necrotic tumor, and also peritumor muscle. The results suggest that with further technical development, sd-SFDI may represent a non-destructive screening tool for analysis of excised tissue or a non-invasive approach to investigate suspicious lesions without the need for exogenous labels or spectrally resolved imaging.



1. Introduction

Diffuse optical measurements of tissue can provide sensitivity to physiology, metabolism, and structure over wide fields of view. Such information is obtained by spectroscopic and/or spatial analysis of radiant photon propagation and attenuation. Model-

based interpretation of diffuse remission uses the simplifying assumption that multiply scattered light can be described using isotropic reduced scattering. However, diffuse measurements offer limited sensitivity to microscopic heterogeneity in tissue composition due to volumetric averaging over tortuous photon path lengths. Conversely, sub-diffusive meas-

* Corresponding author: e-mail: David.M.McClatchy.III.TH@dartmouth.edu

urements that collect remission close to the source of entry provides sensitivity to anisotropic aspects of scatter direction. Directional preferences in scatter are dictated by the microscopic distribution of mass density in the sampled tissue, and in turn, are sensitive to the density, organization, and fractal dimension of structural features within biological tissue [1–3]. Techniques utilizing confocal [4], fiber based [5], or interferometric [6] methods are capable of localizing reflectance remission to the superficial layers of tissue and preserving sensitivity to anisotropic remission. Such measurements are capable of sensing variations in cellular internal machinery (e.g. nuclear morphology) and/or extracellular matrix (e.g. stromal density) that are considered hallmarks of the onset of cancer [7]. However, adapting these approaches to image variations in tissue morphology for clinical applications is a challenge, as raster-scanning these microscopic point-sampling approaches over large fields of view is cumbersome and time consuming. Recently, sub-diffusive spatial frequency domain imaging (sd-SFDI) was shown to provide sensitivity to superficial, weakly scattered photons over a wide-field geometry, and provide images of tissue microarchitecture that may be relevant for surgical guidance [8].

Previous investigations of sd-SFDI have used model-based analysis of multiple spatial frequencies sampled over multiple wavelengths to recover quantitative scattering parameter maps [8–10]. This parameter set includes the reduced scattering coefficient, μ'_s , and a phase function parameter, $\gamma = \frac{1-g_2}{1-g_1}$, which characterizes the backscatter probability of the scattering phase function, and is expressed as a weighted ratio of the first two Legendre moments of the distribution of scattering angles, g_1 and g_2 [11]. The reduced scattering coefficient, μ'_s , quantifies the frequency of isotropic scattering, which is related to the density of scattering features, weighted by their effective scattering cross sections and the relative directionality of scattering. The γ parameter represents an implicit metric of the size-scale distribution of scattering features that are relatively large or small compared to the wavelength of light. This parameter can indicate contributions from larger Mie-type scatterers, which tend to scatter predominantly in the forward-direction, or smaller Rayleigh-type scatterers, which scatter more isotropically [12]. Furthermore, it has been numerically and experimentally shown that γ is proportional to the fractal dimension of a distribution of spherical scatterers [8, 12]. In biological tissues, these sub-diffusive scattering parameters have been identified as a basis for differentiating morphological changes between malignant and normal human brain tissues [13] and also human breast tissues [8]. Previously, our group employed sd-SFDI to show significant changes in scattering parameters be-

tween aggregate cancerous and normal tissues [8]. The present proof-of-principle study considers variations in sub-diffusive parameters observed within malignant tissues. Specifically, the study considers how spatial maps of μ'_s and γ extracted at a single wavelength of light show spatial clustering that is associated with variations in aspects of tumor morphology that are extracted from quantitative histological analysis. This pilot study uses a few samples ($n=2$) to demonstrate the sensitivity of these sub-diffusive parameter maps to changes in tissue ultrastructure within a given tumor specimen.

2. Experimental methods

While a complete description and validation of sd-SFDI can be found in previous work [8], a concise summary is described below. A modified commercial spatial frequency domain imaging system from Modulated Imaging, Inc. (Irvine, CA) [14] with a maximum field of view of roughly $10.5\text{ cm} \times 14\text{ cm}$, sampling resolution of $200\text{ }\mu\text{m}$, and projection resolution of $150\text{ }\mu\text{m}$ was used for imaging. The basic set-up of the camera and projector is shown in Figure 1, where imaging is done in an inverted geometry through a glass slide in order to mitigate surface curvature artifacts of the sample, arising when the sam-

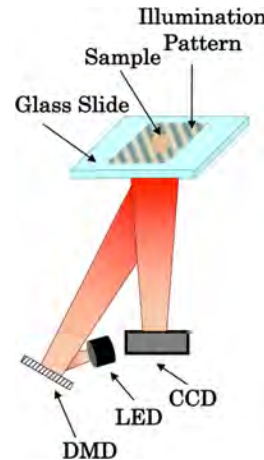


Figure 1 Schematic of major components of sd-SFDI device. A red (658 nm) light emitting diode (LED) illumination source reflects off a digital micromirror device (DMD) to spatially modulate the light intensity. The sinusoidal illumination pattern is focused onto the sample, which is lying flat on a glass slide. A charged coupled device (CCD) captures the perturbed intensity patterns, which are used to calculate the optical property maps.

ple is non-normal to the optical axis. Although these artifacts pose a challenge for *in-vivo* translation, recent work aims to mitigate these effects [15]. The digital micromirror based projection device is coupled to multiple LEDs as light sources. To emphasize translation, this study reports a monochromatic analysis at the 658 nm source, which corresponds to a red channel in a commercial surgical microscope, which are commonly employed for surgical resection of tumors. Cross-polarizers were removed to provide sensitivity to weakly scattered photons.

The structured illumination patterns were sinusoids of the form $I_i(x, y, f_x) = 0.5[\sin(2\pi f_x x + \Phi_i) + 1]$ with $\Phi_i = [0, \frac{2\pi}{3}, \frac{4\pi}{3}]$ where $I_i(x, y, f_x)$ represent the image stack of sinusoids with spatial frequency, f_x sampled over 18 linearly spaced values between 0 and 0.85 mm^{-1} , for three phase offsets, $i = [1, 2, 3]$, used for demodulation. While spatial frequencies where $\mu'_s/f_x \leq 3$ have strong sub-diffusive sensitivity, it may be possible to use fewer non-linearly spaced spatial frequencies; however, a full analysis of spatial frequency sensitivity to each optical property is beyond the scope of this letter and is also the subject of a recent study by Bodenschatz et al. [16]. The demodulated reflectance, $I_d(x, y, f_x)$ was calculated with the following formula:

$$I_d(x, y, f_x) = \sqrt{\frac{2}{3}} \sqrt{(I_1 - I_2)^2 + (I_1 - I_3)^2 + (I_2 - I_3)^2}.$$

The Modulated Imaging system produced a 16-bit image per acquisition, and MATLAB (Mathworks, Inc.) was used to read in and demodulate the raw images. Demodulated images of measured tissue samples were referenced through a normalization by a liquid phantom containing 1% Intralipid (IL). Because the illumination source was not collimated and the cross polarizers were removed, measurements of a non-turbid phantom containing water were used to estimate specular reflection within the imaged field of view. These demodulated images of water were subtracted from both the sample and IL as a dark reference. These normalized and referenced raw sample images were then calibrated by a model predicted reflectance value for the 1% IL normalization phantom. The optical properties of IL were calculated according to Michels et al. [17] with an estimated batch to batch variation in reduced scattering of less than 2% as shown by Ninni et al. [18]. For spatial frequencies below 0.2 mm^{-1} a diffusion theory model is used [14], and for spatial frequencies above 0.5 mm^{-1} a sub-diffusive model is used [9].

$$R_d(x, y, f_x) = R_{\text{Model}}(f_x) \frac{I_d(x, y, f_x) - I_{d_{\text{water}}}(x, y, f_x)}{I_{d_{\text{IL}}}(x, y, f_x) - I_{d_{\text{water}}}(x, y, f_x)}$$

$$R_{\text{Model}}(f_x) = \begin{cases} R_{\text{Diff}} & \text{if } f_x \leq 0.2 \text{ mm}^{-1} \\ R_{\text{SubDiff}} & \text{if } f_x \geq 0.5 \text{ mm}^{-1} \end{cases}$$

Calibrated reflectance intensity images, $R_d(x, y, f_x)$ were inverted to maps of μ_a , μ'_s , and γ

using a non-linear least squares minimization. The difference between the log of model predicted reflectance and log of experimental reflectance was minimized on a pixel-by-pixel basis, with μ_a , μ'_s , and γ at the imaged wavelength being the fit variables. The MATLAB *lsqnonlin* routine was utilized with the *levenberg-marquardt* algorithm and the fit variables bound to a positive real set. This model and inversion algorithm was extensively validated with both simulated and experimental data [8]. Optical properties of simulated Monte Carlo data with $\mu'_s = [0.3 - 10] \text{ mm}^{-1}$ and $\gamma = [1.3 - 1.9]$ for a Modified Henyey-Greenstein phase function and also with $\gamma = [1.2 - 2.4]$ for a Mie Theory phase function were accurately recovered with the inversion algorithm [8]. For experimental validation, fractal distributions of polystyrene spheres with $\mu_a = [0.02 - 0.18] \text{ mm}^{-1}$, $\mu'_s = [1.2 - 2.4] \text{ mm}^{-1}$, and $\gamma = [1.28 - 1.68]$ at 658 nm were imaged and accurately inverted. Three experimental validations were performed: constant μ'_s with γ variation, both μ'_s and γ variation, and both μ_a and γ variation. Recovered optical property maps were median filtered with a 10×10 pixel ($2 \times 2 \text{ mm}$) kernel to remove noise. Analysis of spatially heterogeneous step-change phantoms characterized the optical resolution, defined as the length over which 75% of the maximum contrast of the step change has been reached, to be $2000 \mu\text{m}$ (10 pixels) for μ'_s and $800 \mu\text{m}$ (4 pixels) for γ [8].

The sd-SFDI setup was used to image cross-sections of a murine subcutaneous breast tumor model. All animal procedures were conducted under a protocol approved by the Dartmouth College Institutional Animal Care and Use Committee (IACUC) in accordance with all Personal Health Service (PHS), federal, Association for Assessment and Accreditation of Laboratory Animal Care (AAALAC), and institutional guidelines. The tumor line used for this study was a mouse mammary adenocarcinoma/MTG-B. Tumor cells were implanted intradermally (1×10^6 cells) in the flank region and were allowed to grow to a volume of approximately 650 mm^3 . When tumors reached this volume, the mice were humanely sacrificed, and the tumors were excised and bisected into two equal hemispheres. The tumor hemispheres were then placed cut surface down on a glass slide and imaged as shown in Figure 1(a). This *ex-vivo* imaging procedure was completed within 5 minutes of excision. The tissue sections were then fixed in 4% neutral buffered formaldehyde, embedded in paraffin, and cut to a $4 \mu\text{m}$ thick histologic section. The resulting slides were stained with hematoxylin and eosin (H&E). The sections represented a well approximated anatomical match to the sd-SFDI optical scatter parameter maps, limited only by distortions brought on by histological processing of the tissue. A specialty trained veterinary

pathologist (PJH) provided detailed morphological descriptions of various regions within in tissue section. Areas of high and low grade tumor were holistically determined based on morphological features such as cell differentiation, nuclear to cytoplasmic ratio, and production of extra-cellular collagen. These sections were co-registered to the scatter parameter maps for cluster based analysis.

3. Results

Figure 2 presents optical imaging data for two tumor cross-sections and correlation between the histopathological and scattering parameters. Color photographs in Figure 2(a1), (b1) and full-field H & E sections in Figure 2(a4), (b4) present clearly discernible differences in morphology both between and within the two tumors. Regional inspection of the H & E reveals a link between color-coded microscopic features in Figure 2(a5–a7), (b5–b8) and the recovered optical property maps in Figure 2(a2–a3), (b2–b3). Clusters of pixels from each region show separation on the μ'_s vs. γ plot in Figure 2(a9), (b9).

Tumor A shows a highly necrotic core region surrounded by solid low grade tumor in the white light

and full field H & E images, Figure 2(a1), (a4) respectively. Low grade tumor cells, located in regions near the tumor boundary in Figure 2(a6) (cyan), are intermixed with diffusely distributed necrotic tissue in Figure 2(a5) (magenta). However, in Figure 2(a7) (red) there is primarily necrotic tissue that has retained semi-normal tumor morphology. The necrotic tumor region in Figure 2(a8) (blue), which appears as a void on the H & E, exhibited lower γ values, associated with primarily Rayleigh scattering. A decrease in scatter density (μ'_s) is shown between the still-solid region in Figure 2(a7) (red) and the liquid/necrotic region in Figure 2(a8) (blue).

Tumor B shows high-grade morphology in the center region with neighboring areas of lower grade tumor, necrosis, and muscle. This appears as white in the center with an increase in transparency near the less dense tumor and muscle, while the area of necrosis shows a slight reddening. Figure 2(b5) (purple) shows peritumor muscle characterized by large aligned myofibrils; these properties relate to a low μ'_s and high γ that are representative of large Mie-type scatterers. Figure 2(b6) (yellow) shows high-grade viable malignant cells near the tumor border with aggressive stromal growth. The region identified in Figure 2(b7) (cyan) is also on the tumor border, but appears to be of a lower grade with less voluminous

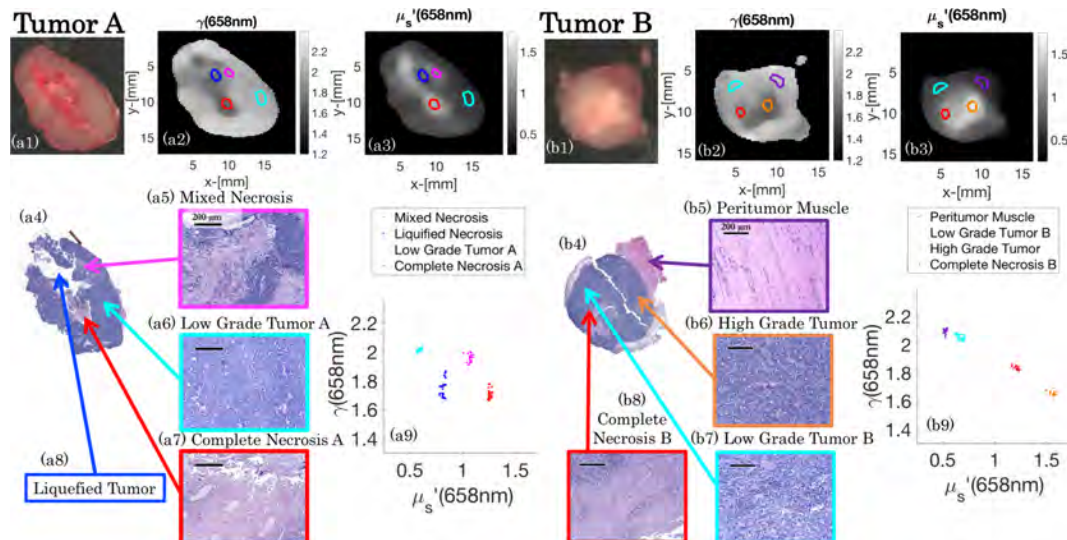


Figure 2 In (a1) and (b1), photographs of the bisected cut surfaces of two mouse mammary tumors are shown. The γ maps in (a2) and (b2) represent the scatter size scale distribution, while the μ'_s maps in (a3) and (b3) represent isotropic scatter density in the tumor sections. In (a4) and (b4), low magnification composite histological sections of the tumors are shown. The higher magnification images shown in (a5–a7) and (b5–b8) illustrate morphological variation observed within the histological sections. The morphological features include viable tumor, necrotic tumor, cavitated/liquefied tumor, and peritumor muscle. The scatter plots in (a9) and (b9) demonstrate the specific scatter parameters associated with each individual pathological change.

proliferation as compared with Figure 2(b6) (yellow). Another largely necrotic region is identified in Figure 2(b8) (red), again with similar semi-normal tumor morphology. Whereas the viable tumor has a normal morphology.

In Figure 3(a), thumbnails of viable tumor sections from both tumors are shown with the extra-cellular matrix (ECM) highlighted green through a color based segmentation done in MATLAB. In short, the images of viable tumor are converted from RGB space to HSV space, thresholds for hue, color saturation, and brightness are applied to isolate extra-cellular collagen based on its unique affinity for the eosin stain, and finally the fraction of segmented pixels is calculated. In Figure 3(b), (c), γ and μ'_s are plotted versus the fraction of ECM in the respective histologic sections. While in Figure 3(d), thumbnails of various sections from both tumors are shown with the areas of low-grade viable tumor shaded yellow and areas of necrosis shaded green, and Figure 3(e),

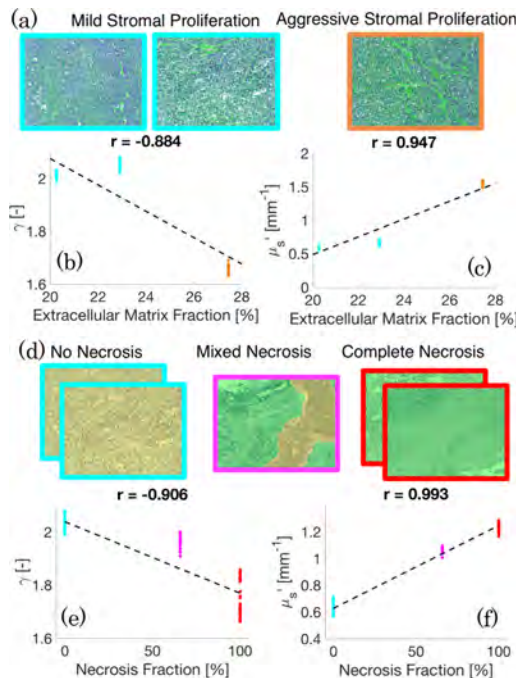


Figure 3 In (a), histological sections of viable tumor are shown with the extra-cellular matrix (ECM) segmented and highlighted green. In (b) and (c), the fraction of ECM is shown as a function of μ'_s and γ respectively. In (d), histological sections with low grade tumor, mixed necrosis, and complete necrosis are shown with areas of necrosis shaded green and areas of viable tumor shaded yellow. In (e) and (f), the fraction of necrosis is shown as a function of μ'_s and γ respectively.

(f), γ and μ'_s are respectively plotted versus the fraction of necrosis in the histologic sections.

The effect of stromal proliferation on optical properties for low grade tumor (cyan) and high grade tumor (orange) is shown in Figure 3(b), (c). With an increasing fraction of ECM, optical parameters showed an increase μ'_s ($r = 0.947$) that are representative of densely packed scattering structures, and a decrease in γ ($r = -0.884$) as the stromal collagen acts like a Rayleigh-type scatterer with refractive index fluctuations much smaller than the wavelength of light. These correlations suggest that stromal proliferation, which is related to tumor grade, has a strong effect on optical properties. However, it is important to note many other ultrastructural changes on length scales much smaller than the diffraction limit also have profound impact on the optical properties. The transition in optical properties from the low-grade tumor sections (cyan) to the mixed necrotic section (magenta) and totally necrotic sections (red) is shown in Figure 2(e), (f), with an increase in scatter frequency (i.e. increase in μ'_s as function of % necrosis, $r = 0.993$) and decrease in Mie-forward scattering (i.e. decrease in γ as function of % necrosis, $r = -0.906$). A possible explanation for this trend in optical properties is as the cells lyse during necrosis, the individual Mie regime cells, nuclei, and mitochondria become a chaotic suspension of Rayleigh regime proteins.

4. Discussion and conclusions

The data in Figures 2 and 3 show that quantitation of light scattering provided by sd-SFDI reveals information about tissue microstructure that is not readily discernible from qualitative inspection of white light imaging. Reflectance imaging over multiple spatial frequencies allows independent estimation of metrics of scatter frequency (i.e. μ'_s) and scatter size scale distribution (i.e. γ). The present study shows, for the first time, the use of sd-SFDI to quantify spatial variations in microarchitecture of tumors highlighting the sensitivity of the measurement to changes in structure associated with tumor grade and viability. This study also demonstrates the use of sd-SFDI at a single wavelength, reducing the requirements for spectrally resolved acquisition and potentially enhancing the ability to translate the approach to existing surgical imaging equipment.

Previously reported validation studies have demonstrated accurate quantification of each sub-diffusive parameter independently, with systematic variation in both the density and the size scale distribution of scatterers and also with variations in background absorption [8]. To investigate the independence of these two parameters in biological

media, the Pearson Product correlation coefficient was calculated for μ'_s and γ on a pixel-by-pixel basis for the full image of Tumor A ($r = -0.56$) and Tumor B ($r = -0.63$) (data not shown). These results suggest mild cross-talk between the recovered scattering parameters, which can be explained by biophysical correlations in sub-regions of the tumor such as those shown in Figures 2 and 3, but such cross-correlations were not observed in phantom data [8], these results do motivate further development of the optical property inversion algorithm.

Coupled interpretation of these sub-diffusive scattering parameters, which are recovered at each pixel in the imaged field of view, provides a multi-parametric basis to characterize tissue types. The results presented in this study represent, to the knowledge of the authors, the first quantitative sub-diffusive analysis of internal tumor architecture, and demonstrate the ability of light scattering to detect specific changes in tumor morphology. Results highlight that the biological variability in malignant tissue is substantial, and are consistent with previous claims that the use of scatter imaging for diagnostic evaluation of tumor margins may require the spatial interpretation of optical maps, as done in Laughney et al. [4]. While non-uniqueness of optical properties, i.e. multiple tissue type having similar optical properties, presents a limitation of this method, contextual information about the sample can guide the interpretation of the signal as is commonly done in flow cytometry. It also is important to note that the data presented in this study are from a limited representative set of individual tumors, limiting the ability to make meaningful generalizations. Furthermore, orthotopic murine models with diffusely mixed tissues and more aggressive perfusion may provide a more realistic tumor model for clinical applications than the subcutaneous model utilized in this study. Future work is needed with increased statistical power to fully assess the sensitivity of this method, but the comparison of micro-structural morphology with sub-diffusive optical parameters in this study provides insight as a proof-of-principle demonstration into the use of sd-SFDI for multi-length scale imaging of biological tissue. Without the need for exogenous dyes, spectroscopic analysis, or raster scanning, monochromatic sd-SFDI is a promising technique for rapid *in situ* tissue characterization.

Acknowledgements This work has been supported by NIH/NCI grants R01CA192803 and K25CA164248.

References

- [1] J. M. Schmitt and G. Kumar, *Applied Optics* **37**(13), 2788–2797 (1998).
- [2] M. Xu and R. R. Alfano, *Optics letters* **30**(22), 3051–3053 (2005).
- [3] J. D. Rogers, I. R. Çapoğlu, and V. Backman, *Optics letters* **34**(12), 1891–1893 (2009).
- [4] A. M. Laughney, V. Krishnaswamy, E. J. Rizzo, M. C. Schwab, R. J. Barth, B. W. Pogue, K. D. Paulsen, and W. A. Wells, *Clinical Cancer Research* **18**(22), 6315–6325 (2012).
- [5] S. C. Kanick, C. van der Leest, R. S. Djamin, A. M. Janssens, H. C. Hoogsteden, H. J. C. M. Sterenborg, A. Amelink, and J. G. J. V. Aerts, *J Thorac Oncol* **5**(7), 981–987 (2010).
- [6] A. Wax, C. Yang, V. Backman, M. Kalashnikov, R. R. Dasari, and M. S. Feld, *JOSA A* **19**(4), 737–744 (2002).
- [7] A. Wax, C. Yang, V. Backman, K. Badizadegan, C. W. Boone, R. R. Dasari, and M. S. Feld, *Biophysical journal* **82**(4), 2256–2264 (2002).
- [8] D. M. McClatchy, E. J. Rizzo, W. A. Wells, P. P. Cheaney, J. C. Hwang, K. D. Paulsen, B. W. Pogue, and S. C. Kanick, *Optica* **3**(6), 613–621 (2016).
- [9] S. C. Kanick, D. M. McClatchy, V. Krishnaswamy, J. T. Elliott, K. D. Paulsen, and B. W. Pogue, *Biomedical optics express* **5**(10), 3376–3390 (2014).
- [10] N. Bodenschatz, P. Krauter, S. Nothelfer, F. Foschum, F. Bergmann, A. Liemert, and A. Kienle, *Journal of biomedical optics* **20**(11), 116006 (2015).
- [11] F. Bevilacqua and C. Depeursinge, *JOSA A* **16**(12), 2935–2945 (1999).
- [12] S. Chamot, E. Migacheva, O. Seydoux, P. Marquet, and C. Depeursinge, *Optics express* **18**(23), 23664–23675 (2010).
- [13] J. J. Bravo, K. D. Paulsen, D. W. Roberts, and S. C. Kanick, *Optics letters* **41**(4), 781–784 (2016).
- [14] D. J. Cuccia, F. Bevilacqua, A. J. Durkin, F. R. Ayers, and B. J. Tromberg, *Journal of biomedical optics* **14**(2), 024012 (2009).
- [15] Y. Zhao, S. Tabassum, S. Piracha, M. S. Nandhu, M. Viapiano, and D. Roblyer, *Biomed Opt Express* **7**(6), 2373–2384 (2016).
- [16] N. Bodenschatz, P. Krauter, A. Liemert, J. Wiest, and A. Kienle, *Applied optics* **54**(22), 6725–6731 (2015).
- [17] R. Michels, F. Foschum, and A. Kienle, *Opt Express* **16**(8), 5907–5925 (2008).
- [18] P. Di Ninni, Y. Bérubé-Lauzière, L. Mercatelli, E. Sani, and F. Martelli, *Appl Opt* **51**(30), 7176–7182 (2012).

Chapter 6: Prediction of Stromal Versus Epithelial Proportions in Freshly Resected Human Breast Specimens

6.1. Background and Goals

The results in Chapters 4 and 5 demonstrated that the sub-diffusive light scattering parameters were sensitive to neoplastic changes in tissue morphology. But a limitation of these results was the lack of a direct relationship between clinical or biological endpoints and light scattering measurements in breast tissue. But a qualitative analysis of the data in Chapter 4 and 5 resulted in the following hypothesis: collagen acts as a strong Rayleigh-like scatterer and organelles within epithelial cells act as Mie-like scatterers, which could be quantified with the light scattering parameters. The goal of this work was to test this hypothesis by further developing and applying the quantitative histology methods developed in Chapter 5 to an expanded data set of scatter parameter maps of freshly resected breast tissue specimens discussed in Chapter 4, to determine if the stromal, epithelium, and adipose volume fractions could be predicted from the scattering parameters thus giving a biologic interpretation of these physical signals. This work is outlined in the following manuscript, and demonstrated that the physical light scatter parameters are in fact explicitly related to and predictive of these clinically relevant, quantitative histologic metrics, with reported preliminary estimates for sensitivity and specificity of distinguishing malignant from benign lesions.

6.2. Submitted Manuscript for Publication

The following manuscripts will be submitted to the Journal of Biomedical Optics:

McClatchy DM, Rizzo EJ, Wells WA, Paulsen KD, Kanick SC, Pogue BW.
Label-free light scatter imaging can predict stromal versus epithelial proportions in
freshly resected human breast cancer specimens. *Prepared for Submission.*

D. M. McClatchy was responsible for all experimental data acquisition, data analysis and quantification, model conception and fitting, development of the histology segmentation algorithm, statistical analysis, and writing the manuscript. E. J. Rizzo was responsible for receiving and dissecting the surgical human breast tissue. W. A. Wells was responsible for the creation and diagnosis of the digitized histology slides and was in charge of the protocol to image surgical human breast tissue. K. D. Paulsen, S. C. Kanick, B. W. Pogue provided advising, authored the NIH grant supporting this research, and participated in editing and writing the manuscript.

Label-free light scatter imaging can predict stromal versus epithelial proportions in freshly resected human breast cancer specimens

David M. McClatchy III,^{1} Elizabeth J. Rizzo,² Wendy A. Wells,^{2,3} Keith D. Paulsen,^{1,3} Stephen C. Kanick,^{1,&} Brian W. Pogue^{1,3}*

¹ Thayer School of Engineering, Dartmouth College, 14 Engineering Drive, Hanover, NH 03755

² Department of Pathology, Geisel School of Medicine, Dartmouth College, 1 Rope Ferry Road, Hanover, NH 03755

³ Norris Cotton Cancer Center, Dartmouth-Hitchcock Medical Center, 1 Medical Center Drive, Lebanon NH 03766

& Current address: Profusa Inc., 345 Allerton Ave. South San Francisco, CA 94080

Running Title: Predicting Epithelial and Stromal Proportions with Light Scattering Imaging, Light Scatter Imaging, Tissue Classification

Financial Support: This work is supported by NIH/NCI grants R01CA192803 and F31CA196308.

Key words: Breast Conserving Surgery, SFDI, Structured Light

Disclosure: The authors declare no potential conflicts of interest.

Corresponding Author:

David M. McClatchy III, Thayer School of Engineering, Dartmouth College, 14 Engineering Dr., Hanover, NH 03755; Tel: +1 410-507-4518; E-mail: david.m.mcclatchy.iii.th@dartmouth.edu

Statement of Translational Relevance

Determining tumor margin status during a lumpectomy procedure remains a significant clinical challenge, with 20-40% patients requiring a residual resection. While frozen-section analysis and innovative microscopy modalities could offer diagnostic value, tissue processing and staining along with evaluating a macroscopic specimen over microscopic fields of view remain as practical challenges. Structured light imaging is a wide-field, process-free, and stain-free technique capturing superficially scattered light, which has been previously shown to be sensitive to malignant versus benign pathologies in freshly resected human breast tissue specimens with sub-millimeter resolution. Here we present and validate a method to directly predict and spatially map stromal, epithelial, and adipose volume fractions in freshly resected breast tissue from light scattering parameters, and demonstrate a potential for diagnostic utility. Furthermore, the methods and results described here reveal a biological link between empiric light scattering parameters and histologically relevant information.

Abstract

Purpose: This study aims to determine if light scatter parameters could be used to accurately predict stromal, epithelial, and adipose fractions in freshly resected, unstained human breast specimens, and if these predicted metrics could be diagnostically useful.

Experimental Design: An imaging study was conducted with $N = 31$ freshly resected human breast tissue specimens, which were measured with a structured light imaging system, and subsequently underwent standard histological processing. A model was developed to predict stromal, epithelial, and adipose fractions as a function of light scattering parameters, and was validated against a quantitative analysis of digitized histology slides. A simple threshold based classification scheme was analyzed with leave-one-out cross fold validation (LOO-CV) to test the accuracy and potential diagnostic value of the predicted histological metrics.

Results: Specimen mean stromal, epithelial, and adipose volume fractions predicted from light scattering parameters strongly correlated with those calculated from digitized histology slides ($r = 0.90, 0.77, 0.91$ respectively, $p\text{-value} < 1e-6$). Thresholding of the predicted fat and ratio of epithelium to stroma fractions classified malignant specimens with a sensitivity and specificity of 90% and 81%, and classified all pixels in malignant lesions with 63% and 79%. All specimens and pixels were classified as malignant, benign, or fat with 84% and 75% accuracy, respectively.

Conclusions: These findings demonstrate how light scattering parameters acquired with structured light imaging can be used to accurately predict and spatially map stromal, epithelial, and adipose proportions in fresh unstained, human breast tissue, and suggest that these estimations could provide diagnostic value.

Introduction

Breast conserving surgery (BCS) combined with radiation therapy is becoming an increasingly popular treatment for localized breast cancer. However, it still remains a challenge for surgeons to obtain clear surgical margins, with 20%-40% of patients requiring follow-up re-excision procedures¹. While histopathology is the “gold-standard” for determining the margin status, it can take multiple days to process and analyze a specimen, which requires specimen sectioning, dehydrating, fixing, paraffin embedding, microtoming, slide mounting, and slide staining. Because of this challenge, there has been a great effort to determine novel ways to rapidly triage breast tissue specimens, with the ultimate goal of intraoperative tumor margin assessment.

A common technique to overcome this time barrier is frozen section pathology (FSP), where cut tissue specimens are flash frozen and mounted during the surgery, in order to have slides diagnosed by a pathologist before closing the surgical cavity. While this technique has shown some diagnostic value despite known imaging artifacts from freezing, it remains extremely time consuming, costly, and still suffers from under sampling of the tissue^{2,3}. There have been promising advances in various novel microscopy techniques, which can create virtual histology slides in thick unprocessed tissue, with^{4,5} or without^{6,7} the application of topical fluorescent dyes. And similarly, optical coherence tomography can provide, microscopic resolution in unprocessed human breast tissue^{8,9}. However, in the BCS workflow, there is still an issue of under sampling with these techniques, as the time it takes to scan and evaluate microscopic fields of view over an entire lumpectomy specimen creates a clinical translation challenge.

Wide-field optical imaging can provide rapid sensing of an entire specimen surface, and while it lacks microscopic resolution, it can provide molecular or morphological sensitivity^{10,11}. In particular, label-free reflectance imaging techniques utilizing multi-spectral and/or structured illumination, have employed machine learning techniques to back out tissue diagnoses from raw reflectance spectra or optical properties^{12,13}. While machine learning can act as a conduit between raw optical signals and tissue diagnoses, the cloaking of the biological mechanism between the source data and predicted pathology can often hinder clinical acceptance of these technologies. And although optical properties related to light scattering have specifically shown enhanced sensitivity to tissue morphology¹³⁻¹⁶, these parameters lack a clear clinical or biological definition.

Therefore, the ultimate purpose of this study is to elucidate the relationship between clinically relevant histologic features from optical reflectance signatures, and furthermore develop and validate a method to predict these histologic features from optical signals. For this study, a cohort of n=31 freshly resected human breast tissue specimens imaged with a structured light system, resulting in light scattering parameter maps co-registered to histopathology, is investigated¹⁴. The explicit relationships between optical scattering properties and stromal, epithelial, and adipose volume fractions segmented from co-registered digitized histopathology is presented. Furthermore, a model by which these histologic features can be predicted is validated and its diagnostic potential in distinguishing malignant from normal human breast tissue is demonstrated.

Materials and Methods

Imaging of Fresh Breast Tissue Samples Study Protocol

An *ex-vivo* breast specimen imaging study conducted in the Department of Pathology at Dartmouth Hitchcock Medical Center (DHMC) was approved by the Institutional Review Board for the protection of human subjects as detailed in a previous publication¹⁴. To briefly summarize, excised breast tissue from patients undergoing elected and consented breast surgery was immediately transported to the Department of Pathology. Tissue that was in excess of what was needed to make a clinical diagnosis and was sent to the tissue-bank, and was considered for imaging in this study. Tissues that were grossly identified as invasive cancer, fibroglandular, fibroadenoma, or adipose were cut to a size of roughly 25 mm x 25 mm x 5 mm, placed on a glass slide, and immediately imaged from below with a commercial structured light imaging system (Modulated Imaging, Inc.)^{17,18}, described in Section 2.2. After imaging, the specimens were immediately returned to the Department of Pathology and underwent standard histological processing of dehydration, fixation, paraffin embedding, slide mounting, and staining with hematoxylin and eosin (H&E). The resulting H&E slides were read by an expert pathologist (W.A.W.) and included in the patient's report.

In total 37 specimens were imaged, which represents an expanded data set obtained from a previous study¹⁴ where only 22 specimens were collected. Furthermore, fibroadenoma (N=5) and mucinous ductal carcinoma (N=1) specimens were excluded from this study to predict stromal from epithelial proportions from optical imaging, as these specimens have very unique morphological features, which would be known *a priori* to surgery, and also were not amenable to the color-based histological analysis described in Section 2.3. Thus, N=10 invasive cancer specimens were included (N=7 invasive ductal (IDc), N=2 intra lobular (ILc), and N=1 male invasive ductal IDc), N=14 normal fibroglandular specimens (N=2 with fibrocystic disease (FCD) and N=1 male Gynecomastia), and N=5 pure fat specimens. A total of N = 31 specimens, were included as tabulated in Figure 2(f).

Structured Light Imaging and Light Scattering Parameters

A complete description of the structured light imaging system and light scattering parameters are thoroughly described in previous publications^{14,19}. A description of the main features pertaining to this study is summarized below. The structured light imaging system consisted three light emitting diodes (LEDs) at $\lambda = [658, 730, 850]$ nm, which focused light on a digital micro-mirror device (DMD) to sequentially project sinusoidal intensity patterns with spatial frequencies, f_x , in the range of $[0 - 0.9]$ mm⁻¹ onto the tissue surface, and a charged coupled device (CCD) camera to capture the remitted intensity patterns. Offline, the image stacks were read into MATLAB (v2016a, Mathworks, Inc.) and demodulated and calibrated, which yielded reflectance maps over

the acquired wavelengths and spatial frequencies. These reflectance maps were inverted into maps of optical properties through a pixel-by-pixel least square fitting routine, *lsqnonlin*, which minimized the difference between measured reflectance and light propagation model predicted reflectance.

The resulting optical properties of interest quantifying light scattering were the phase function parameter γ , reduced scattering coefficient μ_s' , and wavelength vs scatter power, B. The phase function parameter quantified directional light scattering (relative amount of forward to backward scatter) and is related to the amount of scattering features smaller and larger than the wavelength of light^{20,21}. The reduced scattering coefficient is related to the overall density of scattering features²². The scatter power quantifies the exponential power of which μ_s' varies with the wavelength of light (assuming $\mu_s'(\lambda) = A \lambda^{-B}$), and has been shown to be related to size-scale distribution of scattering features^{23,24}. Previous studies have shown the spatial resolution of μ_s' to be ~2 mm with a 1-2 mm depth penetration, while both the spatial resolution and depth penetration and γ was <1 mm¹⁴.

Quantitative Digital Histology Analysis

Physical H&E stained histology slides of the study specimens were digitized with a slide scanner with a resolution of 500 or 1000 pixels per mm. The methodology of processing the digitized H&E slides is shown in Fig. 1(a-d). First, scanned slides were de-convolved into monochromatic hematoxylin and eosin intensity channels, shown in Fig. 1(b), using a well-established spectral unmixing technique²⁵. This was implemented using the “Color Deconvolution” plugin (v1.7) in Fiji (v2.0.0), a distribution of the open-source image processing software package ImageJ²⁶. Next, the hematoxylin and eosin intensity images were converted to binary images of epithelium, stroma, and adipose, shown in Fig. 1(c) as follows. Each hematoxylin and eosin intensity image was converted from a RGB (red, green, blue) to HSV (hue, saturation, value) color space using the *rgb2hsv* function in MATLAB, and the color saturation was used to compare each stain’s affinity. Pixels with greater hematoxylin saturation than eosin saturation were labeled epithelium, while pixels with greater eosin than hematoxylin saturation were labeled stroma. Pixels without significant hematoxylin or eosin saturation (less than 1/10th maximum value) being white space, were assigned as adipose. Next, these binary images were binned down to calculate volume fractions, shown in Fig. 1(d), by defining 200 $\mu\text{m} \times 200 \mu\text{m}$ voxels over which the fraction of pixels labeled epithelium, stroma, or adipose was calculated. Because of distortions through histological processing steps (e.g. dehydration and fixation), exact pixel-to-pixel correlation between the histological and optical maps could not be made. Instead, a region of interest was defined to segment the lesion in both the optical and histological images, over which the mean and standard deviation was calculated for each specimen, as outlined in cyan in Fig. 1(d) and (e).

Optical-Histological Model Creation

With the paired light scattering parameters and segmented epithelium, stroma, and adipose fractions, models were created using the *fit* function in the Curve Fitting Toolbox in MATLAB (v2016a). The mean epithelium, stroma, and adipose fractions are plotted as

functions of μ_s' in Fig. 2(a), γ in Fig. 2(b), and B in Fig. 2(c), where each data point represents each specimen mean and the error-bars represent one standard deviation. The fitted relationships are shown as solid lines and the 95% prediction intervals are shown as dotted lines. The explicit form of each relationship is shown in Fig. 2(d), along with the specific fitted parameters and corresponding 95% confidence intervals of each parameter. Given the monotonic nature of the stroma and adipose volume fractions, a 2 parameter logistic like equation well described the data. A 3 parameter Gaussian-like equation described the peaked epithelium volume fraction response, with fat and fibroglandular specimens both having a diminished epithelium volume fraction but separate optical properties. The root mean square error (rmse) and degree of freedom adjusted coefficient of determination (r^2_{adj}) was calculated for each relationship are shown in Fig. 2(a-c). The mean rmse over all models was 0.16, while the mean r^2_{adj} was 0.69. In the supplementary material, linear plots of H&E segmented histologic fractions versus optical property model predicted values are shown for all nine models, with corresponding correlation coefficients and p-values (mean Pearson correlation coefficient $r = 0.84$; all $p < 1e-4$).

Prediction of Histological Metrics and Malignancy Status

Based on the fitted models described in Section 2.4, a predictive model of the epithelium, stroma, and adipose fractions as a function of the light scattering parameters was created and tested, in addition to a simple threshold based tissue classification model, as illustrated in Fig. 3. To test the accuracy of the predictive model, a leave one out cross fold validation (LOO-CV) scheme was used. For a given test specimen, such as Fig. 3(a), the models, Fig. 3(b), were fitted without the test data point, and this process was repeated over all specimens. The stoma, epithelium, and adipose fractions, shown in Fig. 4(d), were simply calculated as the mean of the predicted values from each of the three light scattering properties, Fig. 3(c).

From these optical property predicted histologic fractions, a simple threshold based tissue classification scheme was implemented. Pixels with adipose volume fractions greater than 50% were classified as fat. For pixels with adipose less than 50%, the ratio of epithelium to stroma, shown in Fig. 4(e), was used to classify remaining pixels as malignant or benign based on whether there was more epithelium than stroma or vice-versa. A “soft” classification map is shown in Fig. 4(f), where the color of each pixel is determined by the classification and the color saturation is determined by the continuous histologic fractions. From this classification map, regions of the malignant lesion, the lesion bordering with fat, and a region of pure adipose are confirmed from the H&E section. Furthermore, a small false-negative region within the larger malignant lesion can been.

Statistical Methods

For the LOO-CV, performance metrics were calculated for on all specimen lesion pixels and also specimen averaged values. The sensitivity, specificity, and accuracy were calculated for each of the three output classes for specimens and pixels, and confidence intervals were calculated using the Clopper-Pearson method according to a binomial

distribution using the MATLAB function *binofit*. A two sided two sample t-test was used to test statistical significance of differences in distributions.

Results

Histologic Predictions from Label-Free Scatter Images

Case examples for a typical invasive ductal carcinoma (IDc), fibroglandular, and fat specimen are shown in Fig. 4. The color images, along with the optical property predicted stroma, epithelium, and adipose volume fraction maps, are shown in Fig. 4(a), (b), (c), and (d) respectively for each specimen. As expected, the IDc, fibroglandular, and fat specimens presented uniformly high epithelium, stroma, and adipose volume fractions, respectively. The resulting soft classification maps are shown in Fig. 4(e), which broadly corresponded to each specimens' known pathology, as confirmed by the whole specimen digitized H&E sections shown in Fig. 4(f). Representative regions within each section are shown in Fig. 4(g-j), highlighting typical microscopic features associated with each pathology. Interestingly, there was a small false negative region within the IDc soft classification map, suggesting a stronger optical signal from extracellular stroma than cellular epithelium. The H&E section corresponding to this region, shown in Fig. 4(h), revealed an increased proportion of stroma, compared to the more cellular section, shown in Fig. 4(g), despite both regions coming from the same invasive ductal lesion. Additionally, a slight artifact can be seen in the fibroglandular soft classification map, as a false positive region between the transition fat to benign tissue at the specimen boundary.

The quantitative results of the LOO-CV analysis to test the accuracy predicting stroma, epithelium, and adipose volume fractions from optical property measurements are presented in Fig. 4(k). The optical property model histologic predictions are plotted as a function of the corresponding H&E segmented values, with data-points and error-bars representing the mean and standard deviation within each specimen, respectively. The resulting linear relationships provided evidence that the optical property predictions were strongly correlated to the values obtained from the digitized H&E slides, as quantified by the Pearson correlation coefficients (stroma $r=0.90$, $p<1e-11$, epithelium $r=0.77$, $p<1e-6$, adipose $r=0.91$, $p<1e-11$). A complete report of the distributions of both optical property predicted and H&E segmented epithelium, stroma, and adipose volume fractions stratified by invasive cancer, fibroglandular, and fat pathologies is located in the supplementary information. This confirmed that invasive cancer specimens presented a significantly higher mean epithelium volume fraction than fibroglandular as measured by from digitized histology ($p<10^{-8}$) and the optical property model ($p<0.01$). Conversely, fibroglandular specimens presented a significantly higher mean stroma volume fraction than invasive cancer as measured by from digitized histology ($p<0.001$) and the optical property model ($p<0.01$).

Benign versus Malignant Classification Performance

A summary of the quantitative performance analysis of the tissue classification algorithm is shown in Fig. 5. The optical property predicted adipose volume fraction boxplots in Fig. 5(a) showed a clear separation between the fat specimens and the aggregated invasive cancer and fibroglandular specimens at a threshold of 0.5 ($p < 1e-14$). But more importantly, the optical property predicted epithelium to stroma ratio boxplots in Fig. 5(b) showed a clear separation between the invasive cancer and fibroglandular specimens at a threshold of 1 ($p = 0.007$). For all boxplots, the means of each specimen are plotted with error-bars representing one standard deviation within each specimen, characterizing intra-specimen variation.

Confusion matrices tabulating the fraction of true versus predicted classifications of all specimens (left) and pixels (right) are shown in Fig. 5(c). The values along the diagonals of each matrix denote the fraction of correctly classified specimens or pixels for a given class, while off-diagonal values denote those incorrectly classified. The sensitivity, specificity, and accuracy were quantified from these data and are tabulated in Fig. 5(d). While the fraction of correctly classified malignant specimens was 0.9 when specimen averaging is applied, the fraction of correctly classified malignant pixels drops to 0.63. Furthermore, when the specimens mean data is classified versus all pixels within each specimen lesion, the malignant sensitivity drops from 0.9 to 0.63 and the benign specificity drops from 0.93 to 0.8. The apparent heterogeneity in cellular versus stromal densities in malignant lesions suggests that lesion based averaging may increase robustness. Nevertheless, the overall accuracy of correctly classifying a given pixel was 0.75, while the overall accuracy of classify a given specimen was 0.84.

Spatial quantification of histologic metrics and tissue classification

Side by side comparisons of the model predicted metrics and digitized H&E data are shown for a heterogeneous specimen in Fig. 6. Spatially resolved maps of H&E segmented and optical property predicted epithelium, stroma, and adipose volume fractions are shown sided by side in Fig. 6(a), (b), and (c) respectively. Soft classification maps, shown in Fig. 6(d), were calculated from both the H&E segmented and optical property predicted histologic metrics. For both the soft classification and histologic metrics, similar spatial features were seen in both the H&E segmented and optical property predicated maps, despite the notable difference in spatial resolution and expected minor co-registration differences arising from specimen dehydration, fixation, and sectioning. The whole digitized H&E slide of the is shown in Fig. 6(e), with malignant, benign, and fatty regions outlined. The presence of these outlined lesions can be seen in both of the soft classification maps, albeit with some spatial noise. Representative sections of the malignant invasive lesion and benign fibroglandular region are shown in Fig. 6(f), the locations of which are marked by a red and green asterisk respectively in both the soft classification maps, Fig. 6(d), and the annotated H&E slide, Fig. 6(e). A simple overlay of the optical property predicted soft classification map onto the white light image in shown in Fig. 6(g), which are inherently co-registered as they were acquired with the same imaging system. The original specimen color image is along

with the graph of the overlay transparency is shown in Fig. 6(h). When epithelium and stroma have a similar predicted strength, and thus the classification is less certain, the overlay becomes transparent. The adipose volume fraction was not overlaid as fat is distinguishable by inspection.

Discussion and Conclusions

Label-free light scattering measurements have shown sensitivity to morphological changes between malignant and benign tissues through a multitude of studies across a myriad of optical sensing devices over the last 20 years^{11-14,16,27-36}. However, in all of these studies light scattering is quantified either empirically or with physical radiative transport terms, both of which lack biological or clinical meaning. Therefore, the aim of this study was to determine if quantitative light scattering measurements could be related to and predictive of clinically relevant histologic metrics, specifically the volume fraction of stroma, epithelium, and adipose. This hypothesis was systematically tested by investigating the relationship between optical scattering properties of freshly resected breast tissue determined from structured light imaging to histology metrics segmented from co-registered and digitized H&E sections of whole specimens. Logistic and Gaussian responses were observed between the optical scattering properties and volume fractions of stroma, epithelium, and adipose. From these observations, a simple model demonstrated that in fact common optical properties could explicitly predict and spatially map volume fraction of stroma, epithelium, and adipose, which in turn provided diagnostic accuracy in predicting malignant from benign lesions.

The physical origins of light scattering arise from spatial fluctuations in the refractive index over size scales both smaller and larger than the wavelength of light, each of which uniquely contribute to the spectral and angular intensities of light scattering^{22,23,37-39}. While these fluctuations can not be resolved with a conventional microscope, the staining of hematoxylin and eosin allows for an estimate of the relative proportions of stroma, epithelium, and adipose, each of which have very unique ultrastructural size-scale features. This has been demonstrated in previous studies where fibroglandular tissues have presented both increased scattering intensity and increased collagen content when compared to more cellular malignant lesions as measured in human breast tissue with phase contrast microscopy³³ and dark-field microscopy²⁹, as well as in human ovarian tissue measured with optical coherence tomography³². Furthermore, weak positive correlations have been reported between spectroscopic scattering and the fraction of stroma or collagen measured by spatial frequency domain imaging¹³ and diffuse reflectance spectroscopy³⁴. However in this study, light scattering was further decoupled into spectroscopic and angular components, which was achieved by increased signal localization, allowing for more sensitive measurements^{14,19}.

Although strong correlations between optical property predicted and H&E segmented histology metrics were found and shown to be diagnostically relevant, there are a few notable limitations with this technique. First the spatial correlations between the optical images and the H&E slide are not exact, as the tissue shrinks during the fixation process. Although lesion based averaging was used to overcome this common limitation, a further

issue is depth co-registration, as the H&E section represents a superficial slice of the tissue only a few microns in thickness, while the optical measurements have a depth sensitivity of a few hundred microns. The inexactness of the depth co-registrations was likely the dominant source variability in the model. Second, the endpoints of stroma, epithelium, and adipose volume fractions are imperfect for both the description for origins of scattering signals and the metrics to classify benign from malignant lesions. As mentioned previously, there are many ultrastructural features not quantified through histology, such as chromatin packing, mitochondria density, and collagen reformation, which could greatly affect both the light scattering properties and pathological diagnosis. One such example is that benign associated stroma in human breast tissue was shown to be more strongly scattering than tumor associated stroma³³. However, further studies could analysis stratify benign and malignant regions into levels of organization or grade as a proxy for neoplastic architectural changes. Despite these limitations, this study was able to show that these scatter parameters acquired from fresh, unprocessed, and unlabeled tissue could be used to quantified morphological parameters, which can currently only be obtained through timely histopathology processing.

In conclusion, it was shown that label free light scattering measurements of freshly resected human breast tissue acquired with structured light imaging, were explicitly related to and predictive of clinically relevant histology metrics, as quantified from digitized, whole specimen H&E slides. Three optical properties related the scatter density, spectroscopic scattering intensity, and directional scattering intensity were found to have a logistic relationship to the stroma and adipose volume fraction and a Gaussian relationship to the epithelium volume fractions. From these relationships, a predictive model was created and validated with LOO-CV, which demonstrated that the optical property predicted epithelium to stroma ratio was diagnostically relevant in distinguishing malignant from benign glandular tissue. With future development, this technology may aid in the surgical triaging of large, freshly resected BCS specimens.

Acknowledgments

This work was funded in part by National Cancer Institute grants F31CA196308 and R01CA192803.

Author Contributions

D.M.M. imaged the specimens, developed the models, and performed all of the statistical analysis. E.J.R. performed the gross analysis of surgical specimens. W.A.W. was responsible for the pathological diagnoses of the specimens and creating the digitized histology slides. K.D.P, S.C.K, B.W.P, and W.A.W. were responsible for developing the specimen acquisition protocol and study design. D.M.M, K.D.P, S.C.K, B.W.P, and W.A.W. all contributed to interpreting the data and preparing the manuscript.

Additional Information

The authors declare no conflicts of interest.

References

1. Pleijhuis RG, Graafland M, de Vries J, Bart J, de Jong JS, van Dam GM. Obtaining adequate surgical margins in breast-conserving therapy for patients with early-stage breast cancer: current modalities and future directions. *Ann Surg Oncol* 2009;16:2717-30.
2. Barakat FH, Sulaiman I, Sughayer MA. Reliability of frozen section in breast sentinel lymph node examination. *Breast cancer* 2014;21:576-82.
3. St John ER, Al-Khudairi R, Ashrafian H, et al. Diagnostic accuracy of intraoperative techniques for margin assessment in breast cancer surgery: a meta-analysis. *Annals of surgery* 2017;265:300-10.
4. Glaser AK, Reder NP, Chen Y, et al. Light-sheet microscopy for slide-free non-destructive pathology of large clinical specimens. *Nature Biomedical Engineering* 2017;1:0084.
5. Tao YK, Shen D, Sheikine Y, et al. Assessment of breast pathologies using nonlinear microscopy. *Proceedings of the National Academy of Sciences* 2014;111:15304.
6. Wong TTW, Zhang R, Hai P, et al. Fast label-free multilayered histology-like imaging of human breast cancer by photoacoustic microscopy. *Science Advances* 2017;3:e1602168-e.
7. Fereidouni F, Harmany ZT, Tian M, et al. Microscopy with ultraviolet surface excitation for rapid slide-free histology. *Nature Biomedical Engineering* 2017;1:957-66.
8. Allen WM, Chin L, Wijesinghe P, et al. Wide-field optical coherence micro-elastography for intraoperative assessment of human breast cancer margins. *Biomedical optics express* 2016;7:4139-53.
9. Erickson-Bhatt SJ, Nolan RM, Shemonski ND, et al. Real-time imaging of the resection bed using a handheld probe to reduce incidence of microscopic positive margins in cancer surgery. *Cancer research* 2015;75:3706-12.
10. Davis SC, Gibbs SL, Gunn JR, Pogue BW. Topical dual-stain difference imaging for rapid intra-operative tumor identification in fresh specimens. *Opt Lett* 2013;38:5184-7.
11. Krishnaswamy V, Elliott JT, McClatchy DM, et al. Structured light scatteroscopy. *Journal of biomedical optics* 2014;19:070504-.
12. Lu G, Little JV, Wang X, et al. Detection of Head and Neck Cancer in Surgical Specimens Using Quantitative Hyperspectral Imaging. *Clinical Cancer Research* 2017;23:5426.
13. Laughney AM, Krishnaswamy V, Rizzo EJ, et al. Spectral discrimination of breast pathologies *in situ* using spatial frequency domain imaging. *Breast Cancer Res* 2013;15:R61.
14. McClatchy DM, 3rd, Rizzo EJ, Wells WA, et al. Wide-field quantitative imaging of tissue microstructure using sub-diffuse spatial frequency domain imaging. *Optica* 2016;3:613-21.

15. McClatchy DM, Hoopes P, Pogue BW, Kanick SC. Monochromatic subdiffusive spatial frequency domain imaging provides in-situ sensitivity to intratumoral morphological heterogeneity in a murine model. *Journal of biophotonics* 2016;In Press.
16. McClatchy DM, 3rd, Hoopes PJ, Pogue BW, Kanick SC. Monochromatic subdiffusive spatial frequency domain imaging provides in-situ sensitivity to intratumoral morphological heterogeneity in a murine model. *Journal of biophotonics* 2017;10:211-6.
17. Cuccia DJ, Bevilacqua F, Durkin AJ, Tromberg BJ. Modulated imaging: quantitative analysis and tomography of turbid media in the spatial-frequency domain. *Opt Lett* 2005;30:1354-6.
18. Cuccia DJ, Bevilacqua F, Durkin AJ, Ayers FR, Tromberg BJ. Quantitation and mapping of tissue optical properties using modulated imaging. *Journal of biomedical optics* 2009;14:024012-.
19. Kanick SC, McClatchy DM, 3rd, Krishnaswamy V, Elliott JT, Paulsen KD, Pogue BW. Sub-diffusive scattering parameter maps recovered using wide-field high-frequency structured light imaging. *Biomedical optics express* 2014;5:3376-90.
20. Chamot S, Migacheva E, Seydoux O, Marquet P, Depeursinge C. Physical interpretation of the phase function related parameter γ studied with a fractal distribution of spherical scatterers. *Optics express* 2010;18:23664-75.
21. Bevilacqua F, Depeursinge C. Monte Carlo study of diffuse reflectance at source--detector separations close to one transport mean free path. *JOSA A* 1999;16:2935-45.
22. Schmitt JM, Kumar G. Optical scattering properties of soft tissue: a discrete particle model. *Applied Optics* 1998;37:2788-97.
23. Xu M, Alfano RR. Fractal mechanisms of light scattering in biological tissue and cells. *Optics letters* 2005;30:3051-3.
24. Rogers JD, Capoglu IR, Backman V. Nonscalar elastic light scattering from continuous random media in the Born approximation. *Optics letters* 2009;34:1891-3.
25. Ruifrok AC, Johnston DA. Quantification of histochemical staining by color deconvolution. Analytical and quantitative cytology and histology / the International Academy of Cytology [and] American Society of Cytology 2001;23:291-9.
26. Schindelin J, Arganda-Carreras I, Frise E, et al. Fiji: an open-source platform for biological-image analysis. *Nature methods* 2012;9:676-82.
27. Mulvey CS, Sherwood CA, Bigio IJ. Wavelength-dependent backscattering measurements for quantitative real-time monitoring of apoptosis in living cells. *Journal of biomedical optics* 2009;14:064013-.
28. Zonios G, Perelman LT, Backman V, et al. Diffuse reflectance spectroscopy of human adenomatous colon polyps *in vivo*. *Applied Optics* 1999;38:6628-37.
29. Laughney AM, Krishnaswamy V, Rizzo EJ, et al. Scatter spectroscopic imaging distinguishes between breast pathologies in tissues relevant to surgical margin assessment. *Clinical Cancer Research* 2012;18:6315-25.
30. Gurjar RS, Backman V, Perelman LT, et al. Imaging human epithelial properties with polarized light-scattering spectroscopy. *Nature medicine* 2001;7:1245-8.
31. Zhang L, Pleskow DK, Turzhitsky V, et al. Light scattering spectroscopy identifies the malignant potential of pancreatic cysts during endoscopy. *Nat Biomed Eng* 2017;1.
32. Yang Y, Wang T, Biswal NC, et al. Optical scattering coefficient estimated by optical coherence tomography correlates with collagen content in ovarian tissue. *J Biomed Opt* 2011;16:090504.

33. Wells WA, Wang X, Daglian CP, Paulsen KD, Pogue BW. Phase contrast microscopy analysis of breast tissue: differences in benign vs. malignant epithelium and stroma. *Analytical and quantitative cytology and histology / the International Academy of Cytology [and] American Society of Cytology* 2009;31:197-207.
34. Kennedy S, Caldwell M, Bydlon T, et al. Correlation of breast tissue histology and optical signatures to improve margin assessment techniques. *J Biomed Opt* 2016;21:66014.
35. Mourant JR, Bigio IJ, Boyer J, Conn RL, Johnson T, Shimada T. Spectroscopic diagnosis of bladder cancer with elastic light scattering. *Lasers in surgery and medicine* 1995;17:350-7.
36. Wallace MB, Perelman LT, Backman V, et al. Endoscopic detection of dysplasia in patients with Barrett's esophagus using light-scattering spectroscopy. *Gastroenterology* 2000;119:677-82.
37. Radosevich AJ, Yi J, Rogers JD, Backman V. Structural length-scale sensitivities of reflectance measurements in continuous random media under the Born approximation. *Optics letters* 2012;37:5220-2.
38. Mourant JR, Freyer JP, Hielscher AH, Eick AA, Shen D, Johnson TM. Mechanisms of light scattering from biological cells relevant to noninvasive optical-tissue diagnostics. *Appl Opt* 1998;37:3586-93.
39. Wang X, Pogue BW, Jiang S, et al. Approximation of Mie scattering parameters in near-infrared tomography of normal breast tissue *in vivo*. *Journal of biomedical optics* 2005;10:051704-.

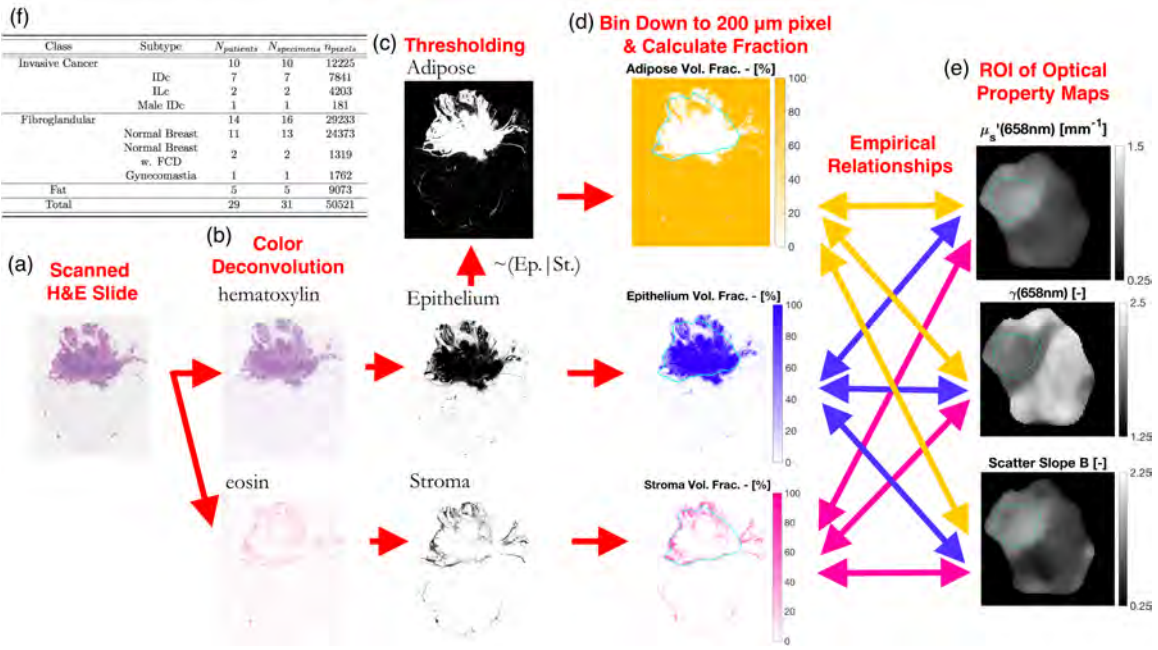


Figure 1: (a) A digitally scanned H&E slide with resolution of 500 pixels/mm. (b) Intensity images of the hematoxylin and eosin stains calculated through a color deconvolution of the H&E slide. (c) Binary images of epithelium and stroma calculated from a manual threshold of the hematoxylin and eosin intensity images, with a binary image of adipose calculated as a lack of stain intensity. (d) Volume fractions of epithelium, stroma, and adipose calculated over 200 $\mu m \times 200 \mu m$ areas of the binary images. (e) Corresponding optical property maps of the fresh specimen acquired pre-fixation and pre-staining. The lesion outlined in cyan in both (d) and (e) denotes the region over which empirical relationships are determined between the histologic and optical data. (f) A table listing patient and specimen sample sizes.

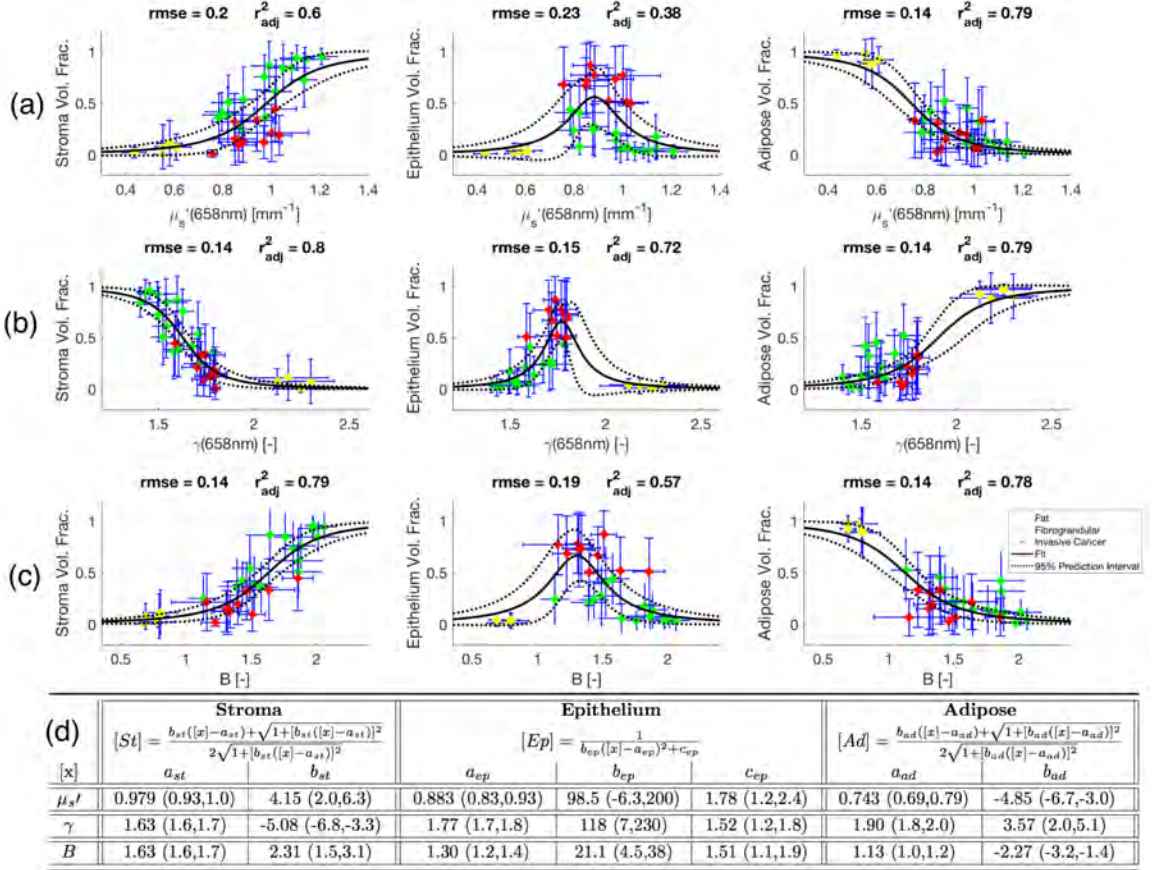


Figure 2: A summary of the relationships between the volume fractions of stroma, epithelium, and adipose calculated from the H&E sections and the optical properties μ_s' in (a), γ in (b), and B in (c), which describe overall light scattering intensity, intensity change with scatter angle, and intensity change with wavelength of light respectively. The root mean square error (rmse) and the adjusted coefficient of determination (r^2_{adj}) are shown for each relationship. The solid line is the fitted equation and the dotted line is 95% prediction interval. Data points represent means within each specimen, while error-bars represent one standard deviation. In (d), the equations for fitting the volume fractions of stroma, epithelium, and adipose as a function of each optical property are shown, along with the values of the fitted parameters. Values in parenthesis are 95% CIs.

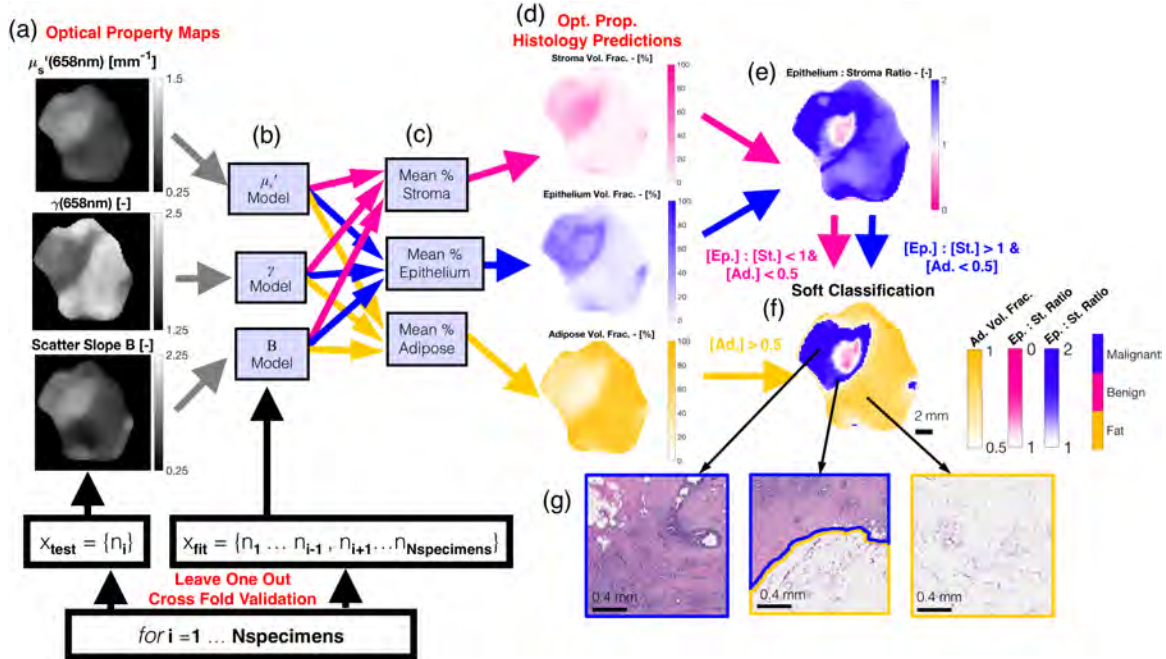


Figure 3: (a) Optical property maps of a test specimen. (b) Each optical property model is fitted with all specimens except the test specimen. This process is repeated over each specimen for the leave one out cross fold validation (LOO-CV). (c) The histologic volume fractions are predicted from the three optical property models and averaged together, resulting in the histology prediction maps in (d). A predicted epithelium to stroma ratio is calculated in (e), which is simply the ratio of the epithelium and stroma predictions. In (f), a soft classification map is shown where each pixel is one of three colors for a classification of malignant, benign, or fat based on a threshold of 1 for the epithelium to stroma ratio and 0.5 for adipose volume fraction. The color saturation is varied based on how close the epithelium to stroma ratio and adipose volume fraction are close to their respective thresholds. In (g), H&E sections are shown for areas within the malignant lesion, on the border of the lesion, and for the background fat, confirming the optical property predictions.

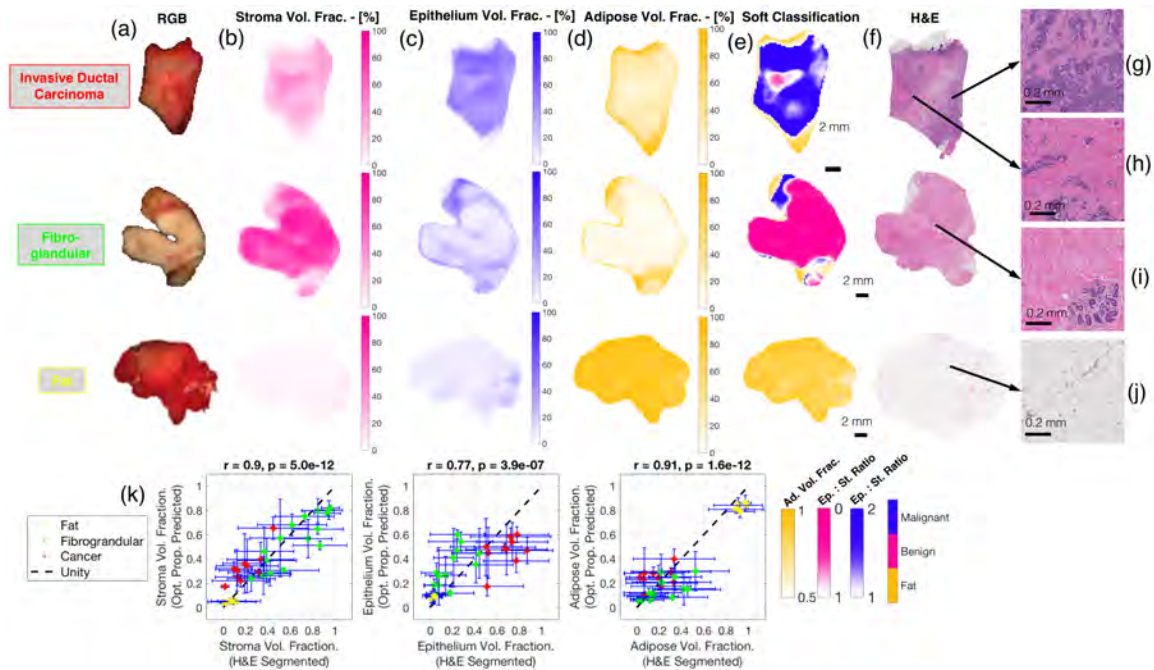


Figure 4: (a) Color photographs of representative invasive cancer, fibroglandular, and fat specimens. Stroma, epithelium, and adipose volume fractions predicted from the optical property maps are shown in (b), (c), and (d) respectively, with corresponding classification maps shown in (e). Whole specimen digitized H&E sections are shown in (f), while representative regions within each specimen are shown in (f)-(i). The sections in (f), (h), and (i) confirm the prediction of malignant, benign, and fat respectively, but a small false negative region shown in (g) with stromal proliferation. Plots of the H&E segmented histologic volume fractions versus the optical property predicted volume fractions, calculated using a LOO-CV are shown in (j). Data points represent means of each specimen, while the H&E segmented error bars represent one standard deviation within each specimen and the optical property predicted error bars represent the standard deviation of the predicted values from each optical property.

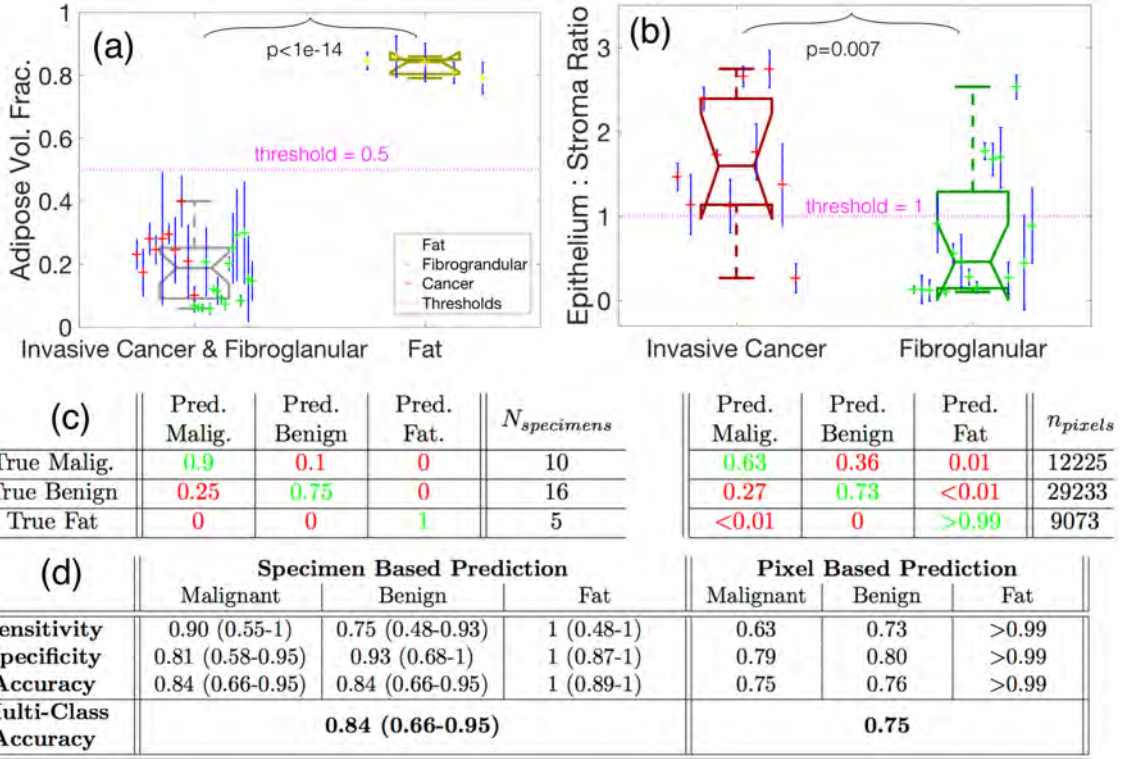


Figure 5: (a) Boxplot of the optical property predicted adipose volume fraction between glandular specimens (both malignant and benign) versus fat specimens. (b) Boxplot of the optical property predicted epithelium to stroma ratio between malignant and benign specimens. Thresholds used for classification are shown in magenta and p-values of a two-sample t-test are shown in black. (c) Confusion matrixes which display the fraction of correctly classified data points in green and those incorrectly classified in red. (d) Performance tables listing classification performance metrics. In (c) and (d), the left table represents specimen averaged classification while the right table represents classification over all individual pixels. Values in parenthesis represent Clopper-Pearson 95% CIs, while no parenthesis represents 95% CIs are within +/- 1%. All prediction and classification data were obtained with LOO-CV.

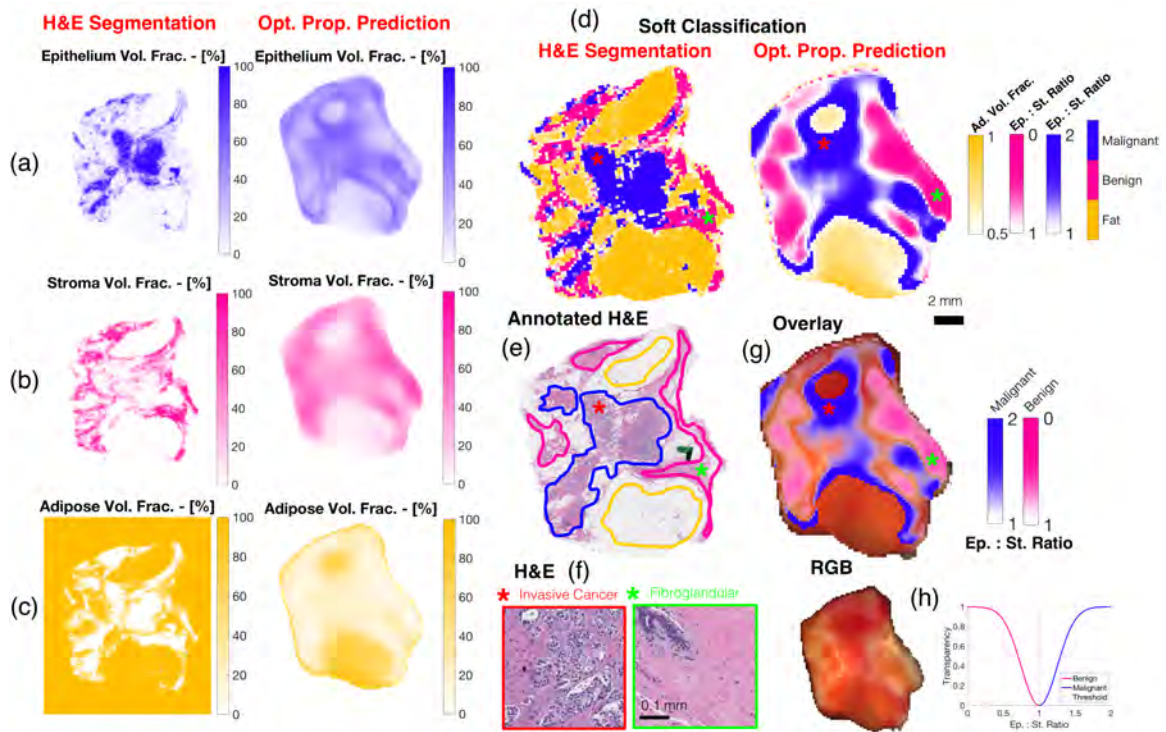


Figure 6: Side by side comparisons of H&E segmented and optical property predicted epithelium, stroma, and adipose volume fraction maps in (a), (b), and (c), respectively, for a specimen with malignant and benign regions. In (d), H&E segmented and optical property predicted classification maps are shown, and a corresponding H&E section of the entire specimen is shown in (e) with outlined malignant, benign, and fat regions. Zoomed in H&E sections of invasive ductal carcinoma and benign connective tissue regions are shown in (f). An overlay of the epithelium to stroma ratio onto the photograph of the specimen is shown in (g), with a graph of the overlay transparency and original photograph of the specimen in (h).

Supplementary Material: Label-free light scatter imaging can predict stromal versus epithelial proportions in freshly resected human breast cancer specimens

David M. McClatchy III,^{1,*} Elizabeth J. Rizzo,² Wendy A. Wells,^{2,3} Keith D. Paulsen,^{1,3} Stephen C. Kanick,^{1,4} Brian W. Pogue^{1,3}

¹ Thayer School of Engineering, Dartmouth College, 14 Engineering Drive, Hanover, NH 03755

² Department of Pathology, Geisel School of Medicine, Dartmouth College, 1 Rope Ferry Road, Hanover, NH 03755

³ Norris Cotton Cancer Center, Geisel School of Medicine, Dartmouth College, 1 Rope Ferry Road, Hanover, NH 03755

⁴ Currently at Profusa Inc., 345 Allerton Ave. South San Francisco, CA 94080

S1. Expanded Validation of Histologic Prediction

Additional model validation is provided in Figure S1, in which plots of the H&E segmented versus model predicted stroma, epithelium, and adipose volume fractions are shown for all specimens in rows (a,b,c) respectively. The columns correspond to the individual optical properties. The black dotted lines represent perfect model predictions, and strong linear correlations along the dotted line represent accurate model predictions. For each histologic metrics predicted by each optical property, the Pearson's correlation coefficient and corresponding p-value are calculated and displayed. For all histological metrics predicted by each optical property, all p-values are less than 8e-5, providing strong evidence that the optical property predicted values have a non-zero relationship with the H&E segmented values. The predicted adipose volume fractions appear to have the strongest correlations to the H&E segmented values, with a minimum $r = 0.89$ and $p = 1.1\text{e-}11$. The predicted stroma volume fractions have the next strongest correlations with a minimum $r = 0.79$ and $p = 1.6\text{e-}7$, and the predicted epithelium volume fractions have the least strong correlations with a minimum $r = 0.65$ and $p = 7.7\text{e-}5$. While stroma and adipose exhibited strong monotonic relationships with each optical property, epithelium has a more bell-curved relationship, which may explain the less accurate predictions and motivates further research towards other histologic features. The reduced scattering coefficient was the least accurate predictor for both epithelium and stroma, suggesting this parameter has the least sensitivity distinguishing cellular versus connective glandular tissue. This is expected as reduced scattering is related simply to scatter density rather than a scatter size scale feature, like the scatter slope or phase function parameter, which is sensitive to Rayleigh like scattering of collagen from Mie like scattering of cellular organelles.

S2. Summary of Raw Data: H&E Segmented and Optical Property Predicted Histology

A complete and concise summary of all data points in this study are shown in Figure S2. Box-plots displaying the distributions of specimen mean epithelium, stroma, and adipose

volume fractions are shown in Figure S2 (a,b,c) respectively for H&E segmented data and in Figure S2 (d,e,f) respectively for optical property predicted data. Individual data points represent specimen mean values, and a p-value range is displayed between each pair of distributions. While similar trends in distributions along the top and bottom rows can be qualitatively seen, highlighting the accuracy of the two methods, there are a few subtle differences. The inter-quartile ranges (IQR) for the H&E segmented epithelium volume fractions in Figure S2 (a) are completely distinct between the invasive cancer and fibroglandular, but the corresponding optical property predicted IQRs in Figure S2 (d) are closer together, with epithelium being under-estimated for invasive cancer specimens and over-estimated for fibroglandular specimens. This suggests that future improvements to the epithelium volume fraction prediction model could provide increased diagnostic power to distinguish malignant from benign lesions. Another interesting feature is that the distributions H&E segmented adipose volume fractions for invasive cancer and fibroglandular shown in Figure S2 (c), appear to have extremely similar distributions being the only paired data without statistically significant different means. This suggests that quantifying fat content within breast tissue may not be useful for determining malignant from benign glandular tissue, but rather simply segments glandular tissue from background subcutaneous fat.

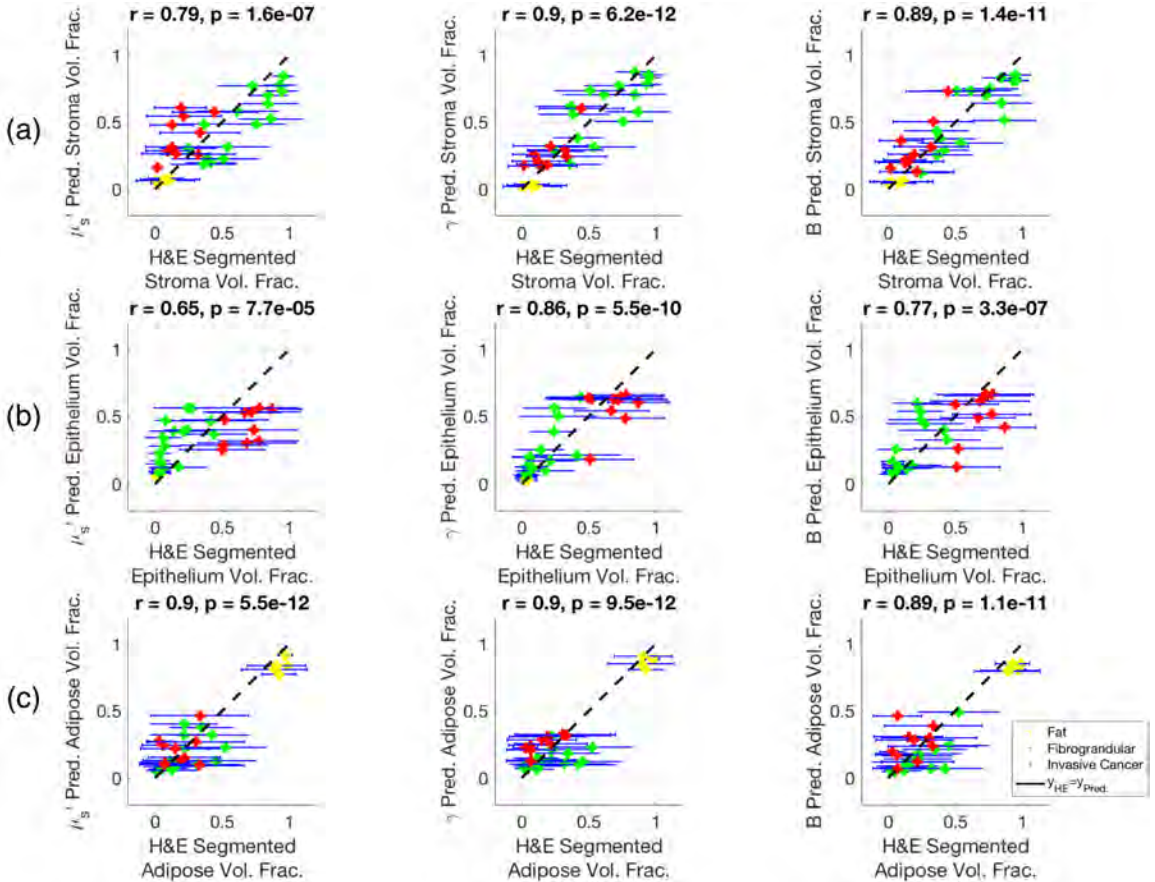


Figure S 1: H&E segmented versus optical property predicted stroma volume fractions in row (a), epithelium volume fractions in row (b), and adipose volume fraction in row (c). The first, second, and third columns correspond to μ'_s , γ , and B predicted volume fractions respectively. Pearson correlation coefficients and corresponding p-values are listed for each relation. Data-points represent mean values for each specimen and the H&E segmented error-bars represent one standard deviation within each specimen.

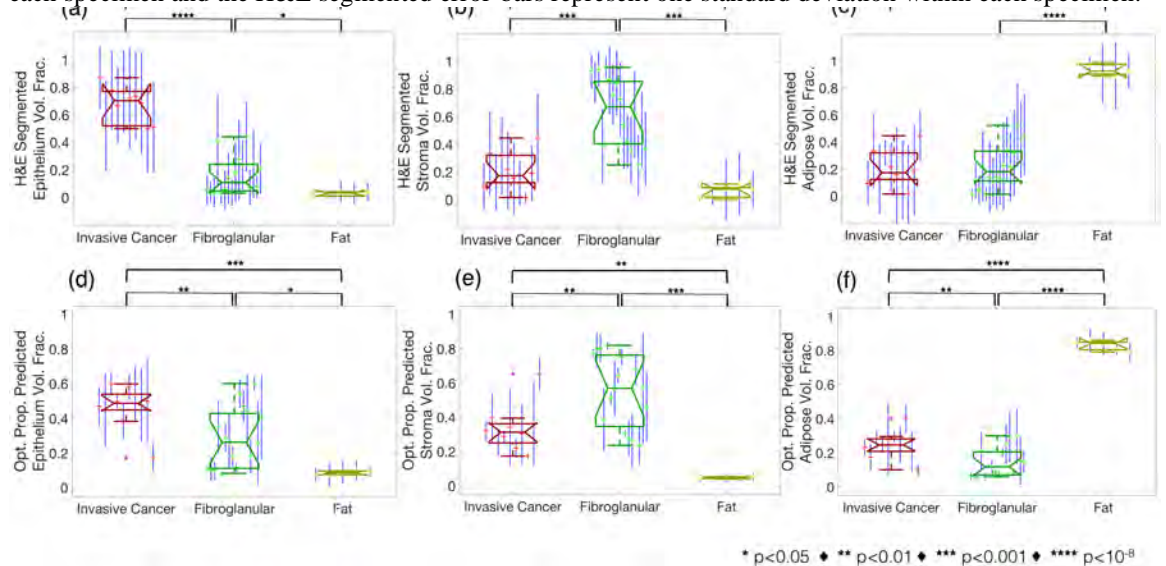


Figure S 2: Boxplots of H&E segmented epithelium, stroma, and adipose volume fractions are shown in (a), (b), and (c) respectively, while corresponding boxplots of optical property predicted epithelium, stroma, and

adipose volume fractions are shown in (d), (e), and (f) respectively. Data points represent means of each specimen, while the H&E segmented error bars represent one standard deviation within each specimen and the optical property predicted error bars represent the standard deviation of the predicted values from each optical property. For each pair of classes, a p-value range is shown calculated from two-sample student's t-tests.

Chapter 7: Calibration and Analysis of a Multimodal Micro-Computed Tomography and Structured Light Imaging System

7.1. Background and Goals

In Chapters 4-6, the development, validation, and clinical evaluation of quantitative light scatter imaging methods utilizing structured illumination were described. This Chapter builds upon this work, with the goal of developing the next generation structured light imaging system, with an increased SNR, finer projection and imaging resolution, and wider spectral range, and then combining this technology with a micro-CT system. Additionally, a methodology for spatial co-registering, overlaying, and simultaneously rendering the 3D micro-CT and 2D structured light imaging needed to be developed and validated. The following manuscript describes the development of a second-generation multispectral SLI system spanning the visible and NIR spectrums spatially co-registered to a micro-CT. Experimentally measured technical performance metrics of the system are reported along with illustrative data from a proof-of-principle freshly resected BCS specimen slice. Since the publication of this manuscript a large cohort of dissected BCS specimens have been imaged, with n=69 specimens having co-registered and annotated histopathology to date, as part of an ongoing clinical study.

7.2. Published Work

The following published manuscripts is reprinted from:

McClatchy DM, Rizzo EJ, Meganck J, Kempner J, Vicory J, Wells WA, Paulsen KD, Pogue BW. Calibration and analysis of a multimodal micro-CT and structured light imaging system for the evaluation of excised breast tissue. Physics in medicine and biology. 2017;62(23):8983-9000. <http://dx.doi.org/10.1088/1361-6560/aa94b6>

This article was published in a journal managed by IOP publishing who have the following copyright transfer agreement policy: *"IOP and/or the copyright owner grants back to authors a number of rights. These include the right to include the Final Published Version of the article in your research thesis or dissertation."*

<https://publishingsupport.iopscience.iop.org/permissions-faqs>

D. M. McClatchy was responsible for all experimental data acquisition, data analysis and quantification, fabrication of phantoms, design of phantom experiments, integration of structured light imaging into the IVIS system, development of the data acquisition routine, and writing the manuscript. E. J. Rizzo was responsible for receiving and dissecting the surgical human breast tissue. J. Meganck and J. Kempner were responsible for the development of the original IVIS Spectrum CT system. J. Vicory developed a module in 3D Slicer to co-register the micro-CT the optical data based upon experiments done by D. M. McClatchy. W. A. Wells was responsible for the creation and analysis of the digitized histology and was in charge of the protocol to image surgical human breast tissue. K. D. Paulsen and B. W. Pogue were responsible for the original conception of the multimodal system, provided advising, authored the NIH grant supporting this research and participated in editing and writing the manuscript.

OPEN ACCESS**IOP Publishing** | Institute of Physics and Engineering in Medicine

Physics in Medicine & Biology

Phys. Med. Biol. **62** (2017) 8983–9000<https://doi.org/10.1088/1361-6560/aa94b6>

Calibration and analysis of a multimodal micro-CT and structured light imaging system for the evaluation of excised breast tissue

David M McClatchy III¹, Elizabeth J Rizzo², Jeff Meganck³,
Josh Kempner³, Jared Vicory⁴, Wendy A Wells^{2,5},
Keith D Paulsen^{1,5} and Brian W Pogue^{1,5}

¹ Thayer School of Engineering, Dartmouth College, 14 Engineering Dr., Hanover, NH 03755, United States of America

² Department of Pathology, Dartmouth Hitchcock Medical Center, 1 Medical Center Dr., Lebanon, NH 03756, United States of America

³ PerkinElmer Inc., 68 Elm St. Hopkinton, MA 01748, United States of America

⁴ Kitware Inc., 101 E Weaver St, Carrboro, NC 27510, United States of America

⁵ Norris Cotton Cancer Center, Dartmouth Hitchcock Medical Center, 1 Medical Center Dr., Lebanon, NH 03756, United States of America

E-mail: David.M.McClatchy.III.TH@Dartmouth.edu and
Brian.W.Pogue@Dartmouth.edu

Received 28 June 2017, revised 9 October 2017

Accepted for publication 19 October 2017

Published 10 November 2017



CrossMark

Abstract

A multimodal micro-computed tomography (CT) and multi-spectral structured light imaging (SLI) system is introduced and systematically analyzed to test its feasibility to aid in margin delineation during breast conserving surgery (BCS). Phantom analysis of the micro-CT yielded a signal-to-noise ratio of 34, a contrast of 1.64, and a minimum detectable resolution of 240 μm for a 1.2 min scan. The SLI system, spanning wavelengths 490 nm to 800 nm and spatial frequencies up to 1.37 mm^{-1} , was evaluated with aqueous tissue simulating phantoms having variations in particle size distribution, scatter density, and blood volume fraction. The reduced scattering coefficient, μ'_s and phase function parameter, γ , were accurately recovered over all wavelengths independent of blood volume fractions from 0% to 4%, assuming a flat sample geometry perpendicular to the imaging plane. The resolution of the optical system was tested with a step phantom, from which the modulation transfer



Original content from this work may be used under the terms of the [Creative Commons Attribution 3.0 licence](#). Any further distribution of this work must maintain attribution to the author(s) and the title of the work, journal citation and DOI.

function was calculated yielding a maximum resolution of 3.78 cycles per mm. The three dimensional spatial co-registration between the CT and optical imaging space was tested and shown to be accurate within 0.7 mm. A freshly resected breast specimen, with lobular carcinoma, fibrocystic disease, and adipose, was imaged with the system. The micro-CT provided visualization of the tumor mass and its spiculations, and SLI yielded superficial quantification of light scattering parameters for the malignant and benign tissue types. These results appear to be the first demonstration of SLI combined with standard medical tomography for imaging excised tumor specimens. While further investigations are needed to determine and test the spectral, spatial, and CT features required to classify tissue, this study demonstrates the ability of multimodal CT/SLI to quantify, visualize, and spatially navigate breast tumor specimens, which could potentially aid in the assessment of tumor margin status during BCS.

Keywords: structured light imaging, micro-computed tomography, breast conserving surgery, spatial frequency domain imaging

(Some figures may appear in colour only in the online journal)

1. Introduction

Breast conserving surgery (BCS) is common treatment for localized breast cancer, being less invasive than a full breast removal and having similar long term survival rates when combined with radiation therapy (Fisher *et al* 2002). However, 20–40% of patients undergoing BCS endure follow-up re-excision procedures due to an incomplete original resection (Pleijhuis *et al* 2009), as determined 1–2 days after the surgery through histopathology. Current standard of care includes intraoperative frozen section pathology and touch-prep cytology. Despite seeming diagnostic value, these procedures are extremely resource intensive to process and analyze just a small subset of the specimen, thus limiting widespread adoption (St John *et al* 2017). With the high incidence of breast cancer, a critical need exists for surgical guidance tools to aid in assessing tumor involvement at the margin of a resected breast specimen during a BCS procedure in order to limit painful and costly re-excision procedures.

A plethora of biomedical devices have been proposed for this task, including electrical impedance spectroscopy (Kaufman *et al* 2016), photoacoustic tomography (Wong *et al* 2017), optical coherence tomography (Erickson-Bhatt *et al* 2015), non-linear microscopy (Tao *et al* 2014), dark field-confocal microscopy (Laughney *et al* 2012), and Raman spectroscopy (Wang *et al* 2016), among others. However, all of these methods either require exogenous dyes, chemically processing or fixing of tissue, or combing through point sampling volumes with a probe. But, a recently demonstrated imaging method, broadly referred to as high spatial frequency structured light imaging (SLI), has shown label free sensitivity to changes in freshly resected breast morphology over a large field of view (FOV) ($\sim 10^{0-2} \text{ cm}^2$) (McClatchy *et al* 2016).

This approach, originally termed spatial frequency domain imaging (SF DI), was first demonstrated by Cuccia *et al* to spatially map diffuse optical properties (Cuccia *et al* 2005, 2009) and later applied to optical tomography (Bélanger *et al* 2010), spectroscopic imaging (Gioux *et al* 2011, Laughney *et al* 2013), and fluorescence imaging (Sibai *et al* 2015). The key advantage of structured illumination is the ability to tune depth sensitivity with the spatial modulation frequency. While the contrast at low spatial frequencies is dictated by absorption features

(presence of blood, fat) and diffuse scattering (density of tissue), the contrast of sub-diffusive high spatial frequency images is dictated by both scattering intensity and the angular distribution of scattering events, or phase function, as photon propagation is constrained to superficial volumes with minimal volumetric averaging over tortuous photon path-lengths (Bodenschatz *et al* 2014, Krishnaswamy *et al* 2014). The phase function arises from the underlying physical properties of tissue ultrastructure (Bartek *et al* 2006, Rogers *et al* 2009, Radosevich *et al* 2015). Recent studies have used sub-diffusive structured light imaging to quantify angular scattering distributions through the phase function parameter γ , which is related to the size-scale distribution of scattering features (Kanick *et al* 2014, Bodenschatz *et al* 2015). This phase function parameter, along with the reduced scattering coefficient μ'_s , was used to cluster benign and malignant breast tissue pathologies in freshly resected human breast specimens (McClatchy *et al* 2016) and morphologies within murine tumors (McClatchy *et al* 2017), as different tissue morphologies with unique densities and size-scale fluctuations manifest unique light scattering properties.

Although SLI can generate wide-field images of the specimen surface, it is unable to provide high resolution (<1 mm) depth contrast or a tomographic reconstruction through the specimen volume. Micro-computed tomography (CT) is a promising technique for intraoperative visualization of breast specimens, which can be manufactured in a shelf shielded, mobile form factor. By reconstructing x-ray absorption in three dimensions (3D) thereby resolving overlaying features, micro-CT increases low contrast resolution relative x-ray projection imaging, and thus, yields a more accurate delineation of the tumor core extent and proximity to the margin in surgical breast specimens (Tang *et al* 2013, 2016). Furthermore, micro-CT and SLI can be symbiotic as the former inherently loses image quality at the tissue-air interface, as the latter becomes the most sensitive.

In this manuscript, a novel multimodal imaging system, utilizing volumetric micro-CT and superficial SLI, is introduced and analyzed for future application in evaluation of excised breast tissues. Image quality and accuracy of both imaging modalities are assessed, as well as the co-registration of the two image systems. Accuracy of the optical property inversion method is validated on comprehensive sets of flat phantoms perpendicular to the imaging plane. As a proof-of-principle, an *ex-vivo* breast specimen is imaged during gross examination, yielding visualization of the tumor extent in 3D with co-registered structured light images and scatter parameter maps. Further work is needed to develop classification algorithms, at which point the clinical value of this multi-modality system can be tested.

2. Methods

2.1. Multimodal micro-CT and multi-spectral SLI system

The multimodal SLI/micro-CT system was created from a modified and re-purposed IVIS SpectrumCT, which is a pre-clinical bioluminescence imaging and micro-CT system (PerkinElmer Inc., Hopkinton, MA). The SLI addition consisted of the native IVIS charged coupled device (CCD) camera (Andor iKon, Andor Technologies Ltd., Belfast, UK) and a retrofitted digital light projector (DLP) (CEL5500 Fiber, Digital Light Innovations Inc., Austin, TX) with a 3.6X telephoto lens. Due to size constraints within the imaging cabinet, the DLP is rotated 22° with respect to the CCD, as shown in the schematic of the SLI system depicted in figure 1(a). Light was delivered through an optical fiber to the DLP, was focused onto the digital mirror device (DMD) creating the structured light patterns, and was then focused on the specimen. The DLP was connected to an external virtual monitor which controls the illumination pattern at a frame rate of 60 Hz. The illumination source was a supercontinuum

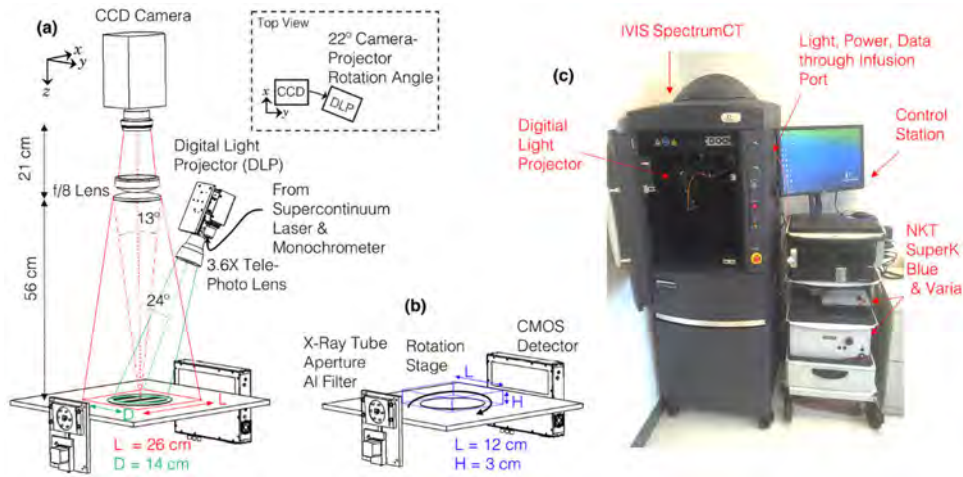


Figure 1. Schematics of the major components of the SLI and micro-CT systems are labeled in (a) and (b), respectively. A photograph of the system located in the gross specimen processing lab is shown in (c). The system is self-shielded and housed in a mobile form factor as shown in (c). There is a maximum radiation exposure of $\leq 0.01 \text{ mR h}^{-1}$ above background during operation.

laser (SuperK Blue, NKT Photonics, Denmark) with a tunable line filter (SuperK Varia, NKT Photonics, Denmark) to select the wavelength band. At the shelf stage height used for imaging, the diameter of the circular illumination field of the DLP was $\sim 14 \text{ cm}$ with a projection resolution of $168 \mu\text{m}$, while the imaging field was $\sim 26 \text{ cm} \times \sim 26 \text{ cm}$ with a sampling resolution of $126 \mu\text{m}$. Only a subset of the CCD corresponding to $\sim 13 \text{ cm} \times \sim 13 \text{ cm}$ covering the illumination field was read out to minimize acquisition time. The self-shielded micro-CT of the PerkinElmer system was a cone-beam CT in a ‘pancake’ geometry, with the specimen rotating through 360° on a turntable as shown in figure 1(b).

2.2. Data acquisition and processing

For the multimodal acquisition, micro-CT and SLI data were sequentially acquired with separate software packages. The specimen was placed on the rotation stage shown in figure 1(b), and the micro-CT scan was natively acquired and reconstructed through the PerkinElmer Living Image software. A 1 mA current was used and the tube peak kilovoltage (kVp) and exposure time were set to either 25 kVp and 200 ms/exposure or 50 kVp and 100 ms/exposure, yielding 2.4 min and 1.2 min total scan times for the low and high energy settings, respectively. The filtered back-projection reconstruction time was $\sim 2 \text{ min}$ for a reconstructed FOV of $12 \text{ cm} \times 12 \text{ cm} \times 3 \text{ cm}$ with 150 micron cubic voxels.

After the micro-CT scan was completed, an SLI acquisition occurred with a custom LabView routine (National Instruments, Inc., Austin, TX). For all scans in this study, seven wavelengths were acquired, $\lambda = [490, 550, 600, 650, 700, 750, 800] \text{ nm}$, with a 15 nm bandwidth, and at each wavelength, 18 one-dimensional sinusoidal projections were recorded at 6 spatial frequencies, $f_x = [0.05, 0.15, 0.61, 0.78, 0.92, 1.37] \text{ mm}^{-1}$ with 3 phase offsets, $\phi = [0, 120, 240]^\circ$. Although previous research has shown sensitivity of the rotation angle of the modulation pattern to oriented features (DAndrea *et al* 2010, Konecky *et al* 2011), in this protocol only one rotation angle was considered to minimize the time of a SLI scan, which was $\sim 8 \text{ min}$ for both acquisition and saving. After specimen scanning, an 8 in. \times 8 in. silicone

TiO₂ phantom and a 10 in. × 10 in. 99% reflectance standard (Labsphere, Inc., Sutton, NH) were imaged for calibration.

SLI data processing occurred off-line with custom scripts in MATLAB (2016a). Images were demodulated by $I_d = \frac{\sqrt{2}}{3} \sqrt{(I_{\phi 1} - I_{\phi 2})^2 + (I_{\phi 1} - I_{\phi 3})^2 + (I_{\phi 2} - I_{\phi 3})^2}$, where $I_{\phi 1}, I_{\phi 2}, I_{\phi 3}$ are the three phase offsets for a given spatial frequency and wavelength. Due to minor fluctuations in laser power, phase images were scaled so that each had the same mean over the illuminated area to minimize demodulation artifacts. Also, a median filter with 3x3 pixel kernel was applied to demodulated images to remove noise and any specular reflections arising from minor fluctuations of the tissue surface profile. These specular reflections were mitigated by flattening the tissue surface between two transparent acrylic plates and also using an oblique projection scheme. Optical property maps were calculated with a sub-diffusive model inversion method described in a previous manuscript (Kanick *et al* 2012a, McClatchy *et al* 2016). The sub-diffusive model was semi-empirically derived from a series of forward Monte-Carlo simulations utilizing a modified Henyey–Greenstein phase function (Kanick *et al* 2012b). To summarize briefly, demodulated images were calibrated by the TiO₂ phantom as $R_{d_{\text{sample}}}(x, y, f_x, \lambda) = R_{d_{\text{TiO}_2}}(x, y, f_x, \lambda) \frac{I_{d_{\text{sample}}}(x, y, f_x, \lambda)}{I_{d_{\text{TiO}_2}}(x, y, f_x, \lambda)}$, where $R_{d_{\text{TiO}_2}}(x, y, f_x, \lambda)$ are sub-diffusive model-predicted reflectance values for the calibration phantom. A non-linear least squares routine determined optical properties by minimizing the difference between measured calibrated reflectance and model-based predicted reflectance over all spatial frequencies and wavelengths. Scattering was assumed to follow a power law such that $\mu'_s = A(\frac{\lambda}{800 \text{ nm}})^{-B}$, where A, B are the scattering amplitude and power, respectively. The phase function parameter γ was a free fit variable at each wavelength. For tissue specimens, the absorption coefficient, μ_a , was assumed to be a linear sum of oxygenated hemoglobin, deoxygenated hemoglobin, and β-Carotene with basis spectra obtained from the Oregon Laser Medical Center (OLMC) spectra database (<http://omlc.ogi.edu/spectra/index.html> Accessed May 2017).

Color images were also reconstructed from the multi-spectral SLI data. For the 5 wavelengths in the visible spectrum, $\lambda = [490, 550, 600, 650, 700]$ nm, SLI images were transformed into a RGB color-space using the 1931 International Commission on Illumination (CIE) tristimulus values (Smith and Guild 1931). For each illumination band, the x, y, z chromaticity values were calculated and normalized, and multiplied by the demodulated intensity of the specimen and the 99% reflectance standard for each respective wavelength band. The resulting x, y, z image stack was converted to RGB space with the value of the 99% reflectance standard set to be the white point.

2.3. 3D–2D co-registration and visualization

Accurate calibration and co-registration of the 2D image coordinates to the 3D CT coordinates are needed for a multimodal visualization. Camera calibration with the optical system was performed to account for lens and perspective distortion. This was done using the Open Source Computer Vision Library (OpenCV) Camera Calibration and 3D Reconstruction Software (Open Source Computer Vision Library 2016), with which the intrinsic camera matrix and radial and tangential lens distortion coefficients were calculated. Images acquired were corrected using the *undistortImage* function in the MATLAB Computer Vision System Toolbox (version 2016a). The transformation matrix from the optical image coordinates to the CT coordinates in the XY plane was calculated using procrustes alignment method. Because the optical and micro-CT systems were rigidly fixed, these calibrations were performed once, and were used in all imaging experiments reported here.

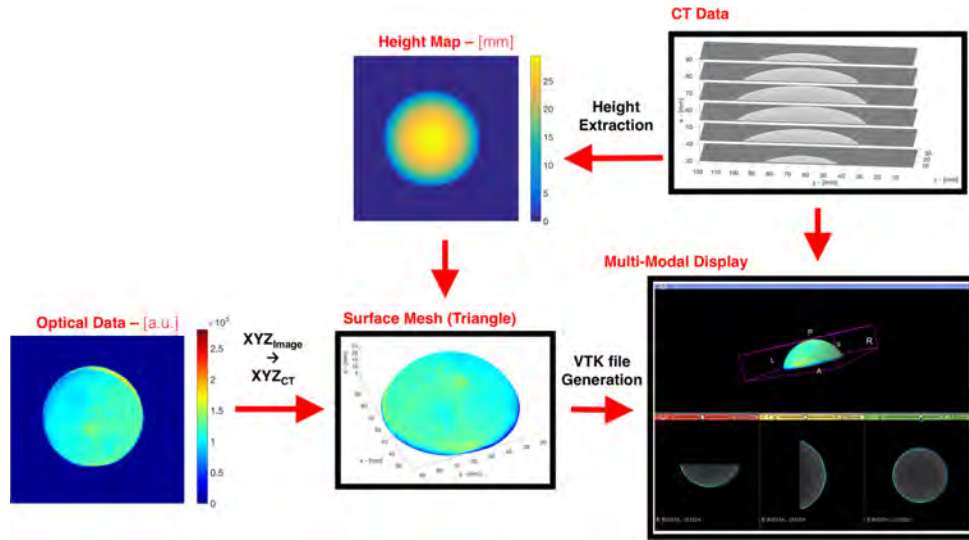


Figure 2. Flow diagram of the multimodal data processing and work-flow is shown for a hemispherical phantom. First, optical and CT data are sequentially acquired with the SLI/CT system. A height map is extracted from the CT and the optical data undergoes a coordinate transformation from image coordinates to CT coordinates, from which a 3D surface mesh is created as a VTK file. Both the VTK file and CT DICOM can be simultaneously rendered in the open source Slicer environment, shown in the bottom right view.

With the optical system calibrated, a module was created to co-register and display an acquired CT/optical scan automatically which was integrated into NIRFAST Slicer software (www.dartmouth.edu/~nir/nirfast/) (Dehghani *et al* 2009, Jermyn *et al* 2013). A diagram of the data-processing and work-flow is shown in figure 2 for a hemispherical gelatin phantom. The height map was extracted from the CT volume by determining the most superficial CT voxel above a manual threshold, for each x, y vector of voxels. Next, the optical image was undistorted and then co-registered to CT coordinates through the linear transformation. Finally, for each point on the height map, the scalar value of the nearest optical data point was assigned. With this 3D scalar data, a triangular surface mesh was created in the Visualization Toolkit (VTK) file format, which was then simultaneously rendered with the CT volume in the Slicer environment (Taka and Srinivasan 2011).

2.4. Micro-CT, optical, and co-registration phantoms

To quantify image quality of the micro-CT system, a mammography target phantom (Mammo 156 Phantom, Gammex Inc., Middleton, WI) was utilized. This mammography accreditation phantom is composed of acrylic with a wax insert containing various fibers, hemispherical masses, and specs. It has been designed to simulate a compressed breast comprised of 50% glandular and 50% adipose tissue and size of 10.2 cm \times 10.8 cm \times 4.2 cm. While the phantom was larger than the micro-CT FOV, surgical specimens are smaller than the entire breast and contain less background tissue; thus, only the wax insert was imaged. Furthermore, if the entire phantom were imaged, partial volume artifacts would have greatly degraded image quality, with a large portion of phantom having been outside of the x-ray beam.

The spatial resolution of the SLI system was analyzed with a step phantom. A sheet of highly absorbing black paper was placed on a 99% reflectance standard creating a sharp edge between a highly reflective and nearly non-reflective surface. The spatial resolution was analyzed by characterizing the response of the imaging system across the edge.

To validate the sensitivity of the SLI system and accuracy of the optical property inversion method, two sets of tissue simulating aqueous phantoms were imaged. In the first set of phantoms, the size-scale distributions of scatterers were varied by selectively titrating various concentrations of Intralipid (IL) and a solution of 140 nm polystyrene spheres. The optical properties of the sphere solution was calculated with Mie theory (Bohren and Huffman 2008), while the optical properties of IL were taken from a previous publication (Michels *et al* 2008), and a discrete particle model was used to calculate the optical properties of different ratios of each solution (Gélibart *et al* 1996). The various solutions contained $\gamma \in [0.99 - 2.00]$ and μ'_s of each phantom was matched at $\lambda = 650$ nm. In the second set of phantoms, absorption and scattering were varied independently with various concentrations of IL and whole porcine blood (Lampire Biologicals, Pipersville, PA). The hemoglobin concentration of the blood was measured at 13.4 g dl^{-1} , and to maintain neutral pH, phosphate buffered was used for dilution. Solutions were made with $[0.5, 1, 2]\%$ IL and $[0, 0.5, 1, 2, 4]\%$ blood volume fractions (BVF), yielding phantoms with $\frac{\mu'_s}{\mu_a} \in [0.8 - 10^5]$ over the acquired wavelength range assuming fully oxygenated blood. The influence of blood on the scattering properties were considered to be negligible compared the influence of IL, based upon previous studies measuring the optical properties of blood (Friebel *et al* 2006, Bosschaart *et al* 2014). Each phantom set was imaged in a 24-well plate having black, non-transparent walls and 2.5 ml of each solution per well.

Accurate co-registration between the micro-CT and optical imaging system was experimentally validated and quantified with a custom-made phantom containing radio-opaque and optically bright markers. The markers were 1/8 in. acetal pins, the top surfaces of which were coated in commercial liquid paper to increase optical reflection. Two orthogonal lines of 7 markers with approximately 1 cm spacing were set on optically dark paper creating a cross-hair pattern. The co-registration accuracy was measured as the co-localization of the marker positions in the CT and SLI datasets.

2.5. Imaging a surgically resected breast specimen

To demonstrate feasibility of the system to acquire and display a multimodal clinical dataset, a freshly resected breast tissue specimen was scanned. The imaging protocol did not interfere with standard of care posing minimal risk to the patient, and was approved by the Dartmouth Hitchcock Medical Center (DHMC) Internal Review Board (IRB) and the Committee for the Protection of Human Subjects (CPHS). After a breast surgery specimen was received by the Department of Pathology, it was subsequently ‘bread loafed’ and grossly assessed per standard of care. Cut tissue specimens with superficial lesions were imaged with system, which was located in the surgical specimen lab. To maintain the orientation of the specimen through imaging and also provide a flat imaging surface, it was placed in a customized holder, consisting of two 1/8 in. thick, optically-clear acrylic plates, between which the specimen was secured with elastic bands. The silicone calibration phantom, having a refractive index similar to tissue (Ayers *et al* 2008), was likewise imaged with the acrylic plate. Immediately after imaging, the specimen was cut into cassette sized sections (~ 1 cm), photographed, and underwent standard histological processing of dehydration, fixation, wax embedding, sectioning and hematoxylin and eosin (H&E) staining. Resulting histology was evaluated by a trained pathologist (W.A.W) and included in the patient’s report.

Table 1. Summary of micro-CT performance metrics and size of minimum detectable objects (MDO) in the mammography target phantom.

	SNR	Contrast	Exposure time (s)	Fiber _{MDO} (mm diameter)	Specks _{MDO} (mm diameter)	Masses _{MDO} (mm thick)
25 kVp	23.8	1.81	144	0.54	0.24	0.25
50 kVp	34.0	1.64	72	0.54	0.24	0.25

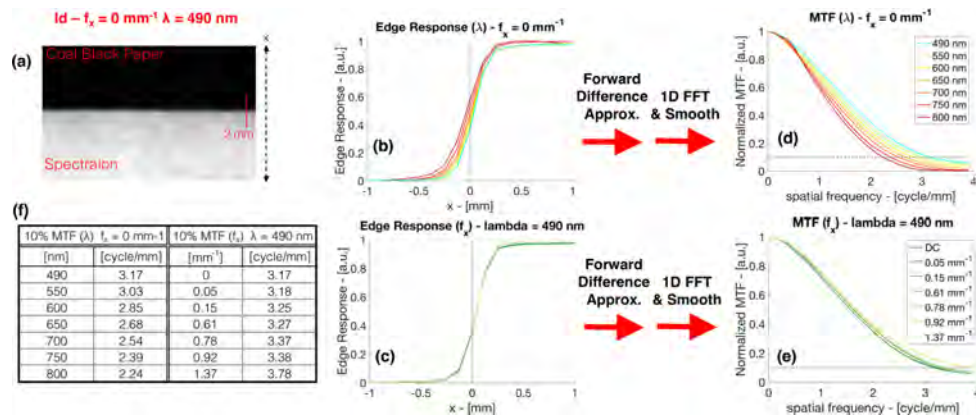


Figure 3. (a) Diffuse image of the step phantom at $\lambda = 490 \text{ nm}$. Edge response functions (ERF) are shown in (b) for each sampled wavelength at $f_x = 0 \text{ mm}^{-1}$ and (c) for each sampled spatial frequency at $\lambda = 490 \text{ nm}$. Corresponding modulated transfer functions (MTF) appear in (d) and (e), as the Fourier Transform of the derivative of the ERF. In (f), the limiting cycles per mm at 10% of the max MTF are tabulated.

3. Results

3.1. Micro-CT analysis of mammography target phantom

The micro-CT target phantom analysis resulted in the same minimum detectable objects (MDO) for the low and high energy scans, with only the smallest fiber and smallest speck cluster not clearly visible. This yielded a limiting resolution of $240 \mu\text{m}$ for a high-contrast spherical object. To assess image quality of the micro-CT, the signal-to-noise ratio (SNR) and Contrast were evaluated for each kVp scan. A single slice through the largest mass was analyzed, with the mean, μ , and standard deviation, σ , of the linear attenuation coefficient calculated in a region of interest (ROI) in both the largest mass and in the abutting background. SNR was calculated as $\text{SNR} = \mu_{\text{mass}}/\sigma_{\text{background}}$ and Contrast = $\mu_{\text{mass}}/\mu_{\text{background}}$. The 50 kVp scan yielded an SNR of 34 for a 72 sec acquisition, while the 25 kVp scan yielded an SNR of only 23.8, despite compensating for higher attenuation by doubling the exposure time. The 25 kVp did have a slightly higher Contrast of 1.81, compared to 1.64 for the 50 kVp scan. A tabulated summary of the metrics quantifying the micro-CT performance is shown in table 1. Because of the shorter scan time, superior SNR, and similar Contrast, subsequent micro-CT scans displayed this point forward were acquired with the 50 kVp, 100 ms/exposure scan settings.

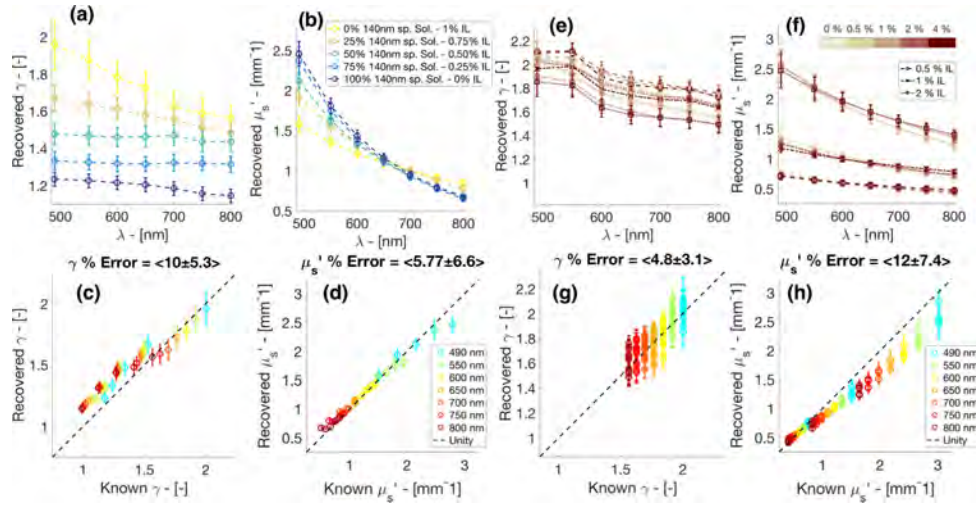


Figure 4. A summary of optical property recovery data is shown. In (a) and (b), respectively, the recovered phase function parameter, γ , and recovered reduced scattering coefficient, μ'_s , appear as functions of wavelength for the various concentrations of Intralipid (IL) and a solution of 140 nm spheres. Clear stratification between each particle size-scale distribution occurs in the magnitude of γ and the spectral slope of μ'_s . In (c) and (d), known versus recovered plots are shown for γ and μ'_s , respectively, over all wavelengths for the various particle size-scale distribution. The recovered values of γ and μ'_s versus wavelength are presented in (e) and (f) respectively, for the various blood volume fractions (BVF) and IL concentrations. In (g) and (h), known versus recovered plots are displayed for γ and μ'_s , respectively, over all wavelengths for the various BVF and IL concentrations. Error-bars represent one standard deviation within the measured region of interest (ROI) for each phantom well.

3.2. Multi-spectral structured light imaging analysis

The spatial resolution of the demodulated intensity as a function of spatial frequency and wavelength was tested by analyzing the response of a step phantom. In figure 3(a), a captured image of the step phantom is shown for $f_x = 0 \text{ mm}^{-1}$ and $\lambda = 490 \text{ nm}$. The direction of the illumination frequency is at a 68° angle with the step, while the y-axis of the CCD is parallel, so that the captured image can be averaged along the step. Measured edge responses across the step are shown for each imaged wavelength at $f_x = 0 \text{ mm}^{-1}$ in figure 3(b). A forward difference approximation and subsequently a fast Fourier transform (FFT) was applied to each edge response to calculate the corresponding modulation transfer functions (MTF), shown in figure 3(c). Each MTF was normalized by its maximum value and smoothed with a 5 pixel moving average filter. Edge responses and MTFs are likewise shown in figures 3(d) and (e) respectively, for each imaged spatial frequency at $\lambda = 490 \text{ nm}$. The limiting spatial resolution is quantified as the point where the MTF reaches 10% of its maximum value. These values are tabulated for the variation in wavelength and spatial frequency in figure 3(f). For the case of diffuse illumination, a clear trend of increasing spatial resolution from 2.24 cycles mm^{-1} to 3.17 cycles mm^{-1} , occurs as wavelength decreases from 800 nm to 490 nm. Although the reflectance standard is near completely reflective, this wavelength dependent behavior is still expected as the lower edge of the phantom will have a higher scattering cross section with shorter wavelength light, and therefore, a shorter transport length resulting in a sharper response. Also, as the spatial illumination frequency increases, a slight increase is

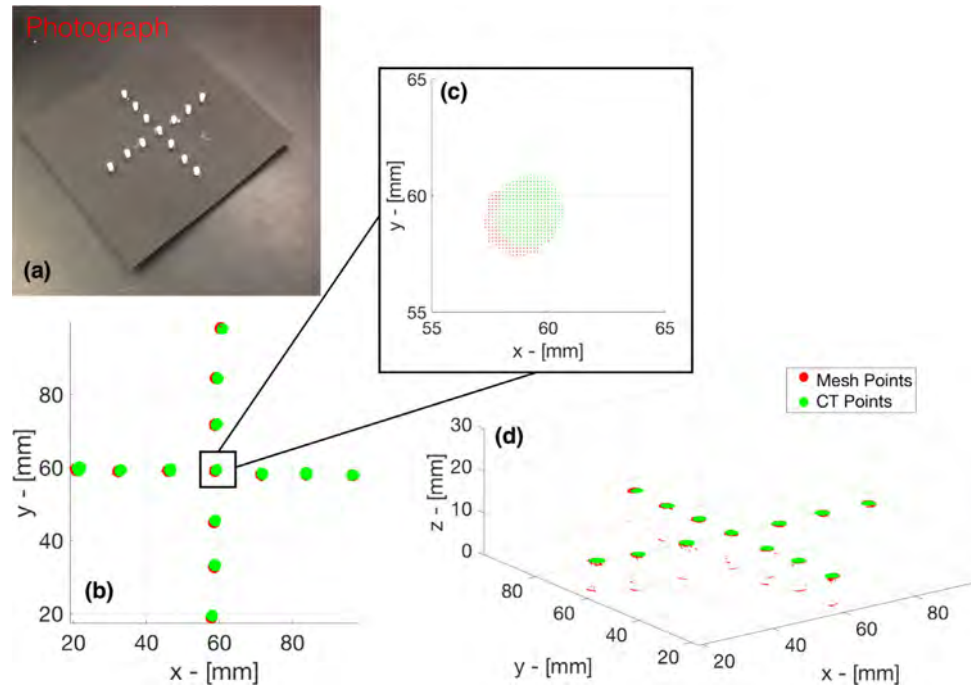


Figure 5. In (a), the photograph of CT/Optical co-registration phantom is shown. In (b), the 2D XY plane view of the segmented CT and co-registered optical mesh points is presented, with a zoomed-in view of the center marker in (c). In (d), the same segmented CT and co-registered optical pixels are displayed in 3D space.

found in spatial resolution, which is also expected as increasing the spatial illumination frequency constrains the light transport to become more superficial and localized, also resulting in a sharper response. Results revealed a maximum spatial resolution of $3.78 \text{ cycles mm}^{-1}$ at $\lambda = 490 \text{ nm}$ and $f_x = 1.37 \text{ mm}^{-1}$.

The sensitivity and accuracy of the SLI system was evaluated with aqueous tissue simulating phantoms, mimicking the expected contrast and background absorption in human breast tissue. Two sets of phantoms were characterized: a first set with variations in particle size scale distribution, and a second set with variations in BVF and IL concentration to alter both absorption and scattering, independently. The recovered values of γ and μ'_s for each particle size scale distribution are shown in figures 4(a) and (b), respectively. The magnitude of γ was unique over all wavelengths for each particle size scale distribution, with γ exhibiting a linear relationship with wavelength. The magnitude of γ decreased with the increasing contribution of the more isotropic 140 nm spheres compared to the more forward scattering IL. Likewise, the spectral slope of μ'_s also stratified for each particle size scale distribution, with an increasing slope for greater contributions of the 140 nm spheres and a flatter slope for IL. The greatest dynamic range for both γ and μ'_s to changes in particle size scale distribution appear to be towards the shorter wavelengths of light. The known versus recovered values of γ and μ'_s for each particle size distribution at each measured wavelength are plotted in figures 4(c) and (d) respectively. Error was calculated as $\text{Error} = 100 \times \frac{|\text{recovered-known}|}{\text{known}}$, and the mean and standard deviation were computed over all phantoms at each wavelengths, yielding $\langle 10 \pm 5.4 \rangle \%$ for γ and $\langle 5.77 \pm 6.6 \rangle \%$ for μ'_s . The recovered values of γ and μ'_s for variations in IL concentration and BVF are shown in figures 4(e) and (f) respectively. As expected, the recovered γ spectra

Table 2. Optical micro-CT co-registration accuracy. Mean distances between centroids of phantoms for CT points and Image mesh points with varying phantom locations.

	Center phantom ($n = 1$)	1 cm from center ($n = 4$)	2 cm from center ($n = 4$)	3 cm from center ($n = 4$)	Total ($n = 13$)
$\Delta C = C_{\text{CT}} - C_{\text{Mesh}} $ (mm)	0.7	0.6 ± 0.2	0.6 ± 0.3	0.6 ± 0.4	0.6 ± 0.3

cluster together, independent of both IL concentration and background absorption from BVF. Additionally, the magnitude of the μ'_s values stratify by the various IL concentrations, independent of the BVF. Plots of the corresponding known versus recovered values are presented in figures 4(c) and (d) for γ and μ'_s , respectively. The mean error in recovering γ in the presence of various scattering and absorption concentrations was $\langle 4.8 \pm 3.1 \rangle \%$, while the mean error for μ'_s was $\langle 12 \pm 7.4 \rangle \%$. These phantom studies experimentally validated the ability of the multi-spectral SLI system to accurately recover and quantify sub-diffusive scatter parameters accurately over a broad range of optical properties, which can be expected for surgical tissues in the visible to NIR wavelength bands.

3.3. Optical and micro-CT co-registration accuracy

Co-registration accuracy between the micro-CT imaging space and optical imaging spaces was evaluated and quantified. A phantom with radio-opaque pegs having an optically bright coating, shown in figure 5(a), was measured with the multimodal system, yielding a micro-CT scan and a co-registered 3D surface mesh of SLI reflectance data. The micro-CT and SLI data were manually thresholded to segment the surface pegs. A top down 2D view of the segmented CT and optical mesh points is presented in figure 5(b). A zoomed in view of the center peg is shown in figure 5(c), where individual locations are shown with an apparent offset of a few points, each being $150 \mu\text{m}$ apart. In figure 5(d), the segmented CT and optical mesh points are plotted in 3D, showing the minor error in co-registration resulting in slight misalignment. The co-registration accuracy is quantified for each peg as the Euclidean distance in x, y, z between the centroids of the CT surface and the optical mesh surface. These results are tabulated in table 2, and shown a mean co-registration accuracy of $620 \mu\text{m}$ with little variation across the coordinate space. Furthermore, this implies that in future studies, optical and CT data of breast cancer specimens can be spatially interpreted together within a range $620 \mu\text{m}$.

3.4. Visualization of a freshly resected breast tissue specimen

Illustrative multimodal data of a freshly resected breast specimen are shown in figure 6. A photograph of the cut specimen appears in figure 6(a) with tessellated H&E stained histology slides displayed in figure 6(b). Evaluation of the histology from a trained pathologist (W.A.W) revealed a 2.5 cm lesion of invasive and *in situ* lobular carcinoma with adjacent, benign fibro-cystic disease (FCD) surround by background adipose. While the background adipose exhibits a shade of yellow in the photograph, the invasive versus benign areas both appeared in shades of white. The demodulated intensity is shown at $f_x = [0, 1.37] \text{ mm}^{-1}$ for $\lambda = 490 \text{ nm}$ in figures 6(c) and (d) respectively and for $\lambda = 600 \text{ nm}$ in figures 6(e) and (f), respectively. For the diffuse images at $f_x = 0 \text{ mm}^{-1}$, significantly more contrast occurred between the glandular tissue and adipose for $\lambda = 490 \text{ nm}$ compared to the longer wavelengths, due to absorption from β -Carotene. However, the superficial high-spatial frequency images at $f_x = 1.37 \text{ mm}^{-1}$, revealed similar spatial features for both the shorter and longer wavelengths. Contrast was

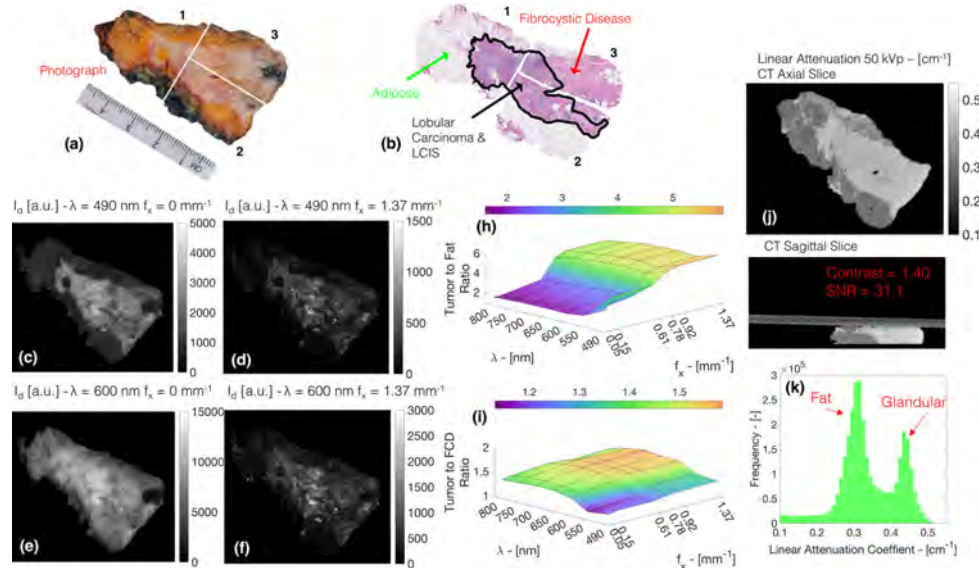


Figure 6. In (a), a photograph of the resected breast specimen is shown, with white lines indicating where the specimen was cut for histological processing. In (b), tessellated H&E sections of the specimen appear with a malignant region out-lined in black. Demodulated images of $f_x = [0, 1.37] \text{ mm}^{-1}$ for $\lambda = [490, 600] \text{ nm}$ are presented in ((c)–(f)), with the tissue specimen segmented from the background. For the areas of tumor, FCD, and adipose marked by arrows in (b), surfaces of ratios in the demodulated intensity between tumor to fat and tumor to FCD over spatial frequency and wavelength are shown in (h) and (i), respectively. Axial and sagittal cross sections of the linear attenuation coefficient are displayed in (j) for a 50 kVp micro-CT scan of the specimen. A histogram of the reconstructed linear attenuation coefficient values of the breast tissue specimen is shown in (k), where an apparent bimodal distribution is observed with separate fat and glandular peaks.

further quantified over all wavelengths and spatial frequencies. Surfaces of the ratio of the demodulated intensity between tumor and adipose and between tumor and FCD are shown in figures 6(h) and (i), respectively, for the areas marked by arrows in figure 6(b). Tumor to adipose had much greater maximum contrast of 5.6 than tumor to FCD, which had a maximum contrast of 1.6, because of the greater dissimilarity in tissue ultrastructure. For both ratios, contrast increased with spatial frequency with the maximum contrast occurring at $f_x = 1.37 \text{ mm}^{-1}$, but at $\lambda = 490 \text{ nm}$ for tumor to adipose and at $\lambda = 700 \text{ nm}$ for tumor to FCD. In figure 6(j), axial and sagittal slices of the specimen are shown for the 50 kVp micro-CT scan. In the axial slice, the tumor mass and spiculations were visible. In the sagittal slice, micro-calcifications appeared as bright specks and the acrylic specimen holder was also visible. A histogram showing the distribution of the measured linear attenuation coefficients of the tissue is shown in figure 6(k). Fat and glandular peaks were centered at 0.31 cm^{-1} and 0.435 cm^{-1} respectively, and yielded a SNR of 30.1 and Contrast of 1.40. While contrast was clearly visible between the glandular tissue and background, negligible contrast occurred within the glandular region between areas of tumor and FCD, unlike the SLI data.

Processed optical maps from the raw SLI reflectance data are presented in figure 7. A color image reconstructed from the visible diffuse images at $f_x = 0 \text{ mm}^{-1}$ is shown in figure 7(a) with green, black, and red boxes outlining regions of adipose, lobular carcinoma, and FCD, respectively. In figure 7(b), another color image reconstructed from visible demodulated data

is displayed, but for a high spatial frequency of $f_x = 1.37 \text{ mm}^{-1}$ highlighting the superficial, finer spatial features. In figure 7(c), a map of the scatter slope of μ'_s is shown, which represents the spectral change in scattering intensity and is related to particle size distribution of scatters. The mean values of μ'_s versus wavelength are plotted in figure 7(d) for the three regions, with error bars representing the standard deviation within each region. The elevated scatter slope of FCD ((1.94 ± 0.21)) compared to that of carcinoma ((1.33 ± 0.35)) can be seen, as well as the characteristically flat scatter slope and low scatter magnitude of adipose ((0.53 ± 0.21)). Mean values of γ versus wavelength are plotted in figure 7(e), showing decreased values for FCD and carcinoma with little wavelength variation and increased values for adipose with an apparent negative linear relationship with wavelength ($r = -0.992$). Spatial features of the optical properties can be observed in the various optical property maps. In figures 7(f) and (g), μ'_s maps and in figures 7(h) and (i) corresponding γ maps are shown for $\lambda = 490 \text{ nm}$ and 600 nm , respectively. For both μ'_s and γ , maximum contrast between the tumor and adipose is achieved at $\lambda = 490 \text{ nm}$, but with minimal contrast between tumor and FCD. At $\lambda = 600 \text{ nm}$, contrast between tumor and FCD increased for μ'_s and γ , while contrast between tumor and adipose decreased.

Superficial SLI and volumetric micro-CT data were simultaneously rendered in the open-source Slicer environment (Fedorov *et al* 2012). A screen-shot of the multimodal display appears in figure 8. A false colored surface of $\mu'_s(490 \text{ nm})$ is shown in figure 8(a), exhibiting spatial detail in optical scattering intensity. In figure 8(b), the μ'_s surface is shown co-registered to a maximum intensity projection of the micro-CT volume, which was processed with the Slicer Volume Rendering module to create a segmented semi-transparent object. Fat was made virtually transparent while the tumor mass and spiculations arms were more opaque. An apparent cluster of micro-calcifications, marked by a yellow star, appear as completely non-transparent, having a markedly high radio-density. The sagittal and coronal slices through the co-registered optical surface and micro-CT volume are displayed in figures 8(c) and (d), respectively. Standard navigation tools in the Slicer environment enabled annotation between the different views and planes. In figure 8(e), the diffuse color image is also shown to guide spatial recognition of features in the multimodal data set to how the specimen appears to the naked eye. In figure 8(f), axial micro-CT slices are shown in 0.9 mm steps below the imaging surfacing illustrating the overlapping structural features of the tissue. The micro-calcification cluster is shown to be 1.8 mm below surface and is marked with a yellow star. A corresponding H&E section taken at 1.8 mm depth likewise shows a cluster of type-II micro-calcifications in figure 8(g).

4. Discussion

Results from both phantom experiments and clinical tissue demonstrated the ability of the micro-CT/SLI system to quantify scattering maps and co-register them with a micro-CT image volume. Target phantom analysis and specimen imaging with the micro-CT demonstrated $\text{SNR} > 30$, and sub-millimeter resolution. Micro-calcifications were detectable during specimen imaging, and while the presence of calcifications is not considered diagnostically relevant, microscopic pleomorphic calcifications can be related to malignancy status (Tse *et al* 2008). Resolution tests of SLI also yielded sub-millimeter resolution, and tissue simulating phantoms demonstrated accuracy in the model inversion well beyond diffusion limited transport. While a previous study has accurately quantified optical properties in aqueous phantoms over a range of $\gamma \in [1.3 - 1.7]$ and $\frac{\mu'_s}{\mu_a}$ as low as 5.6 with modest accuracy (McClatchy *et al*

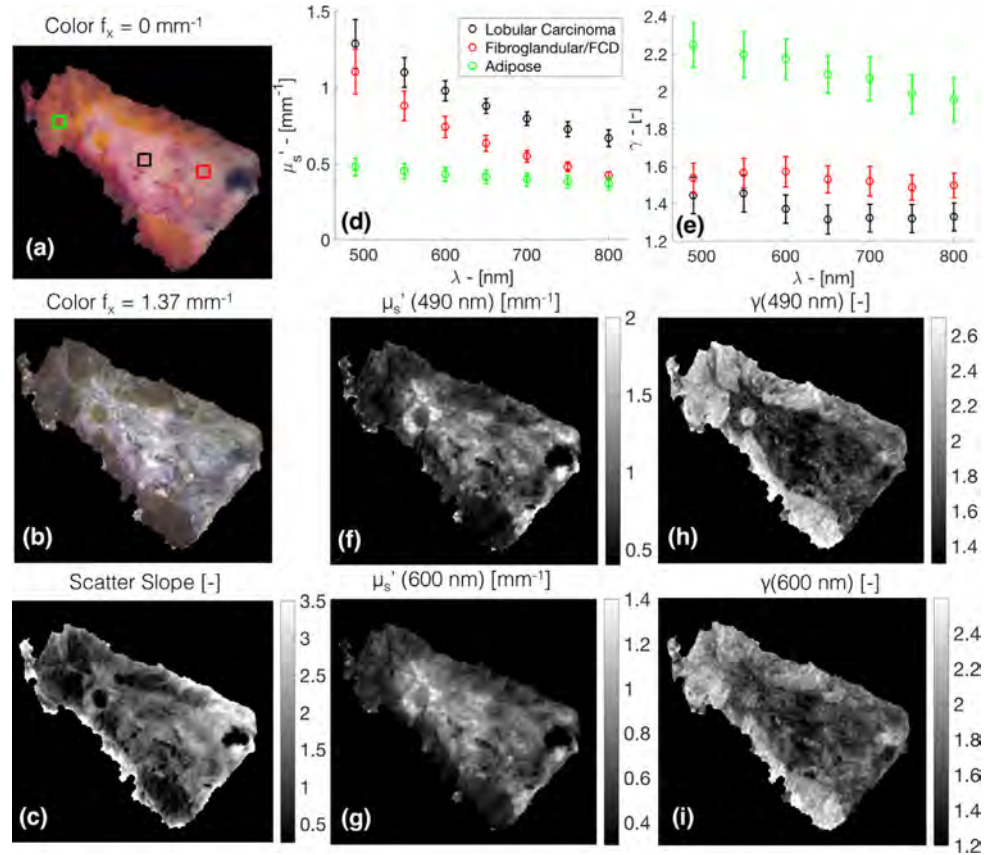


Figure 7. A summary of reconstructed SLI data of the segmented tissue specimen is shown. Color images, reconstructed from multi-spectral SLI data at $f_x = [0, 1.37] \text{ mm}^{-1}$ appear in (a) and (b), respectively. An image of the spectral slope of μ'_s is presented in (c). Black, red, and green boxes in (a) outline regions of lobular carcinoma, fibrocystic disease, and adipose. The means within each region of μ'_s and γ are plotted as a function of wavelength in (d) and (e), respectively, with error-bars representing the standard deviation within the region. Maps of μ'_s are shown in (f) and (g) and maps of γ appear in (h) and (i) for $\lambda = 490 \text{ nm}$ and 600 nm , respectively.

2016), this study experimentally recovers $\gamma \in [0.99 - 2.00]$ and $\frac{\mu'_s}{\mu_a}$ as low as 0.8 with double the accuracy in μ'_s recovery. Imaging of the breast specimen demonstrated co-localization of scattering information with a volumetric micro-CT scan. Imaging irregular specimen surfaces may pose a challenge in the future studies aimed at whole specimen imaging; however, if flattening the tissue surface with the custom acrylic holder does not suffice, a recently published modified Lambertian model has shown to effectively mitigate surface curative artifacts in spatial frequency domain imaging applications (Zhao *et al* 2016).

The preliminary data suggests SLI and micro-CT are likely to be complementary, as the micro-CT lacks contrast between benign and malignant glandular tissues but provides a 3D reconstruction of the tumor core within a specimen, whereas SLI offers enhanced superficial contrast between more subtle morphological changes. Sensitivity to the surface of tissue is substantiated by a current consensus report which states that ‘no tumor on ink’ is appropriate

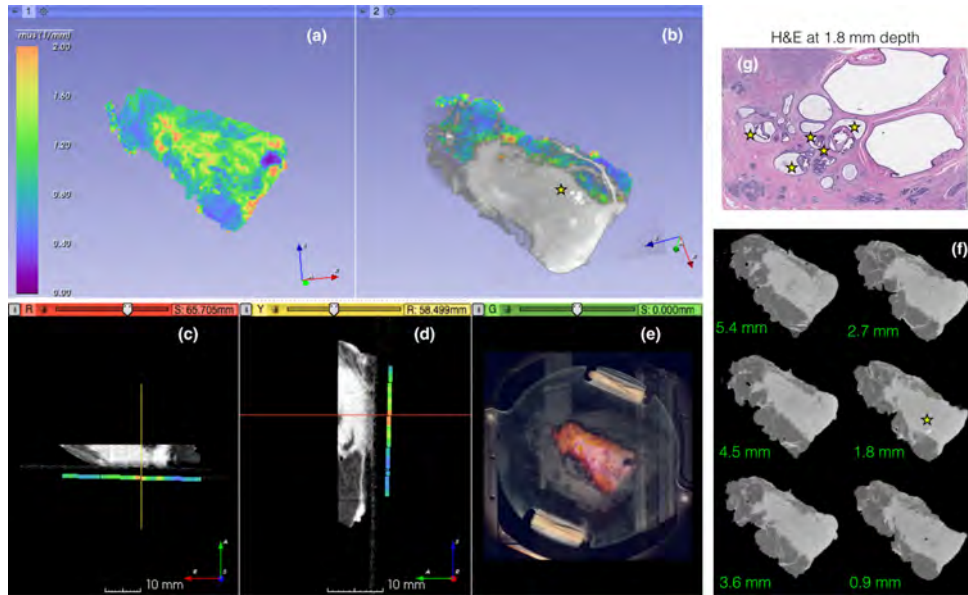


Figure 8. Multimodal display of the resected breast specimen using NIRFAST Slicer. In panel (a), the μ'_s surface is shown, while in panel (b), the μ'_s surface is co-registered to the MIP volume of the micro-CT is shown. In panels (c) and (d), the sagittal and coronal planes of the co-registered μ'_s surface and micro-CT volume are presented. In panel (e), a diffuse reconstructed color image of the specimen in the acrylic holder is shown. In (f), various axial slices of the micro-CT are displayed in 0.9 mm increments below the imaging surface. In the MIP volume and in the micro-CT slice at 1.8 mm below the imaging surface, micro-calcifications appear as a cluster of white specs, which are marked with a yellow star. In (g), an H&E section taken at 1.8 mm depth corroborate the presence of micro-calcifications. A cluster of type-II calcifications can be seen and are marked with yellow stars.

for early stage invasive breast cancer (Buchholz *et al* 2014). With this work flow, the micro-CT could guide selection of surfaces to be optically imaged and provide the proximity of suspicious lesions to the tumor mass. Additionally, contextualizing SLI measurements with the subsurface proximity of the tumor-core, as calculated from the micro-CT, could potentially aid in interpretation of the multimodal data.

Future development of this technology will require creation of a robust classification model to determine margin status based on the multimodal data. A previous study has shown optical scattering parameters of freshly resected human breast tissue recovered with sub-diffusive structured light are sensitive to changes in tissue morphology (McClatchy *et al* 2016). However, with model based inversion methods, fitting time is a limitation. While look-up-table approaches could provide a substantial improvement, a direct calculation of optical properties from an empirically fitted function has demonstrated faster inversion times without the need for a look-up routine (Angelo *et al* 2016). A classification model based on raw multi-spectral reflectance over multiple spatial frequencies may overcome the computational barrier. Previous research has used raw spatial frequency images captured at multiple rotation angles to map the alignment of avian muscle tissue (Konecky *et al* 2011). This technique could potentially be useful in determining the degree of stromal alignment in breast specimens, which could be related to disease progression (Provenzano *et al* 2006, Conklin *et al* 2011). Furthermore, spatial and spectral analysis of raw reflectance images of excised breast

tissue have offered great diagnostic potential in a dark-field confocal microscopy configuration, where scatter contrast was enhanced similarly to high-spatial frequency SLI (Laughney *et al* 2012, Pardo *et al* 2017). With future development of a classification model validated with histopathology, the technology described here can be evaluated in the clinical theater.

5. Conclusions

In this manuscript, a novel multimodal imaging system combining superficial SLI and volumetric micro-CT was systematically evaluated in phantoms, and as a proof-of-principle, a freshly excised human breast specimen was scanned. To the authors knowledge, these results appear to be the first demonstration of SLI or SFDI combined with a standard medical tomography system for imaging excised tumor specimens. System performance quantified through the phantom experiments suggests that the contrast, resolution, SNR, and co-registration accuracy needed for surgical guidance can be obtained within a time frame meeting clinical work flow requirements. The preliminary breast specimen imaging further suggests that the system could aid in visualization of a resected specimen. Further studies in a large cohort of resected specimens are needed to determine the optimal spatial, spectral, and tomographic features required for assessment of margin status before the system can be clinically evaluated.

Acknowledgments

This work was funded through National Institutes of Health (NIH) Academic-Industrial Partnership grant R01CA192803 awarded by the National Cancer Institute (NCI) to Dartmouth College and PerkinElmer. The development and analysis of the SLI imaging system was in part funded by NIH/NCI grant F31CA196308 supporting DMM. We would like to disclosure that authors JM and JK are employees of PerkinElmer Life Sciences Inc., who make products used in this research. Also, the Slicer module described in this research was developed through a subcontract with Kitware Inc., of which author JV is an employee. The authors would like to thank Dr Stephen Kanick, Dr Jonathan Elliott, Dr Venkataramanan Krishnaswamy, Dr Samantha Horvath, and Dr Andinet Enquobahrie for helpful discussions.

References

- Angelo J, Vargas C R, Lee B T, Bigio I J and Gioux S 2016 Ultrafast optical property map generation using lookup tables *J. Biomed. Opt.* **21** 110501
- Ayers F, Grant A, Kuo D, Cuccia D J and Durkin A J 2008 Fabrication and characterization of silicone-based tissue phantoms with tunable optical properties in the visible and near infrared domain *Proc. SPIE* **6870** 687007–9
- Bartek M, Wang X, Wells W, Paulsen K D and Pogue B W 2006 Estimation of subcellular particle size histograms with electron microscopy for prediction of optical scattering in breast tissue *J. Biomed. Opt.* **11** 064007
- Bélanger S, Abran M, Intes X, Casanova C and Lesage F 2010 Real-time diffuse optical tomography based on structured illumination *J. Biomed. Opt.* **15** 016006
- Bodenschatz N, Brandes A, Liemert A and Kienle A 2014 Sources of errors in spatial frequency domain imaging of scattering media *J. Biomed. Opt.* **19** 071405
- Bodenschatz N, Krauter P, Nothelfer S, Foschum F, Bergmann F, Liemert A and Kienle A 2015 Detecting structural information of scatterers using spatial frequency domain imaging *J. Biomed. Opt.* **20** 116006

- Bohren C F and Huffman D R 2008 *Absorption and Scattering of Light by Small Particles* (New York: Wiley)
- Bosschaart N, Edelman G J, Aalders M C, van Leeuwen T G and Faber D J 2014 *Lasers Med. Sci.* **29** 453–79
- Buchholz T A, Somerfield M R, Griggs J J, El-Eid S, Hammond M E H, Lyman G H, Mason G and Newman L A 2014 Margins for breast-conserving surgery with whole-breast irradiation in stage I and II invasive breast cancer: American society of clinical oncology endorsement of the society of surgical oncology/american society for radiation oncology consensus guideline *J. Clin. Oncol.* **32** 1502–6
- Conklin M W, Eickhoff J C, Riching K M, Pehlke C A, Eliceiri K W, Provenzano P P, Friedl A and Keely P J 2011 Aligned collagen is a prognostic signature for survival in human breast carcinoma *Am. J. Pathol.* **178** 1221–32
- Cuccia D J, Bevilacqua F, Durkin A J and Tromberg B J 2005 Modulated imaging: quantitative analysis and tomography of turbid media in the spatial-frequency domain *Opt. Lett.* **30** 1354–6
- Cuccia D J, Bevilacqua F, Durkin A J, Ayers F R and Tromberg B J 2009 Quantitation and mapping of tissue optical properties using modulated imaging *J. Biomed. Opt.* **14** 024012
- DAndrea C, Ducros N, Bassi A, Arridge S and Valentini G 2010 Fast 3D optical reconstruction in turbid media using spatially modulated light *Biomed. Opt. Express* **1** 471–81
- Dehghani H, Eames M E, Yalavarthy P K, Davis S C, Srinivasan S, Carpenter C M, Pogue B W and Paulsen K D 2009 Near infrared optical tomography using nirfast: algorithm for numerical model and image reconstruction *Commun. Numer. Methods Eng.* **25** 711–32
- Erickson-Bhatt S J et al 2015 Real-time imaging of the resection bed using a handheld probe to reduce incidence of microscopic positive margins in cancer surgery *Cancer Res.* **75** 3706–12
- Fedorov A et al 2012 3D slicer as an image computing platform for the quantitative imaging network *Magn. Reson. Imaging* **30** 1323–41
- Fisher B, Anderson S, Bryant J, Margolese R G, Deutsch M, Fisher E R, Jeong J H and Wolmark N 2002 Twenty-year follow-up of a randomized trial comparing total mastectomy, lumpectomy, and lumpectomy plus irradiation for the treatment of invasive breast cancer *New Engl. J. Med.* **347** 1233–41
- Friebel M, Roggan A, Müller G and Meinke M 2006 Determination of optical properties of human blood in the spectral range 250 to 1100 nm using Monte Carlo simulations with hematocrit-dependent effective scattering phase functions *J. Biomed. Opt.* **11** 034021
- Gélibert B, Tinet E, Tualle J M and Avrillier S 1996 Phase function simulation in tissue phantoms: a fractal approach *Pure Appl. Opt.: J. Eur. Opt. Soc. A* **5** 377
- Gioux S et al 2011 First-in-human pilot study of a spatial frequency domain oxygenation imaging system *J. Biomed. opt.* **16** 086015
- Jermyn M, Ghadyani H, Mastanduno M A, Turner W, Davis S C, Dehghani H and Pogue B W 2013 Fast segmentation and high-quality 3D volume mesh creation from medical images for diffuse optical tomography *J. Biomed. Opt.* **18** 086007
- Kanick S C, McClatchy D M, Krishnaswamy V, Elliott J T, Paulsen K D and Pogue B W 2014 Sub-diffusive scattering parameter maps recovered using wide-field high-frequency structured light imaging *Biomed. Opt. Express* **5** 3376–90
- Kanick S, Krishnaswamy V, Gamm U, Sterenborg H, Robinson D, Amelink A and Pogue B 2012a Scattering phase function spectrum makes reflectance spectrum measured from intralipid phantoms and tissue sensitive to the device detection geometry *Biomed. Opt. Express* **3** 1086–100
- Kanick S, Robinson D, Sterenborg H and Amelink A 2012b Semi-empirical model of the effect of scattering on single fiber fluorescence intensity measured on a turbid medium *Biomed. Opt. Express* **3** 137–52
- Kaufman Z, Paran H, Haas I, Malinger P, Zehavi T, Karni T, Pappo I, Sandbank J, Diment J and Allweis T 2016 Mapping breast tissue types by miniature radio-frequency near-field spectroscopy sensor in *ex vivo* freshly excised specimens *BMC Med. Imaging* **16** 57
- Konecky S D, Rice T, Durkin A J and Tromberg B J 2011 Imaging scattering orientation with spatial frequency domain imaging *J. Biomed. Opt.* **16** 126001–18
- Krishnaswamy V, Elliott J T, McClatchy D M, Barth R J, Wells W A, Pogue B W and Paulsen K D 2014 Structured light scatteroscopy *J. Biomed. Opt.* **19** 070504

- Laughney A M, Krishnaswamy V, Rizzo E J, Schwab M C, Barth R J Jr, Cuccia D J, Tromberg B J, Paulsen K D, Pogue B W and Wells W A 2013 Spectral discrimination of breast pathologies *in situ* using spatial frequency domain imaging *Breast Cancer Res.* **15** R61
- Laughney A M, Krishnaswamy V, Rizzo E J, Schwab M C, Barth R J, Pogue B W, Paulsen K D and Wells W A 2012 Scatter spectroscopic imaging distinguishes between breast pathologies in tissues relevant to surgical margin assessment *Clin. Cancer Res.* **18** 6315–25
- McClatchy D M, Hoopes P J, Pogue B W and Kanick S C 2017 Monochromatic subdiffusive spatial frequency domain imaging provides *in situ* sensitivity to intratumoral morphological heterogeneity in a murine model *J. Biophoton.* **10** 211–6
- McClatchy D M, Rizzo E J, Wells W A, Cheney P P, Hwang J C, Paulsen K D, Pogue B W and Kanick S C 2016 Wide-field quantitative imaging of tissue microstructure using sub-diffuse spatial frequency domain imaging *Optica* **3** 613–21
- Michels R, Foschum F and Kienle A 2008 Optical properties of fat emulsions *Opt. Express* **16** 5907–25
- Open Source Computer Vision Library* 2016 <https://github.com/itseez/opencv> (accessed: June 2016)
- Pardo A, Real E, Krishnaswamy V, López-Higuera J M, Pogue B W and Conde O M 2017 Directional kernel density estimation for classification of breast tissue spectra *IEEE Trans. Med. Imaging* **36** 64–73
- Pleijhuis R G, Graafland M, de Vries J, Bart J, de Jong J S and van Dam G M 2009 Obtaining adequate surgical margins in breast-conserving therapy for patients with early-stage breast cancer: current modalities and future directions *Ann. Surgical Oncol.* **16** 2717–30
- Provenzano P P, Eliceiri K W, Campbell J M, Inman D R, White J G and Keely P J 2006 Collagen reorganization at the tumor-stromal interface facilitates local invasion *BMC Med.* **4** 38
- Radosevich A J, Eshein A, Nguyen T Q and Backman V 2015 Subdiffusion reflectance spectroscopy to measure tissue ultrastructure and microvasculature: model and inverse algorithm *J. Biomed. Opt.* **20** 097002
- Rogers J D, Çapoğlu İ R and Backman V 2009 Nonscalar elastic light scattering from continuous random media in the born approximation *Opt. Lett.* **34** 1891–3
- Sibai M, Veilleux I, Elliott J T, Leblond F and Wilson B C 2015 Quantitative spatial frequency fluorescence imaging in the sub-diffusive domain for image-guided glioma resection *Biomed. Opt. Express* **6** 4923–33
- Smith T and Guild J 1931 The cie colorimetric standards and their use *Trans. Opt. Soc.* **33** 73
- St John E R, Al-Khudairi R, Ashrafian H, Athanasiou T, Takats Z, Hadjiminas D J, Darzi A and Leff D R 2017 Diagnostic accuracy of intraoperative techniques for margin assessment in breast cancer surgery: a meta-analysis *Ann. Surg.* **265** 300–10
- Taka S J and Srinivasan S 2011 Nirviz: 3D visualization software for multimodality optical imaging using visualization toolkit (vtk) and insight segmentation toolkit (itk) *J. Digit. Imaging* **24** 1103–11
- Tang R et al 2013 Micro-computed tomography (micro-ct): a novel approach for intraoperative breast cancer specimen imaging *Breast Cancer Res. Treat.* **139** 311–6
- Tang R 2016 Intraoperative micro-computed tomography (micro-ct): a novel method for determination of primary tumour dimensions in breast cancer specimens *Br. J. Radiol.* **89** 20150581
- Tao Y K et al 2014 Assessment of breast pathologies using nonlinear microscopy *Proc. Natl Acad. Sci.* **111** 15304–9
- Tse G, Tan P H, Pang A L, Tang A P and Cheung H S 2008 Calcification in breast lesions: pathologists perspective *J. Clin. Pathol.* **61** 145–51
- Wang Y et al 2016 Quantitative molecular phenotyping with topically applied sers nanoparticles for intraoperative guidance of breast cancer lumpectomy *Sci. Rep.* **6** 21242
- Wong T T, Zhang R, Hai P, Zhang C, Pleitez M A, Aft R L, Novack D V and Wang L V 2017 Fast label-free multilayered histology-like imaging of human breast cancer by photoacoustic microscopy *Sci. Adv.* **3** e1602168
- Zhao Y, Tabassum S, Piracha S, Nandhu M S, Viapiano M and Roblyer D 2016 Angle correction for small animal tumor imaging with spatial frequency domain imaging (sfdi) *Biomed. Opt. Express* **7** 2373–84

Chapter 8: Assessment of Whole Lumpectomy Specimens with Micro-CT

8.1. Background and Goals

With the multimodal system developed in Chapter 7, a cohort of grossly dissected BCS specimens have been imaged with both optical structured light imaging, and tomographic micro-CT. However, given both the short acquisition time of the micro-CT and the physical location of multimodal system in Surgical Gross Lab, a study was designed to use micro-CT to scan entire BCS specimens upon their arrival and before their dissection. This study yielded tomographic reconstructions of specimens similar to what would be expected if scanning had been performed intraoperatively. With the data set of n=32 specimens, we sought to determine what potential diagnostic value the micro-CT scanning could provide on its own. The following manuscript details the first systematic analysis comparing radiologic readings of whole BCS specimen micro-CT scans to the final margin diagnoses determined by pathology, and yielded the initial diagnostic performance of this imaging technology for BCS guidance.

8.2. Submitted Manuscript for Publication Work

The following manuscripts has been prepared for submission to the journal Radiology:

McClatchy DM, Zuurbier RA, Wells WA, Paulsen KD, Pogue BW. Evaluating surgical breast tumor margins using micro-computed tomography (micro-CT): results in 32 resected Breast Conserving Surgery (BCS) specimens. *Prepared for Submission.*

D. M. McClatchy was responsible for all experimental data acquisition, data analysis and quantification, statistical analysis, and writing the manuscript. R. A. Zuurbier was responsible for reading the micro-CT scans. W. A. Wells was responsible for creating the final histology report and was in charge of the protocol to image whole

lumpectomy specimens. K. D. Paulsen and B. W. Pogue conceived the idea for a reader study, provided advising, authored the NIH grant supporting this research, and participated in editing and writing the manuscript.

Article Title: Evaluating surgical breast tumor margins using micro-computed tomography (micro-CT): results in 32 resected Breast Conserving Surgery (BCS) specimens

David M. McClatchy III, AB,¹ Rebecca J. Zuurbier, MD,² Wendy A. Wells, MD, MS,^{3,4} Keith D. Paulsen, PhD,^{1,4} Brian W. Pogue, PhD,^{1,4}*

¹ Thayer School of Engineering, Dartmouth College, 14 Engineering Drive, Hanover, NH 03755

² Department of Radiology, Geisel School of Medicine, Dartmouth College, 1 Rope Ferry Road, Hanover, NH 03755

³ Department of Pathology, Geisel School of Medicine, Dartmouth College, 1 Rope Ferry Road, Hanover, NH 03755

⁴ Norris Cotton Cancer Center, Geisel School of Medicine, Dartmouth College, 1 Rope Ferry Road, Hanover, NH 03755

***Corresponding Author:** email: David.M.McClatchy.III.th@Dartmouth.edu; telephone: +1 410 507-4518; address: 14 Engineering Drive, Hanover, NH 03755

Financial Support: This work is supported by NIH/NCI grant R01CA192803.

Disclosure: The authors declare no potential conflicts of interest.

Manuscript Type: Technical Developments

Unblinded Acknowledgements: The authors would like to like Elizabeth Rizzo, PA, Steven Boyle, PA, Peter Seery, PA, and Rebecca Kinney, PA, for assisting with specimen handling.

This manuscript has not been presented at a RSNA meeting.

Article Title: Surgical breast tumor margins evaluated with micro-CT: results in 32 resected Breast Conserving Surgery (BCS) specimens

Article Type: Technical Developments

Summary Statement: Experience with micro-CT scanning of resected BCS specimens provided high resolution visualizations of the tumor core, tumor spiculations, micro-calcifications, and the specimen margin in 3 dimensions, highlighting spatially resolved information not obtained with conventional specimen projection radiography.

Implications for Patient Care: The ability of micro-CT to rapidly scan BCS specimens and spatially resolve the proximity of anatomical features to the margin in 3D may provide benefit as a tool for intraoperative BCS guidance.

Abbreviations:

BCS = Breast Conserving Surgery
Micro-CT = micro-Computed Tomography
2D, 3D = two, three dimensional
ICa = Invasive Breast Cancer
IDc = Invasive Ductal Carcinoma
ILc = Invasive Lobular Carcinoma
DCIS = Ductal Carcinoma In-Situ
LCIS = Lobular Carcinoma In-Situ
FCD = Fibrocystic Disease
CSL = Complex Sclerosing Lesion

Abstract

Purpose: To investigate the feasibility and value for micro-Computed Tomography (micro-CT) to be used as a surgical guidance tool during breast conservation therapy (BCS).

Materials and Methods: A cohort of 32 resected breast lumpectomy specimens were prospectively imaged with a preclinical micro-CT system upon specimen arrival to the surgical gross pathology lab, under an institutional review board approved protocol. Reconstructed micro-CT scans were retrospectively evaluated by an expert breast radiologist, who gave a binary reading for each scan as to whether lesion tissue extended to the specimen margin, which was then compared to the final pathological diagnosis. Fisher's exact test was used to calculate statistical significance, and a binomial distribution was used to calculate confidence intervals.

Results: Of the 32 specimens imaged, 28 had malignant and 4 had benign lesions. Overall 5 (4 malignant, 1 benign) of the 32 specimens had lesion tissue extending to the margin. For all 32 specimens, CT reconstructions were calculated (<4 min. acquisition + reconstruction time) and read by a radiologist. Of the 32 readings, 21 matched the final pathological diagnosis (66%, CI = [47%-81%]). The anterior-posterior margins were more likely to be within 2 mm than the orthogonal margins ($p < 0.02$). Imaging artifacts from the tumor localization wire posed a significant challenge.

Conclusions: These findings demonstrate the feasibility of micro-CT to provide accurate 3D reconstructions of lumpectomy specimens, highlighting spatially resolved information not obtained with conventional 2D projection radiography. Micro-CT should be examined for level 1 evidence as a potential BCS guidance tool.

Introduction

Breast conserving surgery (BCS) in combination with radiotherapy has become a widely practiced treatment for early stage breast cancer, offering equivalent survival to a full mastectomy, but with a far less invasive surgical procedure¹. However, this holds true only if the resected specimen has negative margins, meaning no residual tumor on the inked surface of the specimen^{2,3}. The current foundation for BCS surgical guidance includes preoperative wire^{4,5} or radioactive seed tumor localization⁶, along with intraoperative specimen mammography⁷. Yet, 20-40% of patients who undergo BCS require a follow-up re-excision procedure because of a positive or close margin, with great variability among surgeons and clinics^{8,9}, clearly highlighting the clinical need for better BCS surgical guidance.

A recent pre-clinical imaging technology, micro-Computed Tomography (micro-CT), offers three dimensional (3D) image reconstructions, but at much smaller fields of view with sub-millimeter scale resolution. While this technology has been utilized for pre-clinical specimen and animal studies¹⁰⁻¹², it has only just been proposed as a possible tool for imaging surgically resected breast specimens¹³. Tang et al. have motivated a possible value of this technology in assessing shaved cavity margins¹⁴ and have also shown the technology to accurately measure the largest tumor dimension in resected BCS specimens¹⁵. However, the diagnostic potential of micro-CT to assess whole resected BCS specimens has not yet been investigated. Therefore, the purpose of this pilot study is to explore the feasibility and potential for micro-CT to be used as a surgical guidance tool for BCS, by quantifying an initial correlation of micro-CT analysis to the final histopathologic diagnosis and qualitatively comparing specimen micro-CT to specimen mammography.

Materials and Methods

Overview of Specimen Imaging Protocol

From May of 2017 to January of 2018, a cohort of 32 BCS specimens was prospectively imaged under a HIPPA compliant, Institutional Review Board approved observational protocol. Patients undergoing consented and elective BCS were treated with standard of care, including intraoperative specimen mammography to confirm the lesion was excised. After each specimen was excised and inked on all sides to record its orientation¹⁶, it was sent to the Pathology specimen grossing laboratory. Upon arrival to the Gross lab, each specimen was scanned with the micro-CT and was then immediately returned to the pathologists' assistant for standard gross analysis and histological processing. Each micro-CT scan was retrospectively analyzed by an expert radiologist (R.A.Z), blinded to the pathological diagnosis. Participant consent was waived by IRB as the study did not interfere with standard of care nor did it disclose or analyze protected health information (PHI).

Micro-CT Imaging Device and Reconstructions

Upon arrival in the Gross lab, specimens were compressed between two acrylic plates and imaged with a pre-clinical micro-CT imaging device (IVIS SpectrumCT, PerkinElmer, Hopkinton, MA), which was physically located in the Pathology specimen grossing laboratory in order to minimize tissue handling time. Imaging was performed at X-ray settings of 50 kVp, 1 mA, and with a 440 μm aluminum filter. The X-ray source-detector pair was fixed, with the specimen rotation through 360 degrees with a 100 ms exposure at each 0.5 degree (72 s acquisition). Standard filtered back projections (FBP) was used to reconstruct a volume of 12 cm x 12 cm x 3 cm with 0.15 mm cubic voxels (~2 min. reconstruction time). A previous report of this device has shown a

resolution of 240 μm and an SNR of 34¹⁷. For two selected scans, 3D visualization models were created using the “Volume Rendering” tool in 3D Slicer (v4, <https://www.slicer.org>)¹⁸.

Pathological Diagnosis

After micro-CT scanning, the specimens were immediately returned to the pathologists’ assistants in the Gross lab, who performed standard of care gross analysis to determine both representative sections of lesional tissue as well as all areas of possible lesion involvement with the specimen margin. These tissue sections underwent standard histological processing to create hematoxylin and eosin (H&E) stained slides, which were diagnosed by an expert histopathologist (W.A.W.) with 28 years of experience. From these slides, the distances of lesion involvement to each margin was measured, per standard of care. The tabulated diagnoses and distances for each margin of each specimen can be found in the Supplemental Material.

Micro-CT Image Interpretation

After scans were acquired, an expert breast radiologist (R.A.Z.) with 27 years of experience retrospectively analyzed the scans, which were sequential (scan-mode) presented in two orthogonal views. Features such as speculated masses, distorted tissue architecture, and clustered micro-calcifications were analyzed to yield a binary reading of positive or negative margins. The radiologist was blinded to both the final pathological diagnosis as well as the pathological diagnosis of the preoperative needle core biopsy. For four specimens, micro-CT scans were retrospectively compared to de-identified specimen mammograms, to qualitatively view the effect of reconstruction overlapping structures in projection space with micro-CT.

Statistical Methods

All statistical analyses were performed using MATLAB (v2016a, Mathworks, Natick, MA). For the reader performance metrics, confidence intervals were calculated using a binomial distribution. A one-sided Fisher’s exact test was used to calculate statistical significance between observed involvement in the different surface planes.

Results

Specimen Characteristics

A tabulation of both specimen characteristics and associated margin statuses are shown in Table 1. For this study, a positive margin defined as malignant or benign lesion tissue extending to the specimen surface, was the measured end-point. Of all of the specimens, 16% (5/32) had a positive margin and of those, 80% (4/5) had a malignant positive margin (or 13% (4/32) of all specimens). However, the true re-excision rate would likely be higher as a close ($\leq 2\text{mm}$) DCIS margin may result in re-excision depending of patient characteristics and physician preference³. In-situ cancer was more likely to be present with invasive cancer (13/32) than on its own (3/32) ($p<.005$), and conversely, invasive cancer was just as likely to be present with in-situ (13/32) than on its own (12/32) ($p=0.5$).

Micro-CT Findings and Comparison to Specimen Mammography

In Fig. 1, summary data for a positive specimen with an IDC+DCIS lesion is shown. In both the specimen mammogram (Fig. 1(a)) and the x-y plane of the micro-CT (Fig. 1(b)), a high contrast, highly speculated lesion was centrally located surrounded by adipose tissue (green arrows). But in x-z plane of the micro-CT (Fig. 1(c)), the lesion came close to anterior margin (orange arrow) and touched the posterior margin (red arrow) 12.1 mm apart. This specimen was correctly read as

positive, and highlights the ability to resolve lesion involvement in the mammography projection plane with micro-CT. A rendering of the specimen is shown in Fig. 1(d), with the adipose tissue thresholded to be transparent, revealing the structure of the lesion in 3D (video in Supplemental Material).

In Fig. 2, summary data for a negative specimen with an IDc+DCIS lesion is shown. A peripherally located, wire localized, lesion with a cluster of micro-calcifications (orange arrows) can be seen in the specimen mammography (Fig. 2(a)). In the x-y plane views of the specimen micro-CT (Fig. 2(b)), the lesion can likewise be seen at z=8.85 mm; however, at z=7.50 mm, notable artifacts can be seen from the wire. In the x-z plane, the lesion was read as close to the peripheral margin at y=20.40 mm in agreement with the specimen mammogram, but at y=24.60 mm the lesion was also read as close to the deep posterior margin, which inherently could not be detected with the mammogram. The micro-CT rendering of this specimen (Fig. 4(d)) was able to resolve the 3D formation and organization of the micro-calcification cluster near the surgical clip and calcified vasculature (white arrows) (video in Supplemental Material).

In Fig. 3(a-b), summary data for a specimen with ILc lesion are shown. In the specimen mammogram (Fig. 3(a)), centrally located bright, diffuse features were present. However, in the orthogonal micro-CT slices (Fig. 4(b)), the overlapping structures were resolved revealing an adipose-glandular tissue interface. Although this specimen did have a positive margin but was read as negative, the micro-CT was still able to resolve the overlapping structures. The specimen mammogram for another IDc+DCIS lesion is shown in Fig. 3(c), and the orthogonal micro-CT slices are shown in Fig. 3(d). While lesion appeared to be centrally located on both the mammogram and the x-y plane of the micro-CT, the lesion was read as positive on the anterior margin of the x-z plane. However, the margin was negative with the lesion 2.5 mm deep, illustrating a potential limitation of micro-CT with poor tumor glandular contrast. A summary of illustrative orthogonal micro-CT slices through the lesion of each specimen can be found in the Supplemental Material.

Comparison of Micro-CT Reading to Final Pathological Diagnosis

The final results comparing the micro-CT readings against the final pathological diagnosis are tabulated in Table 2. Of the 5 specimens with a positive margin, 3 were correctly read, and of the 27 specimens without a positive margin, 18 were correctly read, yielding a sensitivity, specificity and accuracy of 60% (3/5, CI=[15%-95%]), 67% (18/27, CI=[46%-84%]), and 66% (21/32, CI=[47%-81%]). While there were a notable number of false positives, resulting in a positive predictive value of 25% (3/12, CI=[12%-45%]), the negative predictive value of 90% (2/18, CI=[75%-96%]) was far superior. However, these results represent an initial data point for this imaging method, as this study is the first to systemically compare micro-CT scans of whole BCS specimens to a pathologic diagnosis, and so there was no formal training on how to interpret the micro-CT scans.

Frequency of Margin Specific Lesion Involvement

The frequency of positive (0 mm), close (<= 2 mm), and distant (> 2 mm) lesions for each of the six margins is tabulated in Fig. 4(a). It should be noted that six margins are listed positive in total, as one positive specimen had two separate positive margins. Similarly, there were a total of 25 close margins, from 15 positive and close specimens. While, ICa+in-situ lesions resulted in the most frequent number of positive and close margins for malignant lesions, this result is not statistically significant and limited by a small sample size. The percentage of aggregate positive and close lesions for each margin is plotted in Fig. 4(b). Interestingly, anterior and posterior

margins have significantly higher frequency of positive and close margins (16/64) compared to the orthogonal margins (15/128) ($p=0.017$).

Discussion

Positive surgical margins after BCS remain a critical challenge, with wire localization and specimen mammography as the primary form of guidance resulting in a re-excision rate upwards of 20%. Microscopic point assessment techniques, such as frozen-section pathology and touch prep cytology, have been commonly used for directed BCS guidance with apparent diagnostic accuracy, but wide-spread adoption has been limited due to the increasing labor cost of microscopic sampling over a macroscopic specimen¹⁹. And so the key advantage of micro-CT demonstrated in this study is the ability to fully and rapidly resolve the entire specimen in 3D allowing for a complete analysis of the specimen at each pixel. Specifically, the ability to read the cross section of specimen in the projection plane of the specimen mammography appears to provide valuable information regarding the lesion location.

Although modest sensitivity and specificity (60%, 3/5, 67%, 18/27) was reported in this pilot study, there were significantly more false positives (9/32) than false negatives (2/32) ($p=0.02$). While excising unnecessary tissue is always undesirable, it may be less harmful than another surgical procedure, and indeed the practice of undirected whole margin cavity shaving on all BCS procedures has been investigated²⁰. Furthermore, single projection specimen mammography has reported sensitivity and specificity of 36% and 71%⁷. However, two projection specimen mammography has reported sensitivities and specificities of 54.6% and 87.8%²¹ and more recently 58.5% and 91.8%²². While micro-CT appears to have superior sensitivity and comparable specificity to single projection mammography and comparable sensitivity and inferior specificity to two projection mammography, a prospective, fully powered, head to head study of micro-CT against single or two projection specimen mammography is needed to accurately compare performance. Additionally, reading micro-CT scans was done in an ad-hoc manner as no atlas of micro-CT scans of BCS specimens exists. These data could serve as a training set for the presentation of various pathologies in micro-CT.

While this inceptive study is limited by sample size, with only five specimens having lesion involvement at the margin, it does provide initial evidence suggesting potential diagnostic value, which could be quantified in a larger prospective future study. A key limitation of the micro-CT was lack of contrast between tumor-glandular tissue, resulting in poor diagnosis of tumor-glandular interfaces. Another limiting factor was the presence of metal streaking reconstruction artifacts arising from the tumor localization wire. In Tang et al., this was mitigated by first doing a single projection image to confirm the wire and surgical clip have been surgical excised, removing the wire from the specimen, and then performing the full micro-CT scan¹³. However, this method poses a challenge as the wire and clip are regularly used as lesion landmarks during subsequent gross analysis in Pathology. An alternative solution would be to implement a metal artifact reduction algorithm²³.

In summary, these findings demonstrate the feasibility of micro-CT to provide fully volumetric 3D reconstructions of lumpectomy specimens, highlighting spatially resolved features not obtained with conventional 2D projection radiography. Furthermore, this study provides an initial measure of the correlation between micro-CT analysis of whole BCS specimens and gold-standard histology. Micro-CT should continue to be investigated as a potential BCS guidance tool.

Acknowledgments

The authors would like to thank the Pathology Assistants (PAs) for assisting with specimen handling and processing, and also Josh Kemper and Jeff Meganck at PerkinElmer for technical assistance with the micro-CT.

Tables

Table 1: Pathological Diagnoses of 32 BCS Specimens

Note: DCIS=Ductal Carcinoma In Situ, LCIS=Lobular Carcinoma In-Situ, FCD=Fibrocystic Disease, CSL=Complex Sclerosing Lesion, NAC pCR=Neoadjuvant Chemotherapy Complete Pathologic Response

		Margin Status			
		N (w/wire, w/o wire)	Positive 0 mm	Negative “Close” >0 mm &≤2mm	Negative “Distant” >2mm
Invasive Only		12 (9,3)	1	3	8
	Ductal Carcinoma	4	0	0	4
	Lobular Carcinoma	4	1	0	3
	Mucinous	2	0	2	0
	Ductal and Lobular	2	0	1	1
In-Situ Only		3 (2,1)	1	1	1
	DCIS	2	0	1	1
	Pleomorphic LCIS	1	1	0	0
Invasive + In-Situ		13 (8,5)	2	4	7
Benign		4 (4,0)	1	2	1
	FCD	1	0	1	0
	CSL	1	1	0	0
	Fibroadenoma	1	0	1	0
	NAC pCR	1	0	0	1
Total		32 (23,9)	5	10	17

Table 2: Comparison of micro-CT Reading to Pathologic Evaluation

Note: PPV=Positive Predictive Value, NPV=Negative Predictive Value, Parenthesis = 95% Confidence Intervals

	Positive Margin	Negative Margin	Total
Positive Reading	3	9	12
Negative Reading	2	18	20
Total	5	27	32
Sensitivity	60% (15%-95%)		
Specificity	67% (46%-84%)		
Accuracy	66% (47%-81%)		
PPV	25% (12%-45%)		
NPV	90% (75%-96%)		

Figures

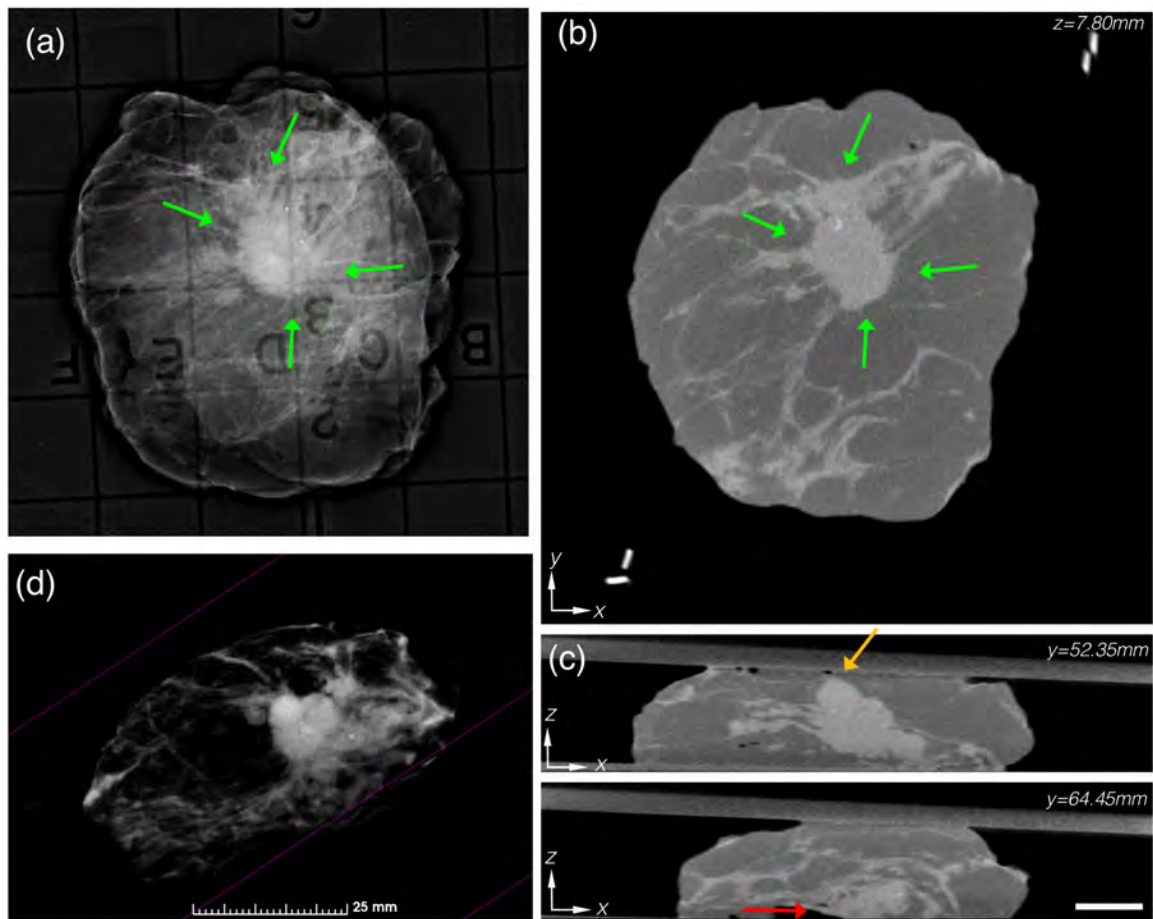


Figure 1: (a) Specimen mammography showing a centrally located IDc + DCIS lesion. (b) Reconstructed micro-CT slice similarly showing centrally located lesion. (c) Orthogonal micro-CT slices 12.1 mm apart showing a close ($\leq 2\text{mm}$) anterior margin (orange arrow) and a positive deep margin (red arrow), which was in agreement with the final pathologic diagnosis. Micro-CT scale bar is 1 cm. (d) A 3D volume rendering of the specimen, with the adipose tissue thresholded to be transparent, showing the architecture of the lesions and its spiculations (video in Supplemental Materials).

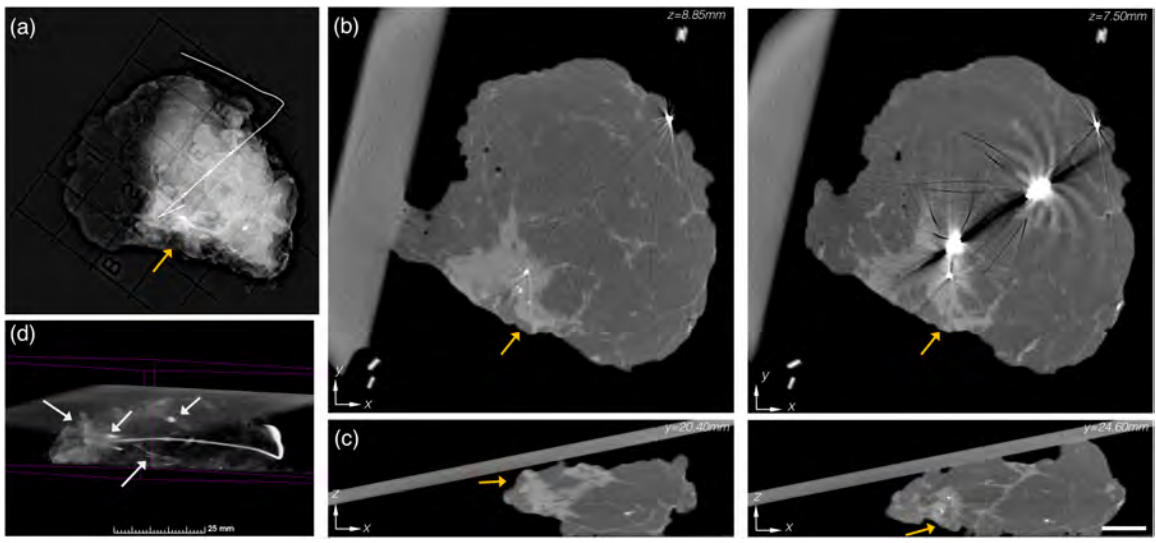


Figure 2: (a) Specimen mammography showing a peripherally located IDC + DCIS lesion (orange arrow). (b) Reconstructed micro-CT slices 1.35 mm apart similarly showing the peripherally located lesion. Notable metal reconstruction artifacts can be seen arising from the localization wire. (c) Orthogonal micro-CT slices 4.2 mm apart showing a close peripheral margin, and also a close deep margin, which would not be seen in the 2D specimen mammogram. Micro-CT scale bar is 1 cm. (d) A 3D volume rendering of the specimen, with the adipose tissue thresholded to be transparent, revealing a micro-calcification cluster, a large smooth calcification, tumor location metal clip, and calcified vasculature (white arrows) in 3D (video in Supplemental Materials).

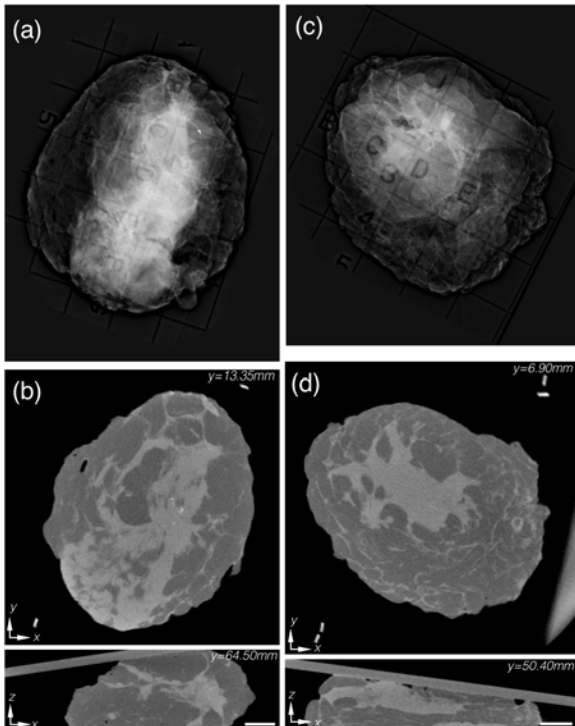


Figure 3: (a) Specimen mammography showing a diffuse ILCa with poor contrast due to diffuse overlapping structures. (b) Orthogonal reconstructed micro-CT slices resolving the glandular-fat

interface in 3D. Pathology confirms this specimen to have a positive margin, although this was not detected by micro-CT analysis. (c) Specimen mammography showing a centrally located IDC + DCIS lesion. (d) Orthogonal reconstructed micro-CT slices showing a centrally, but also superficially, located lesion. However, pathology confirms the lesion to be 2.5 mm from superficial margin, illustrating a limitation of micro-CT being unable to resolve a tumor-connective tissue interface. Micro-CT scale bar is 1 cm.



Figure 4: (a) Table summarizing the frequency of positive, close, and distant lesion involvement for each specific margin. (b) Bar graph of fraction of lesions $\leq 2\text{mm}$ for each margin, showing a significant increase in close anterior-posterior margins compared to the orthogonal margins. (16/64 $\leq 2\text{mm}$, 15/128 $> 2\text{mm}$, $p < 0.02$). ICa=Invasive Breast Cancer.

References (25 max)

1. Fisher B, Anderson S, Bryant J, et al. Twenty-year follow-up of a randomized trial comparing total mastectomy, lumpectomy, and lumpectomy plus irradiation for the treatment of invasive breast cancer. *N Engl J Med* 2002;347:1233-41.
2. Moran MS, Schnitt SJ, Giuliano AE, et al. Society of Surgical Oncology-American Society for Radiation Oncology consensus guideline on margins for breast-conserving surgery with whole-breast irradiation in stages I and II invasive breast cancer. *Ann Surg Oncol* 2014;21:704-16.
3. Morrow M, Van Zee KJ, Solin LJ, et al. Society of Surgical Oncology-American Society for Radiation Oncology-American Society of Clinical Oncology Consensus Guideline on Margins for Breast-Conserving Surgery with Whole-Breast Irradiation in Ductal Carcinoma In Situ. *Ann Surg Oncol* 2016;23:3801-10.
4. Frank HA, Hall FM, Steer ML. Preoperative localization of nonpalpable breast lesions demonstrated by mammography. *N Engl J Med* 1976;295:259-60.
5. Kopans DB, DeLuca S. A modified needle-hookwire technique to simplify preoperative localization of occult breast lesions. *Radiology* 1980;134:781.
6. Lovrics PJ, Goldsmith CH, Hodgson N, et al. A multicentered, randomized, controlled trial comparing radioguided seed localization to standard wire localization for nonpalpable, invasive and in situ breast carcinomas. *Ann Surg Oncol* 2011;18:3407-14.
7. Kaufman CS, Jacobson L, Bachman BA, et al. Intraoperative digital specimen mammography: rapid, accurate results expedite surgery. *Ann Surg Oncol* 2007;14:1478-85.

8. Pleijhuis RG, Graafland M, de Vries J, Bart J, de Jong JS, van Dam GM. Obtaining adequate surgical margins in breast-conserving therapy for patients with early-stage breast cancer: current modalities and future directions. *Ann Surg Oncol* 2009;16:2717-30.
9. McCahill LE, Single RM, Aiello Bowles EJ, et al. Variability in reexcision following breast conservation surgery. *JAMA : the journal of the American Medical Association* 2012;307:467-75.
10. Samei E, Saunders RS, Badea CT, et al. Micro-CT imaging of breast tumors in rodents using a liposomal, nanoparticle contrast agent. *International journal of nanomedicine* 2009;4:277-82.
11. Hainfeld JF, O'Connor MJ, Dilmanian FA, Slatkin DN, Adams DJ, Smilowitz HM. Micro-CT enables microlocalisation and quantification of Her2-targeted gold nanoparticles within tumour regions. *The British journal of radiology* 2011;84:526-33.
12. Willekens I, Van de Casteele E, Buls N, et al. High-resolution 3D micro-CT imaging of breast microcalcifications: a preliminary analysis. *BMC cancer* 2014;14:9.
13. Tang R, Buckley JM, Fernandez L, et al. Micro-computed tomography (Micro-CT): a novel approach for intraoperative breast cancer specimen imaging. *Breast cancer research and treatment* 2013;139:311-6.
14. Tang R, Coopey SB, Buckley JM, et al. A pilot study evaluating shaved cavity margins with micro-computed tomography: a novel method for predicting lumpectomy margin status intraoperatively. *The breast journal* 2013;19:485-9.
15. Tang R, Saksena M, Coopey SB, et al. Intraoperative micro-computed tomography (micro-CT): a novel method for determination of primary tumour dimensions in breast cancer specimens. *The British journal of radiology* 2016;89:20150581.
16. Gibson GR, Lesnikoski BA, Yoo J, Mott LA, Cady B, Barth RJ, Jr. A comparison of ink-directed and traditional whole-cavity re-excision for breast lumpectomy specimens with positive margins. *Ann Surg Oncol* 2001;8:693-704.
17. McClatchy DM, Rizzo EJ, Meganck J, et al. Calibration and analysis of a multimodal micro-CT and structured light imaging system for the evaluation of excised breast tissue. *Physics in medicine and biology* 2017;62:8983-9000.
18. Fedorov A, Beichel R, Kalpathy-Cramer J, et al. 3D Slicer as an image computing platform for the Quantitative Imaging Network. *Magnetic resonance imaging* 2012;30:1323-41.
19. St John ER, Al-Khudairi R, Ashrafian H, et al. Diagnostic Accuracy of Intraoperative Techniques for Margin Assessment in Breast Cancer Surgery: A Meta-analysis. *Annals of surgery* 2017;265:300-10.
20. Chagpar AB, Killelea BK, Tsangaris TN, et al. A Randomized, Controlled Trial of Cavity Shave Margins in Breast Cancer. *N Engl J Med* 2015;373:503-10.
21. McCormick JT, Keleher AJ, Tikhomirov VB, Budway RJ, Caushaj PF. Analysis of the use of specimen mammography in breast conservation therapy. *Am J Surg* 2004;188:433-6.
22. Bathla L, Harris A, Davey M, Sharma P, Silva E. High resolution intra-operative two-dimensional specimen mammography and its impact on second operation for re-excision of positive margins at final pathology after breast conservation surgery. *Am J Surg* 2011;202:387-94.
23. Katsura M, Sato J, Akahane M, Kunimatsu A, Abe O. Current and Novel Techniques for Metal Artifact Reduction at CT: Practical Guide for Radiologists.

Radiographics : a review publication of the Radiological Society of North America, Inc
2018;38:450-61.

Article Title: Evaluating surgical breast tumor margins using micro-computed tomography (micro-CT): results in 32 resected Breast Conserving Surgery (BCS) specimens

Supplemental Material:

Case	Lesion Pathology		Anterior	Posterior	Caudal	Cranial	Lateral	Medial	Wire	Reading	Diagnosis
1	IDCa, IG with DCIS	Invasive	2.5 mm	>10.0 mm	>10.0 mm	2.5 mm	>10.0 mm	>10.0 mm	N	POS	FP
		DCIS	>2.0 mm	>2.0 mm	>2.0 mm	>2.0 mm	>2.0 mm	>2.0 mm			
2	IDCa, LG	Invasive	>10.0 mm	>10.0 mm	>10.0 mm	>10.0 mm	>10.0 mm	>10.0 mm	Y	NEG	TN
3	IDCa, IG with DCIS	Invasive	0.7 mm	5.0 mm	>10.0 mm	>10.0 mm	>10.0 mm	>10.0 mm	N	POS	TP
		DCIS	7.0 mm	POSITIVE	>10.0 mm	>10.0 mm	>10.0 mm	>10.0 mm			
4	DCIS in Papilloma	DCIS	>10.0 mm	2.0 mm	>10.0 mm	2.0 mm	>10.0 mm	>10.0 mm	Y	NEG	TN
5	ILCa	Invasive	>2.0 mm	>2.0 mm	>2.0 mm	>2.0 mm	>2.0 mm	>2.0 mm	Y	NEG	TN
6	ILCa	Invasive	>10.0 mm	>10.0 mm	9.0 mm	>10.0 mm	6.0 mm	>10.0 mm	Y	NEG	TN
7	ILCa	Invasive	7.0 mm	3.0 mm	POSITIVE	5.0 mm	5.0 mm	>10.0 mm	N	NEG	FN
8	IDCa, LG with DCIS	Invasive	>10.0 mm	5.0 mm	>10.0 mm	6.0 mm	>10.0 mm	>10.0 mm	N	NEG	TN
		DCIS	>10.0 mm	<1.0 mm	>10.0 mm	4.0 mm	>10.0 mm	>10.0 mm			
9	IDCa and ILCa	Invasive	>10.0 mm	4.0 mm	>10.0 mm	>10.0 mm	>10.0 mm	8.0 mm	Y	NEG	TN
10	IDCa, LG with DCIS	Invasive	7.0 mm	>10.0 mm	5.0 mm	>10.0 mm	>10.0 mm	>10.0 mm	Y	NEG	TN
		DCIS	7.0 mm	>10.0 mm	>10.0 mm	>10.0 mm	>10.0 mm	>10.0 mm			
11	ILCa	Invasive	5.0 mm	>10.0 mm	4.5 mm	>10.0 mm	>10.0 mm	>10.0 mm	N	NEG	TN
12	IDCa, IG	Invasive	>10.0 mm	>10.0 mm	9.0 mm	>10.0 mm	>10.0 mm	>10.0 mm	Y	NEG	TN
13	IDCa, HG with DCIS	Invasive	>10.0 mm	<1.0 mm	>10.0 mm	>10.0 mm	9.0 mm	>10.0 mm	Y	NEG	TN
		DCIS	>10.0 mm	<1.0 mm	>10.0 mm	>10.0 mm	9.0 mm	>10.0 mm			
14	Inv. mucinous Ca	Invasive	>10.0 mm	7.0 mm	>10.0 mm	1.0 mm	2.0 mm	>10.0 mm	N	NEG	TN
15	IDCa, LG with DCIS	Invasive	>10.0 mm	6.0 mm	>10.0 mm	>10.0 mm	>10.0 mm	>10.0 mm	Y	POS	FP
		DCIS	>10.0 mm	6.0 mm	>10.0 mm	>10.0 mm	>10.0 mm	>10.0 mm			
16	IDCa, LG with DCIS	Invasive	<1.0 mm	3.0 mm	<1.0 mm	>10.0 mm	<1.0 mm	>10.0 mm	Y	NEG	FN
		DCIS/LCIS	<1.0 mm	3.0 mm	POSITIVE	9.0 mm	POSITIVE	>10.0 mm			
17	Solid Papillary Ca, HG with DCIS	Invasive	>10.0 mm	9.0 mm	>10.0 mm	>10.0 mm	>10.0 mm	>10.0 mm	Y	NEG	TN
		DCIS	2.0 mm	7.0 mm	>10.0 mm	>10.0 mm	>10.0 mm	>10.0 mm			
18	NAC, Complete PR	No tumor	-	-	-	-	-	-	Y	POS	FP
19	IDCa, LG	Invasive	>10.0 mm	>10.0 mm	>10.0 mm	>10.0 mm	8.5 mm	8.0 mm	Y	POS	FP
20	IDCa, IG with DCIS	Invasive	>10.0 mm	>10.0 mm	>10.0 mm	>10.0 mm	>10.0 mm	>10.0 mm	N	POS	FP
		DCIS	>10.0 mm	>10.0 mm	>10.0 mm	>10.0 mm	>10.0 mm	>10.0 mm			
21	IDCa, HG with DCIS	Invasive	>10.0 mm	>10.0 mm	>10.0 mm	>10.0 mm	>10.0 mm	>10.0 mm	N	NEG	TN
		DCIS	>10.0 mm	>10.0 mm	>10.0 mm	>10.0 mm	>10.0 mm	>10.0 mm			
22	Cellular Fibroadenoma	Benign	0.6 mm	0.8 mm	3.4 mm	0.6 mm	2.1 mm	1.4 mm	Y	NEG	TN
23	Benign FCD	Benign	1.0 mm	1.5 mm	0.6 mm	2.0 mm	0.8 mm	1.3 mm	Y	NEG	TN
24	IDCa, LG with DCIS	Invasive	2.7 mm	>10.0 mm	>10.0 mm	>10.0 mm	>10.0 mm	>10.0 mm	Y	NEG	FN
		DCIS	4.5 mm	>10.0 mm	>10.0 mm	>10.0 mm	>10.0 mm	>10.0 mm			
25	Mucinous Ca, IG	Invasive	>10.0 mm	>10.0 mm	>10.0 mm	2.0 mm	>10.0 mm	>10.0 mm	Y	POS	FP
26	IDCa, LG	Invasive	>10.0 mm	4.5 mm	>10.0 mm	7.8 mm	7.5 mm	>10.0 mm	Y	POS	FP
27	IDCa, IG with DCIS	Invasive	>10.0 mm	<1.0 mm	>10.0 mm	>10.0 mm	>10.0 mm	>10.0 mm	Y	POS	FP
		DCIS	>10.0 mm	<1.0 mm	>10.0 mm	>10.0 mm	>10.0 mm	>10.0 mm			
28	DCIS only	DCIS	3.0 mm	>10.0 mm	9.0 mm	>10.0 mm	>10.0 mm	>10.0 mm	N	NEG	TN
29	IDCa, LG with DCIS	Invasive	>10.0 mm	9.0 mm	9.0 mm	3.0 mm	>10.0 mm	10 mm	Y	POS	FP
		DCIS	>10.0 mm	>10.0 mm	>10.0 mm	4.0 mm	>10.0 mm	>10.0 mm			
30	IDCa (Tubular-lobular), LG	Invasive	2.0 mm	>10.0 mm	>10.0 mm	>10.0 mm	>10.0 mm	8.0 mm	Y	NEG	TN
31	Complex sclerosing lesion	Benign	>10.0 mm	POSITIVE	2.0 mm	4.0 mm	>10.0 mm	>10.0 mm	Y	POS	TP
32	LCIS, pleomorphic	LCIS	0.7 mm	POSITIVE	>10.0 mm	<1.0 mm	17.0 mm	13.0 mm	Y	POS	TP

Figure S 1: A complete summary of the distance to lesional involvement for each margin of each specimen.

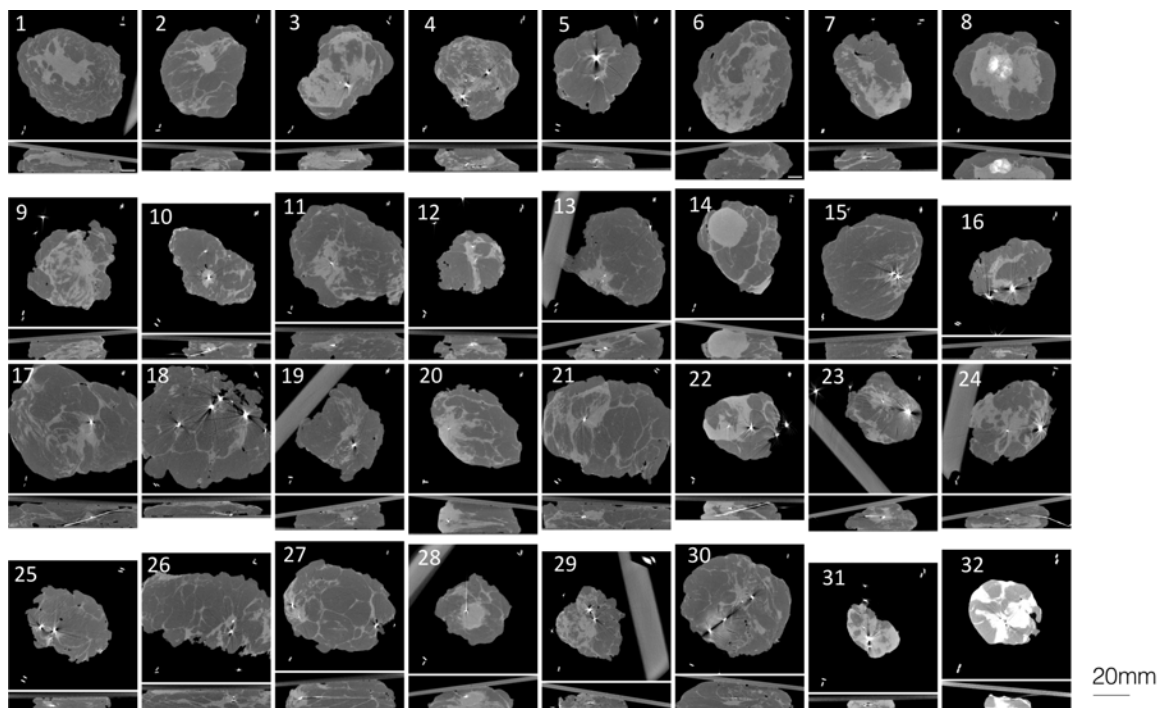


Figure S 2: A montage of illustrative orthogonal micro-CT slices through each lesion of all 32 specimens.

Chapter 9: Conclusions

9.1. Key Findings and Impact

9.1.1. Molecular Dyes for Intraoperative NIR Imaging during BCS

In Chapter 3, a novel margin system was developed for intraoperative imaging of BCS specimens, allowing for NIR sensing of the tissue surface without compromising the surgeon's inking procedure. This technique was validated in a small cohort of n=6 specimens. Whole, dyed, BCS specimens were imaged on all 6 surface planes with NIR structured light imaging directly after excision in the Department of Surgery at DHMC. This novel marking technique could be applied to any BCS assessment device that uses NIR optical sensing.

9.1.2. Light Scatter Imaging and Quantification

In Chapters 4-6, extensive work was performed measuring, quantifying, and analyzing sub-diffusive light scattering in fresh, unprocessed human breast cancer specimens acquired with high spatial frequency structured illumination. In Chapter 4, it was experimentally demonstrated that parameters related to the scatter density and scatter size could be accurately deconvolved, quantified, and imaged in aqueous phantoms, where the scatter size and density were independently varied within the imaging field. Furthermore, spatially resolved sub-diffusive light scattering parameters were measured in a small cohort of n=22 adipose, fibroglandular, fibroadenoma, and invasive carcinoma freshly resected breast tissue specimens. Measured distributions of the light scattering parameters were shown to be sensitive to changes in the breast tissue morphology and also shown to be statistically distinct from one another. Spatially resolved sub-diffusive light scattering

parameters were shown to cluster a malignant lesion from connective and adipose regions within a heterogeneous specimen.

In Chapter 5, this method was extended to analyze morphological change within two murine mammary tumors, but only using monochromatic scattering features (i.e. neglecting the scatter slope). The reduced scattering coefficient and phase function parameter were able to uniquely cluster regions of stromal proliferation and necrosis within each tumor, which was validated against a quantitative analysis of co-registered digitized histology.

In Chapter 6, the hypothesis that these light scattering parameters are related to and predictive of the stromal, epithelial, and adipose volume fractions within human breast tissue was tested utilizing an expanded data set of n=31 specimens. These histologic metrics were calculated from a color-based analysis of co-registered, digitized H&E slides. Explicit relationships between the light scattering parameters and the histologic metrics were determined. Specimen mean stromal, epithelial, and adipose volume fractions predicted from light scattering parameters strongly correlated with those calculated from digitized histology slides ($r = 0.90, 0.77, 0.91$ respectively, $p\text{-value}<1e-6$). The ratio of predicted epithelium to stroma volume fractions classified malignant specimens with a sensitivity and specificity of 90% and 81%, and classified all pixels in malignant lesions with a sensitivity and specificity of 63% and 79%. These findings demonstrate how light scattering parameters acquired with structured light imaging can be used to accurately predict and spatially map stromal, epithelial, and adipose proportions in fresh unstained, human breast tissue, and suggest that these estimations could provide diagnostic value. Finally, this work provides a biological model describing

how light scattering in human breast tissue is explicitly related to changes in collagen, cellularity, and adipose.

9.1.3. Optical-CT Multimodal System Development & Translation

In Chapter 7, a novel multimodal system was developed combining multispectral structured light imaging (SLI) with micro-CT, and its performance metrics were experimentally quantified. The SLI system demonstrated a maximum spatial resolution of 3.78 cycles/mm at the highest spatial illumination frequency of 1.37 mm^{-1} and at the shortest projection wavelength of 490 nm. Optical scattering properties were accurately recovered with ratios of μ_s'/μ_a as low as 0.8. Furthermore, an algorithm was developed to co-register and visualize the 3D volumetric micro-CT data and the superficial SLI data, which was experimentally shown to be accurate within 0.7 mm. Proof-of-principle was demonstrated on a surgically excised and dissected BCS specimen, in which the micro-CT was able to detect micro-calcifications and also had an SNR of 31. The optical system showed maximum contrast between adipose and an invasive lobular carcinoma lesion at the highest spatial frequency of 1.37 mm^{-1} with 490 nm illumination, and showed maximum contrast between fibrocystic disease and the invasive lobular carcinoma lesion again at the highest spatial frequency with 700nm illumination. Finally, to handle large BCS tissue specimens and create a flat imaging surface, an in house custom made optically clear tissue holder apparatus was developed.

A clinical study began with this new system to accrue multimodal data of surgically excised and dissected BCS specimen slices of various tumor subtypes, which began during manuscript preparation and is currently ongoing. To date, n=69 BCS specimen slices across 8 tumor subtypes have been measured with the next generation

multimodal system and co-registered to annotated histopathology, revealing qualitative morphological difference that were not considered in the previous analyses. Specifically, in the previous study imaging resected breast tissue specimens, discussed in Chapter 4 and 6, all tumor subtypes were lumped together and broadly characterized as invasive cancer. But with this expanded data set of higher quality SLI images, stratified across 8 tumor sub-types, new analysis can be performed to distinguish more subtle morphological features. It is worth mentioning that during a BCS procedure, the tumor subtype will already be confirmed from the needle core biopsy, and so future diagnostic classification algorithms may assume that a particular, known tumor subtype is of interest. In Fig. 9.1, color images at both diffuse (top row) and high spatial frequency (bottom row) illuminations are shown for representative case examples of some common malignant tumor subtypes, with the lesions outlined in red. Below the images, is a table summarizing the distribution of malignant and benign pathologies for primary lesions from all specimens imaged to date for which corresponding pathology is available

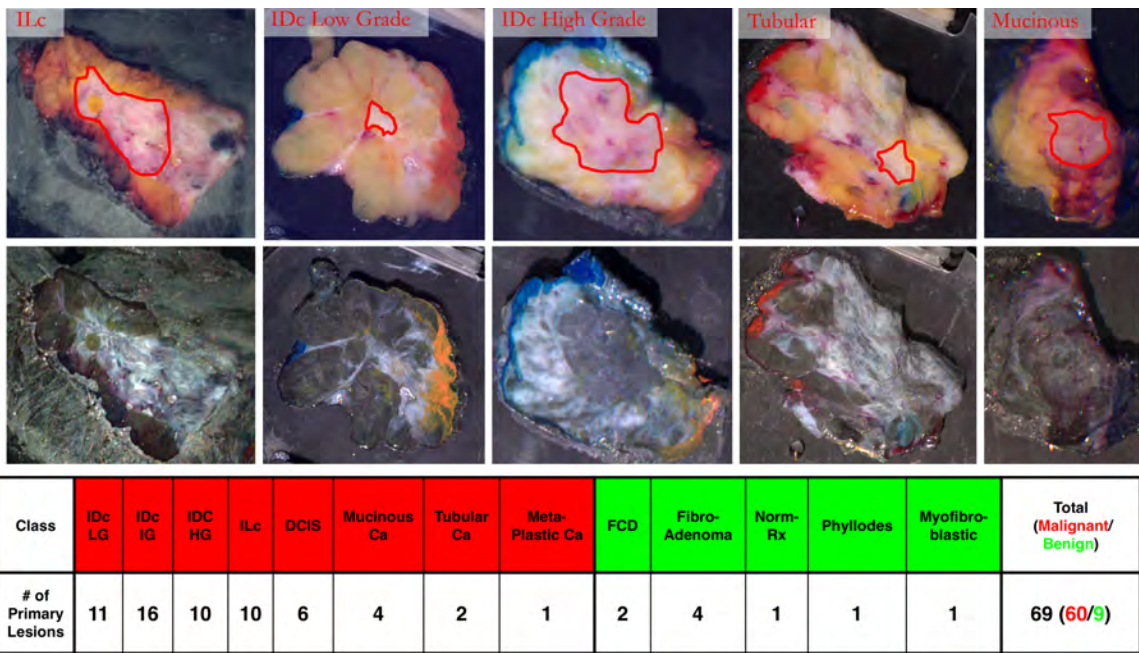


Figure 9.1 Representative color images of five common malignant lesion diagnoses, which were reconstructed from diffuse ($f_x = 0 \text{ mm}^{-1}$, top row) and high spatial frequency ($f_x = 1.37 \text{ mm}^{-1}$, bottom row) visible wavelengths as described in McClatchy et al. 2017. Lesions boundaries are outlined in red. Below the images is a table summarizing the pathologic distribution of primary lesions from all specimens imaged to date for which corresponding pathology is available. Abbreviations: Ca = Invasive Cancer; IDc = Invasive Ductal Carcinoma; LG = Low Grade; IG = Intermediate Grade; HG = High Grade; ILc = Invasive Lobular Carcinoma; FCD = Fibrocystic Disease; Norm-Rx = Treated with Neoadjuvant Chemotherapy.

9.1.4. Micro-CT Analysis of Whole Lumpectomy Specimens

The work presented in Chapter 8 represents the first systematic study comparing micro-CT readings of whole lumpectomy specimens to the final pathological margin status, which was performed on a cohort of n=32 specimens. The blinded observational study yielded promising results with a 66% accuracy between the radiologist's diagnosis and the final pathological diagnosis. The vast majority (9/11) of the misread cases were false positives, resulting in a poor positive predictive value of 25% but a good negative predictive value of 90%. Furthermore, while a false positive and excising unnecessary tissue is always undesirable, it may be more desirable than a false negative leading to a subsequent surgical procedure, and indeed the practice of undirected whole margin cavity

shaving on all BCS procedures has been investigated with this in mind[1]. Additionally, there was no initial training of the radiologist, who had never read a BCS specimen micro-CT. The data also showed that at DHMC, a margin less than 2 mm was significantly more likely to occur on the anterior or posterior (AP) margins, compared to the orthogonal margins ($p<0.02$). This is extremely interesting as AP projection radiography is standard of care at DHMC, but AP projections are inherently insensitive to superficial or deep lesions. Thus, this study demonstrated that 3D specimen micro-CT can provide an accurate anatomical information not obtained with specimen radiography, and may provide value in determining margin status.

9.2. Limitations

Despite the several key findings developed and demonstrated in this thesis, some potential drawbacks limiting clinical translation and impact of this work have been identified. In the following subsections, the most notable drawbacks are aggregated and stratified into biological and technical limitations, and solutions to potentially overcome these drawbacks are considered.

9.2.1. Biological Limitations

- The vast majority optical imaging of resected breast tissues analyzed in this thesis has been on slices of tissue cut through the lesion. A possible limitation for clinical translation is the potential change in optical signal experienced when a lesion is imaged superficially at the margin, rather than on its cut surface. Ideally this hypothesis should be investigated by observationally imaging the margins of whole BCS specimens, utilizing the specimen holder device developed in Chapter 7, and comparing the superficial margin signal to cross-section cut tissue signal.

- Lack of X-ray contrast between stromal and malignant lesions remains a notorious challenge as illustrated in Fig. 9.2. A gross image and corresponding histology are shown in Fig. 9.2 (a) and (b), respectively, for a specimen with an invasive ductal carcinoma lesion, approximately 0.5 cm in size, with roughly 0.2 cm of connective tissue between the lesion and specimen margin, as indicated by the green arrow. Unfortunately, there is essentially no contrast between the lesion and connective tissue in the co-registered micro-CT slice, shown Fig. 9.2 (c). In the micro-CT reader study described in Chapter 8, this specimen in particular shown in Fig. 9.2 was falsely diagnosed from the micro-CT reading to have a positive margin. However, this limitation of X-ray CT does motivate the need for superficial light scattering measurements, as light scattering is able to distinguish purely stromal from cellular tissue as demonstrated in Chapter 6.

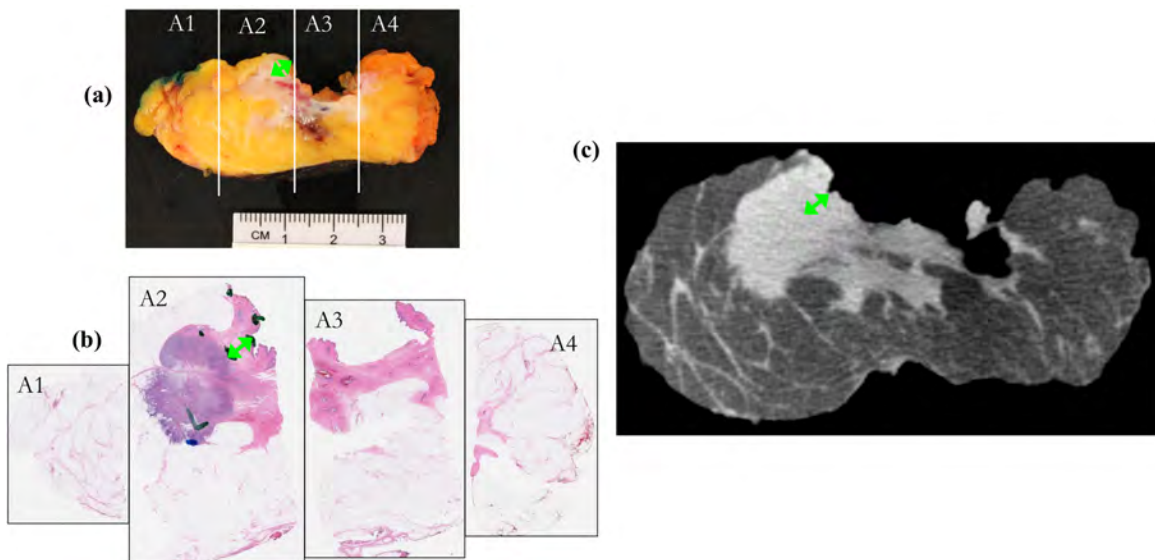


Figure 9.2 (a) Annotated gross analysis image of a “bread loafed” invasive ductal carcinoma surgical specimen. (b) Corresponding tessellated histology reveals a negative margin with connective stroma between the invasive lesion and specimen margin (green arrows). (c) A superficial micro-CT slice of the “bread loafed” specimen. The lack of contrast between the invasive region and the connective stroma is a well-known limitation of X-ray CT.

9.2.2. Technical Limitations

- A potential limitation of the molecular dye specimen marking method described in Chapter 3 is that this method inherently only works in NIR spectrum, as the dyes strongly absorb visible light to create visible contrast. However, if a light scattering technique is being considered, the dyes maybe adequate as they are primarily an absorbing medium. Furthermore, an optically clear tissue holding device could be used to maintain specimen orientation, such as the tissue holding device used in Chapter 7.
- A potential limitation of using sub-diffusive scattering parameters to classify breast tissue intraoperatively is the time needed to fit all of the optical properties at each pixel. One potential solution would be to build a computer with many GPUs to parallelize the optical property computation over all pixels. However, a better solution may be to create a purely empiric model, where optical properties are directly calculated as a function of a few selected reflectance values as was done by Angelo et al.[2], rather than having a least squares minimization routine or a searching routine through a look up table.
- To acquire images over all spatial frequencies and all wavelengths as was done in Chapter 7, the total acquisition time is roughly 8 minutes, which is suboptimal. This could be decreased in the near-term by eliminating redundant data in acquisition protocol determined through a sensitivity analysis. However, a better solution would be to replace the current charged coupled device (CCD) camera and implement a high speed scientific complementary metal oxide semiconductor (CMOS) camera, as the majority of the acquisition time is readout of the CCD.

- A technical limitation observed with the micro-CT is the presence of metal streaking artifacts arising from the surgical clip and wire. A solution would be to implement a metal artifact reduction algorithm[3]. However, most of these reconstruction algorithms operate on the raw projection sinograms, which are not natively saved with the IVIS SpectrumCT acquisition software.

9.3. Proposed Recommendations for Future Work

Over the course of this dissertation work, there has been exciting scientific advances in the microscopy field utilizing ultraviolet light (UV) illumination for superficial depth sectioning and UV autofluorescence as a contrast mechanism[4, 5]. To date, there have been zero published studies or demonstrations of SFDI with a UV source. In Chapter 7, it was demonstrated that highly spatially modulated blue light ($\lambda=490\text{nm}$) provided the best spatial resolution. It follows that a UV sourced SLI system could provide both increased resolution, and also an intrinsic contrast mechanism through spectrally resolved autofluorescence [6] in addition to the endogenous light scattering. Furthermore, the structured illumination of UV autofluorescence could further section the autofluorescence signal to the outermost, superficial of tissue[7]. UV excitation could easily be integrated into the SLI system described in Chapter 7, as the projector receives a standard SMA fiber, which could be coupled to a UV diode laser. The imaging system is contained within a light shielding enclosure, optimized for low light bioluminescence imaging, and currently has a variety of visible and NIR filters on a filter wheel which could be utilized.

References:

1. Chagpar, A.B., et al., *A Randomized, Controlled Trial of Cavity Shave Margins in Breast Cancer*. N Engl J Med, 2015. **373**(6): p. 503-10.
2. Angelo, J., et al., *Ultrafast optical property map generation using lookup tables*. Journal of Biomedical Optics, 2016. **21**(11): p. 110501-110501.
3. Katsura, M., et al., *Current and Novel Techniques for Metal Artifact Reduction at CT: Practical Guide for Radiologists*. Radiographics : a review publication of the Radiological Society of North America, Inc, 2018. **38**(2): p. 450-461.
4. Fereidouni, F., et al., *Microscopy with ultraviolet surface excitation for rapid slide-free histology*. Nature Biomedical Engineering, 2017. **1**(12): p. 957-966.
5. Wong, T.T.W., et al., *Fast label-free multilayered histology-like imaging of human breast cancer by photoacoustic microscopy*. Science Advances, 2017. **3**(5): p. e1602168-e1602168.
6. Croce, A.C. and G. Bottiroli, *Autofluorescence spectroscopy and imaging: a tool for biomedical research and diagnosis*. Eur J Histochem, 2014. **58**(4): p. 2461.
7. Mazhar, A., et al., *Structured illumination enhances resolution and contrast in thick tissue fluorescence imaging*. J Biomed Opt, 2010. **15**(1): p. 010506.

Appendices

Appendix: Selected MATLAB Code

```
function [A,B,musp,gamma,mua] =
Calc_OptProp_Phantom(Id,Id_ref,Rd_ref,fx,lambda,ModelCoeff,n)

% Id - sample x spfq x wv
% musp - sample x wv
% mua - sample x wv
% fx
% n - sample

Rd_exp = Id.*Rd_ref./Id_ref;

start_point=[1 2 1.3.*ones(1,length(lambda)) 10^-2.*ones(1,length(lambda))];
opts = optimset('Algorithm','trust-region-reflective','Display','off','TolFun',10^-
12,'TolX',10^-12,'MaxFunEvals',10^7,'MaxIter',10^7,'ScaleProblem','Jacobian');
% opts = optimset('Algorithm','levenberg-
marquardt','Display','off','ScaleProblem','Jacobian');
model = @expfun;
ub=[10 10 3.*ones(1,length(lambda)) 3.*ones(1,length(lambda))];
lb=[0 0 zeros(1,length(lambda)) zeros(1,length(lambda))];
Params=lsqnonlin(model,start_point,lb,ub,opts);
Params=abs(Params);

A=Params(1);
B=Params(2);
musp(:,1)=A.*(lambda./800).^( -B);
gamma(:,1) = Params(3:3+length(lambda)-1);
mua(:,1) = Params(3+length(lambda):end);
%%
function [ErrorVector] = expfun(Params)

Params=abs(Params);

A=Params(1);
B=Params(2);
musp(:,1)=A.*(lambda./800).^( -B);
gamma(:,1) = Params(3:3+length(lambda)-1);
mua(:,1) = Params(3+length(lambda):end);

for i=1:length(lambda)
    [Rmodel] = Get_R_HYBRID(musp(i),gamma(i),mua(i),fx,ModelCoeff,n);
    Modelpoints(:,i) = Rmodel;
end
Datapoints = Rd_exp;

ErrorVector = (log(Datapoints(:)) - log((Modelpoints(:)))); % Error term to be minmized
during LSR
end
end



---


function [A,B,SO2,THb,Bcar_mm,musp,gamma,mua] =
Calc_OptProp_Tis(Rd_exp,fx,lambda,ModelCoeff,n,mua_nm,mua_oxy,mua_deoxy,mua_fat,mua_water
,mua_Bcar)
% function [musp,gamma,mua] =
Calc_OptProp_Tis(Rd_exp,fx,lambda,ModelCoeff,n,mua_nm,mua_oxy,mua_deoxy,mua_fat,mua_water
,mua_Bcar)

% Id - sample x spfq x wv
% musp - sample x wv
% mua - sample x wv
% fx
% n - sample

start_point=[1 2 .5 0 .05 1.3.*ones(1,length(lambda))];
```

```

opts = optimset('Algorithm','trust-region-reflective','Display','off','TolFun',10^-
12,'TolX',10^-12,'MaxFunEvals',10^7,'MaxIter',10^7,'ScaleProblem','Jacobian');
model = @expfun;

ub=[10 10 1 1 1 3.*ones(1,length(lambda))];
lb=[0 0 0 0 zeros(1,length(lambda))];
[Params,RESNORM,RESIDUAL,EXITFLAG,OUTPUT,LAMBDA,JACOBIAN]=lsqnonlin(model,start_point,lb,
ub,opts);
Params=abs(Params);

A=Params(1);
B=Params(2);
SO2=Params(3);
THb=Params(4);
Bcar_mM = Params(5);
musp(:,1)=A.* (lambda/800).^( -B);
gamma(:,1) = Params(6:6+length(lambda)-1);
mua(:,1) = SO2.*THb.*interp1(mua_nm,mua_oxy,lambda,'spline')+(1-
SO2).*THb.*interp1(mua_nm,mua_deoxy,lambda,'spline')+Bcar_mM.*interp1(mua_nm,mua_Bcar,lambda,
'spline');

function [ErrorVector] = expfun(Params)

Params=abs(Params);

A=Params(1);
B=Params(2);
SO2=Params(3);
THb=Params(4);
Bcar_mM = Params(5);
musp(:,1)=A.* (lambda/800).^( -B);
gamma(:,1) = Params(6:6+length(lambda)-1);
mua(:,1) = SO2.*THb.*interp1(mua_nm,mua_oxy,lambda,'spline')+(1-
SO2).*THb.*interp1(mua_nm,mua_deoxy,lambda,'spline')+Bcar_mM.*interp1(mua_nm,mua_Bcar,lambda,
'spline');

for i=1:length(lambda)
    [Rmodel] = Get_R_HYBRID(musp(i),gamma(i),mua(i),fx,ModelCoeff,n);
    Modelpoints(:,i) = Rmodel;
end
Datapoints = Rd_exp;

ErrorVector = (log(Datapoints(:)) - log((Modelpoints(:)))); % Error term to be minimized
during LSR
end
end

```

```

function [CT_LinAtnCoef,HU,CT_raw] = Calibrate_CT(filepath,filename)

pth_i = [filepath '/' filename '_SEQ/SequenceInfo.txt'];

fid_i = fopen(pth_i,'r');

[filedata] = textscan(fid_i,'%s',-1);
metadata = filedata{1,1};

recon_min = str2double(metadata{191});
recon_max = str2double(metadata{195});
H_air = str2double(metadata{199});
H_h20 = str2double(metadata{203});

CT_raw = double(squeeze(dicomread([filepath '/' filename '_SEQ/CT Data/' filename
'.dcm'])));

CT_LinAtnCoef = (CT_raw./65535).*(recon_max-recon_min)+recon_min;
HU = 1000.* (CT_LinAtnCoef-H_h20)./(H_h20-H_air);
end



---


function [Hc,Hpe,rho_e,zeff] = Calibrate_DualEnergy_CT(filepath,filenameL,filenameH,h)

```

```

mu_water = [0.6697 0.4263];
mu_air = [0.0280 0.0184];
filename = {filenameL,filenameH};
for i = 1:2
    pth_i = [filepath //' filename{i} '_SEQ/SequenceInfo.txt'];
    fid_i = fopen(pth_i,'r');

    [filedata] = textscan(fid_i,'%s',-1);
    metadata = filedata{1,1};

    recon_min = str2double(metadata{191});
    recon_max = str2double(metadata{195});
    H_air = mu_air(i);
    H_h20 = mu_water(i);

    CT_raw = double(squeeze(dicomread([filepath //' filename{i} '_SEQ/CT Data/' filename{i} '.dcm'])));

    CT_LinAtnCoef = (CT_raw./65535).*(recon_max-recon_min)+recon_min;
    if i == 1
        if(exist('h','var')==0)
            HU_A25 = 1000.*((CT_LinAtnCoef-H_h20)./(H_h20-H_air));
        else
            for ind = 1:size(CT_raw,1)
                HU_A25(ind,:,:)=
    1000.*imfilter(squeeze(CT_LinAtnCoef(ind,:,:)),ones(h)./h^2)-H_h20)./(H_h20-H_air);
            end
        end
    else
        if(exist('h','var')==0)
            HU_A50 = 1000.*((CT_LinAtnCoef-H_h20)./(H_h20-H_air));
        else
            for ind = 1:size(CT_raw,1)
                HU_A50(ind,:,:)=
    1000.*imfilter(squeeze(CT_LinAtnCoef(ind,:,:)),ones(h)./h^2)-H_h20)./(H_h20-H_air);
            end
        end
    end
end

Q_A25 = 2.138029703287481;
Q_A50 = 1.241402925185459;

Hc = HU_A50 - (HU_A25-HU_A50).*Q_A50.*(1+Q_A25).*(Q_A25-Q_A50);
Hpe = HU_A25 + (HU_A25-HU_A50).* (1+Q_A50).*(Q_A25-Q_A50);

rho_e_h20 = 3.340*10^23;
Zeff_h20 = 7.42;

rho_e = rho_e_h20.* (1+Hc./1000);
Zeff = nthroot((rho_e_h20.*Zeff_h20.^3.* (1+Hpe./1000)./rho_e),3);
end



---


function [corrCT,segMetal,segArt] =
CT_metalArtifactReduction(CT,level_metal,level_art,sig,method,filter)

% CT      -> Lin Atn. Coef. (important for thresholding metal)
% level_metal -> threshold levold to segment metal (linear attenuation coef.)
% level_art -> threshold levold to segment artifacts (scaled linear attenuation coef.
with distance from metal)
% method -> int [0-6], indicates what inpainting method to use
% filter -> binary flag to indicate whether to suppress very high frequency noise

% corrCT -> CT with metal artifact reduction
% segMetal -> raw CT of metal with all other voxels=0

% defaults
if nargin<2; level_metal = 1.5;level_art = 0.75; sig= 0.02;method=6;filter = true;
end;
if nargin<3; level_art = 0.75;sig= 0.02;method=6;filter = true; end;
if nargin<4; sig= 0.02;method=6;filter = true; end;

```

```

if nargin<5; method=6;filter = true; end;
if nargin<6; filter = true; end;

if filter
    [X,Y] = meshgrid(1:800,1:800);
    R = ((X-400.5).^2+(Y-400.5).^2).^0.5;
    Kernal = exp(-R.^2./30000);
end

corrCT = zeros(size(CT));
segMetal = zeros(size(CT));

proj_xy = 0.5; % half angle rotation
dist = 2044; % 306.6 mm from center 2 source

D = bwdist(CT>level_metal);
R = D./max(D(:));
G = exp(-R.^2/sig^2);
W = G.*CT;

for z = 1:size(CT,1)
    testImage=squeeze(CT(z,:,:)); %Get slice

    testSegImage = testImage;
    testSegImage(W(z,:,:)<level_art) = 0; %Segment metal artifact

    if sum(testSegImage(:)>0)

        % Forward Project Sinogram
        Ir =
fanbeam(testImage,dist,'FanRotationIncrement',proj_xy,'FanSensorGeometry','line');
        IrSeg =
fanbeam(testSegImage,dist,'FanRotationIncrement',proj_xy,'FanSensorGeometry','line');

        Idiff = Ir;
        Idiff(IrSeg>0) = NaN;
        if method<6
            Idiff=inpaint_nans(Idiff,method); %Inpaint Metal in Sinogram
        else
            sensors = 1:size(Idiff,1);
            for i = 1:size(Idiff,2)
                temp =
interp1(sensors(~isnan(Idiff(:,i))),Idiff(~isnan(Idiff(:,i)),i),sensors(isnan(Idiff(:,i))
),'spline');
                Idiff(isnan(Idiff(:,i)),i) = temp;
            end
        end

        testReconDiff =
ifanbeam(Idiff,dist,'FanRotationIncrement',proj_xy,'FanSensorGeometry','line','OutputSize
',800);

        testReconCorr = testReconDiff;
        testReconCorr(testImage>level_metal) = testImage(testImage>level_metal); %Put
CT of metal back to CT with metal artifact removed from sinogram

        if filter
            testReconCorr =
real(ifft2(ifftshift(fftshift(fft2(testReconCorr)).*Kernal)));
        end

        testReconCorr(testReconCorr<0) = 0;

        corrCT(z,:,:)= testReconCorr;
        segMetal(z,:,:)= testImage.*(testImage>level_metal);
        segArt(z,:,:)= testSegImage;
    else
        if filter
            testImage = real(ifft2(ifftshift(fftshift(fft2(testImage)).*Kernal)));
        end
        corrCT(z,:,:)= testImage;
        segMetal(z,:,:)= zeros(size(testImage));
        segArt(z,:,:)= zeros(size(testImage));
    end
end

```

```

        end
    end
end



---


function [] = Get_Demod(filepath,scan_name,output_filepath,output_name,exp,rot)

wv = [490 550 600 650 700 750 800]; % nm
dim = 1024; % pixel
crop = [469 425]; %left and top coord;

if rot == 0
    %NoArt%
    spfq = 5.9523./[128 40 9+5/6 7+2/3 6+1/2 4+1/3];
    % spfq = 0.0465      0.1488      0.6053      0.7764      0.9157      1.3736
else
    %NoArt ROTATION%
    spfq = 5.9523./[40 9+5/6 4+1/3 4+1/3 4+1/3 4+1/3];
    % spfq = [0.1488      0.6053      1.3736 (0 deg) 1.3736 (45 deg) 1.3736 (90 deg) 1.3736
(135 deg)];
end

exp_scale = zeros(length(wv),length(scan_name));
im_scale = zeros(length(spfq)*3,length(wv),length(scan_name));
Im = zeros(dim,dim,length(spfq)*3,length(wv),length(scan_name));
Idemod = zeros(dim,dim,length(spfq)+1,length(wv),length(scan_name));

for k = 1:length(scan_name)
    % read in file for heights plus sample
    fid = fopen([filepath scan_name{k} '.bin']);
    for j = 1:length(wv)
        for i = 1:length(spfq)*3
            temp = flip(imrotate(fread(fid,[dim dim],'uint32',0,'b'),-90),2);
            Im(:,:,i,j,k) = Undistort(temp,1,1,crop(1)-512,crop(2)-512);
        end
    end
    fclose(fid);

    %calc exp times
    exp_scale(:,k) = Scale_Exp(exp(k),wv);

    %demodulate
    for i = 1:length(spfq)
        for j = 1:length(wv)
            i1 = Im(:,:,i-1)*3+1,j,k);
            i2 = Im(:,:,i-1)*3+2,j,k);
            i3 = Im(:,:,i-1)*3+3,j,k);

            % scale each phase so that they have they same mean
            roi1 = i1(295:730,255:795); roi2 = i2(295:730,255:795); roi3 =
i3(295:730,255:795);
            scl1 = mean(roi1(:))./mean([roi1(:); roi2(:); roi3(:)]);
            scl2 = mean(roi2(:))./mean([roi1(:); roi2(:); roi3(:)]);
            scl3 = mean(roi3(:))./mean([roi1(:); roi2(:); roi3(:)]);

            im_scale((i-1)*3+1:(i-1)*3+3,j,k) = [scl1; scl2; scl3];
            if i == 1
                Idemod(:,:,i,j,k) = ((i1./scl1 + i2./scl2 + i3./scl3)./3);
            end
            Idemod(:,:,i+1,j,k) = (2^0.5/3)*((i1./scl1 - i2./scl2).^2+(i1./scl1 -
i3./scl3).^2+(i3./scl3 - i2./scl2).^2).^0.5;
        end
    end

    Data.scl = im_scale;
    Data.Id = Idemod;
    Data.wv = wv;
    Data.dim = dim;
    Data.spfq = spfq;
    Data.date = date;
    Data.exp = exp_scale;
    Data.name = scan_name;

```

```

Data.pth = filepath;
Data.crop = crop;

mkdir(output_filepath);

save([output_filepath output_name '.mat'],'Data','-v7.3')

end



---


function [mip,slice] = Get_MIP_CT(CT_LinAttnCoef)

p(:,1) = (CT_LinAttnCoef(185:-1:1,260,90));
p(:,2) = (CT_LinAttnCoef(185:-1:1,530,725));
p(:,3) = (CT_LinAttnCoef(185:-1:1,20,560));
p(:,4) = (CT_LinAttnCoef(185:-1:1,770,245));

h = zeros(4,1);
for i = 1:4
    tmp = find(p(:,i)>0.15);
    if ~isempty(tmp)
        h(i) = tmp(1);
    else
        h(i) = 184;
    end
end

mip = imrotate(squeeze(max(CT_LinAttnCoef(185-min(h):185,:,:),[],1)),90);
slice = imrotate(squeeze(CT_LinAttnCoef(185-min(h),:,:)),90);
end



---


function [mua_il,musp_il,gamma_il,PF_il,CosT_il]=Get_OptProp_IL(lambda,IL_percent)

%percent in set [0 100], lambda in nm
%scattering coefficients from Michaels and Kienle paper
kpset=[8.261E+1 -1.288E-1 6.093E-5];

%Calculate musp in stock 20% IL solution
ILbasemusp=kpset(1) + kpset(2).*lambda +kpset(3).*lambda.^2;

%absorption coefficients from Michaels and Kienle paper
kwater=[3.066E+5 5.413E+1 1.770E+3];
ksoy=[1.171E+5 -3.659E+1 -3.210E+2];

%Calculate musp in stock 20% IL solution
ILbasemusa_water=kwater(1)./(1+ exp(-(lambda-kwater(3))./kwater(2))) ;
ILbasemusa_soy=ksoy(1)./(1+ exp(-(lambda-ksoy(3))./ksoy(2)));
ILbasemusa_stock=0.226.*ILbasemusa_soy+(1-0.226).*ILbasemusa_water;

%Calculate gamma in stock 20% IL solution
CT=[-1:0.0001:1]; %cos(theta)
kIL=[-1.913e0;-1.292e0;6e-1;1.079e-4;1.854e-1;-1.423e-3;2.857e-6;9.945e-1;5.503e-2]; %params

for i = 1:length(lambda)
    PfIL20(i,:)=10.^((kIL(1) + kIL(2).*(-CT) + kIL(3).*(-CT).^2 + kIL(4).*lambda(i))./(1 + kIL(5).*(-CT) + kIL(6).*lambda(i) + kIL(7).*lambda(i).^2));
    PfIL20(i,:)=PfIL20(i,:)/(sum(pi.*PfIL20(i,:).*sin(acos(CT))./(length(CT)-1))*2*pi);
    gIL20_est(i,:)=trapz((CT).*PfIL20(i,:))/trapz(PfIL20(i,:));
    g2IL20_est(i,:)=(3*(trapz(PfIL20(i,:)*(CT).^2)/trapz(PfIL20(i,:)))-1)/2 ;
    gamma_il(i,:)=(1-(g2IL20_est(i,:)))./(1-gIL20_est(i,:));
end

ILfrac=IL_percent./22.6;

for i=1:length(ILfrac)
    musp_il(:,i)=ILfrac(i).*ILbasemusp';
    mua_il(:,i)=ILfrac(i).*ILbasemusa_stock'+(1-ILfrac(i)).*ILbasemusa_water';
end

CosT_il=CT;
PF_il=PfIL20;

```

```

end



---


function [musp_pb,gamma_pb] = Get_OptProp_PB(lambda,Df,muspAT658 )
%lambda in nm vector, Df vector, muspAt658 used for scaling musp, data is based
%on musp at 658, one musp at a time!
%mua is assumed to be negligible compared to water

load('~/Users/d29957h/Documents/MATLAB/IVIS_SFDI_FILES/Polybead_Opt_Params_FullWavelength.
mat');

lambda = lambda./1000;

musp_pb = ones(length(lambda),length(Df));
gamma_pb = ones(length(lambda),length(Df));

for i = 1:length(Df);
    ind_df = find(Df(i)==fract_dim,1);
    if isempty(ind_df)
        [~,isort]=sort(abs(Df(i)-fract_dim));
        musp_pb(:,i) = (muspAT658/1.2)*interp2([fract_dim(isort(1))
fract_dim(isort(2))],wv,musp_mix_scale(:,[isort(1) isort(2)]),Df(i),lambda,'spline');
        gamma_pb(:,i) = interp2([fract_dim(isort(1))
fract_dim(isort(2))],wv,gamma_PF(:,[isort(1) isort(2)]),Df(i),lambda,'spline');
    else
        musp_pb(:,i) =
(muspAT658/1.2)*interp1(wv,musp_mix_scale(:,ind_df),lambda,'spline');
        gamma_pb(:,i) = interp1(wv,gamma_PF(:,ind_df),lambda);
    end
end
end



---


function [ Rmodel ] = Get_R_HYBRID(musp, gamma, mua, fx, ModelCoeff, n)

Reff=-1.440/n^2+0.710/n+0.668+0.0636*n;%assumes air-tissue interface
ETA=(1-Reff)/2/(1+Reff);
mutr=musp+mua;
DS=musp./(fx+eps);

ind_d = fx<=0.2;
ind_sd = fx>=0.45;

etafit=ModelCoeff(1);
rho1=ModelCoeff(2).*gamma.^2;
rho2=ModelCoeff(3).*gamma;
rho3=ModelCoeff(4).*gamma;
rho4=ModelCoeff(5)./gamma.^2;

%diffuse
mueff = (3*mua*mutr+(2*pi*fx(ind_d)).^2).^0.5;

Rmodel_hybrid_d(:,1)=(etafit).*[(3*ETA*musp/mutr)./((1+mueff./mutr).*(3*ETA+mueff./mutr))
];
Rmodel_hybrid_sd(:,1)=etafit.*((1+(rho4).*(DS_sd).^( -(rho3)).*[(DS_sd.^rho2)./(rho1+(DS_sd.^rho2))]));
Rmodel=[Rmodel_hybrid_d;Rmodel_hybrid_sd];
end



---


function [RGB_L,RGB_H,HSF_B] = Get_RGB_IM(Data,indTis,isRot)

%only does lowest and highest spatial frequency
%if is rot, averages the last 4 spatial frequencies

Id = Data.Id;
exp = Data.exp;
wv = Data.wv;
spfq = Data.spfq;

```

```

dim = Data.dim;
roi = zeros(1024); roi(400:600,400:600) = 1;roi = roi>0;

indSpec = size(Id,5);

wv_length = sum(wv<=700);

% get xyz values for visible wavelengths
[x, y, z, nm, xyz] = Get_CIE();
for j = 1:wv_length
    ind = find(wv(j) == nm);
    x_test(j)=sum(x(ind-1:ind+1,2));
    y_test(j)=sum(y(ind-1:ind+1,2));
    z_test(j)=sum(z(ind-1:ind+1,2));
end
x_test = x_test./sum(x_test(:));
y_test = y_test./sum(y_test(:));
z_test = z_test./sum(z_test(:));

% create rgb image for phantom
rgb = zeros(dim,dim,3,2);
rgb_wball = zeros(dim,dim);rgb_wbal2 = zeros(dim,dim);rgb_wbal3 = zeros(dim,dim);
for k = [indSpec indTis]
    ind = 1;
    for i = [1 length(spfq)+1]
        if k == indSpec
            for j = 1:wv_length
                rgb_wball(:,:,j) = rgb_wball(:,:,j)+(medfilt2(Id(:,:,i,j,k),[3
3])./exp(j,k)).*x_test(j);
                rgb_wbal2(:,:,j) = rgb_wbal2(:,:,j)+(medfilt2(Id(:,:,i,j,k),[3
3])./exp(j,k)).*y_test(j);
                rgb_wbal3(:,:,j) = rgb_wbal3(:,:,j)+(medfilt2(Id(:,:,i,j,k),[3
3])./exp(j,k)).*z_test(j);
            end
            rgb_wbal_val(1,ind) = squeeze(mean(mean(rgb_wball(roi),1),2));
            rgb_wbal_val(2,ind) = squeeze(mean(mean(rgb_wbal2(roi),1),2));
            rgb_wbal_val(3,ind) = squeeze(mean(mean(rgb_wbal3(roi),1),2));
            rgb_wball = zeros(dim,dim);rgb_wbal2 = zeros(dim,dim);rgb_wbal3 =
zeros(dim,dim);
        else
            for j = 1:wv_length
                if isRot==1 & i == length(spfq)+1
                    rgb(:,:,1,ind) = rgb(:,:,1,ind)+(medfilt2(mean(Id(:,:,i-
3:i,j,k),3),[3 3])./exp(j,k)).*x_test(j);
                    rgb(:,:,2,ind) = rgb(:,:,2,ind)+(medfilt2(mean(Id(:,:,i-
3:i,j,k),3),[3 3])./exp(j,k)).*y_test(j);
                    rgb(:,:,3,ind) = rgb(:,:,3,ind)+(medfilt2(mean(Id(:,:,i-
3:i,j,k),3),[3 3])./exp(j,k)).*z_test(j);
                else
                    rgb(:,:,1,ind) = rgb(:,:,1,ind)+(medfilt2(Id(:,:,i,j,k),[3
3])./exp(j,k)).*x_test(j);
                    rgb(:,:,2,ind) = rgb(:,:,2,ind)+(medfilt2(Id(:,:,i,j,k),[3
3])./exp(j,k)).*y_test(j);
                    rgb(:,:,3,ind) = rgb(:,:,3,ind)+(medfilt2(Id(:,:,i,j,k),[3
3])./exp(j,k)).*z_test(j);
                end
            end
            rgb(:,:,:,:,ind) = xyz2rgb(rgb(:,:,:,:,ind),'WhitePoint',rgb_wbal_val(:,:,ind)');
            temp_p = rgb(:,:,:,:,ind);
            rgb(:,:,:,:,ind) = rgb(:,:,:,:,ind)-prctile(temp_p(:,0.25);
            rgb(:,:,:,:,ind) = rgb(:,:,:,:,ind)./prctile(temp_p(:,99.75);
        end
    ind = ind+1;
end
end

rgbl = (rgb(:,:,1));
rgbh = (rgb(:,:,end));
rgbl(rgbl>1) = 1;
rgbh(rgbh>1) = 1;
rgbl(rgbl==0) = 1;
rgbh(rgbh==0) = 1;

```

```

RGB_L = rgbl(101:900,101:900,:);
RGB_H = rgbh(101:900,101:900,:);

hsf = medfilt2(Data.Id(:,:,end,1,indTis),[3 3]);
hsf = hsf-prctile(hsf(:,0.1);
hsf = hsf./prctile(hsf(:,99.9);
hsf(hsf>1) = 1;

HSF_B = hsf(101:900,101:900,:);
end



---


function [RGB_WHOLE] = Get_RGB_WHOLE_LUMP(filepth,name,spec)

crop = [469 425];
exp = Scale_Exp(0.2,[490 550:50:700]);
exp_spec = Scale_Exp(0.1,[490 550:50:700]);
wv = [490 550:50:700];
dim = 1024;
roi = zeros(1024); roi(400:600,400:600) = 1;roi = roi>0;

% read tissue image (projection file of repeat 6)
fid = fopen([filepth name '.bin']);
for j = 1:length(wv)
    for rep = 1:5
        temp = flip(imrotate(fread(fid,[dim dim],'uint32',0,'b'),-90),2);
        Im(:,:,j,rep) = Undistort(temp,1,1,crop(1)-512,crop(2)-512);
    end
end
fclose(fid);
Id = mean(Im,4);

% read spec image (NoArt or NoArt_wRotation)
fid = fopen([filepth spec '.bin']);
for j = 1:length(wv)
    for rep = 1:18
        temp = flip(imrotate(fread(fid,[dim dim],'uint32',0,'b'),-90),2);
        Im_spec(:,:,j,rep) = Undistort(temp,1,1,crop(1)-512,crop(2)-512);
    end
end
fclose(fid);
Id_spec = mean(Im_spec,4);

% get xyz values for visible wavelengths
[x, y, z, nm, xyz] = Get_CIE();
for j = 1:length(wv)
    ind = find(wv(j) == nm);
    x_test(j)=1.*trapz(x(ind-1:ind+1,2));
    y_test(j)=1.*trapz(y(ind-1:ind+1,2));
    z_test(j)=1.*trapz(z(ind-1:ind+1,2));
end
x_test = x_test./sum([x_test(:)]);
y_test = y_test./sum([y_test(:)]);
z_test = z_test./sum([z_test(:)]);

for j = 1:length(wv)
    Id_scl(:,:,j) = (medfilt2(Id(:,:,j),[3 3])./exp(j));
    Id_scl(:,:,j) = (medfilt2(Id(:,:,j),[3 3])./exp(j));
    Id_scl(:,:,j) = (medfilt2(Id(:,:,j),[3 3])./exp(j));

    Id_spec_scl(:,:,j) = (medfilt2(Id_spec(:,:,j),[3 3])./exp_spec(j));
    Id_spec_scl(:,:,j) = (medfilt2(Id_spec(:,:,j),[3 3])./exp_spec(j));
    Id_spec_scl(:,:,j) = (medfilt2(Id_spec(:,:,j),[3 3])./exp_spec(j));
end

% create rgb image for phantom
rgb = zeros(dim,dim,3);
rgb_spec = zeros(dim,dim,3);
for j = 1:length(wv)
    rgb(:,:,1) = rgb(:,:,1)+Id_scl(:,:,j).*x_test(j);
    rgb(:,:,2) = rgb(:,:,2)+Id_scl(:,:,j).*y_test(j);
    rgb(:,:,3) = rgb(:,:,3)+Id_scl(:,:,j).*z_test(j);

```

```

rgb_spec(:,:,1) = rgb_spec(:,:,1)+Id_spec_scl(:,:,j).*x_test(j);
rgb_spec(:,:,2) = rgb_spec(:,:,2)+Id_spec_scl(:,:,j).*y_test(j);
rgb_spec(:,:,3) = rgb_spec(:,:,3)+Id_spec_scl(:,:,j).*z_test(j);
end

rgb(:,:,1) = rgb(:,:,1) - mean(mean(rgb(1:25,1:25,1)));
rgb(:,:,2) = rgb(:,:,2) - mean(mean(rgb(1:25,1:25,2)));
rgb(:,:,3) = rgb(:,:,3) - mean(mean(rgb(1:25,1:25,3)));

rgb_spec(:,:,1) = rgb_spec(:,:,1) - mean(mean(rgb_spec(1:25,1:25,1)));
rgb_spec(:,:,2) = rgb_spec(:,:,2) - mean(mean(rgb_spec(1:25,1:25,2)));
rgb_spec(:,:,3) = rgb_spec(:,:,3) - mean(mean(rgb_spec(1:25,1:25,3)));

r = rgb_spec(:,:,1);g = rgb_spec(:,:,2);b = rgb_spec(:,:,3);
xyz2rgb(rgb(:,:,1),'WhitePoint',[1.*prctile(prctile(r(400:600,400:600),95),95)
1.*prctile(prctile(g(400:600,400:600),95),95)
1.*prctile(prctile(b(400:600,400:600),95),95)]);

rgb(:,:,:) = rgb(:,:,:)-prctile(rgb(:,0.25);
rgb(:,:,:,:) = rgb(:,:,:,:)/prctile(rgb(:,99.75);

rgb(rgb>1) = 1;
rgb(rgb<0) = 0;

RGB_WHOLE = rgb;
end

```

```
function [SOI_B, SOI_R] = Get_Rotation_SOI(Data_ROT,indTis)
```

```

tmp_b = Data_ROT.Id(:,:,4:7,1,indTis);
tmp_r = Data_ROT.Id(:,:,4:7,5,indTis);

SOI_B = abs(log(medfilt2((max(tmp_b,[],3)-
min(tmp_b,[],3))./(max(tmp_b,[],3)+min(tmp_b,[],3)),[3 3])));
SOI_R = abs(log(medfilt2((max(tmp_r,[],3)-
min(tmp_r,[],3))./(max(tmp_r,[],3)+min(tmp_r,[],3)),[3 3])));

SOI_B = SOI_B-0.5; SOI_B = SOI_B./3.5;
SOI_R = SOI_R-0.25; SOI_R = SOI_R./3.25;
end

```

```
function [Surface3D,Height2D,Thickness2D] = Get3DSurfaceFromCT(CT)
% This function Segments the tissue surface from the tissue holder for
% CT scans of whole lumpectomies
```

```

% input      :   CT -> CT scan
% outputs    :   Surface3D -> binary 3D volume of the segmented tissue
%                 :   Height2D -> 2D image of the height of height of the tissue
%                 :   specimen in mm
%                 :   Thickness2D -> 2D image of the width of the segmented tissue
%                 :   specimen in mm

[X,Y] = meshgrid([1:800],[1:800]);

% Binarize CT scan into background and tissue/holder
CT = imfilter(CT,ones(10,10,10)./10.^3);
CT = imfilter(CT,ones(10,10,10)./10.^3);

level = 0.05;
CT_bin = CT;
CT_bin(CT_bin<=level) = 0;
CT_bin(CT_bin>level) = 1;

% segment top and bottom surfaces of plastic holder by
% finding vectors which go through just top and bottom holder, and not
% tissue
height_top = NaN(800,800);
height_bottom = NaN(800,800);
width = NaN(800,800);

```

```

for i = 1:800
    for j = 1:800
        shape_top = diff(squeeze(CT_bin(1:end,i,j)));
        h = find(shape_top~=0);
        if length(h) == 4 && ...
            (shape_top(h(1))>0) && (shape_top(h(2))<0) && (shape_top(h(3))>0) &&
            (shape_top(h(4))<0) && ...
                ((h(2)-h(1))<30) && ((h(4)-h(3))<30)
                height_top(i,j) = h(1);
                height_bottom(i,j) = h(3);
                % calc width of top plate
                width(i,j) = h(2) - h(1);
        end
    end
end
width = median(width(~isnan(width)));

% erode top and bottom surface (location of non-NaN pixels are the same
% for top and bottom, but values are different)
SE = strel('square',3);
height_morph = imerode(~isnan(height_bottom),SE);
height_morph = imerode(height_morph,SE);

% segment the biggest object in top & bottom surface which will be
% plastic plate, this step may unnessecary
ind = 1:800^2;
stats = regionprops(height_morph,'Area');
imax = find(cell2mat(struct2cell(stats))==max(cell2mat(struct2cell(stats))));
px_idx = regionprops(height_morph,'PixelIdxList');
idx = cell2mat(struct2cell(px_idx(imax)));
height_bottom(setdiff(ind,idx)) = NaN;
height_top(setdiff(ind,idx)) = NaN;

%fit surface to top and bottom tissue holder
Vb =
fit([X(~isnan(height_bottom)),Y(~isnan(height_bottom))],height_bottom(~isnan(height_bottom)), 'poly11');
BottomSurface = round(feval(Vb,X,Y));
BottomSurface(BottomSurface<0) = 0; BottomSurface(BottomSurface>200) = 200;

Vt =
fit([X(~isnan(height_top)),Y(~isnan(height_top))],height_top(~isnan(height_top)), 'poly11');
TopSurface = round(feval(Vt,X,Y));
TopSurface(TopSurface<0) = 0; TopSurface(TopSurface>200) = 200;

% Remove plastic holder from CT
Surface3D = CT_bin;
for ix = 1:800;
    for iy = 1:800;
        if (((ix-400)^2+(iy-400)^2)^0.5<325)
            Surface3D(1:TopSurface(ix,iy)+width,ix,iy) = 0;
            Surface3D(BottomSurface(ix,iy):end,ix,iy) = 0;
        else
            Surface3D(:,ix,iy) = 0;
        end
    end
end

%erode surface
SE = strel('cube',3);
Surface3D = imerode(Surface3D,SE);
Surface3D = imerode(Surface3D,SE);

% segment biggest object, which is the tissue, to get rid of rubber bands
stats = regionprops(Surface3D>0,'Area');
i_tis = find(cell2mat(struct2cell(stats))==max(cell2mat(struct2cell(stats))));
px_idx = regionprops(Surface3D>0,'PixelIdxList');
idx_tis = cell2mat(struct2cell(px_idx(i_tis)));
Surface3D(idx_tis) = 2;
Surface3D = Surface3D>1;

%dilate surface

```

```

Surface3D = imdilate(Surface3D,SE);
Surface3D = imdilate(Surface3D,SE);
% fill in holes (air bubbles in tissue)
Surface3D = imfill(Surface3D,'holes');

% calc 2D Height
for ix = 1:800;
    for iy = 1:800;
        temp = find(diff(squeeze(Surface3D(:,ix,iy)))>0);
        if ~isempty(temp)
            Height2D(ix,iy) = ((200-temp(1))+0.5)*.15;
        else
            Height2D(ix,iy) = ((200-200)+0.5)*.15;
        end
    end
end
% calc 2D Thickness
Thickness2D = squeeze(sum(Surface3D,1)).*.15;
end



---


function [height] = GetSurfaceFromCT(CTdata)

% 200 x 800 x 800

height = zeros(800,800);

for i = 1:800
    for j = 1:800
        temp = CTdata(:,i,j);
        shape = diff(smooth(temp));
        h = find(shape>2000);
        if ~isempty(h)
            height(i,j) = ((200-h(1))+0.5)*.15;
        else
            height(i,j) = ((200-200)+0.5)*.15;
        end
    end
end
end



---


function [ exp_scl ] = Scale_Exp( exp, wv )

params = [1.1109e-12 -7.8132e-10 2.1288e-07 -2.4963e-05 9.9686e-04 6.2859e-03
1.3840e+00];

x = wv-550;

scl = params(1).*x.^6 + params(2).*x.^5 + params(3).*x.^4 + ...
params(4).*x.^3 + params(5).*x.^2 + params(6).*x + params(7);

exp_scl = round(exp.*scl./(1/60)).*(1/60);

end



---


function Im = Undistort(i,bin_,vf_,cx_, cy_)

% bin - binning of image; default 1 (no bin)
% vf - vertical flip needed if acquired with labview; default 1 (need flip)
% cx_, cy_ - coordinates (in pixels) of the optical center (offset from
% center values)

if nargin == 1
    cx = 511.5;
    cy = 511.5;
    vf = 1;
    bin = 1;
elseif nargin == 2
    cx = 511.5;
    cy = 511.5;
    vf = 1;

```

```

        bin = bin_;
    elseif nargin == 3
        cx = 511.5;
        cy = 511.5;
        vf = vf_;
        bin = bin_;
    else
        cx = 511.5+cx_;
        cy = 511.5+cy_;
        vf = vf_;
        bin = bin_;
    end

    if vf
        i = flip(i,1);
    end

    fx = 2.00404203e4; % camera focal lengths
    fy = 2.00404203e4;

    scl = size(i,1).*bin/2048; %scale center if image is cropped
    cx=scl.*cx; cy=scl.*cy;

    I = (2/bin).*[fx 0 0; 0 fy 0; cx cy 1];

    r = [-5.655328826e1 -1.27512604e3 -1.58745666e0]; %radial distortion parameters
    t = [7.1659384e-2 -7.5840314114e-2]; %tangential distortion parameters

    cp = cameraParameters('IntrinsicMatrix',I,'RadialDistortion',r,'TangentialDistortion',t);

    Im = undistortImage(i,cp,'OutputView','same');

    if vf
        Im = flip(Im,1);
    end
end



---


function [outI, outZ] = createSurfaceMesh(CTImage, opticalImage, cx, cy, t, outMesh)
% createSurfaceMesh Creates a mesh of a CT surface and colors it using an image
%   Inputs:
%     CTImage: File name for the CT image
%     opticalImage: File name for the optical image
%     cx: X coordinate of camera center in optical image
%     cy: Y coordinate of camera center in optical image
%     t: Transform from camera space to CT space
%     outMesh: Output mesh file name
%
%   Outputs:
%     outI: Version of the optical image in CT voxel coordinates
%     outZ: The height map generated from CT, should be aligned
%           with OutI
%
%   The resulting mesh can be previewed in MATLAB using:
%     surf(outZ,outI,'linestyle','none'); axis equal;

%% Set up images

im = imread(opticalImage);
im2 = Undistort(im, cx, cy);
im3 = rot90(im2,3);
% im2 = imrotate(flip(imread(opticalImage)),90); %edit by Bo: assume image is
undistorted at rotated
% im3 = flip(imread(opticalImage),2);

ncx = cy; % new x and y camera center coordinates
ncy = size(im2,2) - cx + 1; % done to correct for the image rotation
[rs,cs] = size(im3);

ct = double(squeeze(dicomread(CTImage)));
[s,r,c] = size(ct);

%% Find surface of object in CT

```

```

Z = zeros(r,c);
for i=1:r
    for j=1:c
        for k=1:s
            if ct(k,i,j) > 17015
                Z(i,j) = s - k;
                break;
            end
        end
    end
end

%% For each voxel in the CT, color it with closest point from scatter image
ct_cx = 436; % x and y coordinates of camera center in CT space
ct_cy = 327; % hard-coded values based on previous experiment

I = zeros(r,c);
for i=1:r
    for j=1:c
        xcoord = ( ((i-ct_cx)*.15)/.126 ) + ncx;
        ycoord = ( ((j-ct_cy)*.15)/.126 ) + ncy;
        if xcoord >= 1 && ycoord >= 1 && xcoord <= rs && ycoord <= cs
            I(i,j) = im3(round(xcoord),round(ycoord));
        end
    end
end

%% Create output mesh
outI = I;
outZ = Z;

[X,Y] = meshgrid(1:r,1:c);
X = X(:); Y = Y(:);
Z = Z'; Z = Z(:);
I = I'; I = I(:);

TRI = delaunay(X,Y);
TRI = TRI-1;

num_node = size(X,1);
num_ele = size(TRI,1);

head{1,:} = '# vtk DataFile Version 2.0';
head{2,:} = 'NIRFAST mesh with solutions';
head{3,:} = 'ASCII';
head{4,:} = 'DATASET POLYDATA';
head{5,:} = ['POINTS ' num2str(num_node) ' float'];
head{6,:} = ['POLYGONS ' num2str(num_ele) ' ' num2str(4*num_ele)];
head{7,:} = ['POINT_DATA ' num2str(num_node)];
head{8,:} = 'SCALARS scattering float 1';
head{9,:} = 'LOOKUP_TABLE default';

fid_o = fopen(outMesh, 'w');

for i =1:5
    fprintf(fid_o, '%s\n', head{i,:});
end

for i = 1:num_node
    pt = [(X(i)*.15)-70.449, (30-Z(i)*.15)-.35, (Y(i)*.15)-70.449];
    % edited by Bo
    %     pt = pt*t.T + t.c(1,:);
    %     fprintf(fid_o,'%.6f %.6f %.6f\n',[pt(3) pt(2) pt(1)]);
    pt_xy = pt([3 1])*t.T + t.c(1,:);
    fprintf(fid_o, '%.6f %.6f %.6f\n', [pt_xy(2) pt(2) pt_xy(1)]);
end

fprintf(fid_o, '%s\n', head{6,:});
for i = 1:num_ele
    fprintf(fid_o, '%d %d %d %d\n', [3 TRI(i,:)]);
end

fprintf(fid_o, '%s\n', head{7,:});

```

```

fprintf(fid_o,'%s\n',head{8,:});
fprintf(fid_o,'%s\n',head{9,:});

for i = 1:num_node
    fprintf(fid_o,'%e\n',I(i));
end

fclose(fid_o);

end

=====
%
% nrrdwriter_dan
%
% filename - 'myimage.ext' - 'veins.nrrd'
% matrix   - data - Matlab matrix
% encoding - raw, ascii, gzip
%
=====

function ok = nrrdWriter(filename, matrix, encoding)

% This line gets the path, name and extension of our file:
% pathf = /home/mario/.../myfile.myext
% fname = myfile
% ext = .myext
[pathf, fname, ext] = fileparts(filename);

format=ext(2:end); % We remove the . from .ext
% so we extract the output format from the argument filename, instead of
% put two different arguments

matrix = permute(matrix, [2 1 3]); % so we undo permute of index in nrrdreader

dims=(size(matrix));      % matrix dimensions (size NxMxP)
ndims=length(dims);      % number of dimensions (dim n)

=====

% Conditions to make sure our file is going to be created successfully.
%
% First the code puts the argument 'encoding' in lowercase
encoding = lower(encoding);

encodingCond = isequal(encoding, 'ascii') || isequal(encoding, 'raw') ||
isequal(encoding, 'gzip');
assert(encodingCond, 'Unsupported encoding');

% The same with output format
format = lower(format);
formatCond = isequal(format,'nhdr') || isequal(format,'nrrd');
assert(formatCond, 'Unexpected format');

%Require 2 or 3 dimensions
dimsCond = isequal(ndims, 2) || isequal(ndims, 3);
assert(dimsCond, 'Only 2 or 3 dimensions supported');

=====

% Now, if our conditions are satisfied:
if (encodingCond && formatCond)

    % Header

    % Open, filename (which specifies output format) and write binary
fid = fopen(filename, 'wb');
fprintf(fid,'NRRD0004\n');           % NRRD type 4

    % Type of variable we're storing in our file
mtype=class(matrix);

```

```

outtype=setDatatype(mtype);
fprintf(fid,['type: ', outtype, '\n']);

%
fprintf(fid,['dimension: ', num2str(ndims), '\n']);

fprintf(fid,['sizes: ', num2str(dims), '\n']);

fprintf(fid,['space dimension: ', num2str(ndims), '\n']);

fprintf(fid,['encoding: ', encoding, '\n']);

[~,~,endian] = computer();

if (isequal(endian, 'B'))
    fprintf(fid,' endian: big\n');
else
    fprintf(fid,' endian: little\n');
end

if (isequal(format, 'nhdr')) % Si hay que separar
    % Escribir el nombre del fichero con los datos
    fprintf(fid, ['data file: ', [fname, '.', encoding], '\n']);

    fclose(fid);
    if isequal(length(pathf),0)
        fid = fopen([fname, '.', encoding], 'wb');
    else
        fid = fopen([pathf, filesep, fname, '.', encoding], 'wb');
    end
else
    fprintf(fid, '\n');
end

ok = writeData(fid, matrix, outtype, encoding);
fclose(fid);
end

% =====
% Determine the datatype --> From mtype (matlab) to outtype (NRRD) -->
% =====
function datatype = setDatatype(metaType)

% Determine the datatype
switch (metaType)
case {'int8', 'uint8', 'int16', 'uint16', 'int32', 'uint32', 'int64',...
    'uint64', 'double'}
    datatype = metaType;

case {'single'}
    datatype = 'float';

otherwise
    assert(false, 'Unknown datatype')
end

% =====
% writeData -->
% fidIn is the open file we're overwriting
% matrix - data that have to be written
% datatype - type of data: int8, string, double...
% encoding - raw, gzip, ascii
% =====
function ok = writeData(fidIn, matrix, datatype, encoding)

switch (encoding)
case {'raw'}

    ok = fwrite(fidIn, matrix(:, ), datatype);

case {'gzip'}
```

```

% Store in a raw file before compressing
tmpBase = tempname(pwd);
tmpFile = [tmpBase '.gz'];
fidTmpRaw = fopen(tmpBase, 'wb');
assert(fidTmpRaw > 3, 'Could not open temporary file for GZIP compression');

fwrite(fidTmpRaw, matrix(:), datatype);
fclose(fidTmpRaw);

% Now we gzip our raw file
gzip(tmpBase);

% Finally, we put this info into our nrrd file (fidIn)
fidTmpRaw = fopen(tmpFile, 'rb');
tmp = fread(fidTmpRaw, inf, [datatype '>' datatype]);
cleaner = onCleanup(@() fclose(fidTmpRaw));
ok = fwrite(fidIn, tmp, datatype);

delete (tmpBase);
delete (tmpFile);

case {'ascii'}
    ok = fprintf(fidIn, '%u ',matrix(:));
%ok = fprintf(fidIn,matrix(:), class(matrix));

otherwise
    assert(false, 'Unsupported encoding')
end

```